Title
Exploring Competing Orders in the High-Tc Cuprate Phase Diagram Using Angle Resolved Photoemission Spectroscopy

Author
Garcia, Daniel Robert

Publication Date
2010

Peer reviewed|Thesis/dissertation

Exploring Competing Orders in the High-T_c Cuprate Phase Diagram Using Angle Resolved Photoemission Spectroscopy

by

Daniel Robert Garcia

A dissertation submitted in partial satisfaction
of the requirements for the degree of

Doctor of Philosophy

in

Physics

in the

GRADUATE DIVISION

of the

UNIVERSITY OF CALIFORNIA, BERKELEY

Committee in charge:

Professor Alessandra Lanzara, Chair
Professor Dung-Hai Lee
Professor Yuri Suzuki

Fall 2010

Exploring Competing Orders in the High-T_c Cuprate Phase Diagram Using Angle Resolved Photoemission Spectroscopy

by

Daniel Robert Garcia

Abstract

Exploring Competing Orders in the High-T_c Cuprate Phase Diagram Using Angle Resolved Photoemission Spectroscopy

by

Daniel Robert Garcia

Doctor of Philosophy in Physics

University of California, Berkeley

Professor Alessandra Lanzara, Chair

With more than a quarter century of study, the high temperature superconducting cuprates still represent one of the most active areas of research in condensed matter physics. Its complex phase diagram continues to present challenges to our understanding, stemming from its correlated electronic nature. Being able to tease out the effect of different lattice orderings and their effects on electronic states may be crucial to understanding the physics of the cuprates where such orderings may be crucial to the phase diagram. Thus, because of its ability to directly probe electronic band structure, Angle Resolved Photoemission Spectroscopy (ARPES) is an ideal probe to study the effects of competing orders on electronic states near E_F.

This thesis will be organized in the following way. Chapter 1 provides a broad introduction to the physics central to our work including concepts of band structure and Fermi liquid theory, as well as more exotic phenomena explored throughout the thesis. Chapter 2 introduces the ARPES technique, how it is physically understood via concepts like Green's functions, and traditional methods of data analysis. Chapter 3 explores magnetic ordering and its effect on both core level and valance band states in the iron oxypnictides. From the near-E_F electronic states, we find that the magnetic physics of the parent compound may still be present even at superconducting dopings. Chapter 4 explores charge density wave (CDW) ordering by looking at the rare earth ditellurides. This ARPES work establishes $LaTe_2$ as the first quasi-2D CDW system to behave like a true Peierls transition, with both Fermi surface nesting tied to a metal - to - insulating transition. Chapter 5 explores the effect of lattice strain on electronic states by studying the single layered Bi2201 cuprates with lanthanide substitution. The effect of this substitution competes with superconductivity and appears to enhance bosonic modes acting on the nodal point states which are otherwise unaffected. Chapter 6 takes the specific case of Nd-Bi2201 and finds evidence of a distinct crossover point in the electronic states near E_F segregating the nodal point states. Finally, Chapter 7 provides a summary of our work and its conclusions.

Contents

Acknowledgements

When undertaking a doctoral journey, there are so many people who deserve thanks and recognition for the manifold ways they have made this entire enterprise possible.

First, and foremost, I wish to thank my advisor, Prof. Alessandra Lanzara, who has made this journey possible for me. I thank you for your guidance, wisdom, and faithful support of this work and my studies as well as the generous number of conferences, talks, and experiments you have enabled me to attend. The complicated relationship between a student and their advisor can never be adequately summarized in so few words as these. But I am, in all senses, defined by my experience as your student, and whether the waters we sailed were turbulent or placid, I thank God to have been in your research group.

I wish to thank Prof. Gey-Hong Gweon who, perhaps more than anyone else, taught me what Angle Resolved Photoemission is all about when I was just beginning. His intelligence, experience, and attention to detail gave me a model of what a physics experimentalist could be. I thank you for your patience with me, your training on equipment and sample preparation, and for your scientific guidance particularly towards my work on the Ditellurides.

Our group has been enriched by numerous postdocs and visiting scientists, all of whom I wish to thank. For Prof. Andreas Bill, thank you for simply being so giving of your time to a first year physics grad student who didn't know a mean field theory from a hole in the ground. Your patience and perspective of the parallel world of a physics theorist not only encouraged me during that difficult first year, but I believe your presence was good for our entire group. For Prof. Kyle McElroy, thank you for your physics insights, personal discussions, and the breadth of your knowledge as well as numerous times on the beamline taking data with me. For Marco Papagno, thank you for your kindness and the numerous experiments that you participated with. For Choonkyu Hwang, beyond the obvious assistance with data taking and all-nighters, as well as assisting the work which became part of both the pnictide and crossover papers, thank you for numerous times of just talking about the physics and where our work and careers were going. It has always been a pleasure.

I owe a debt of gratitude to the older graduate students of our group. Each one of them has "shown me the ropes" of the Lanzara Group and their immediate mentorship has made this journey possible on a regular basis. All of them have endured many long nights on the beamlines, teaching me the self-sacrificial nature of our group, that we all help each other's projects when we can. All of them taught me the nuances of the beamlines and in house equipment, without which none of this would be possible. For Chris Jozwiak, your even-temper, your experimental brilliance, your patience, and, in the later years, your leadership, have made my time here all the better and richer. For Shuyun Zhou, you were always a bright star in our group, and well deserved. Your effort and energy admittedly set the bar quite high for us. You, particularly, were important to my beginnings in the group, introducing me to the IGOR analysis package, and the analysis techniques I needed to know to proceed. And for Jeff Graf, as I transitioned into the cuprates, your assistance, knowledge, comedy, procedures, perspective, all of it made what appeared a frustrating project, surmountable and even achievable.

For David Siegel, we were always peers, and it is a significant gift to progress through one's time as a doctoral student with another. Thank you not only for the beamtimes, the discussions, the humor, and all the other ways in which you have helped make this dissertation possible. But thank you for the times in the courtyard talking, venting, and reflecting.

For the "younger" students, many thanks to Chris Smallwood, Sebastian Lounis, Xiaozhu Yu, Michelle Yong, and Annemarie Kohl, for all the times on beamlines, the discussions, and the life each of you have brought to our group. When times were difficult, I could always lean on the fact that I enjoyed the dynamic and the personalities of our group.

I want to thank the technical staff and the beamlines from which all the data of this thesis comes from. First, at the Advanced Light Source, the team at BL 7 of Eli Rotenberg, and in particular Jessica McChesney, for their assistance in the work on the ditellurides. For the teams at BL 10 who we call up, late into the night at times, particularly Norman Manella, Sung-Kwon Mo, and David Kilcoyne. Finally, at BL 12, Alexei Fedorov who has been so important to our group over the years and for me particularly with our work on the pnictides.

At the Stanford Synchrotron Light Source, where the vast majority of the cuprate work presented here came from, I want to thank the team at BL 5-4 especially Dunghui Lu and Rob Moore. I've always enjoyed working with both of you and it made the entire, sometimes soul crushing, experience of late nights in that windowless facility a little more bearable. Thank you for all your support and training.

The best experiments without theoretical support are like a ship with no charts. And so I wish to thank the groups who have, in one way or another provided those charts. For Prof. Dung-Hai Lee, thank you for your guidance for our entire group and for your participation on my qualifying exam committee. For Prof. Antonio Castro-Neto, thank you for your insights during the early times with tellurides. And thank you to Prof. Philip Phillips and his group for their valuable theoretical support when it came to the pnictide work.

I would like to also thank Feng Wang for his participation on my qualifying exam committee and similarly for Yuri Suzuki who might be one of the only other people to have actually read this thesis.

And of course, without samples, we would have very little to do. So I want to thank our sample growing colleagues from the Birgeneau and Bourret-Courchesne Groups for our pnictide samples. I also want to thank our Korean colleagues M.H. Jung and Y.S. Kwon for the telluride samples. Finally, I want to thank H. Eisaki for supplying so many of our group's samples and my strained cuprate samples in particular.

All of these colleagues have made this work possible. But anyone who has gone through such a program knows that it is more than just your colleagues which make all of this possible. And for me, this has been particularly true as I wish to acknowledge now.

I have been undeservedly blessed to have communities of both undergraduates and graduate students with me on the journey. To begin, I want to acknowledge the Veritas Fellowship

and the work of Carrie Bare in helping to create, with staying power, a community of graduate and professional students who deeply believe that the life of the mind and the Christian walk are essential partners. In particular, I want to thank all of the members and alumni of the Tuesday Men's Group, too many for me write (though I wish I could!), who week in and week out, come together to share life and food and prayer and insights and laugher and grief together over these years. From this group I wish to acknowledge Onsi Fakhouri, my dear friend who has been with me since the day we both arrived at the end of the summer 2004 to start our doctoral programs. To have an apartment mate whom you get along with is a great blessing. But to have one, who is so perfectly suited to the journeys that both of us have been on as doctoral students, is grace upon grace.

I also want to acknowledge the Physics Prayer group and all the members (both physics and non-physics) who have sat there on the grass, in the shadow of the Campanile, venting and hoping as we made our way slowly through our doctoral studies. From this group I wish to acknowledge Xiaosheng Huang whose experience, wisdom, perspective, candor, and presence continued to bless me in different ways during the different seasons of my graduate work.

If am truly honest with myself and ask, "Why do you think you ended up at Berkeley?" I cannot help but suspect that the Ph.D was simply a means for me to be among the students particularly (but not exclusively) of the Intervarsity Christian Fellowship. If my grad community gave me wisdom and guidance, the undergraduates gave me hope and purpose when nothing in my research was working. I wish to acknowledge the campus staff of this group, in particular Erina, Carol, Casey, Nikki, Ryan, Wendy, Jen, Javier, and Collin.

I wish I could list and name every one of the students over the last six years I have had the privilege to talk to and be with as they shared life and faith and struggles with me. A special thank you Class of '05 for helping me find a welcoming community (all the more impressive since you were all seniors) and a place to be on Monday nights that kept me going that first crazy year. For the Class of '06 for all the laughs and all the good times at Manhouse when my research was beginning to sap away my soul. For the Class of '07 for the privilege of teaching you and you teaching me, in that wonderful year before my research made it increasingly impossible. For the Class of '08 for watching you grow up from freshman to seniors and giving me hope that the world is still in good hands. For the Class of '09, you will always be both young yet wise to me, and hanging out with you at the College apartments, doing my data analysis, fun times always. For the Class of '10 for still embracing an old timer like me and again proving what I've always known: that life is more than the work we do.

To all the students, current and alumni, Intervarsity or otherwise, my thanks to you for sharing life together and showing me that when I was most down, most demoralized, and most without purpose, you allowed me feel brilliant again, purpose again, useful again. There is more that I have learned than you realize. Even if all my papers, research, and studies be for naught, you have given me ample purpose to my time here. Thank you.

I want to thank my friends at First Presbyterian Church of Berkeley, particularly the

pastoral staff for your wisdom and guidance, in particular Joshua McPaul. If I have gained wisdom, First Pres has been important in that journey. And in writing that, I can't help but thank the Stephen Ministry community and the work of Carol Johnston. It has been a privilege to serve with you.

Of course, there is the journey to even come to Berkeley and so I wish to thank all of the MIT faculty, friends, and communities who supported me, encouraged me, taught me, and trained me that I could even get to this point. I particularly wish to thank my undergraduate thesis adviser, Prof. Young Lee, whose guidance during my senior year was incredibly gracious and valuable. I also want to thank Prof. Eric Hudson who not only was a good mentor, but continues to be a great mentor and excellent teacher and physicist.

And quite possibly none of this would have come to pass if not for Jim Hicks. So much of how I teach science or work with students, has its origins in your example. It's been more than 10 years since I curiously wandered into your AP Physics class. Thank you.

For Mom and Pop and Laura and all my family, thank you for supporting me along the way, to allow me to do something nobody in our family has ever attempted before. There are no words I have which can due justice beyond, thank you.

And from the beginning, I have wrestled with you Lord. Though the match is not over, I will take joy in Your final victory. When the light became dim, it did not go out. If I have done anything of worth or value, it was from You. Thank You, gracious and eternal God, for everything, because ultimately it is all grace.

Curriculum Vitæ

Daniel Robert Garcia

Education

2010 University of California, Berkeley, CA, USA
Ph.D., Physics

2008 University of California, Berkeley, CA, USA
M.A., Physics

2004 Massachusetts Institute of Technology, Cambridge, MA, USA
B.S., Physics

Chapter 1

Introduction

1.1 Electronic Structure

It is no exaggeration to claim that at the heart of all modern understanding of electronic behavior in solids is the concept of band structure. Within it lies our most successful attempt at deciphering the mystery behind electrically insulating and metallic behaviors, though puzzles still remain. It is fitting that given the nature of the Angle Resolved Photoemission Spectroscopy (ARPES) technique, which is central to the work in this thesis, that we give an appropriate introduction the physical ideas and terminology used in the study of band structure. Indeed, ARPES represents an experimental probe whose ability to directly access this electronic band structure, with all its complex physical phenomena hidden therein, is truly unique in all of condensed matter physics.

Presented with the challenge of finding quantum mechanical wavefunctions appropriate for describing 10^{23} particles interacting with one another via simply coulombic forces within a Hamiltonian would be enough to discourage most researchers. And yet, through sequential approximations, the problem begins descending from the utterly impossible to merely challenging. Such approximations include treating the nuclei as closed shell ions, modeling these ions as classical potentials, and invoking Born-Oppenheimer approximation to eliminate the contribution of their motion to solutions. Most notably, when we turn our minds to the actual electrons themselves, we are still confronted with such a hurdle that even the complete absence of a lattice would render little consolation. The apparent way forward is a massive divide and conquer, to treat each electron as being in a state where they know about the lattice potential but do not interact directly with other electrons. In its place, the interaction between electrons is either averaged or, potentially, removed all together, save the most unavoidable phenomenon, Pauli exclusion. The fact that this *single electron model*

works so well is possibly one the most pleasant surprises of solid state physics. A fact borne out by probes like ARPES, this model is essential for all electronic structure calculations, though reasons for this will be mentioned later. Even still, we remain at a point where a breakthrough is greatly needed. One could resort to a complete removal of all coulombic potentials, resulting in a *free electron model*. But this is hardly an accurate model of reality. In fact, even its unexpected success in describing electron-related properties in the alkali metals raises more questions than it answers. With all the ionic potentials due to the nuclei, how can electrons ever hope to move through the lattice? Can their states be described by good quantum numbers, and if so how?

The Schrödinger equation was hardly two years old when Bloch first discovered his eponymous theorem which allows one to speak at all about band structure or electronic behavior in general. Considering the aforementioned success of the free electron model, Bloch's result is not entirely surprising. In the absence of any potential, the electrons are free and thus, plane waves, given by $\Psi(r) = e^{ikr}$. Pauli exclusion keeps them from occupying the same state, and so we can easily index the states by their wave number, k, and their spin. But could something similar be more generally true for a single electron model? Bloch's theorem demonstrates that in any periodic potential, $U(r) = U(r + R)$, the single electron solutions to the Schrödinger equation are of the form

$$\psi(r) = u(r)e^{ikr} \tag{1.1}$$

where $u(r) = u(r+R)$. The function $u(r)$ encapsulates the information related to the periodic lattice. With this seminal result, we can begin talking about band structure made up of electronic states indexed by the wave number and spin, as well as an additional band index, n. The reason for this index is that Bloch's theorem assures us that there are wavefunctions, ψ, which are energy eigenstates of the periodic potential hamiltonian. But given a single k, one can find many energy eigenstates satisfying

$$\widehat{H}\psi = E_{nk}\psi \tag{1.2}$$

which are thus indexed by n, just as one finds in the solutions to simpler quantum problems like the harmonic oscillator. It is this function, E_{nk}, and its determination that is the band structure of the material. Each electron in the system, at least those not tightly bound to the nuclei, exists in one of these *Bloch states*, characterized by a specific momentum value and energy. The relation between momentum (related to k) and energy is the dispersion, which we will write as $E(k)$ since though k is actually a discrete quantity (hence the earlier subscript), the density of k states is so high, it can easily be made a continuous variable. It is this function that, at a basic level, the ARPES technique is uniquely suited to probe. We can use k to define the momentum of the state, raising it to a multi-dimensional vector and writing, $\mathbf{p}=\hbar\mathbf{k}$. This type of momentum is somewhat unlike what we are used to from classical mechanics, and is often defined as the *crystal momentum* associated with the electronic state. Because of its correspondence to the actual linear momentum of electrons photoemitted in ARPES experiments, we often drop the "crystal" preface when we describe the momentum state of the electrons. Additionally, throughout this thesis, we will often the term electronic dispersion and band structure interchangeably to refer to this function $E(k)$.

Given its importance, it is worth taking a moment to reflect on the dispersion relation, its calculation, and terminology. Sometimes, especially to a new student of solid state physics or of the ARPES technique, the complexity of electronic dispersions can hide the simplicity of their meaning. Take an electron moving through free space, where the energy of the particle can be described classically as $p^2/2m_e$ or quantum mechanically with the momentum operator, $-i\hbar\vec{\nabla}_r$. The states the electron can exist in have energy $E = (\hbar k)^2/2m_e$ This is the dispersion relation, telling us that every possible state indexed by k has a certain necessary energy associated with it, $E(k)$. As we introduce interactions with the lattice ions, other electrons, and other more exotic phenomena, all these do is alter this relationship. In this way, $E(k)$ can provide an abundance of information on the numerous physical phenomena at work in the crystal. In fact, given the surprising success of the free electron model (as well as nearly-free electron models) one will find many band structures that remain, basically, parabolic. The electronic band structure of a crystal is a description of the electronic states that single electrons can exist in given the Hamiltonian they have within the crystal. The fact that there exist a finite number of electrons but an infinite number of possible states, means not all of these states will be filled. Being fermions, the occupation of these electronic states is given by the well-known Fermi-Dirac distribution

$$f(E,T) = \frac{1}{e^{(E/k_BT-\mu)}+1} \tag{1.3}$$

where μ is the chemical potential and k_B is the Boltzmann constant. In instances where the electronic structure has states with energy all the way up to μ, these materials are said to have a *Fermi surface* and the energy associated with this highest most state is called the *Fermi energy*, E_F. At T = 0, $E_F = \mu$, and though they differ somewhat at finite temperatures, the difference is generally unimportant for the data presented here and so throughout this work, E_F will represent the energy of the Fermi surface. It is worth pointing out that the existence of a Fermi surface is the most accurate definition of a metal that one can currently provide. Insulating compounds have no Fermi surface as their electronic dispersions are completely "filled" meaning the highest energy states the electrons can exist in are separated in energy from other states the electrons could occupy at higher energy. The probability of a thermally related transition from one filled Bloch state of certain E and k to a higher E′ Bloch state allowed by the crystal's electronic structure goes as e^{-E_g/k_BT} where E_g is the energy separation or energy gap. Therefore, only materials with unoccupied states immediately above E_F can potentially be metals given the application of an E-field. Otherwise, the gap is too large and the resulting behavior is insulating. If the energy gap is sufficiently small, <2eV, the material allow some conduction and is referred to as a semiconductor. We will return to this when we explore the band structure of the rare earth ditellurides in Chapter 4. The additional lesson is that the states nearest E_F are the ones responsible for determining the large scale electrical and thermodynamic properties of the material. States far from E_F can do little to affect the large scale properties of the system since they are effectively blocked from transitioning out of their states due to Pauli exclusion and the substantial energies required to allow them to access unoccupied states near E_F. Thus, studying the near E_F band structure remains a top priority for understanding a material's properties.

This discussion also leads us ultimately to another valuable observation, one that is obvious to a student of solid-state physics and unavoidable to the ARPES practitioner. The primary space we must become comfortable with in our analysis is momentum space or k-space. This can present challenges since, ultimately, the electronic structure is a function of $\mathbf{k}$ in three dimensions making $E(\mathbf{k})$ a 3D function and thus, fundamentally hard to visualize. While this is important to always keep in mind throughout our analysis, certain considerations make this less daunting. For reasons which will be better explained in Chapter 2, ARPES data is easiest to interpret as being done within a k-space of only 2 dimensions, while the third dimension is held fixed. (Generally, this is the k_z component where z is normal to the surface of the sample.) Thus, one should think of the band structure explored using ARPES as being 3-D manifolds, $E(k_x, k_y)$, with the energy of the states on the z-axis, and the data from the experiment as lines and slices through these manifolds. This third dimension of the electronic band structure (i.e. how the energy of the Bloch states varies with k_z) can still be explored, but it is more challenging due, fundamentally, to the breaking of translational symmetry in the z-direction. This will be re-explored in Chapter 2.

Momentum space carries with it another crucial concept to understanding band structure and ARPES data. The real advantage of studying a crystalline lattice is how a macroscopic object can be reduced to a smaller, simpler subset from which all the information about the macroscopic piece can be deduced from. For a crystal, this subset is referred to as the primitive cell and its shifting throughout space by a set primitive translation vectors ($\mathbf{a_1}$, $\mathbf{a_2}$, $\mathbf{a_3}$) entirely recreates the macroscopic object. But since band structure primarily exists in k-space and not position space, it would be wonderful if a similar advantage could be found in k-space as well. Since the components of $\mathbf{k}$ and $\mathbf{r}$ are just inverses of the other (times 2π), the obvious weapon of choice is a Fourier transform

$$F(\mathbf{k}) = \int d\mathbf{r} f(\mathbf{r}) e^{i\mathbf{r}\cdot\mathbf{k}} \tag{1.4}$$

which in both its discrete (summation) and continuous (integral) forms is our ferryman between real and momentum space. Although much more can be said what matters here is that the symmetries of one space correspond to symmetries in the other, and one can additionally create a unit cell in momentum space defined by k-space primitive vectors ($\mathbf{b_1}$, $\mathbf{b_2}$, $\mathbf{b_3}$). And just as all the information of the crystal in position space can be thought of as an r-vector restricted to a primitive cell (any integer number of primitive vectors can take you from any point in the crystal back to a point in the primitive cell), all the information in k-space can be reduced down to a primitive cell in k-space. The *Brillouin zone* is such a primitive cell which is uniquely defined for any crystal and contains the full symmetry of the crystal. Consider the tremendous power of this idea; every Bloch state in the entire crystal is indexed by a k value. But every k-value, no matter whether it sits within this zone (imagine $\mathbf{k}$=0 as the center of the Brillouin zone) or has a value larger that the boundaries of this zone, must necessarily correspond to a value within this zone. Therefore, if you want to know a physical quantity that is a function of $\mathbf{k}$ (e.g. band structure), just determine it for all the k-states within this Brillouin zone, and you now know that physical quantity for all possible k-states because of the k-space translation symmetry. Therefore, to determine the electronic

band structure of just this initial Brillouin zone (referred to as the first Brillouin zone) is enough to determine it for all values of $\mathbf{k}$. There are many other fascinating properties of Brillouin zones, such as their ability to open small energy gaps for bands which crosses the zone boundary (a phenomena we will return to when we study charge density waves in Section 1.4). But it is enough for now to understand the Brillouin zone as the primitive cell of the band structure, $E(\mathbf{k})$. It is worth noting that even within the Brillouin zone, additional symmetries of the crystal may provide further simplifications. For example, determining the band structure of only a quarter of the zone (4-fold symmetric system) is enough to describe the whole band structure. Throughout this thesis, we will be describing momentum space in terms of the k-space lattice (or reciprocal lattice) for this reason. These reciprocal lattice units will be defined (as often used in ARPES) so that the shortest distance from the center of the Brillouin zone (known as the Γ point) to the edge equals unity. This is to say that given an orthorhombic lattice of real space lattice constants a, b, and c, then k_x, k_y, and k_z have units such that π/a=1, π/b=1, and π/c=1, respectively and the total volume of the Brillouin zone is (2*1)(2*1)(2*1) = 8. This should be remembered when comparing to other probes that define the Brillouin zone edges to be 0.5 such that the total volume in these units would be unity: (2*0.5)(2*0.5)(2*0.5) = 1

Having focused our attention on the idea of k-space, we can now return our attention the band structure function $E(\mathbf{k})$ itself to define and describe a few additional quantities of importance to band structure. Previously, we defined a metal as a material with a Fermi surface, meaning that there exist states of k (and n) which are occupied by electrons all the way up to a Fermi energy. When the system experiences an electric field, these states can easily rise to occupy states that are continuously connected, as opposed to having to quantum mechanically tunnel to states separated by a significant energy gap (an in an non-metal.) The Fermi surface is nothing more than the set of all electronic states at the Fermi energy and the particular wavevector which points to these states is the *Fermi wavevector*, k_F. Strictly speaking, it is not a single wavevector but a collection of $\mathbf{k}$ which trace out this 3D surface, which can in practice be quite complicated. Additionally important is understanding that if $E_n(\mathbf{k})$ represents a dispersion relation for each band, n, then we should be able to determine a velocity associated with electronic states in band n at a particular energy. Although a proper derivation requires more motivation, one can appeal to the definition of the group velocity of a wave, $\partial\omega/\partial\mathbf{k}$. Here, this can be rewritten as $\partial E_n(\mathbf{k})/\partial\hbar\mathbf{k}$ and evaluating this at $\mathbf{k} = k_F$ gives us the *Fermi velocity*, v_F for the band being differentiated. On a basic level, we can understand this quantity as providing us with insight into how other interactions within the crystal may affect or "dress" electrons propagating in the crystal within their Bloch states (not only for states at E_F). For instance, in crystals where the electrons strongly interact with the lattice (e.g. polarons), the resulting behavior slows the electrons down resulting in "flatter" or less dispersive bands. In the extreme, a bound state where the electrons are basically localized in space would be perfectly flat (i.e. $\partial E_n(\mathbf{k})/\partial\hbar\mathbf{k}$=0). This is, additionally, a manifestation of the uncertainty principle since a spatially localized electron would have a completely ill defined momentum. One may also think about this as if the electron were like a object moving through a viscous media. If it interacts more strongly with its surrounding (higher viscosity) it acts as if it has a greater mass. This mass would be

related to the velocity of the electronic states along certain directions (keep in mind, $E(\mathbf{k})$ is multi-dimensional manifold.) Since it is a multi-dimensional problem, the *effective mass*, as it is traditionally called, will be a tensor relation $\mathbf{M}_{\alpha\beta}$ that looks at the curvature of the electronic band structure

$$(\mathbf{M}^{-1})_{\alpha\beta} \equiv \frac{1}{\hbar^2}\frac{\partial^2 E_n(\mathbf{k})}{\partial \mathbf{k}_\alpha \partial \mathbf{k}_\beta} \tag{1.5}$$

This tells us that the concavity of the band structure has a major affect on the effective mass, leading to both positive *and* negative values. This initially unintuitive result dramatically plays itself out in actual materials. Electrons in bands that are near E_F, and thus involved in transport, may have either positive or negative concavity. If the band has positive concavity ("cup up"), the electron has positive mass and moves (or more precisely, increases its $\mathbf{k}$ value) oppositely to the applied E-field, as one would expect. But if the electron near E_F is part of a band with negative concavity ("cup down"), the mass is negative and it would actually behave like a *positively* charged particle in response to a field, which are referred to as *holes*. It is this difference of band concavity that leads people to speak of electron bands and hole bands and their individual contributions as charge carriers. This understanding of effective mass will be additionally justified in the next section and its significance for ARPES measurements explored in Chapter 2 as well as the specific case of the cuprate systems examined in Chapters 5 and 6.

An additional point worth mentioning regarding the slope of band structure manifolds is its connection with the energy density of states, $D(E)$. Although the Fermi function provides us with the distribution associated with fermions as a function of energy, there is no information about how many Bloch states exist within a window, dE, which need not be (and in practice is not) uniform. This has significance in the calculation of many quantities, particularly $D(E_F)$ (e.g. specific heat, BCS superconducting gap), and is often among the functions theorists attempt to calculate when presented with a novel new material. Furthermore, Angle Integrated Photoemission is able to measure the density of states by determining raw photocurrent vs. binding energy, although certain caveats must be considered. Chapter 3 explores this further in regards to the iron arsenides. The relationship between $D(E)$ and the band structure $E_n(k)$ comes down to regions of extrema or saddle points in the band structure manifold. If one is taking constant energy slices of some width, dE, of a band structure, the places where the surface is most parallel to the slice will contain the largest amount of the surface (i.e. states) within the dE. Written more precisely

$$D(E) = \frac{2}{(2\pi)^d}\int \frac{d\Sigma}{\nabla_{\mathbf{k}} E(\mathbf{k})} \tag{1.6}$$

where d is the dimension and Σ is a constant energy surface $E = E(\mathbf{k})$ of dimension d-1. Here, extrema in $E(\mathbf{k})$ lead to singularities known as *Van Hove Singularities* which can enhance the band structure seen with ARPES.

1.2 Band Structure Calculation

A word should be said about band structure calculation since comparison with such calculations is important for testing theoretical models and for revealing exotic phenomena. As mentioned earlier, it comes as a surprising fact that assuming free electrons moving through a lattice (subject to only Pauli exclusion) would provide any realistic picture of the physics in metals like the alkali metals. But coming up with an adequate Hamiltonian which strikes that elusive balance between an accurate description and mathematical tractability is really challenging. With this Hamiltonian, the energy eigenvalues of the associated eigenstates (Bloch states) would correspond to the band structure, being indexed by $\mathbf{k}$ and n. Great success for metals can be made by treating the electrons as nearly-free, lightly perturbed by a periodic potential, U, leading to parabolic bands and splitting of the bands near the Brillouin zone edge ($\sim$2U). But in the complicated materials we will be studying, more sophisticated approaches need to be taken. Two such approaches will be described: tight-binding models and local density methods. From the name alone, one gets the sense that tight binding models fall on the other extreme from the nearly-free electron models mentioned. And, consistent with that theme, tight binding models are more advantageous when band gaps are larger. Tight binding methods start from the view point of electrons localized in atomic orbitals. To make the initially unexpected leap from Bloch states to localized wavefunctions, one simply creates orthogonal, localized, wave functions that are constructed from a series of Bloch functions. Such functions would naturally satisfy the requirement for Bloch states (being a summation of Bloch functions) and would have a real-space functional dependence that would localize them near atomic sites. These functions are the well known *Wannier functions* and their ability to fall off as a function of increasing distance from an atomic site is essential to their usefulness. It turns out that this localization is directly related to the energy gap separating the bands associated with the Wannier function from any other band. In insulating materials, this leads to a fast drop-off and thus significant localization. However, Wannier function of metals may not have such localization. When their intensity decays exponentially to a negligible amplitude beyond its nearest neighbor, one can create Hamiltonians such as (in Dirac notation)

$$\widehat{H}_{TB} = \sum_{\mathbf{R}\vec{\delta}} |\mathbf{R}\rangle\, t \left\langle \mathbf{R} + \vec{\delta} \right| + \sum_{\mathbf{R}} |\mathbf{R}\rangle\, U \langle \mathbf{R}| \tag{1.7}$$

where $\vec{\delta}$ represents a vector from the atomic site (indicated by $\mathbf{R}$) to the nearest neighbor site. The meaning of this Hamiltonian is that for an electron to travel from localized site (as determined by the Wannier function) to its nearest neighbors there is an energy cost, t, known as a hopping term, which acts like kinetic energy. For an electron localized to an atomic site there is also the energy associated with being localized at that site, U. Given plane wave states, one can determine the energy eigenvalues of the hamiltonian in Eq. 1.7 to be

$$E(\mathbf{k}) = U + t \sum_{\vec{\delta}} e^{i\mathbf{k}\cdot\vec{\delta}} \tag{1.8}$$

thus giving us our band structure. Given this basic model, a lot can be done to improve it such as using linear combinations of atomic orbitals (LCAO) to create Wannier functions from certain combinations of atomic orbitals and thus get more physically relevant values for the t's and U's. More orbitals and more neighbors (t', t'', etc) improves the model, but at the risk of greater and greater calculational challenge. As we examine the cuprates, in Chapters 5 and 6, the primary band structure model we compare with is that of a tight binding model where the parameters are phenomenologically determined. Additionally, it is a critical extension of this tight binding model, the Hubbard model that is at the heart of so much theoretical work on the cuprates. The Hamiltonian in the Hubbard model effectively adds a term which penalizes the addition of more than one electron to any atomic site, as a method for exploring magnetic phenomena. Unlike the original tight binding Hamiltonian, this one can only be solved exactly in one dimension. We will return to this when we begin exploring the superconducting cuprates in Chapter 5.

The second method of approaching band structure calculation we will explore is local density theory, though we will only address it briefly since it will be used in Chapters 3 and 4. Up to now we have generally neglected the effect of electron-electron interactions, save Pauli exclusion. But this is conceptually suspicious and erroneous in practice for many systems. One can attempt to incorporate the effect of both Pauli exclusion (via a *Slater determinant* antisymmetric wavefunction) and electron-electron interactions in the Hamiltonian. Then, one uses variational techniques to find the appropriate ground state, looking for the extrema of the functional $F_H[\Psi] = \left\langle \Psi \left| \widehat{H} \right| \Psi \right\rangle$. The result of that adventure is the well-known Hartree-Fock equation. But these are of limited use because they do not model electron screening (and are quite time consuming to solve.) Density functional theory as developed by Hohenberg and Kohn starts with the assumption that you could uniquely define the ground state of a many-electron system by just its electron density function alone. The idea is simply that the only things that define a many body problem is the number of bodies (electrons) and the potentials they feel. Given these, there is a one-to-one correspondence between the resulting density and these initial constraints. They also realized that if you could write a functional of the energy of the system with respect to the electron density function, the true ground state electron density function minimizes it. Drawing on information from the Hartree-Fock model used on a uniform electron density (affectionately called *jellium*), allowing the density to vary slowly, and minimizing with respect to wavefunction as opposed to electron density (allowing for a more reasonable kinetic energy term) the result is the Kohn-Sham Equation

$$E_l \psi_l = \left[U(\mathbf{r}) + \int d\mathbf{r}' \frac{e^2 n(\mathbf{r}')}{|\mathbf{r} - \mathbf{r}'|} + \frac{\partial E_{xc}(n)}{\partial n} \right] \psi_l(\mathbf{r}) \tag{1.9}$$

where $n(\mathbf{r})$ is the electron density, U($\mathbf{r}$) the lattice potential, and E_{xc} is the exchange correlation energy which is independently chosen. These type of approximations are generally referred to as *local density approximation* or LDA. In practice, the band structure calculated from this model often needs to be renormalized (i.e. rescaled) in energy, though it is common that the Fermi surface is modeled reasonably well. Chapter 4 will make use of LDA related

band structure calculations and the corrections that ARPES can provide to renormalize the band structure in the energy dimension.

Now at this stage one might be wondering, "Why can we think of single electron states at all if there are all of these electron-electron interactions?" Indeed, we have assumed a lot. Why should the single electron model work at all, considering it forms the basic assumption behind every model we have looked at. How can we use ideas like effective mass as if we are fundamentally dealing with individual free electrons? This takes us to another discussion which is so essential that without it, ARPES on correlated electronic systems would simply make no sense.

1.3 Fermi Liquid Theory

Prior to the incorporation of electron-electron interactions in our discussion of local density theory, we have been effectively working with electrons as a gas of fermions, obeying Pauli exclusion, and existing in Bloch states. As we turn on interactions, we transition from a *Fermi gas* into a *Fermi liquid.* So the question that faces us is if we wish to study correlated electronic systems (like the superconducting cuprates) and in particular their electronic band structure (assuming that makes sense to say), how do we proceed? The path forward was cleared by Landau in 1956 as he was studying the physics ^{3}He. Landau realized that trying to determine the precise nature of the ground state was not the right way forward. Rather, it would be easier to focus on the excitations of the system. It turns out that these excitations, particularly near E_F, are long lasting enough that they could be thought of as if they were particles in their own right and not merely excitations of a complicated ground state, but. Thus, these elementary excitations of the ground state are referred to as Landau *quasiparticles*, and like "real" particles, they can move and have interactions with each other (albeit much weaker) within the system.

At its core, Landau realized that you could start with an excited state in a non-interacting Fermi gas. For example, imagine a single electron promoted to a k state with energy above E_F. If you were to add electron-electron interactions slowly, this excited state would eventually turn into an energy eigenstate of the new Fermi liquid, whatever that is. But if instead one were to add the electron-electron interactions very fast compared to the scattering time, τ, of states near E_F, the system would still have a well defined momentum value, k, but it would not be in an energy eigenstate of the new system. This uncertainty in energy naturally leads to finite lifetime ($\Delta E \Delta t \sim 1$.) It is this decay time that puts the "quasi" in quasiparticle. It is crucial to the success of this theory that the lifetime of these quasiparticles goes to infinity as one approaches E_F. Essentially, this is related to the number of states that can be accessed by excitations near-E_F. For excitations of near-E_F states, the low energy involved in these excitations limits the number of acceptable final states that the electron can actual scatter into. The electrons are like people in a rush to buy car. If they start off with a lot of money (higher energy) there are lots of cars they can buy, even if competition

is steep. So they only remain in the car-buying (quasiparticle) state for a short while. But if they have little money (lower energy) they will have fewer options and have to hunt longer for car to drive away in. And as their money (energy) decreases to zero, the time they have to shop increases (lifetime of the quasiparticle state) towards infinity. A detailed calculation better quantifies this, showing that quasiparticle lifetime, τ, goes as

$$1/\tau = \alpha(E - E_F)^2 + \beta T^2 \tag{1.10}$$

It's worth noting that the T^2 dependence is only valid for energies at or less than $k_B T$, $|E - E_F| < k_B T$. Observing that this lifetime will be related to the energy sharpness of quasiparticle state is valuable to understanding the data from ARPES experiments.

There is far more that can be said about Fermi Liquid theory, but this is sufficient to ally many of our concerns about the study of correlated electron systems with probes like ARPES. What we discover for these systems is that we can think of them as being described by electronic states which have a direct correspondence to low-lying excited states of a non-interacting system. These states have well defined k values but limited lifetimes due to being dressed by excited states, and are particular long lasting near E_F. This is essential since, as mentioned, most of the important physics is determined by the states near E_F. Thus, the single electron model does continue to be valid since one can speak of well defined momentum states for particles (although they are quasiparticles) which still satisfy Bloch's theorem, with their own effective mass due to the interactions involved and are weakly interacting with one another. Now up to this point, we have spoken of electronic dispersions, with their associated velocity and effective mass. However, it would now be proper to instead speak of quasiparticle dispersions, particularly as it relates to the states observed in correlated electronic systems near E_F. But in practice, the terminology gets muddled. In our experimental work, the appearance of quasiparticles and their effect on the energy lineshape of electronic states is significant. This effect is connected to the dependences illustrated in Eq. 1.10. Incorporating all these results as well as any additional affects into our understanding of the electronic structure seen by probes like ARPES is best served by developing the language of Green's functions. For now, we will refrain from this discussion until we better explore the physical understanding of the ARPES technique in Chapter 2.

1.4 Novel Lattice Phenomena

So far, it was necessary to describe the origins and ideas associated with electronic band structure in the absence of more exotic phenomena. Fermi Liquid theory and the introduction of electron-electron interactions provide a prelude to the more elaborate physics one can expect in many crystalline systems. But now we turn our attention to more novel physical phenomena beyond simply electrons moving in a fixed periodic potential. For the purposes of this thesis, we will briefly focus on two areas which, on close examination, are interrelated: 1)

Phonons and the effect of bosonic renormalization, and 2) Charge and Spin Density Waves. We will start with phonons.

Right from the start, we ruled out any effect of the crystalline lattice, save that it provides a periodic potential for the electrons to interact with. This was related to an argument from the Born-Oppenheimer approximation that the relative time scale of the electrons was orders of magnitude different than the nuclei. When a guy is sprinting through a crowded plaza, it is easier to assume the surrounding people are effectively stationary obstacles to avoid then to think about their actual motion. But interactions with lattice remain significant being able to scatter the Bloch states. Sometimes this scattering happens in unintuitive ways like the effective attraction which leads to conventional superconductivity explored later in this chapter. But like the problem of electrons, the lattice with its $\sim 10^{23}$ ions presents us with a daunting task to understand. Thankfully, and perhaps unsurprisingly on closer inspection, a lot of the methods and ideas from our study of electronic band structure is exactly relevant to our study of the lattice.

Instead of turning to the Schrödinger equation and its resulting Bloch's theorem, a purely classical oscillator mentality is sufficient for deriving the expected vibrational modes. Just as with electronic states, the result of this are dispersion relations which relate the energy of the oscillation, ω, with the wavelength of the vibration in the crystal, encapsulated in $\mathbf{k}$. This leads to dispersion relations defining the possible states the crystal's oscillations can exist in. In any lattice with a basis (lattice with more than a single element), one gets the traditional separation of so-called *acoustic* modes with band structure at lower energies ($\omega \sim c|\mathbf{k}|$ as $k \to 0$), from *optical* modes appearing at higher energies (and generally less dispersive.) Once again, given the symmetry of the lattice, these dispersions have a periodicity in k-space and the addition of any reciprocal lattice vector, $\mathbf{K}$, should have no effect. Therefore, just like electronic states, if one can describe the vibrational modes for k's in the first Brillouin zone, one has determined all the information regarding all lattice vibrations because any k can be mapped back to the first Brillouin zone. Where things get exciting is how these modes are different from what we see in the electronic states. Strictly speaking, although the same k-states can be used to describe both these lattice modes and the electronic states (a fact very important as we will soon see), Pauli exclusion requires that electronic states be only doubly occupied (spin) for each point along the E($\mathbf{k}$) manifold. There is no such limitation for these lattice dispersions. So unlike electronic states which can fill up their states beyond the Brillouin zone producing higher and higher energy bands (though reducible back onto the first Brillouin zone), the lattice vibration dispersions are fully described within the first Brillouin zone and have a ceiling of energy. Furthermore, it is already tempting to see these modes as objects in their own right, with well defined states of $\omega(\mathbf{k})$, like the electrons in their Bloch states. Formally, by employing a second quantization, treating the potentials as quantum mechanical oscillators, puts this on a firmer foundation, and gives birth to *phonons* which we can treat as bosonic particles in the lattice.

There are numerous direct probes of phonons and their dispersions taking advantage of different forms of inelastic scattering (e.g. Inelastic Neutron Scattering, Inelastic X-ray Scattering, Raman and Brillouin Scattering). Nevertheless, because of the effect phonons have

on electronic states particularly near E_F, ARPES remains an important probe of phonon physics in many systems, albeit more indirect. Two such phenomena where coupling between electronic and phonon states is particularly important to our later work on the superconducting cuprates are: Kohn Anomalies and the bosonic renormalization of near-E_F band structure. A Kohn anomaly exists when a phonon mode has a wavevector $\mathbf{q} = 2\mathbf{k_F}$. The result is a singularity in the phonon dispersion, which appears as divergences in the plot of $\partial\omega/\partial\mathbf{q}$. The reason for this has to do with the k-dependent dielectric constant, ϵ(k), which, as $k \rightarrow k_F$, takes on a form (the Lindhard dielectric constant for those who care) which has a singularity at a wavevector equal to $2k_F$. This curious relationship between electronic structure and only phonon wavevectors which can connect it can be important and will be revisited in the work discussed near the end of Section 5.1 and extended in Chapter 6.

The idea of bosonic renormalization is even more significant to recent work on done with ARPES on correlated electronic systems. Although the full physical presentation is not necessary, we should provide some motivation. As will be revisited in our introduction to superconductivity, electron-lattice interaction can result in effective electron-electron interactions which are mediated by phonons. This effective interaction between two electrons of wavevectors $\mathbf{k}$ and $\mathbf{k'}$ and energies $E_\mathbf{k}$ and $E_{\mathbf{k'}}$ respectively is given by

$$V_{k,k'} = \frac{4\pi e^2}{q^2 + k_0^2}\left[1 + \frac{\omega(\mathbf{q})^\mathbf{2}}{\omega^2 - \omega(\mathbf{q})^2}\right] \tag{1.11}$$

where $\mathbf{q} = \mathbf{k} - \mathbf{k'}$ and $\omega = \frac{E_\mathbf{k} - E_{\mathbf{k'}}}{\hbar}$ and k_0 is the Thomas-Fermi wavevector. The result of this is a change in the electronic energy, E($\mathbf{k}$), but it has a rather complicated momentum dependent effect. Essentially, the interaction leaves the value of E_F and k_F (the Fermi surface topology) unchanged. However near E_F on the energy scale of $\hbar\omega_D$ (ω_D being the Debye frequency) there is a significant modification of the band structure as seen in the classic figure from Ashcroft and Mermin's text reproduced as Fig. 1.1[1]. Beyond these energies, the effect quickly disappears. This "kink" in the band structure is caused by the phonon-electron interaction, though the result is general enough to apply to a general bosonic field (e.g. magnons).

Evidence of this effect was first discovered a little over 12 years ago[2]. But, as we will see in Chapter 5, the appearance of this effect in the high temperature superconducting cuprates has set off a substantial interest in the identity of this bosonic mode and whether it is phonon or magnon related. Additionally, from the magnitude of this kink, we can estimate the intensity of the electron-bosonic coupling constant, λ. Although more elaborate techniques can be used, a simple approach is sufficient given the quality of the data as well as the needs of our analysis. The band structure at high binding energy remains unaffected and thus represents the unaffected band. But at lower energies, such as at E_F, the deviation is most pronounced. The relative difference between these values is related to the intensity of the coupling between the states. We can quantify the deviation by taking the band velocity, as discussed in Section 1.1, and comparing the ratio of these group velocities above and below the kink energy. The coupling constant is directly related to this ratio as $(1+\lambda) = v_{High}/v_{Low}$.

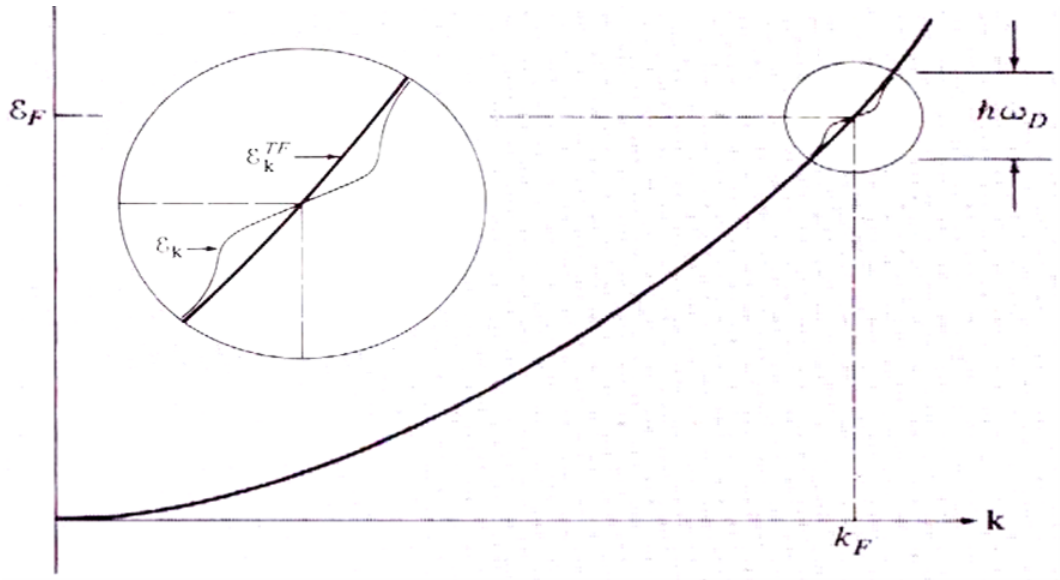

Figure 1.1. The effect of a bosonic renormalization due to electronic-phonon interactions on the electronic structure within $\hbar\omega_D$ of E_F. Figure reproduced from Ashcroft and Mermin[1].

From this, one can quantify the effective interaction due to this bosonic renormalization and, in the case of our work, see how the effect can vary.

Although phonons can lead to novel effects on band structure such as the case of bosonic renormalization, the effect of creating long-range ordering is arguably the most dramatic consequence of the physics of electron-lattice interactions. This occurs with the phenomena of *charge density waves* (CDW) which, like the briefly addressed Kohn anomaly, result from an instability in the lattice made possible by electronic and lattice coupling and are an essential part of the the study of correlated electronic materials.

The story of CDW phenomena reaches back nearly the beginnings of the quantum mechanical study of solids in the 1930's and the work of Peierls[3]. In his studies, Peierls realized that a 1D metal was fundamentally unstable. To understand this, he considered a linear chain of atoms with a regular spacing a. Given a prototypical half-filled metal as described earlier, the system should have a Fermi wave vector $k_F = \pi/2a$. But what would happen if one were to make pairs or dimerize the atoms by using a small distortion, δ? As we discussed in Section 1.1, the electronic band structure is greatly affected by the Brillouin zone which is defined by lattice structure. The dimerization would shrink the Brillouin zone from having boundaries at $\pm\pi/a$ to $\pm\pi/2a$. Furthermore, recalling a nearly free electron model, the periodic potential which normally leads to the splitting of bands at $\pm\pi/a$ now has a nonzero matrix element connecting states at $k = \pm\pi/2a$. Thus, we expect a splitting of the bands at k_F. But, if the splitting occurs at k_F, then states that are occupied will be shifted down in energy by the interaction while states that are empty (given $T = 0$) will be shifted up. The net result would be a decrease in electronic energy since the states shifted up were unoccupied. If the gap had tried to open below E_F, (meaning a different wavevector than

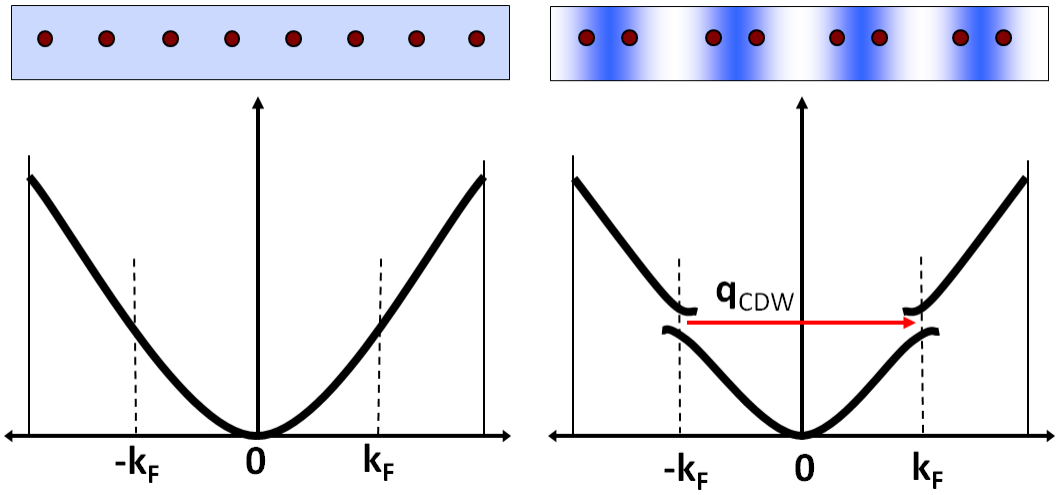

Figure 1.2. The onset of a Peierls transition in a 1D metal taking the original band structure in the first Brillouin zone (left hand side) and introducing a dimerization (right hand side) which expands the real space unit cell, shrinks the Brillouin zone, and causes a modulation associated with $\mathbf{q}_{CDW}$. This nesting wavevector similarly opens a gap at $E_F(k_F)$ lowering the electronic energy of the system.

$2k_F$) an equal amount of filled states would gain and lose energy, resulting in no net change. This is illustrated in the panels of Fig. 1.2.

This is, however, contingent on whether the electronic energy cost of the lattice modulation is made up for in the energy gained by opening the gap. For the 1D metal, Peierls showed this was always the case since the electrical energy saved would always be greater than the energy paid in elastic potential energy for small displacements and small potentials. Thus, the system will transition to a new periodicity, known as a *Peierls transition*. This means a temperature dependent transition could occur when, as the temperature decreases, the number of electrons thermally excited above E_F decreases so that the splitting of the band would gain enough energy to balance a structural distortion. Curiously, this result struck Peierls as such a surprise that although mentioning it in his Quantum Theory of Solids[4], it took him considerable time to convince himself that his argument was sound. Still, he considered it of only academic interest since there are no strictly 1D systems in nature[5]. Nevertheless, in 1973 the organic charge transfer salt TTF-TCNQ, which is a long quasi-1D conductor, was found to undergo a Peierls transition[6].

Since then numerous quasi-1D systems which contain Peierls transitions have been explored. Additionally, quasi-2D systems have been thought to exist which support CDW formation also, and whose physics is intimately related to that of the Peierls transition. This leads to an additional categorization, the difference between commensurate vs. incommensurate CDWs. As suggested from the Peierls transition analysis, in order to create a CDW and its associated periodic structural distortion two conditions must exist. First, the Fermi surface band structure should have the ability to be "nested" by a constant $\mathbf{q}_{CDW}$. Another way

this can be seen is as an instability in the electronic susceptibility at a wavevector equal to the nesting vector, $\mathbf{q}_{CDW}$. Second, the system must have sufficiently strong electron-phonon interactions in order to trigger the structural distortion. Since the CDW wavevector would be determined by the geometry of the Fermi surface the resulting lattice distortion from the CDW is often incommensurate with the original translation symmetry of the crystal lattice. Commensurate CDWs are observed as well, but even in these cases an incommensurate modulation "locks-in" to a nearby periodicity which is commensurate with the lattice[7].

A final aspect, where APRES has played a useful role, is the idea of "imperfect" nesting. The Peierls instability is only expected in quasi-1D systems. Yet, as we will address in Chapter 4, CDW physics has been observed in quasi-2D systems as well. Generally, this has been explained by the idea of imperfect nesting where an unusually strong incommensurate CDW can occur even though a single $\mathbf{q}_{CDW}$ is unable to consistently nest the Fermi surface band structure[8]. Now throughout our work, we have made a distinction between CDW and charge ordering phenomena, such as "stripes" which are observed in materials like the 1/8 hole doped LSCO superconductor. Charge ordering occurs whenever charge density accumulates in areas of the lattice, of which a CDW is an example. But for the physics to be truly CDW, we believe it must have that nesting vector associated with the structural transition, even if the nesting is imperfect. The evidence of CDW physics as seen by ARPES will be addressed better in Section 4.1. For completeness, it is worth noting that all of this applies to static CDW systems. There is the possibility of dynamic CDW systems but any connection between these systems and what ARPES can probe is complicated at the very least and most likely impossible.

However, charge is not the only density wave which can manifest itself in these correlated electronic systems. Up to now we have not discussed the effect of magnetism as an important part of the physics of many correlated systems. In Section 1.6, we explore a little of how magnetism is significant in the cuprates with the Hubbard Hamiltonian. But, given its appearance in our later work on the iron oxypnictides, we should address the physics of *spin density waves* (SDW) as an important aspect of many systems of interest, although not as abundant as the CDW phenomenon[9].

The origins of the SDW phenomenon are very similar to the CDW phenomenon and were first proposed by Overhauser[10]. Rather than a charge-lattice modulation, one finds a periodic spin-density modulation which can be commensurate or incommensurate with the lattice. Just like the idea of a CDW forming under a singularity in the electronic susceptibility, a SDW forms under a finite wavevector singularity in the magnetic susceptibility. This wavevector corresponds to a nesting vector $\mathbf{q}_{SDW}$ which, just as for the CDW, connects large segments of the Fermi surface. Thus, we have a phenomenon where band structure effects are intimately involved in the stabilization of the ordering. Such an ordering would correspond to an antiferromagnetic ground state and people believe that it explains what is seen the physics of materials such as Chromium[11]. This can result in modification of the electronic density of states, as we will explore in Chapter 3.

Before concluding, since we have mentioned phonons as a bosonic mode that can couple to electronic states and lead to a renormalization, magnetic phenomena can do similarly.

For a charge density wave, the essential physics is electron-lattice coupling. The quanta of this coupling are phonons and these can couple to electronic states in the manner previously described. For a spin density wave, the essential physics is magnetic but one can, just like with phonons, describe elementary excitations which carry momentum and energy. These fluctuations can be thought of in terms of the Heisenberg model for spins, where spin flips can propagate in a helical or spiral way through the lattice. These are referred to as *magnons* and, like phonons, the excitation carries no net spin, making the effective particle bosonic. Via spin sensitive probes like INS, one can even map out these dispersions and there is still debate over whether the bosonic renormalization seen in the cuprates could still be due to this phenomenon. This will be revisited in Section 5.1.

1.5 Superconductivty

It is not without reason that superconductivity has occupied such a significant place in the efforts of solid state physicists for nearly a century. In some ways, it was a phenomenon too far ahead of its time, being only understood within the many-body quantum mechanics of solids, yet appearing at a time when Rutherford had just postulated the existence of the nucleus and Bohr's model of the atom was still two years away. Still, the effect that Kamerlingh Onnes discovered when mercury is cooled below 4K, a metal with seemingly no electrical resistance, captures the interest of both the professional and the layman. And yet, its defining feature is really of secondary importance compared to the discovery by Meissner and Ochsenfeld more than 20 years later that all magnetic flux is expelled from a superconductor. (Indeed, a difficult observation to make given the existence of superconductors where this is not precisely true.) For a material to decrease a current flowing through it, it must, by Ampere's Law, reduce its magnetic field. But this would lead to flux lines passing through the material, a condition a superconductor cannot allow. Thus, it is the Meissner effect which can be thought of as the critical physical feature of superconductors.

Lacking the necessary advancements in quantum mechanics and many-body wave functions, significant strides were still made in the phenomenology of superconductivity. Most notably, there was the work of the Londons, which started from a model of electrons moving in the absence of any damping factors. This work was able to explain the result of Meissner and Ochsenfeld, developing the London equation

$$\mathbf{B} + \lambda_L^2 \vec{\nabla} \times \vec{\nabla} \times \mathbf{B} = 0 \tag{1.12}$$

This length scale, λ_L, is of particular significance since it determines the length scale to which the B-field dies off as it approaches the boundary of a superconductor. Further progress was made as it became clear that the superconducting state could be weakened and eventually destroyed by the application of a significant externally applied field, H_c. This result coupled with the reversibility of the transition led to the conclusion (from analysis of the free energy)

that the change in entropy between the normal metal and the superconducting state was

$$\Delta S = \frac{H_c}{4\pi}\frac{\partial H_c}{\partial T} \tag{1.13}$$

Since $H_c \to 0$ as the temperature approaches the zero-field critical temperature, T_c, there is no latent heat ($\Delta S = 0$) so the superconducting transition is second order. This is fortunate since one could then employ the substantial phenomenological firepower of the Ginzberg-Landau theory for second order phase transitions to better understand superconductivity (though it was developed much later and, just like with Fermi liquid theory, with helium in mind.) Among its numerous insights, this approach elucidated the origin of both *Type I* and *Type II* superconductors. Type I superconductors were defined by a single critical field H_c in the way previously described. Type II materials were more mysterious, having two fields, H_c (sometimes called H_{c1}), and H_{c2}. At a given temperature below T_c, if the applied field was less than H_c, it is more energetically favorable to expel all fields. Above H_c, it is more favorable for some field lines to penetrate and form a lattice of superconducting vortices known as an *Abrikosov flux lattice*. Above H_{c2}, the system was entirely in its non-superconducting phase. The theory produced equations which depended on two length scales: the London penetration depth as earlier mentioned, and a coherence length, ξ, which relates to the scale of special variation in the superconducting wavefunction (or strictly speaking, the superconducting order parameter.) Defining $\kappa \equiv \lambda_L/\xi$, for materials where $\kappa < 1/\sqrt{2}$, H_c was larger than H_{c2} and the material was Type I. When $\kappa > 1/\sqrt{2}$, the material was Type II. For all the superconductors we will be examining, $\kappa > 1/\sqrt{2}$ making them Type II, though we will probing them in the absence of external magnetic fields (which are highly undesirable for photoemission due to the Lorentz force on the photoelectrons.)

By the 1950's, there were many encouraging signs regarding the problem of understanding the microscopic nature of superconductivity. The idea that superconductivity could be related to coherence in a quantum state was proposed by London. The recently discovered isotope effect ($T_c \sim M^{-\alpha}$ where M=nuclear mass) focused new attention on the role the lattice may play in superconductivity. The work of Fröhlich developed a Hamiltonian which describes the interactions between electrons and phonons as early as 1950, just prior to the observation of the isotope effect. From his hamiltonian, it was clear that the electron-phonon interaction could lead to an effective attractive potential between two electrons as we discussed with Eq. 1.11. From a classical perspective, one can think of the electron as causing a small distortion of the surrounding ions via electron-lattice coupling. Like the inverse of nuclear screening by electrons, have the electron is screened by the effective positive charge, which then attracts, ever so lightly, the second electron. Thus, the two electrons are coupled together over a length scale which, as it turns out, is the coherence length, ξ, described in Ginzburg-Landau theory. (Although in their seminal works, Bardeen, Cooper and Schrieffer don't cite Ginzburg-Landau theory.) As mentioned in the presentation of CDW phenomena, Fröhlich proposed that a collective state of electrons and atomic displacements could move though a lattice without being disturbed provided that the velocity was small enough, and thus producing a superconducting state in a 1D metal. However, the sliding collective state he envisioned could only move in this way in the absence of impurities, finite phonon

lifetimes, 3D ordering, and other effects. Still the critical role of lattice distortions caused by electrons traveling though the crystal was correct. By 1956, Cooper had discovered that any small attractive interaction would destabilize a conventional electronic ground state into correlated pairs of electrons. With a Hamiltonian inspired by this result and a coherent state wavefunction proposed by Schrieffer, the BCS (Bardeen-Cooper-Schrieffer) theory of superconductivity emerged in 1957.

Over the years, the theory held up against experimental scrutiny, explaining the existence of the Meissner effect, the isotope effect exponent α, the temperature dependence of the superconducting gap as well as its relationship to T_c, specific heat data, and nuclear spin relaxation experiments. But how high could T_c rise to and what materials would we expect to have higher T_c's? The work of McMillian building on Eliashberg (who refined the effective interaction model beyond that of Fröhlich, Bardeen and others) showed that T_c could be roughly approximated as

$$T_c = \frac{\Theta_D}{1.45} exp\left\{ - \left[\frac{(1+\lambda_{ep})}{\lambda_{ep} - \mu^*(1+0.62\lambda_{ep})} \right] \right\} \tag{1.14}$$

where λ_{ep} is an electron-phonon coupling constant (in this situation it is also multiplied the density of states at E_F), μ^* is related to a product between the strength of the Coulomb interaction and the E_F density of states, and Θ_D is the well-known Debye temperature, which corresponds to the temperature where all the phonon modes in a system become thermally active. Inserting some generous estimates, one predicts that T_c should max out around 30K.

It was in the effort to push this limit by searching out materials with greater electron-lattice coupling that initially led Bednorz and Müller to the layered cuprates, in particular $La_{2-x}Ba_xCuO_4$. To the great surprise of everyone, in 1986 they discovered a T_c of 35K, an astounding result given the limitations previously mentioned. But, the situation quickly became substantially more involved than an unexpected T_c. The cuprates are doped antiferromagnetic insulators (specifically Mott insulators, an issue examined in the next section.) This is surprising since superconductivity expels magnetic field, and leads one to surmise that magnetic ordering and superconductivity are competing forms of order in a crystal. And yet one finds the proximity of these phenomena, along the doping axis of the phase diagram. This has been also seen in the *heavy fermion metals* such as UGe_2 where coexistence of ferromagnetic and superconducting phenomena is believed to be seen. From a conductivity perspective, these cuprate systems do enter a metallic phase at temperatures above the superconducting dome in the phase diagram. But, the resistivity is linear up to around 1000K (in the case of YBCO at least), without any evidence of the more complicated temperature dependence (such as Bloch's T^5 law due to phonons).

It is the superconducting gap function which, from an ARPES perspective, marks the novelty of these materials. Within the BCS model, the superconducting gap is associated with the energy of the pairing of electrons into Cooper pairs and is directly related to T_c. The Cooper pairs would be spin singlet structures, where the orbital angular momentum, l, was equal to zero. The result is that the gap would be isotropic, or that gap was the same everywhere throughout k-space. This was demonstrated with techniques like tunneling

given the effect of the gap on the shape of the near E_F density of states. However, in the cuprates, through the work of ARPES and even more dramatically by SQUID interferometry, it was discovered that Cooper pairs exhibit a gap which is anisotropic with four nodal points (locations where the gap goes to zero). Furthermore, the associated wave function undergoes a sign change of its phase after each nodal point (invisible to ARPES, but seen by SQUID interference.) Given the observation from NMR that the Cooper pairs are still in a spin singlet state, this situation corresponds to the Cooper pair wave function being in a state with l=2. Thus, compared to the "s-wave" gap function, $\Delta(\mathbf{k}) = \Delta$, these cuprate superconductors present us with a "$d_{x^2-y^2}$-wave" gap function,

$$\Delta(\mathbf{k}) = \Delta(\cos(k_x a) - \cos(k_y a))/2 \tag{1.15}$$

where a corresponds to the lattice constant of a square lattice. Since the cuprates can be thought of as quasi-2D tetragonal compounds, the gap function has negligible dependence on k_z. More so than any other feature, it is the gap function that best differentiates conventional superconductivity ($\Delta(\mathbf{k}) = \Delta$) from unconventional ($\Delta(\mathbf{k}) \neq \Delta$) superconductivity (regardless of the magnitude of T_c.) Because this gap function effects the density of states near E_F (appearing as linearly going to zero as $E \rightarrow E_F$ for d-wave), it also turns up in other measurements like specific heat which functionally depend on that value.

1.6 Present Issues

In spite of the last twenty five years of intense experimental and theoretical work, unconventional superconductivity continues to elude our understanding. At its heart, the presence of this superconductivity may have much to do with the quasi-2D nature of the materials being studied. For the cuprates, it is generally believed that all of the magnetic ordering and cooper pair formation is occurring in the copper oxide planes. But here we encounter the critical problem. In our basic understanding of band structure, electrons which do not completely fill bands (leaving higher energy states to transition into without the hindrance of a gap) are metallic. But transition metal oxides like NiO and CuO have long been known to violate this basic result. Many density functional calculations predict CuO to be metallic when experiments show it to be semiconducting with a gap around 1.4eV. The mystery surrounding these *Mott insulators* thus gets imported to the cuprate superconductor problem. We do not have a firm grasp on the physics of a doped Mott insulator which results in the remarkable phase diagram seen in Fig. 1.3a. Strides have been made through the simple extension of the tight binding hamiltonian proposed by Hubbard. But, as previously mentioned, it remains frustrating to solve in two and three dimensions. An approximate to the Hubbard model known as the *t-J model* predicts antiferromagnetic insulating behavior at half filling as seen in the cuprates.

And yet, it is here that the problem is the most experimentally interesting. As we hole dope the antiferromagnetic Mott insulator, we observe the demise of the antiferromagnetic

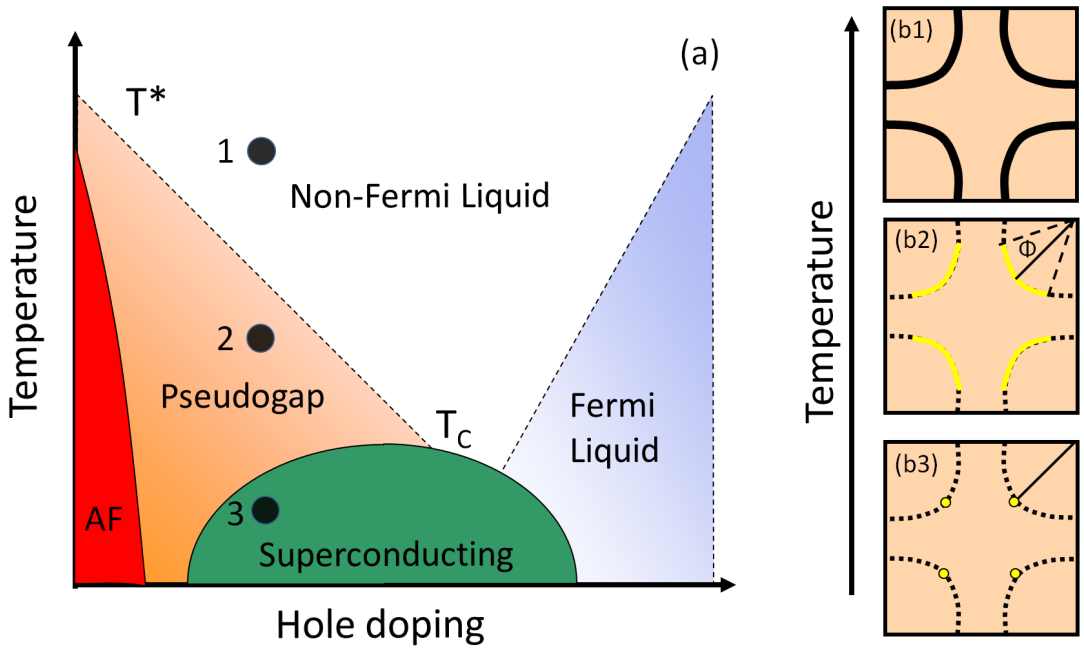

Figure 1.3. (a) Cartoon of the hole doped cuprate phase diagram. (b) The evolution of the underdoped Fermi surface with temperature indicated by the three points in (a): (b1) $T > T^*$ ungapped hole band, (b2) $T^* > T > T_c$ partially gapped Fermi arcs defined by ϕ from the ΓY line, and (b3) $T < T_c$ d-wave gap structure.

insulating phase and the origin of at least three mysterious elements of the phase diagram. (Electron doping is also interesting, but for the purposes of this thesis, we will focus in the hole doped side.) First, the onset of unconventional d-wave superconductivity in a dome generally peaked around a hole doping x=0.16, although even this can be abruptly destroyed such as in LSCO by the onset of stripes at 1/8 doping. Second, we have a rather peculiar normal state which does not follow the predictions of Fermi Liquid Theory. The result is a non-Fermi liquid or so-called *Marginal Fermi Liquid* which is phenomenologically described by Varma[12] where the inverse lifetime goes linearly with energy and not quadratically. We'll return briefly to this in Section 2.3. Finally, and most critically, we have the emergence of a phase, most apparent at dopings less than the optimal doping (where T_c is at its maximum), which neither supports superconductivity, nor appears to be a normal phase metal due to the presence of an incomplete gapping of the Fermi surface. This *pseudogap phase* is broadly defined by a temperature T^* and has particularly bizarre effects on the Fermi surface as seen by ARPES. Whereas the normal phase metal is an ungapped hole band crossing E_F (panel b1), and the superconducting phase is everywhere gapped except for the four symmetric nodal points (panel b3) as required by the $d_{x^2-y^2}$ gap function, Eq. 1.15), Fig. 1.3b shows a band structure in the pseudogap phase seemingly made up of discrete arcs or *Fermi arcs*. These arcs provide states at E_F that make up a Fermi surface, but in other locations a gap opens that qualitatively mirrors the superconducting gap. Other phenomena appear to be associated with this phase such as the Nernst effect measurements which find vortex-like excitations above T_c despite the absence of the Meissner effect[13]. For the purposes of this thesis, we will understand the pseudogap as being defined by a T^* such that above it is a metallic phase, and below it we have a partially gapped Fermi surface yet no superconductivity.

Since understanding the pseudogap forms the background to much of the work presented in Chapters 5 and 6, it deserves a little more development. At first glance the idea of such a Fermi surface should give us pause since it represents a undifferentiable rip in the electronic structure of the hole band manifold. What is happening at the point where the Fermi arc ends? If the density of state is inversely related to $\vec{\nabla}E(\mathbf{k})$, something particularly unusual must be happing at those points. There is even evidence to support that this point moves along the Fermi surface band structure with temperature (i.e. Arc length = T/T^*). Then, there is a question of what could be the microscopic nature of this phase? The challenge of this question mirrors the challenge of theory to explain this doping region. The community remains divided into two camps based on how one sees the relationship of the pseudogap phase to the superconducting dome.

The first camp sees the pseudogap as ultimately a precursor to superconductivity. The observed gap is related to Cooper pairs forming in this doping region, and thus explaining the existence of a gap which is appears d-wave like. But these Cooper pairs are unable to condense down into a macroscopic wave function (like the one proposed by Schrieffer) where there is long range phase coherence. So, the pseudogap phase is a dance hall where all the available couples are partnering up, but the music isn't loud enough to get them to dance in-synch until we finally pass below the associated T_c. In this perspective, the Fermi arc

and its decrease with temperature, represent near E_F states which are gradually pairing up as temperature drops. Thus, the superconducting gap is associated with the states nearest the Brillouin zone edge (often referred to as the anti-nodal point) corresponding to electrons moving along the Cu-O bond direction. One highly contested consequence is that the gap function observed in the superconducting phase should be defined by a single energy scale, Δ_{SC}, within the gap function described by Eq. 1.15. As it turns out, this appears to be well established at dopings on the right hand side of the maximum T_c (the so-called *overdoped region*). But in the area of the phase diagram where the pseudogap happens to also appear (the *underdoped region*) this is being contested.

The second camp sees the pseudogap not as pre-superconductivity but as an additional phenomenon which emerges from the doped Mott insulator. In this model, the pseudogap represents an additional ordering of the crystal which occurs only at low hole doping but which overlaps with dopings conducive towards superconductivity. This phenomena may be competitive with the formation of superconductivity or not, but it brings with it an additional energy scale Δ_{PG}. One example of this could be a charge density wave with a d-wave gap, where the CDW's associated gapping of the Fermi surface provides the Δ_{PG}. The general result would be that within the superconducting phase, the gap function would not be a continuous function of a single d-wave gap. Rather, it could be decomposed into two different d-wave gaps of different energy scales. In the analogy of the dance, our Cooper pair dancers share the hall with others wishing to do a line dance. The line dance is easier to start and may prevent our Cooper pair couples from getting on the floor. But once the music is loud enough the pairs still form up and begin their superconducting dance, awkwardly sharing the floor with remaining line dancers. There are many questions this camp has beyond the nature of the competing order. Does this order fundamentally compete, coexist, or even assist with the development of superconductivity? Work studying the states nearest to the node and antinodal points suggests that we are looking at fundamentally opposing phenomena. What is the true superconducting gap if the states at the antinode are dominated by a gap function unrelated to Δ_{SC}? And how does this phenomenon, either by itself or in conjunction with superconductivity, explain the presence and observed temperature and doping behavior of the Fermi arcs? It will be from these questions that our study of the Fermi surface and the near E_F states in Chapters 5 and 6 will find their origin.

Adding to this whole discussion of unconventional superconductors is the recent observation of superconductivity in iron based compounds (generally known as the iron pnictides.) As if flaunt the previous point regarding the expected incompatibility of magnetic phenomena and superconductivity, the idea of iron based superconductors, some of which have T_c's exceeding the McMillian BCS limit, runs entirely counter to our prevailing understanding of superconducting phenomena. There are strange similarities between the cuprates and the pnictides, most notably, the emergence of superconductivity from a doped magnetically ordered system and thus the proximity of magnetic physics with superconductivity. However, as opposed to an antiferromagnetic Mott insulator, the undoped compound is an antiferromagnetic metal supporting SDW physics and a structural transition of magnetic origin. From an industrial perspective, these iron pnictides would be significantly better candidates

for applications should they produce T_c's which can exceed 77K (the boiling point of liquid nitrogen.) The aforementioned coherence length, ξ, is rather small for the cuprates, making κ large, firmly making them Type II superconductors. The challenge is that the lower field, H_c, is significantly low such that is it easy to form vortices. However, these vortices are not pinned well, and consequently lead to losses in the supercurrent. The iron pnictides, though also Type II, are significant in that this H_c is more isotropic[14] and these dissipative vortices are more pinned, avoiding these losses. Understanding the phase diagram, the similarities and differences between the superconducting physics seen in the cuprates and the iron pnictides, and particularly how magnetism and magnetic ordering manifest themselves have been critical questions for study in these materials. We will return to these questions in Chapter 3.

The field of correlated electronic materials represents the forefront of how to understand and explain a whole host of fundamentally quantum mechanical phenomena in solids. We have discussed the origins of very idea of electronic band structure, some methods of modeling, the manner in which we can understand the addition of further complicating electronic effects, and the variety of ordering phenomena which emerge. Throughout this thesis we will be focusing on materials in which novel orderings and effects as those described in Section 1.4 emerge, and we will be exploring how the electronic states are affected in such situations. In each instance, we have made important advancements to how we understand the physics of these orderings which both illuminate the individual systems as well as larger fields within the solid state community. Our work looking at magnetic ordering in the iron oxypnictides compounds (Chapter 3) has provided important early guidance towards understanding not only the anomalously small magnetic moment, but even more crucially, direct experimental evidence that magnetic orderings may be more robust than normally expected by the field for dopings which support superconductivity. This result and similar work from other techniques, is fundamental to our understanding not only of the superconducting iron pnictides, but the larger field of unconventional superconductivity. Our work looking at charge density wave ordering, particularly in the rare earth tellurides (Chapter 4), addresses a significant debate over the existence of quasi-2D systems which can actually support a Peierls transition. Our work clearly demonstrates the existence of nesting-related charge density wave formation in a layered system that leads to a metal-to-insulator transition. This is, finally, a precise analogue to the ideal 1D CDW systems first proposed by Peierls and seen in quasi-1D systems. All of this work has led to our exploration of the high temperature superconducting cuprates and complexities of their phase diagram. Our work has endeavored to approach the question of the lattice and its effects from a novel direction, using lanthanide substitution to cause lattice mismatch within the single layered cuprates (Chapter 5). The effect of this substitution appears as a new strain axis in the cuprate phase diagram and our work has been among the first to explore the effects of this phenomena which competes with superconductivity and sheds light on the all-important pseudogap phase. This work bore additional fruit in the study of one system in particular, revealing evidence of a sharp crossover in the electronic states near E_F(Chapter 6). Given the issue of the pseudogap phase and the resulting debates previously mentioned, our work both provides strong evidence for two phenomena to be involved within this region of the phase diagram and brings together

other work done on the single layered cuprates in the literature. This is critical for the field as we continue to understand the diversity of results regarding the relationship between the pseudogap and superconducting phases and what types of lattice order may play a role.

However, in order to do any of this, we first need a probe that provides direct access to the electronic states. As previously alluded to, ARPES is such a probe whose power has grown substantially over the last 15 years due in large part to advances in instrumentation. With the power to map Fermi surfaces and band dispersions, reveal subtle changes in near-E_F electronic states, and to take Landau's quasiparticles from an abstract construction to a truly observable electronic state, ARPES's role in solid state physics is well established. Thus, we now turn our attention to the physics of the probe itself, which are simple in concept but remarkably complicated in detail.

Chapter 2

Angle Resolved Photoemission Spectroscopy

2.1 A Brief History of Photoemission

The experimental origins of photoemission predate the identification of the electron by Thompson in 1897 and represent a canonical part of the story of early quantum theory. Hertz first discovered in 1887 that a current was produced when a metal was illuminated, though the phenomena was remarkable for a number of reasons: 1) The metal didn't emit electrons due to heat as in the case of thermionic emission seen in vacuum tubes which was a contemporary phenomenon. 2) Though the current was proportional to the intensity of the light, the frequency had an all-or-nothing effect on the current with red light producing no effect despite intensity while violet light always gave a current. 3) The electrons' maximum kinetic energy was only affected by the color of the light and not the intensity. With Maxwell's equations and their wavelike description of light firmly in place (despite trouble finding the media of propagation), these results presented a puzzle that only a model with a discrete view of light could unravel. For a wave, the energy carried is related to the intensity of the wave. So, the strong correlation with frequency would be completely unexpected. In 1905, Einstein, inspired by Plank's work regarding quantization in the blackbody radiation problem, proposed that light itself is quantized and that each quanta, or photon, carried an energy $h\nu$. The result was that one could write the maximum kinetic energy of the photoelectron current as

$$E_{max} = h\nu - \phi, \tag{2.1}$$

where ϕ is the *work function* of the material. The work function represents the minimum energy needed to excite an electron from the crystal into the vacuum. It is, on closer inspection, a complicated physical quantity which we will return to in following section. In Einstein's model, prefacing the later work of De Broglie, light cannot be seen as either solely a particle (given the success of Maxwell's theory) or solely a wave due to the limitations of the photoelectric effect. Depending on the measurement, it can take on the properties of one or the other. It was for this explanation of photoelectric effect, that Einstein was awarded the Nobel Prize in 1921 (since relativity theory was still considered controversial.)

As the physics of materials began to develop with the advancements in quantum mechanics, being able to probe the electronic states of a solid, whether its tightly bound core levels or its valence states nearer E_F, began to be more important. It was primarily the work of Kai Siegbahn that took the photoelectric effect and raised it to Photo Emission Spectroscopy (PES), a powerful technique in its own right. Historically in the literature, there is a differentiation based on whether the photons are X-rays (XPS) or ultraviolet light (UPS). Through this technique, one could probe the electronic density states and could determine the elemental composition of the surfaces of materials. Additionally, one could observe subtle shifts in atomic orbital core level peaks, revealing information about the local atomic environments. So significant an analytical tool, that his development of XPS earned Seigbahn the 1981 Nobel prize in Physics.

Fundamentally, the technique worked because of conservation of energy between the incident photons, the binding energy of the electronic states, and kinetic energy of the emitted electrons. It seems natural to ask whether one could take advantage of conservation of momentum as well to extract fuller information of the electronic states, specifically those in dispersive electronic states closer to E_F. By collecting photoemitted electrons emerging from a crystal with a particular angle, one can deduce their associated momentum via this angle and their kinetic energy. Varying this angle, one could probe the electronic structure in particular regions of k-space. The result was data of the actual electronic dispersions and the first angle resolved photoemission spectroscopy was demonstrated in 1974[15,16].

Like many techniques, the power of the ARPES technique was continually enhanced by advancements in light sources. As generations of synchrotrons produces higher and higher fluxes, one could monochromate the light to better and better energy resolutions, and create larger photoemission currents. This allows for smaller and smaller slices of the momentum space to be studied while still integrating sufficient counts for statistically significant data. Among the most well known triumphs of the ARPES technique was the its establishment of the nodal character of the d-wave pairing gap in the cuprate superconductors[17]. Since then, detector advancement particularly in the late 1990's led to tremendous enhancements in the ARPES technique through the development of hemispherical analyzers. Through these analyzers, the unit information accumulated in an ARPES experiment went from a 1D spectra taken at point in k-space, into a 2D intensity map which represents a slice in k-space. Thus, band structure could be more rapidly "mapped" out particularly as the angular acceptance of these analyzers became larger and larger. Today, with angular resolution approaching 0.1°, a steadily improving energy resolution exceeding 1meV, as well as numerous experi-

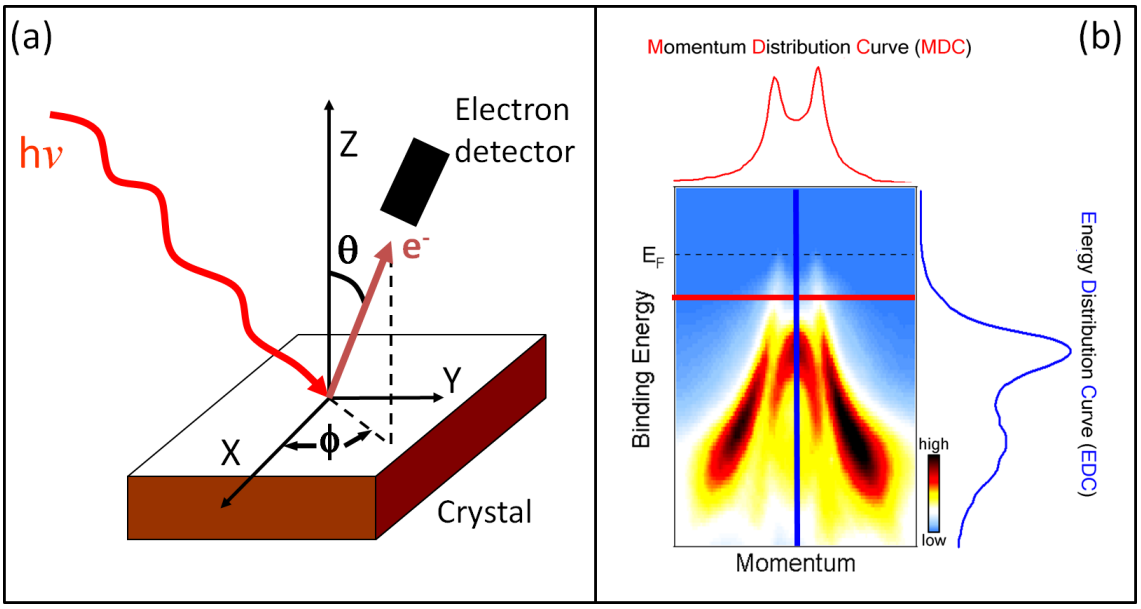

Figure 2.1. (a) Schematic of the angle resolved photoemission process. (b) Sample 2D data set or "cut" taken on CeTeSb illustrating the two main analysis techniques: Momentum Distribution Curves (MDC) and Energy Distribution Curves (EDC).

mental advances involving highly localized beam spots (Nano-ARPES), spin resolution, and laser-based pump-probe experiments, ARPES is and will remain a truly unique experimental probe in the field of correlated electronic systems.

2.2 The ARPES Experiment

Given the power of the technique, ARPES can seem to be a straightforward almost easy technique, and in many respects there is some truth to this perspective. Fig. 2.1 provides a schematic of the photoemission process with a typical data set included in panel b. Light, primarily in the very ultraviolet (VUV) region of the spectrum (5-100eV), is incident on a sample surface. There are obviously many sources for this light, each with their own advantages. Synchrotron light sources are particularly important given their luminosity, though their primary advantage is the ability to change photon energies quickly via adjustment of insertion device parameters (e.g. undulator gap) and monochrometer settings. Increasingly, gas discharge lamps, most notably Helium lamps, can also provide a source of VUV light at 21.2eV (the He I line) and even, although weaker, light at 40.8eV (He II line) in a relatively compact source even considering the additional superstructure for collimating and monochromating. The downside is photon flux and the inability to change photon energies, which is a major limitation. Most recently, the use of lasers in conjunction with frequency doubling, non-linear optics have opened up the possibility of laser based ARPES, using light

around 6-7eV using current technology (most work functions are between 4 and 5eV). These systems can have high energy resolution and already have produced some of the sharpest ARPES band structure data in the literature[18]. Yet there are numerous issues to be overcome: The low energy means that the photoemitted electrons have a lower kinetic energy, thus leading to slower speeds and greater influence from stray fields within the experiment. The intensity of the beam has led some to wonder if our interpretation of the photoemission process (discussed in the next section) is no longer as appropriate, leading to questions of data interpretation. Finally, electronic states that are beyond certain momentum values in the Brillouin zone may be inaccessible since the kinetic energy provides a limit to the possible momentum values, which we will explain shortly. This would be particularly problematic for crystals with small unit cells (large Brillouin zones.) The current inaccessibility and fragility of certain non-linear crystals also adds some complications to developing the technique.

As mentioned in Section 2.1, the essential governing equations of the ARPES technique are rather simple: Conservation of energy taking into consideration the material's work function, and conservation of momentum

$$E_{kin} = h\nu - \phi - |E_B| \tag{2.2}$$

$$|\mathbf{p}| = \sqrt{2mE_{kin}} \tag{2.3}$$

$$\mathbf{p}_{||} = \hbar\mathbf{k}_{||} = \sqrt{2mE_{kin}} \cdot \sin\theta \tag{2.4}$$

where ν is photon frequency, E_B is the electron binding energy as measured with respect to E_F, and θ corresponds to the polar angle from the normal. From these equations, we see the limitation that low incident photon energy has on momentum states. For any $h\nu$, there is a maximum E_{kin}. From Eq. 2.4, there is a maximum value of $\mathbf{k}_{||}$ that can be photoemitted from k-space. Fig. 2.2 (reproduced from Hüfner[19]) graphically illustrates the photoemission process in the energy dimension as a measurement of density of states, N(E). Core level states are long lived states with sharply defined energies (large Δt$\rightarrow$ small ΔE) broadened by the experimental technique. The electron band near E_F represents the dispersive valence band states which, as explained in Chapter 1, are only filled up to roughly E_F (in a metal.) One might also ask how momentum could be conserved in plane unless the photon is always striking the surface normal to the plane (which would make ARPES impossible.) However, if one calculates the associated momentum of a photon with energy <100eV, it is significantly smaller than that of the Bloch states and thus the photoemitted electron as to be negligible in the calculation.

The origin of the work function, ϕ, is complicated, and the potential is predominantly due to three major components: 1) At the atomic scale, when the electron passes across the sample surface, there is always a dipole layer, despite the material being electrically neutral. But, given the metalicity, this is usually effectively screened and only exists over a range of about a few lattice spacings. 2) At the micron scale, the electron leaving the surface of a conductor experiences an attraction due to the formation of an image charge field. The effect of this coulombic attraction fades after a few microns. 3) On a more macroscopic length

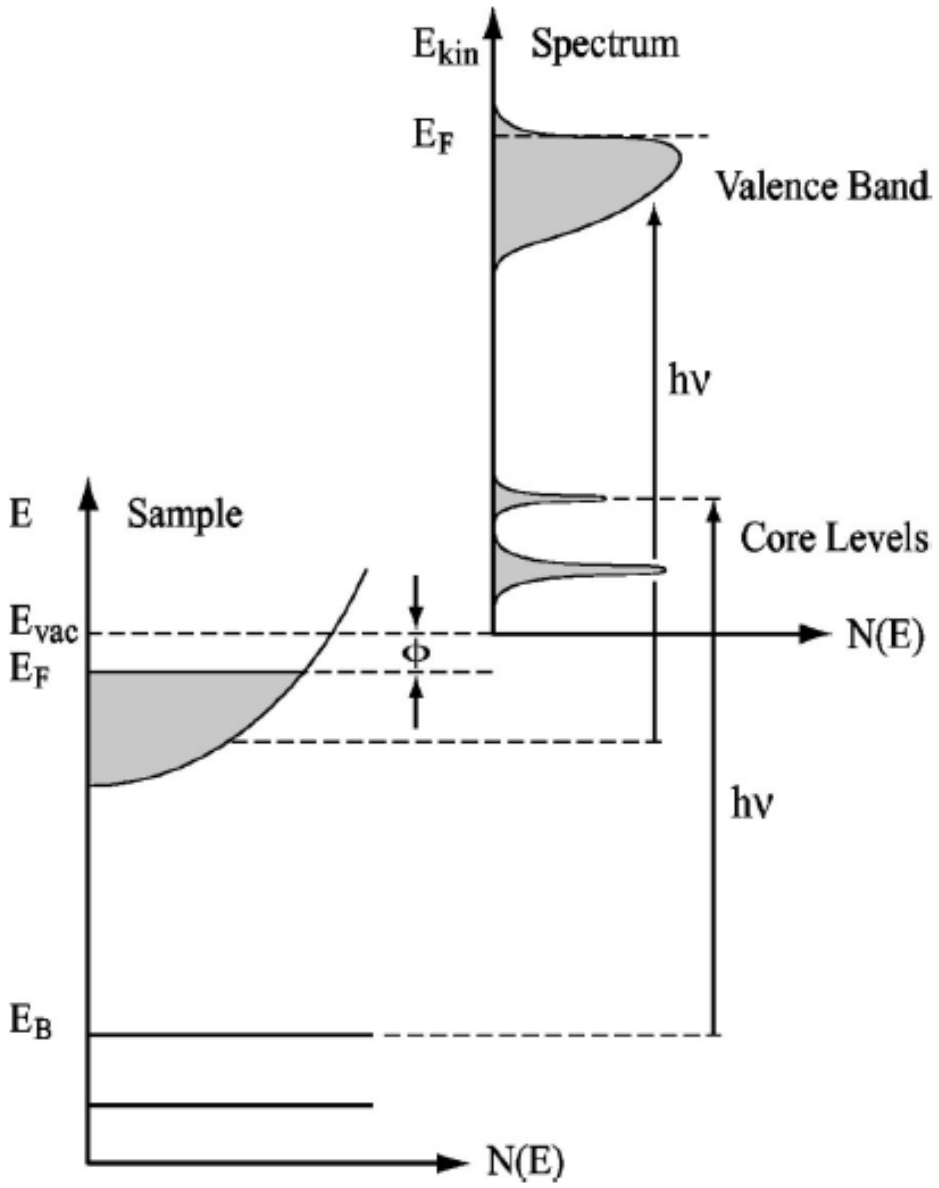

Figure 2.2. Schematic of the photoemission process from the Bloch states in the crystal into the electron analyzer and the resulting energy spectra as a function of E_{kin}. Figure is reproduced from Hüfner[19].

scale, different crystal faces have different dipole layers as addressed in point 1. So there must be different electronic potentials outside of the material to compensate this, otherwise an electron could exit one surface, enter another, and return to the bulk with greater or less energy for the journey. In addition to these three sources of fields, the effect of rough surfaces or adsorbents on the surface also could affect the workfunction in difficult to determine ways.

Finally, as Fig. 2.1 illustrates, the photoemitted electrons with momentum and energy representative of their former lives in the crystal's Bloch states, pass through space to the entrance slit of a hemispherical analyzer. While the electrons are moving from sample to detector, electric fields need to be eliminated by ensuring that the sample is grounded to the analyzer. Also, magnetic fields must be shielded by using μ metal in order to prevent contributions from the Lorentz force leading to distortions in the spectra. Additionally, the mean free path must be sufficiently long to prevent scattering. So high vacuum is required for this ($< 10^{-5}$ Torr), though ultra high vacuum ($< 10^{-10}$ Torr)is used in practice for reasons of sample surface contamination.

Once in the analyzer, entrance slits and electrostatic lenses focus the electrons around the outside of the analyzer and towards a multichannel plate (MCP), acting as a signal enhancement device. Finally, a CCD camera records the raw data as a 2D intensity image. Electrons with different angles (momenta) are directed along one axis of the 2D image, meaning that electrons with no relative angle with respect to the analyzer would strike the screen in the center. Similarly, the electrons with different kinetic energies move along the hemisphere experiencing a radially directed E-field, thus acting like a velocity selector. So, on the other axis of the screen, electrons with higher kinetic energy land on one side while those with less end up on the opposite side. In this way, the 2D intensity image provides information regarding both momenta (after a conversion using spherical geometry is employed) and energy of the electronic states simultaneously.

Before moving on to the physical meaning of the data ARPES provides, a final point should be made. As hinted to in our discussion of light sources, one might wonder why pick any particular photon energy so long as one can cover the entirety of the Brillouin zone for the given binding energies desired. By responding this, we actually highlight many of the fundamental limitations of the ARPES technique. The first issue relates to the fact that although VUV light may penetrate far into a crystal, what fundamentally matters is the mean free path of the photoemitted electrons as they leave the crystal. Here, we encounter the perennial argument against ARPES. Fig. 2.3 shows the photoelectron mean free path as a function of electron kinetic energy[20]. It is immediately clear that given unit cells on the order 10Å, ARPES does not have good bulk sensitivity and is restricted to the first few monolayers on the surface of the crystal. The result of this is that sample surfaces must be pristine either by cleaning the surface (e.g. annealing) or by cleaving the sample in situ. It is for this reason that the experimental vacuum must be in the ultra high range ($<10^{-10}$ Torr) for many samples, to prevent sample surface degradation or "aging." Being able to alter the photon energy does potentially affect the bulk sensitivity by changing the mean kinetic energy of the photoelectrons (thus, giving laser based ARPES better bulk sensitivity.) One might then ask, given the trends of the curve and the reality of the work function at low

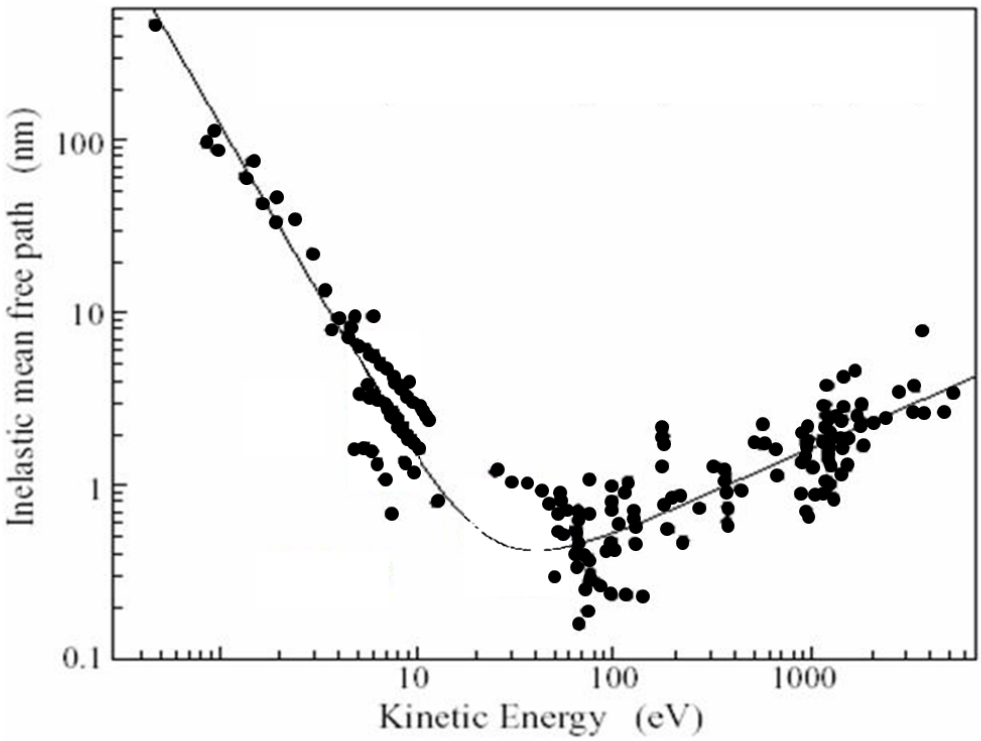

Figure 2.3. The inelastic mean free path for an electron in a solid as a function of energy. Figure is reproduced from Ref.[20].

energies, why not push on to higher photon energies in the soft x-ray range. This is quickly countered by the fact that as photon energy rises, the momentum and energy resolution become significantly worse. In addition, one will eventually reach photon momenta values that are non negligible and the size of the Brillouin zone in angle/momentum space (consider Eq. 2.4 allowing E_{kin} to increase and holding theta fixed) becomes increasingly smaller to study, making a finer survey of the k-space band structure practically more difficult.

A second issue relates to measuring momentum dispersions in the k_z or surface normal direction. As previously mentioned, the translational symmetries that allow for conservation of momentum only exist for the in-plane directions, and is lost in the normal direction. For materials that are quasi-2D, the systems have little dispersion in the k_z direction and so little useful information would be gained. But in many systems this is not true (or at least not guaranteed without experimental evidence.) By varying the incident photon energy, one varies the value of E_{kin}, which changes the size of the momentum space explored. Thus, as we change our photon energy, we are accessing states which may have the same $k_{||}$ but different k_z. Thus, being able to range through different incident photon energies is essential to mapping out the k_z dependence. In practice, an inner potential must be determined from the data, representing the Δp_z that the electrons will lose as they exit the system. This is usually assumed to be a fixed value and can be determined from the periodicity of the band structure in the k_z direction as one goes beyond the first Brillouin zone.

A third and final issue naturally takes us into the physical interpretation of the ARPES data. As we will explore in the next section, one can think of the photoemission process as a quantum mechanical process that takes us from electronic states in the crystal to states in the vacuum. Thus, the probability of the process will be determined by Fermi's Golden Rule (see Eq. 2.5.) Within that formula, there is a matrix element that connects the initial and final states and thus can be modified to promote or inhibit certain transitions. As we will soon see, among the many variables within this matrix element is the energy of the incident light. By varying the incident photon energy, band structure can be enhanced or weakened by changing the value of this matrix element. Additionally, certain photon energies can setup resonances with the core level states that may also enhance the observed band structure. If photons with energies near the binding energies of core levels are used, then electrons from these states can be promoted up to the near E_F valence bands associated with those elements. This further populates them and an increasing the number of electrons can be photoemitted. This technique of *Resonant Photoemission Spectroscopy* will be used in the data presented in Chapter 4. This whole discussion illustrates one of the final critical issues with the ARPES technique. To directly equate the photocurrent with the electronic density of states is not entirely accurate. There are many phenomena which can affect the photocurrent that have absolutely nothing to do with the actual density of states or electronic band structure of the material being studied. So, a degree of care must be taken in equating the results. Therefore, in order to make progress with the ARPES technique, particularly in the complex correlated electronic systems we will be studying, we need to turn our attention to the physical interpretation of ARPES data so that we can best understand and analyze the data which comes from an ARPES experiment.

2.3 The Physical Interpretation of ARPES Data

Since we are describing the transition of an electron from one quantum state to another due to a time dependent perturbation (light), our natural starting point would be to use time dependent perturbation theory and one of its most useful results, Fermi's Golden Rule:

$$w_{fi} = \frac{2\pi}{\hbar} \left| \left\langle \Psi_f^N \left| H_{int} \right| \Psi_i^N \right\rangle \right|^2 \delta(E_f^N - E_i^N - h\nu) \tag{2.5}$$

The w_{fi} represents the transition probability for an excitation due to the perturbation H_{int} (incident photons of energy $h\nu$) causing a transition between the initial N-electron state, Ψ_i^N, to any final electronic states, Ψ_f^N. The final state energy should be the energy of the N-1 electron wavefunction plus the kinetic energy of the now liberated photoelectron which we measure ($E_f^N = E_f^{N-1} + E_{kin}$.) Consequently, the initial energy state would replace E_{kin} with the binding energy of the electron it its electronic state, E_B^k, giving ($E_i^N = E_i^{N-1} - E_B^k$), where E_B^k and E_{kin} are related by the conservation law expressed in Eq. 2.2.

The choice of H_{int} involves considering the hamiltonian of a classical radition field as described in many sources (e.g. Sakurai Eq. 5.7.1[21])

$$H = \frac{\mathbf{p}^2}{2m_e} + e\phi(x) - \frac{e}{m_e c}\mathbf{A} \cdot \mathbf{p} \tag{2.6}$$

where we have assumed that the field is small ($\mathbf{A}$ is small) so that the $|\mathbf{A}|^2$ term is neglected in the hamiltonian, as well as assuming that the change in $\mathbf{A}$ is small over the area over atomic dimensions. This latter approximation is referred to as the *dipole approximation* where $\nabla \cdot \mathbf{A} = 0$. It is worth noting that this approximation may not be appropriate near the surface of the crystal where the field dependences can be more extreme. But in order to make any progress, we will employ the approximation to get our H_{int}

$$H_{int} = -\frac{e}{mc}\mathbf{A} \cdot \mathbf{p} \tag{2.7}$$

Now that we have an initial quantum mechanical model, we need to consider the physics of the transition itself, which has led to two models. The first is to think of the transition in a *one-step model*. In this picture, all the physical phenomena involved in the photoemission process (photon absorption, electron liberation, journey as a free particle, and final detection) are treated as a single coherent process. The result is (despite the name) a more rigorous approach resulting in a very complicated hamiltonian of the crystal (the electronic states, not to be confused with H_{int}) incorporating bulk, surface and vacuum contributions. Because of the inherent difficulties in such a hamiltonian, it is more common to think of photoemission data in terms of a *three-step model*:

1. Incident light excites the electron in the bulk
2. The excited electron travels to the crystal surface

3. The electron escapes into the vaccum as a free particle

The advantage of this model is that we can analyze each part assuming they are effectively independent and the total photoemission intensity is simply a product of the probability associated with each. This allows us to focus the bulk of our attention on the initial excitation which we have already modeled. Step 2 is generally thought of as a mean free path associated with electrons trying to reach the surface without scattering (the universal curve from Fig. 2.3.) This also results in what is called the *inelastic background* which enters into the line shapes of intensity vs. energy spectra. Step 3 is simply related to the work function, ϕ, and the energy of the excited electron. We can thus focus the bulk of our attention on step 1.

Again for the sake of computational convenience, we will assume that the N-particle system when excited has no time to react. We do this so that we can write the wavefunction as the product of a now excited particle (the photoelection) and the remaining states (Ψ^{N-1}) without worrying about how these states now evolve to a new relaxed state. This idea, known as the *sudden approximation*, should be familiar to students of quantum mechanics whereby when a system is changed rapidly, the original wavefunction remains initially unchanged, even if it is no longer an eigenstate of the system. Here we find the justification for the concerns expressed at the outset of the previous section regarding laser based systems. With the low photon energies of laser based systems (or any low photon energy experiment), one must seriously consider whether we are reaching the point which this sudden approximation (or perhaps the entire three step model) is no longer appropriate. Although evidence exists that these approximations work for photon energies at least as low as 20eV [22], single digit eV photon energies are certainly disconcerting and beg the question as to whether our interpretation of the ARPES experiment is appropriate. But, like so much in experimental condensed matter physics, it is often a far better approach to shoot first, and ask questions later.

Having incorporating the three step model along with the sudden approximation to the first of those steps, the results are wavefunctions of the form

$$\Psi_i^N = A\phi_i^k \Psi_i^{N-1} \tag{2.8}$$
$$\Psi_i^{N-1} = c_k \Psi_i^N \tag{2.9}$$
$$\Psi_f^N = A\phi_f^k \Psi_f^{N-1} \tag{2.10}$$

where A is just an antisymmetric operator to satisfy the demands of the Pauli principle. The operator c_k is an annihilation operator, which takes the Ψ^N wave function and turns it into a Ψ^{N-1} function. The ϕ_i^k and ϕ_f^k correspond the wavefunction of the single electron orbital and of the photoelectron respectively. From this we can finally return to Fermi's Golden Rule (Eq. 2.5) and deal with the $\left|\left\langle \Psi_f^N \left| H_{int} \right| \Psi_i^N \right\rangle\right|^2$ term so that

$$\left\langle \Psi_f^N \left| H_{int} \right| \Psi_i^N \right\rangle \tag{2.11}$$

$$= \left\langle A\phi_f^k \Psi_f^{N-1} \left| H_{int} \right| A\phi_i^k \Psi_i^{N-1} \right\rangle \tag{2.12}$$

$$= \left\langle \phi_f^k \left| H_{int} \right| \phi_i^k \right\rangle \left\langle \Psi_f^{N-1} \middle| \Psi_i^{N-1} \right\rangle \tag{2.13}$$

$$= M_{fi}^k \left\langle \Psi_f^{N-1} | \Psi_i^{N-1} \right\rangle \tag{2.14}$$

Since the H_{int} only affects the single electron, we can compact all of the information of light's interaction with the single electron as M_{fi}^k. The overlap term is a little more tricky. The set of final states for the N-1 wavefunction, Ψ_f^{N-1}, are not, strictly speaking, final states but rather are excited states. So, for ease, we will change our index from $f \rightarrow m$ ($\Psi_f^{N-1} \rightarrow \Psi_m^{N-1}$). Thus, with this we can write

$$|c_{mi}| \equiv \left\langle \Psi_m^{N-1} \middle| \Psi_i^{N-1} \right\rangle \tag{2.15}$$

so that we can place all the terms into Eq. 2.5 and include in implicit summation of states within that equation along with writing final energy as expressed earlier to get

$$\sum_{f,i} |M_{fi}^k|^2 \sum_m |c_{mi}|^2 \, \delta(E_m^{N-1} + E_{kin} - E_i^N - h\nu) \tag{2.16}$$

It is characteristic of strongly correlated systems that $|c_{mi}|^2 \neq 1$,. The issue is that the removal of an electron will result in a large change in the potentials of the system resulting in significant overlap between the state before and those after (beyond the unique $|c_{mi}|^2 = 1$ situation which occurs in the non-interacting picture.) Understanding and potentially calculating these results are an important part of explaining the spectra that ARPES provides when done on correlated electronic systems. But how would one able to make such calculations? Understanding the relationship between a single photoemitted electron in its respective orbitals and the interaction term, H_{int}, which goes into the matrix element $|M_{fi}^k|$, seems tractable. But now do we even begin to understand $|c_{mi}|^2$ with its N-1 electrons strongly interacting with each other? We much turn back to the ideas that were explored in Chapter 1 with Fermi liquid theory and approach the problem with some new mathematical tools, the aforementioned *Green's functions*.

It is a fact generally acknowledged among ARPES experimentalists, that Green's functions are part of that elaborate black magic that theorists are (hopefully) the knowledgeable practitioners. The central quantity that ARPES is believed to be revealing is the *single particle spectral function* $A(\mathbf{k}, \omega)$. It is because this quantity is fundamentally related to Green's functions that these mathematical objects are even more significant to ARPES. Indeed its this central ability to directly probe $A(\mathbf{k}, \omega)$ that makes ARPES's experimental insights highly sought after by condensed matter theorists. Therefore, it is worth taking a journey into this world so that we may better understand how to incorporate ideas such as Fermi liquid theory and other aspects of correlated electronic systems into ARPES.

At their most basic, Green's functions are a trick for solving a differential equation which involves a linear operator, $\hat{L}$ (e.g. ∇^2.) Given an equation

$$\hat{L}\Psi = \Phi \tag{2.17}$$

where $\hat{L}$ acts on an unknown function Ψ to create a new function Φ, you can solve the equation (i.e. determine Ψ) if you know the Green's function, G, of the operator $\hat{L}$. This function has the property that when the operator $\hat{L}$ acts on it, the resulting function is a unit impulse in whatever variables are being used. Already one can see how this might be. If you knew a solution to the most basic unit of a problem, you could determine the solution to any problem that could be built from those units (assuming superposition, which comes as a consequence of linearity.) For example, if one understands the field from a single unit charge, they should be able to create any field from adding those units of charge together. Thus, the Green's function is our unit impulse, so that when the operator is applied to it, it can be generalized to provide a solution to any complicated system. Mathematically, this is written as

$$\hat{L}G = \delta \tag{2.18}$$

where δ is the unit response, like the Dirac delta function. Adding variables, we realize that G would actually be written as $G(x, x')$ so that

$$\Phi(x) = \int \Phi(x')\delta(x - x')dx' \tag{2.19}$$

$$\Phi(x) = \int \Phi(x')\hat{L_x}G(x, x')dx' \tag{2.20}$$

$$\hat{L_x}\Psi(x) = \int \Phi(x')\hat{L_x}G(x, x')dx' \tag{2.21}$$

$$\Psi(x) = \int \Phi(x')G(x, x')dx' \tag{2.22}$$

Thus, if you know the Green's function, $G(x, x')$, you can determine the unknown function $\Psi(x)$.

Now, in quantum mechanics, we know of functions that behave a lot like $G(x, x')$, and they usually are associated with how a system evolves. Because of it's relevance to our later discussion, let's remember how a quantum state evolves in time. It is a fundamental result that a state α at time t_0, $|\alpha, t_0\rangle$, evolves such that at a time t, the state $|\alpha, t_0; t\rangle$ (t_0 remains as a parameter) is given by

$$|\alpha, t_0; t\rangle = exp\left[\frac{-i\hat{H}(t - t_0)}{\hbar}\right]|\alpha, t_0\rangle \tag{2.23}$$

Now, let's move away from the Dirac notation and write these as wave functions. It is also worth looking ahead to realize that since it is momentum that best defines our states

(and not position), we should make these wavefunctions of $\mathbf{k}'$ (take the inner product of both sides with $\langle k|$ and integrate appropriately with respect to $\mathbf{k}'$) we get something, after some effort (see Sakurai chapter 2.5 for details[21]), which looks like

$$\psi_\alpha(\mathbf{k},t) = \int d^3k G(k',k;t,t_0)\psi_\alpha(\mathbf{k},t_0) \tag{2.24}$$

where G is the inner product

$$G(k',k;t,t_0) = \left\langle \alpha,\mathbf{k}' \left| exp\left[\frac{-i\hat{H}(t-t_0)}{\hbar}\right] \right| \alpha,\mathbf{k} \right\rangle \tag{2.25}$$

This function actually represents the Green's function associated with the time-dependent Schrödinger equation (in k-space). In other words, $G(k',k;t,t_0)$ is associated with a unit impulse response to the time-dependent Schrödinger equation (with the boundary condition that $G(k',k;t,t_0) = 0$ for t<t_0)

Now, let's think about this function with the mentality of crystalline electronic states. From Eq. 2.24, $G(k',k;t,t_0)$ represents how, starting with an electron in some state $\mathbf{k}$ at time t_0, the system will propagate into a state with momentum related to $\mathbf{k}'$ at time t. Immediately, we can see how this might relate to understanding correlated electronic systems since if we understood the Green's function of such a system (with all its interactions) we could then describe the evolution of its electronic states (e.g. time dependence of quasiparticle states). Now, ARPES is a spectroscopy and as such takes data with respect to energy (which we'll write as ω) and not time. So to make things easier, we will set $t_0 = 0$, and do the Fourier transform of the time dimension of $\hat{G}(\mathbf{k}$,t) to create $\hat{G}(\mathbf{k},\omega)$.

$$\hat{G}(\mathbf{k},t) = e^{\frac{-i\hat{H}(t-t_0)}{\hbar}} \tag{2.26}$$

$$\hat{G}(\mathbf{k},\omega) = \frac{1}{i\hbar}\int_0^\infty dt e^{\frac{-i\hat{H}t}{\hbar}} e^{i\omega t} \tag{2.27}$$

$$\hat{G}(\mathbf{k},\omega) = \frac{1}{\omega - \hat{H}} \tag{2.28}$$

In the final line, the traditional liberty of setting $\hbar$=1 was used (so ω should be read $\hbar\omega$) and the initial $\mathbf{k}$ value has been dropped since, for ARPES, the initial and final $\mathbf{k}$ of the photoexcited electron are identical. The Green's function is written as an operator, $\hat{G}$, since the function was removed from the inner product (Eq. 2.25) and is now a function of $\hat{H}$. It is essential to note that the only way for the integral in Eq. 2.27 to converge is if ω has a positive imaginary part. Thus, we need to allow for ω to take on imaginary values. We can also see that any energy eigenstate of $\hat{H}$ will yield a pole at the associated eigenvalue. So, we can write the Green's function in Eq. 2.28 in more familiar way by evaluating its inner product over Bloch states, $|\mathbf{k}\rangle$, where $\hat{H}|\mathbf{k}\rangle = \epsilon_k|\mathbf{k}\rangle$. Doing this, we find that

$$\sum_k \left\langle \mathbf{k}|\hat{G}(\mathbf{k},\omega)|\mathbf{k}\right\rangle \tag{2.29}$$

$$= \sum_k \left\langle \mathbf{k}|\frac{1}{\omega-\hat{H}}|\mathbf{k}\right\rangle \tag{2.30}$$

$$= \sum_k \langle \mathbf{k}|\mathbf{k}\rangle \frac{1}{\omega-\epsilon_k} \tag{2.31}$$

$$= \frac{1}{\omega-\epsilon_k} \tag{2.32}$$

We can take Eq. 2.32 and explicitly allow ω to take complex values, $\omega \to \omega \pm i\eta$ with ω and η as real and positive. The negative sign in front of the imaginary part corresponds to information about the past, or put differently, an integral like Eq. 2.27 but with limits $(-\infty, 0]$. The most surprising and fortunate result comes when we work at ω in the vicinity of the eigenvalue poles, ϵ_k, where η is very small, we find that isolating real and imaginary parts

$$G(\mathbf{k},\omega) \sim \frac{(\omega-\epsilon_k)}{(\omega-\epsilon_k)^2+\eta^2} \mp \frac{i\eta}{(\omega-\epsilon_k)^2+\eta^2} \tag{2.33}$$

$$\sim \frac{1}{\omega-\epsilon_k} \mp i\pi\delta(\omega-\epsilon_k) \tag{2.34}$$

since for very small η

$$\lim_{\eta\to 0} \frac{\eta}{(x^2+\eta^2)} = \pi\delta(x) \tag{2.35}$$

Now, at last, we can address the original issue. How do we calculate $|c_{mi}|^2$ as defined in Eq. 2.15? Previously, we had no way to determine this quantity because we could not determine how the initial state evolved into the final state. But now, we have a Green's function which can take us from one state to the other in a manner that obeys the Schrödinger equation. We wish to determine the sum of probability amplitudes for transitioning from an initial state, Ψ_i^{N-1}, to the excited states, Ψ_m^{N-1}. By using the Green's function in Eq. 2.32 with complex frequency, we can expand and rewrite it terms of the excited states, m. Then, we can take the inner product with initial state Ψ_i^{N-1} since it is the evolution from this state to the excited state, Ψ_m^{N-1}, that we are interested in

$$G(\mathbf{k},\omega) = \frac{1}{\omega \pm i\eta - \epsilon_k} \tag{2.36}$$

$$\hat{G}(\mathbf{k},\omega) = \sum_m \frac{\left|\Psi_m^{N-1}\right\rangle \left\langle\Psi_m^{N-1}\right|}{\omega \pm i\eta - \epsilon_k} \tag{2.37}$$

$$= \sum_m \frac{\left|\Psi_m^{N-1}\right\rangle \left\langle\Psi_m^{N-1}\right|}{\omega \pm i\eta - (E_m^{N-1} - E_i^N)} \tag{2.38}$$

$$= \sum_m \left|\Psi_m^{N-1}\right\rangle \left\langle\Psi_m^{N-1}\right| \left\{\frac{1}{\omega - \epsilon_k} \mp i\pi\delta(\omega - (E_m^{N-1} - E_i^N))\right\} \tag{2.39}$$

Thus, we find

$$\left\langle \Psi_i^{N-1} \left| \hat{G}(\mathbf{k},\omega) \right| \Psi_i^{N-1} \right\rangle = \sum_m \left|\left\langle \Psi_m^{N-1} | \Psi_i^{N-1} \right\rangle\right|^2 \left\{\frac{1}{\omega - \epsilon_k} \mp i\pi\delta(\omega - (E_m^{N-1} - E_i^N))\right\} \tag{2.40}$$

We take advantage of the fact that the electronic structure is basically the binding energies ($\epsilon_k = -E_B^k$), which can then expressed in terms of the excited states by looking at the change between the initial N particle state and the N-1 excited state ($E_B^k = E_i^N - E_m^{N-1}$). But the most important observation is that the imaginary part of the Green's function Eq. 2.40 looks identical to what we were searching for to complete Eq. 2.16. Put differently, treating Eq. 2.40 as the Green's function associated with the transition from the initial to excited states in step 1 of the photoemission process, we find

$$\frac{-1}{\pi} Im\left\{G(\mathbf{k},\omega)\right\} = \sum_m \left|\left\langle \Psi_m^{N-1} | \Psi_i^{N-1} \right\rangle\right|^2 \delta(\omega - (E_m^{N-1} - E_i^N)) = \sum_m \left|c_{mi}\right|^2 \delta(\omega - (E_m^{N-1} - E_i^N)) \tag{2.41}$$

Recognizing that the energy associated with the photoelectron $\omega = h\nu - E_{kin}$ (and flipping the sign in the delta function argument) and we have recovered the missing piece from Eq. 2.16. This is a significant result since it means that ARPES data provides a direct measure of the Green's function. Given a system modeled by a single particle Green's function, the imaginary part is directly probed by the resulting photoemission current. This imaginary part is referred to as the single particle *spectral function*, $A(\mathbf{k},\omega)$, such that $-\frac{1}{\pi} Im\{G(\mathbf{k},\omega)\} = A(\mathbf{k},\omega)$. Considering that the occupation of electronic states at T$\neq$0 will be additionally affected by the Fermi distribution function $f(\omega)$ (described in Chapter 1), we can bring all these pieces together and re-write Eq. 2.16 to express the transition probability as a photocurrent

$$I(\mathbf{k},\omega) = I_0(\mathbf{k},\nu,\mathbf{A}) f(\omega) A(\mathbf{k},\omega) \tag{2.42}$$

where $I_0(\mathbf{k}, \nu, \mathbf{A})$ is proportional to $|M_{fi}^{\mathbf{k}}|^2$, ω is measured with respect to E_F, and $\mathbf{k}$ is the in-plane momentum $\mathbf{k}_{||}$ (strictly speaking, the in-plane crystal momentum), meaning that this should be thought of as modeling a 2D single band system.

Before we move on to incorporating interactions in this Green's function model, it is worth a moment to better understand $A(\mathbf{k}, \omega)$. At this point, it is a convenient fact that given a Green's function to describe the electronic states of a system, it's imaginary part relates so intimately to the APRES photocurrent deduced from Fermi's Golden Rule and the framework of the three step model. Still, when we look at the form of the imaginary part of Eq. 2.34, it looks like a type of density of states (with the inclusion of an appropriate phase space of states to integrate over.) Indeed, it is traditional to think of the spectral function as related to a local density of states. Though in this case, the local density of states, $\rho(\mathbf{x},E)$, needs to be understood in momentum space, $\rho(\mathbf{k},E)$. $A(\mathbf{k}, \omega)$ satisfies many useful sum rules such as

$$\int_{-\infty}^{\infty} d\omega A(\mathbf{k}, \omega) = 1 \tag{2.43}$$

$$\int_{-\infty}^{\infty} d\omega f(\omega) A(\mathbf{k}, \omega) = n(\mathbf{k}) \tag{2.44}$$

where $n(\mathbf{k})$ is the momentum distribution function. So, since ARPES is directly probing the occupancy of electrons in states of momentum $\hbar\mathbf{k}$ and energy E, the connection between $A(\mathbf{k}, \omega)$ and ARPES is not surprising. At a deeper level, the connection between the imaginary part of the Green's function and a density of states comes from understanding the Green's function as being like the scattering amplitude, f, in the optical theorem, which in its general form due to Heisenberg is,

$$Im\{f(\mathbf{k}', \mathbf{k})\} = \frac{k}{4\pi} \int f(\mathbf{k}', \mathbf{k}'') f(\mathbf{k}'', \mathbf{k}) d\mathbf{k}'' \tag{2.45}$$

But by now, we have said enough about the origins of Green's functions in ARPES for our purposes.

In the language of Green's functions, one can see the addition of interactions on the electronic states as a small perturbation to the hamiltonian, which previously gave us only $\epsilon_{\mathbf{k}}$ (referred to as the *bare band* dispersion.) The perturbation corresponds to an electronic *principle self-energy* term, Σ, being added to Eq. 2.32.

$$G(\mathbf{k}, \omega) = \frac{1}{\omega - \epsilon_{\mathbf{k}} - \Sigma(\mathbf{k}, \omega)} \tag{2.46}$$

$$\Sigma(\mathbf{k}, \omega) = \Sigma'(\mathbf{k}, \omega) + i\Sigma''(\mathbf{k}, \omega) \tag{2.47}$$

Within the real and imaginary parts of $\Sigma(\mathbf{k}, \omega)$, all the information of lifetime and energy renormalization for an electron in the presence of additional interactions (e.g. electron-electron, electron-phonon.) It is also worth noting that causality requires that $Re\Sigma(\mathbf{k}, \omega)$ and $Im\Sigma(\mathbf{k}, \omega)$ are connected to each other by the Kramers-Kronig relation.

In general, $\Sigma(\mathbf{k},\omega)$ is very difficult to calculate making the resulting $A(\mathbf{k},\omega)$

$$A(\mathbf{k},\omega) = -\frac{1}{\pi} ImG(\mathbf{k},\omega) \tag{2.48}$$

$$= -\frac{1}{\pi} \frac{\Sigma''(\mathbf{k},\omega)}{\left[\omega - \epsilon_{\mathbf{k}} - \Sigma'(\mathbf{k},\omega)\right]^2 + \left[\Sigma''(\mathbf{k},\omega)\right]^2} \tag{2.49}$$

very challenging as well. Still, from the functional form of Eq. 2.49, we can see that the energy line shapes ARPES will produce are related to a Lorentzian distribution (or Cauchy-Lorentz distribution) where the imaginary part of the self-energy, $\Sigma''(\mathbf{k},\omega)$, correspond to the linewidth (and thus the lifetime of the state), where the real part, $\Sigma'(\mathbf{k},\omega)$, is a shift in the energy of the peak. We will return to this when we develop the formalism of analyzing ARPES data in the next section.

Fermi-liquid theory provides us with one such model for self-energy due to electron-electron interactions. The creation of quasiparticles as described in Section 1.3, leads to states of finite lifetimes, $\tau_{\mathbf{k}} = 1/\Gamma_{\mathbf{k}}$, and electrons dressed by interactions leads to an effective mass, m*. Using the framework described in Eqs. 2.47 and 2.49, we can introduce a Fermi liquid self-energy term

$$\Sigma_{FL}(\omega) = \alpha\omega + i\beta\left[\omega^2 + (\pi k_B T)^2\right] \tag{2.50}$$

We can quickly see that the imaginary part looks functionally like what we had already written for the inverse lifetime, $1/\tau$, in Eq. 1.10. Making the comparison of the Σ'' to the linewidth shows us that as we approach E_F ($\omega \to 0$) the peaks should become sharper in our ARPES data, corresponding to quasiparticle states of longer and longer lifetime. It is in the real part, Σ', where the effective mass, m*, enters into our analysis shifting the peak and making the total dispersion smaller. In fact, the Fermi liquid self-energy also introduces another additional effect which is somewhat general to electronic states dressed by self-energy interactions. One finds in the spectra, the existence of two kinds of peaks. The first is a sharp peak whose dispersion, particularly near E_F, we can follow and relate to the peak expected in a non-interacting Fermi gas. This is known as the *coherent peak* and, as explored in the following section, is the peak associated with EDC analysis near E_F But there is a second peak feature which appears at higher binding energies for such spectra. This is a broader feature and is related to the quasiparticle dressing. This feature is referred to as the *incoherent peak*. The significance of these peaks is important for EDC analysis as will be described in the following section. Still, where the issue becomes particularly interesting is the appearance of the *peak-dip-hump* feature in the cuprates described in Section 5.1, where Fig 5.2 provides an example. Though the identity of this feature is mysterious, one naturally wonders if it is evidence of additional self-energy effects leading to a similar line shape as expected in Fermi liquids where interactions are significant. So, as we begin analyzing our data, even from systems that are not strictly Fermi liquids, these concepts relating lineshapes to self-energy remain important. In fact, it is believed that the real self-energy for the cuprate

superconductors is not given by a Fermi liquid self-energy but rather by a different self-energy from a model referred to as marginal Fermi liquid theory.

$$\Sigma_{MFL}(\omega) = \lambda \left[\omega \ln \frac{x}{\omega_c} - i\frac{\pi}{2}x \right] \tag{2.51}$$

where x corresponds to $max(|\omega|, T)$, λ is a coupling constant, and ω_c is an ultraviolet cut-off energy. Thus, the real advantage of the self-energy model within the Green's function presents itself. By simply changing the self-energy, we can quickly derive a new $A(\mathbf{k}, \omega)$ to compare with experiments. So, we now turn our attention to the details of ARPES data analysis, keeping in mind what we have learned about self-energy and the spectral function.

2.4 Data Analysis Techniques

Let's return to the equation for ARPES photocurrent intensity, $I(\mathbf{k}, \omega)$, as described in Eq. 2.42 focusing on the three essential contributions

$$I(\mathbf{k}, \omega) = M(\mathbf{k}, \omega) f(\omega) A(\mathbf{k}, \omega) \tag{2.52}$$

As mentioned in Section 2.2, we cannot interpret the ARPES data as strictly equal to information on density of states since the current is modified by the Fermi-function, $f(\omega)$, and the matrix element, $M(\mathbf{k}, \omega)$, associated with the transition from the initial to final electronic state within the solid. This matrix element as described by the Hamiltonian from Eq. 2.7 is affected by such things as incident photon energy and polarization as well as the Brillouin zone of the photoemitted electrons. So, even though the first Brillouin zone, as described in Chapter 1, contains all the information of the electronic band structure, one finds, in practice, that moving to higher Brillouin zones can reveal band structure otherwise suppressed due to these matrix elements. As one may have been inferred so far, because of the temperature scales used for our data, we will not distinguish between the chemical potential (μ) and the Fermi energy, E_F, which (as mentioned in Chapter 1) should match at $T = 0$ for conductors. Since ARPES measures the electron removal part of $A(\mathbf{k}, \omega)$, we use high and low energy to refer to large and small negative ω value, respectively. (Additionally, "Binding energy" and "Energy" are often used for the same axis in figures, differing by a minus sign.) As a final point, one might find the contribution of the matrix element $M(\mathbf{k}, \omega)$ a serious issue to an accurate interpretation of $A(\mathbf{k}, \omega)$ from $I(\mathbf{k}, \omega)$. In practice, the ω dependence is small over an energy range of order 0.1 eV. As for $\mathbf{k}$ dependence of $M(\mathbf{k}, \omega)$, it is very important to consider and in many cases (such as for the cuprates) it is reasonably understood due to theoretical arguments or the substantial work in the literature to compare with.

As described in Section 2.1, the development of hemispherical analyzers allows the unit information of an ARPES experiment to be a two dimensional intensity map of binding

energy and momentum along a "cut" though momentum space. These two dimensional maps suggest two natural and complementary methods for analysis. First, one can fix the momentum space position and observe the photoemission intensity as a function of energy at that momentum value, resulting in an *energy distribution curve* (EDC). This was a more traditional approach to ARPES prior to the advancements in detectors. But on the other hand, one can hold the energy value of the electronic states being studied fixed and observe the photoemission intensity as a function of momentum, resulting in a *momentum distribution curve* (MDC). These two methods constitute the core techniques for the analysis of the spectral function $A(\mathbf{k}, \omega)$ using ARPES.

Thus, "MDC analysis" refers to the method of fitting Lorentzian distributions (or similar curves such as a Voigt distribution) to features in the MDCs as is commonly done in the field. This method of analysis has been very productive for the field and can be understood based on some essential conditions, in particular the condition of "local" linearity for both $\epsilon(\mathbf{k})$ as well as the proper self-energy, $\Sigma(\mathbf{k}, \omega)$. Specifically, both $\Sigma(\mathbf{k}, \omega)$ and $\epsilon(\mathbf{k})$ need to be linear within the narrow energy and momentum range that corresponds to the width of the peak being analyzed. By doing this, each MDC at a given energy ω can be described by a Lorentzian function. This condition is expected to hold in general because one can expand $\Sigma(\mathbf{k}, \omega)$ and $\epsilon(\mathbf{k})$ using simple Taylor expansions in the following way:

$$\Sigma(\mathbf{k}, \omega) \approx \Sigma(k_p(\omega), \omega) + \Sigma_k(k_p(\omega), \omega)(k - k_p(\omega)) \tag{2.53}$$

$$\epsilon(\mathbf{k}) \approx \epsilon(k_p(\omega)) + v(k_p(\omega))(k - k_p(\omega)) \tag{2.54}$$

where k_p is the peak position of the MDC at ω and $\Sigma_k(k_p(\omega), \omega) = [\partial\Sigma/\partial k]_{k=k_p(\omega)}$. Taking these expressions and plugging them into the spectral function as written in Eq. 2.49, we obtain the following equations:

$$A(\mathbf{k}, \omega) = -\frac{1}{\pi} \frac{\Gamma(\omega)}{(k - k_p(\omega))^2 + \Gamma(\omega)^2} \tag{2.55}$$

$$\mathrm{Re}\Sigma(k_p(\omega), \omega) = \omega - \epsilon(k_p(\omega)) \tag{2.56}$$

$$\mathrm{Im}\Sigma(k_p(\omega), \omega) = \Gamma(\omega)[v(k_p(\omega)) + \Sigma_k(k_p(\omega), \omega)] \tag{2.57}$$

One may note that we don't need to assume the momentum independence of $\Sigma(\mathbf{k}, \omega)$ for these results to be valid. As it turns out for the cuprates, this is actually important since momentum dependence does exist for states away from the nodal (Δ=0) cut (which the diagonal direction to the Cu-O bonds.) It is the last two equations which provide us with a precise meaning for $k_p(\omega)$ and $\Gamma(\omega)$ as determined in MDC analysis and, thus, our determination of $\Sigma(\mathbf{k}, \omega)$ from ARPES. Eq. 2.56 demonstrates that a reasonable assumption for $\epsilon(\mathbf{k})$ is needed to determine $\mathrm{Re}\Sigma(k_p(\omega), \omega)$ while $\mathrm{Im}\Sigma(k_p(\omega), \omega)$ presents the additional challenge of requiring the derivative $\Sigma_k(k_p(\omega), \omega)$. This is further complicated since though $\Sigma(\mathbf{k}, \omega)$ is a causal function for a *fixed* $\mathbf{k}$ value, $\Sigma(k_p(\omega), \omega)$ is not. Thus, one cannot invoke the Kramers-Kronig relation to relate real and imaginary parts. Nevertheless, so long as these considerations are kept in mind to prevent over-interpretation, qualitatively $\Gamma(\omega)$ and

$k_p(\omega)$ do offer access to the causal $\Sigma(\mathbf{k},\omega)$ since important structures such as the bosonic renormalization (the ARPES "kink") of the near E_F band structure (Section 1.4) appear in both self-energies.

As mentioned earlier, prior to the instrumental advances which pushed ARPES experimental data from a one dimensional spectra towards a two dimensional map, EDC analysis was the more natural method. There remain many advantages within this line of analysis: 1) The fixed momentum helps simplify the matrix element contribution to the photocurrent ($|M_{fi}^{\mathbf{k}}|^2$ within $I(\mathbf{k},\omega)$ in Eq. 2.42.) 2) Even in a correlated electronic system, momentum is a good quantum number within a single crystal approximation (Fermi liquid theory quasiparticle states have well defined $\mathbf{k}$ but ill-defined energy.) This makes the EDC a more physical quantity, opening up the potential use of spectral weight sum rules (e.g. Eqs. 2.43 and 2.44) as well as providing a clear physical meaning to the dispersion of EDC peaks. 3) In theory, an EDC analysis should be able to provide the causal $\Sigma(\mathbf{k},\omega)$ throughout in the entire two dimensional plane rather than only the particular path determined by MDC peak positions, k_p, as is the case with an MDC analysis. Unfortunately, EDC analysis is uniquely complicated because of contributions from the Fermi function cutoff, $f(\omega)$, as well as both elastic and inelastic photoelectron contributions to the background. This makes for a very challenging lineshape to analyze in practice (see Section 6.2 for our attempt at this.) Still, employing a similar Taylor expansion analysis as we previously used, one can expand the self-energy locally near an EDC peak giving

$$\Sigma(\mathbf{k},\omega) \approx \Sigma(\mathbf{k},\omega_p(\mathbf{k})) + \Sigma_\omega(\mathbf{k},\omega_p(\mathbf{k}))(\omega - \omega_p(\mathbf{k})) \tag{2.58}$$

where $\Sigma_\omega(\mathbf{k},\omega)$ represents the ω-partial derivative of $\Sigma(\mathbf{k},\omega)$. Just like before, we can insert these expressions into Eq. 2.49 and get the following relations in the neighborhood of the peak,

$$\begin{aligned}
A(\mathbf{k},\omega) &= \frac{Z(\mathbf{k})}{\pi}\frac{\Gamma(\mathbf{k},\omega)}{(\omega-\omega_p(\mathbf{k}))^2+\Gamma(\mathbf{k},\omega)^2} && (2.59)\\
\mathrm{Re}\Sigma(\mathbf{k},\omega_p(\mathbf{k})) &= \omega_p(\mathbf{k}) - \epsilon(\mathbf{k}) && (2.60)\\
\mathrm{Im}\Sigma(\mathbf{k},\omega_p(\mathbf{k})) &= \Gamma(\mathbf{k},\omega)/Z(\mathbf{k}) - \\
&\quad \mathrm{Im}\Sigma_\omega(\mathbf{k},\omega_p(\mathbf{k}))(\omega-\omega_p(\mathbf{k})) && (2.61)\\
Z(\mathbf{k}) &= 1/(1-\mathrm{Re}\Sigma_\omega(\mathbf{k},\omega_p(\mathbf{k}))) && (2.62)
\end{aligned}$$

As we turn our attention to MDC analysis, our results begin to reveal the complementary nature of these two approaches. Unlike the Lorentzian lineshape of the MDCs (or more precisely Voigt lineshapes), the EDC lineshape is modified by the asymmetry of the Fermi function and background contributions, which makes EDC analysis particularly challenging (and generally less favorable) for extracting the self-energy near E_F. Thus, in this respect, the MDC analysis provides us with the appropriate tool to study the near-E_F spectral function. However, the spectra at large ω is better analyzed with EDCs due a spectral sum-rule which requires $A(\mathbf{k},\omega) \to 1/\omega$ at large ω, leading us to consequently expect that $Z(\mathbf{k}) \to 1$ and $\Sigma_\omega(\mathbf{k},\omega) \to 0$. This means that the portion of the spectral function which we associate

with the aforementioned incoherent excitations (see the end of Section 2.3) should begin approaching a Lorentzian lineshape. This would make the higher binding energy states better explored with EDC analysis, although one cannot neglect the inelastic background contributions which remain important even at these higher energies. Contrasting this, one finds the MDC's at higher energies begin to be affected by the momentum dependence of the matrix element contributions as well as potential deviations of $\epsilon(\mathbf{k})$ from the aforementioned locally linear behavior. Thus, with both approaches in our ARPES toolbox, we can undertake a more complete understanding of self-energy effects as they appear in $A(\mathbf{k}, \omega)$.

In practice, MDC analysis is more often used for mapping out the electronic bands, particularly highly dispersive bands. Additionally, the ability to determine the Fermi surface ($A(\mathbf{k}, \omega)$ at $\omega = \mathrm{E}_F$) is necessarily done through MDC analysis. Section 4.2, will rely on this type of analysis in order to make comparisons to the band structure predicted previously by theory. As discussed in Section 2.2, we are able to vary incident photon energy and as such move though the momentum space in the k_z direction. But to determine the evolution of the Fermi surface with k_z can be very challenging. This is due to the practical concerns of collecting sufficient ARPES slices to get a single Fermi surface and then to repeat this entire endeavor at multiple photon energies (not even considering the effect of the ARPES matrix element with its photon energy dependence.) The practical solution is to sit at and along high symmetry directions of the band structure, and then proceed to do a photon dependence survey. After converting the resulting cuts into momentum space (since each photon energy will have a different conversion), one can begin to make extrapolations about the band structure dependence on k_z and compare it with theory. The difficulty in working with k_z is one of the primary reasons there is a preference towards quasi-2D or layered materials in ARPES studies (the other being the ability to perform in situ sample cleaving for surface quality). When this is not the case, greater care must be taken, involving initially using ARPES (in conjunction with band structure calculations) to determine the k_z dependence with respect to photon energy (specifically determining the inner potential as described in Section 2.2) and then using this information to make sure that one's experimental setup is probing the specific region of k-space.

In addition, MDC analysis is also critical for determining quanities like v_F and, consequently, m* near E_F where such an analysis can have direct connections to bulk properies like electrical transport[23]. Furthermore, the Fermi surface provides us with information about the doping of the system. Luttinger's theorem tells us that the total volume enclosed by a material's Fermi surface is directly proportional to the particle density. This is intuitive for a free electron gas because of the Pauli principle, but the result is generally true even in the presence of electronic interactions. Thus, by examining the Fermi surface in the first Brillouin zone, and adding together the volumes of the hole and electron bands as representative of the total number of the respective carriers, one can deduce the total carrier density. For materials with significant k_z dependence, this is challenging to determine since these electron and hole pockets will vary in size as a function of k_z. But in materials with little k_z dependence, the 2D volumes should have the same relative ratios for electron and hole bands for all k_z. In such a situation, determining the relative areas associated with hole and electron

bands at the Fermi surface can be added together and should reflect the actual doping of the system. For some systems, like the cuprates, this can be a highly accurate method for determining the doping of a material being studied and can be used to compare with the expected stochiometry from the sample growth process. Thus, through these methods of analysis, the comparison between ARPES and other more bulk sensitive techniques can help establish that despite the surface sensitivity of ARPES, the measurements still represent physical properties of the bulk.

Returning to EDC analysis, a critical strength of ARPES is the ability to determine the momentum dependence of band gaps whether intrinsic like a semiconductor or the result of an additional order such as charge density waves or superconductivity. But despite being a fundamental question, the quantification of the gap measured by ARPES can be a tricky issue. First, determination of the Fermi energy must be calibrated independently. This is done by using a reference metal (e.g. evaporated or freshly scraped gold) in electrical contact with the sample so that the chemical potentials ($\sim$E$_F$) are equal. Fitting this spectrum to a Fermi function (at least near the edge) allows us to extract the kinetic energy associated with E$_F$ which we can determine within $\pm$0.5meV or better. This quantity, however, is dependent on photon energy and the energy settings (pass energy) of the spectrometer.

With independent knowledge of E$_F$, there are three basic components to determining the gap from EDCs:

1) What feature should one use to quantify the gap? Initially, one would be inclined to propose the quasiparticle peak and its binding energy as the Δ associated with the gap. There are two issues which emerge with this. First, with the Fermi function multiplying the spectral function (as well as inelastic scattering background) the peak is effectively shifted to higher binding energy (away from E$_F$) in cases where the gap is small. The result is such that even where the gap should be zero, the peak will not be at E$_F$. This issue can be addressed and we'll return to it. Second, even if that issue could be addressed, there are some materials where no sharp peak in the EDC can be resolved near E$_F$ (e.g. $LaTe_2$ in Chapter 4.) This leaves us with using the binding energy of midpoint of the leading edge to quantify the gap (midpoint corresponding to the point halfway between the above E$_F$ zero baseline and the maximum). This point does reach E$_F$ when the gap is zero and will be employed in our analysis in Section 4.3. The challenge, however, is that comparing this gap with theoretical gap values (e.g. the BCS gap equation) is difficult. Sometimes this leading edge is considered to be $\sim \frac{1}{2}$ of the peak value but this is strictly not true. The sharpness of the peak or other lineshape consideration can also affect this comparison. But despite this, it remains a common approach to quantifying the gap. Of course, one could fit the data to a model EDC incorporates the spectral function from Eqs. 2.49 or 2.59 with the appropriate self-energy. However, this can be difficult in practice, particularly with weaker spectra, and getting a confident convergence can be, at times, elusive.

2) Determining which EDC to use. Initially, this might seem a strange question since the natural choice would be to take the EDC at k$_F$ (though, of course, there is no k$_F$ for a band with a gap.) Still, by employing an MDC analysis, one can determine the band structure dispersion near E$_F$ and linearly extrapolate it to E$_F$. Additionally, one can take a stack of

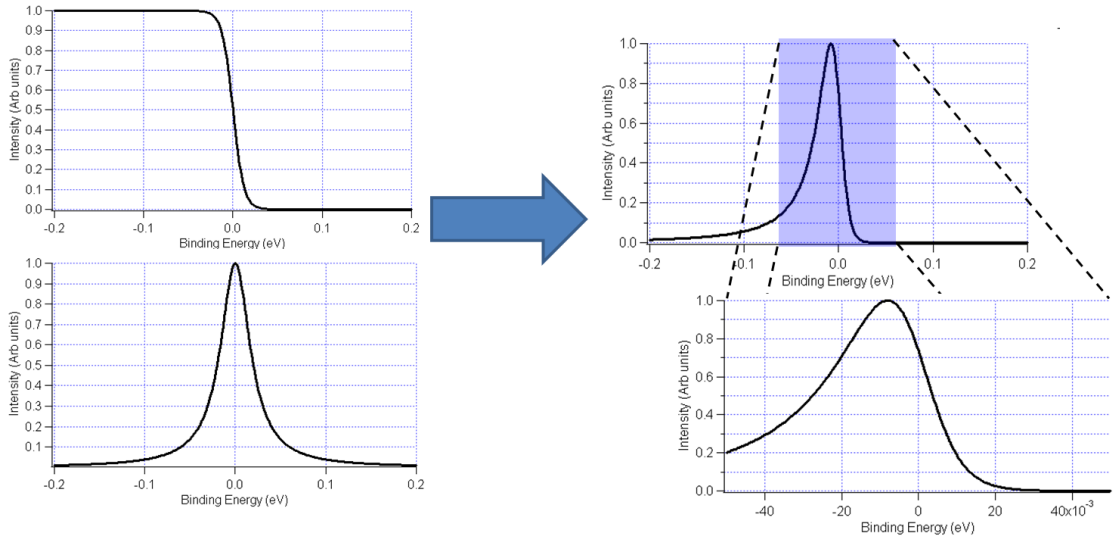

Figure 2.4. Modeling of resolution effect on the leading edge gap. (a) A Fermi function with T = 70K. (b) A spectral function of Γ = 20meV and no gap done using the model from Ref.[24]. (c) multiplying these functions together to produce the ARPES photocurrent as described by Eq. 2.42. (d) Zoomed in region of the EDC spectra near E_F.

EDCs and look for the spectra where the gap is minimized (this should consequently be the EDC at k_F). The problem, in practice, is that this underestimates the gap (in particular, if one uses the leading edge) when the band gap is smaller than the peak width. This is presented in Fig. 2.4 for the example of a zero-gapped spectral function multiplied by a finite width Fermi function. If the Fermi function width is sufficiently wide, spectral weight spills over E_F, and the resulting lineshape can lead to unphysical gap measurements such as finding a leading edge gap *above* E_F in ungapped metallic bands (as seen in panel d.)

To remedy this, ARPES analysis will often be integrated over a larger window of momentum space (otherwise empty of electronic bands) to get a better estimate of the leading edge gap as discussed elsewhere[25]. Effectively, there is no physical reason for this integration other than to provide a systematic method for removing resolution/temperature/peak width effects. As we integrate more and more EDCs, the leading edge gap becomes larger until it reaches a maximum value before it very slowly begins to shrink as the window becomes increasingly larger. This subsequent narrowing is due to the integration of more and more EDCs without spectral weight, whose lineshapes have a leading edge at E_F. Thus, in the limit of large angular integration, the leading edge gap will approach zero. We associate the maximum gap to be the best measure of the true leading edge gap (so long as the same integration window is associated with a zero gap for appropriate momentum space cuts like the nodal point.) Naturally, angle integrating will destroy information regarding the peak gap and should not be used for such gap analysis. Additionally, the need for this analysis

occurs with small gaps, where the energy width of the Fermi function is comparable to the gap. So for larger gaps, this analysis is not necessary.

3) In light of the issues that the Fermi function and other resolution effects bring to the spectra, it is worth asking if there is any analysis methods by which one could remove these contributions to get at a purer spectral function. We will discuss three techniques that are seen in the literature. The first technique is E_F symmetrization[26], which takes advantage of electron-hole symmetry to remove the Fermi function. Mathematically

$$A(\omega)f(\omega) + A(-\omega)f(-\omega) = A(\omega)\left[f(\omega) + f(-\omega)\right] = A(\omega) \tag{2.63}$$

assuming the spectral function $A(\omega) = A(-\omega)$, meaning that there is electron-hole symmetry for the spectral function at that value of $\mathbf{k}$. Thus, the resulting spectra should be free of the Fermi function contribution. With this spectrum, one can employ any of the previously mentioned techniques for quantifying the gap. There are some limitations with this technique. Most obvious, determining the precise value for E_F is essential otherwise a small gap can disappear or a finite gap can appear where it is not physical. Additionally, the resulting lineshape can still present challenges since resolution effects can make identifying the dip at E_F difficult. Finally, one cannot read too much into the spectral shape above E_F since it is, strictly speaking, just a copy of the below E_F spectral function (per our assumption). If we want to have information about the above E_F states, or if electron-hole symmetry is not appropriate, we must turn our attention to other techniques.

The second technique of Fermi function division is similar and also commonly used. This takes advantage of the functional form of the photocurrent described in Eq. 2.42. Given an appropriate Fermi function incorporating the temperature as well the energy resolution, ΔE, of the experiment, one divides the raw photocurrent by this function (strictly speaking, a Gaussian of width ΔE convoluted with the Fermi function.) Despite its complexities (getting the right Fermi function), it has advantages over the symmetrization in that data seen above E_F is real and not merely a product of our symmetric assumption. In practice, however, very little can often been seen above E_F unless the temperature of the experiment is sufficiently high that a significant population of states are occupied (ARPES can never see what isn't occupied.) Even if they are occupied, the sharp increase in the spectra can make analysis challenging (above E_F, $f(\omega, T) \to 0$ so dividing by $f(\omega, T)$ goes to infinity.) Still, this technique, particularly at higher temperatures, can reveal part of the spectral function above E_F allowing one to better quantify the gap and even learn about the dispersion of the above E_F band (e.g. the Bolgoliubov quasiparticle line shape in the cuprates.)

The third technique is relatively new and addresses an issue that we have not given much time. The goal of these techniques has been motivated by a desire to get the best possible spectra which are otherwise marred by the Fermi function. But the situation is further complicated by resolution effects whose effect on the spectra is not merely a multiplication but rather a convolution with the spectra. Thus, if we seek the purest picture of the spectral function, we need to do a deconvolution as well. A common technique from astronomy to deconvolve error from an image to get a sharper (and hopefully more pristine) image is

the *Lucy-Richardson deconvolution* procedure. This iterative procedure has been recently applied to ARPES data on the cuprates[27][28] in order to better observe the evolution of the Fermi surface band structure topology and attempt to resolve an ongoing discrepancy between ARPES and quantum oscillation measurements[28]. The technique is quite challenging, although its effect on the data is significant. This has led to some informal debate over whether its sharpening of the data is artificial or resulting in a truly more realistic spectrum when completed. Since few groups currently use the technique, it is mathematically sophisticated, and we have never used it in any of our analysis of the data in this thesis, we will only acknowledge its existence and point the interested reader to appropriate discussions of it elsewhere[27].

We now have presented a general (albeit brief) introduction to the history, experimental setup, physical interpretation, and analysis methods that are a part of the ARPES experimental technique. For the initial simplicity of Einstein's photoelectric effect, we find that the practical implementation of the technique is far from simple particularly as we push the limits of energy and angular resolution to extract more and more subtle effects. The ARPES practitioner, indeed like any experimentalist, must be constantly asking about the origins of the effects observed keeping in mind the approximations, surface sensitivity, lineshape complications, experimental failings, and other issues which are ever near. Thus, one cannot let the relative ease in which electronic band structure can suddenly appears on a ARPES screen fool one into overzealous analysis, but nor can the complexities sap the resolve to push on with the technique. And so, motivated by that faith, we proceed to our data focusing on three systems where competing orders play important roles within their phase diagrams: the iron pnictides, the rare earth tellurides, and the single layer cuprates.

Chapter 3

Core Level and Valence Band Study of $LaFeAsO_{0.9}F_{0.1}$

3.1 Introduction

As briefly introduced in Section 1.6, the superconducting iron pnictides represent a surprising turn in the story of unconventional superconductivity. The story began with the initial discovery of superconductivity in the fluorine doped $LaFePO_{1-x}F_x$ and $LaFeAsO_{1-x}F_x$ [29]. It is this second compound that truly shook the correlated electronic community with a maximum T_c of around 27K. Fig. 3.1 shows the crystal structure and a theoretical density of states for the parent LaFeAsO compound. Of particular importance, is the critical role the iron states play in the near-E_F electronic structure[30]. It is these iron arsenic planes which appear to be the key to the surprisingly high superconductutivity evidenced by the plethora of compounds: 1) The Lanthanide oxypnictides ($LnO_{1-x}F_xFeAs$ Ln = Sm, Nd, Gd, Pr) were the first to be observed and studied. Known as the 1111 compounds, they currently exhibit the highest superconducting transition temperatures exceeding 50K[31 32 33 34], though growing large single crystals is very challenging. 2) The 122 iron pnictides (e.g. $(Ba,K)Fe_2As_2$, $(Sr,K)Fe_2As_2$, $(Ca,Na)Fe_2As_2$, $Ba(Co,Fe)_2As_2$) came more recently and due to the ability to grow large crystals, have been the subject of much later ARPES work. Their T_c values have remained generally <40K to date[35]. 3) The 111 iron pnictides (e.g. LiFeAs T_c=18K) have recently been gaining attention[36] and are particularly intriguing since it is superconducting without the introduction of any doping. 4) The 11 iron pnictides (e.g. Fe(Te,Se)) have similarly lower T_c values like $Fe_{1.03}Te_{0.7}Se_{0.3}$ with a T_c=13K.

To illustrate the phase diagram of these compounds, panel c of Fig. 3.1 provides a phase

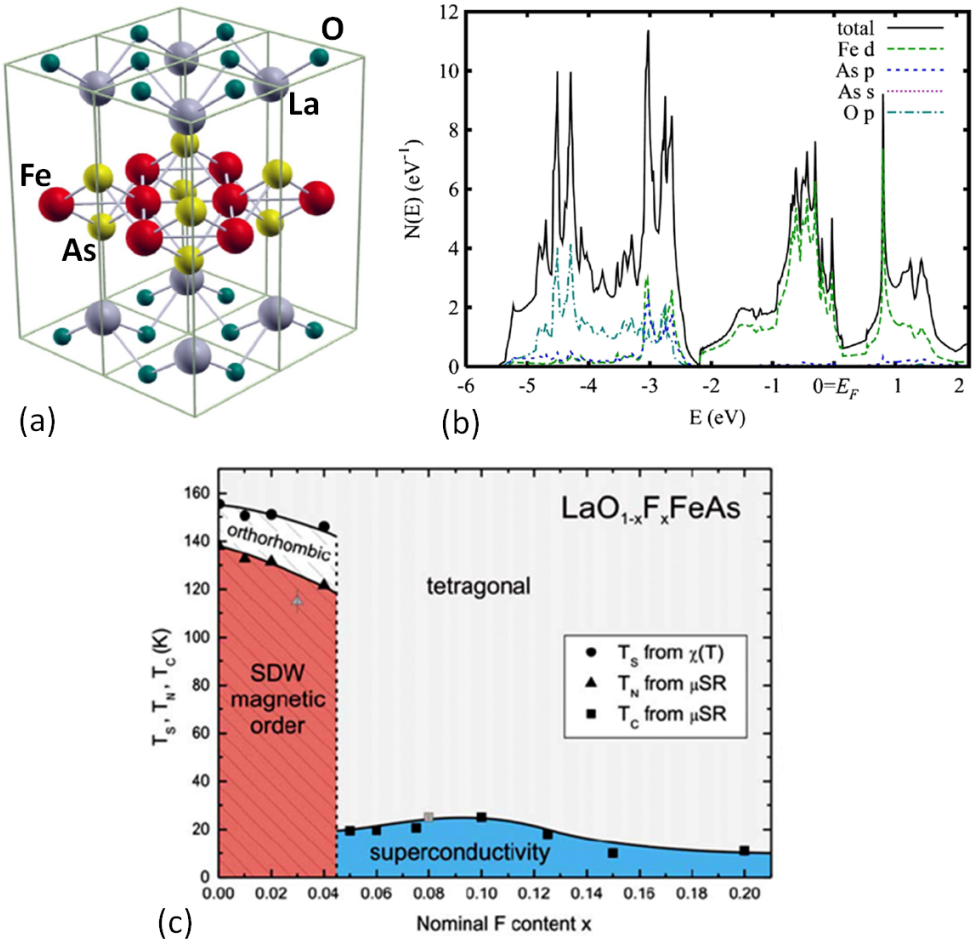

Figure 3.1. (a) The crystal structure of the oxypnictide parent compound LaOFeAs as reproduced from Ref. (b) Valence band density of states for LaOFeAs from Ref.[37]. (c) Phase diagram of the Fluorine doped oxypnictide $LaFeAsO_{1-x}F_x$ as determined by magnetic susceptibility and spin-resolved muon experiments[38].

diagram of $LaFeAsO_{1-x}F_x$ determined by magnetic susceptibility and spin-resolved muon experiments[38], which gives us a picture of the surprising magnetic physics at work in these systems. When we compare it to the general hole doped cuprate phase diagram (Fig. 1.3, the similarities and differences become quickly apparent. The parent compound for both the iron pnictides as well as the cuprates is dominated by magnetic physics. Both host magnetic ordering, but the cuprates antiferromagnetic Mott insulating phase is met by a metallic antiferromagnetic density wave in the pnictides. But the presence of two orders, an antiferromagnetic order in close proximity to superconductivity, is remarkable and once again illustrates the importance of understanding competing orders to such novel systems. As mentioned back in Section 1.6, they seem to have a more isotropic critical field, making these materials less quasi 2D then the highly isotropic cuprates, and consequently more attractive for devices. Also as mentioned earlier, one reason for the potential uniqueness of these compounds is that bands related to iron appear to dominate the near E_F band structure and are hence responsible for superconductivity. This situation, together with the proposed strong hybridization between the Fe 3d and As 4p orbitals needed to explain the anomalously small value of the Fe magnetic moment[39], begins to place the Fe-based superconductors in a strong correlation regime as is already the case for the cuprate superconductors. It is this magnetic ordering that places this work into the broader narrative of this thesis as we attempt to study the way in which magnetic ordering could manifest itself in photoemission data.

As we explore our contribution to the early work in this expansive field, we will begin with a closer exploration of the issues that motivated our photoemission work on the optimally doped $LaFeAsO_{1-x}F_x$ compound. We will then proceed to photoemission work on the core level states, focusing particularly on the As 3d orbitals to give us potential insight into the magnetic physics of the Fe-As plane. We then move towards the Fermi energy and focus on the less defined valence band states (0 - 20eV in binding energy) to provide experimental determination of the electronic density of states by taking advantage of known photon energy dependences of the different elements. Then we zoom in on the electronic states nearest E_F. Employing high resolution Angle Integrated Photoemission Spectroscopy (AIPES), we can make a careful study of the near-E_F electronic density of states, looking for the subtle indicators of superconducting and magnetic physics. We will then conclude with some observations about current issues in the field.

3.2 Overview of $LaFeAsO_{1-x}F_x$

As mentioned, $LaFeAsO_{1-x}F_x$ was among the very first of the novel iron superconductors discovered, and as such was the subject of significant initial study. It was quickly determined that the metallic LaFeAsO parent compound supported both an antiferromagnetic spin density wave (SDW) phenomenon at ∼134K, along with a structural distortion at ∼150K[40,41]. This latter phenomena is believed to be an important parameter for modulating both the Fe 3d - As 4p hybridization (potentially related to the anomalously low magnetic moment)

as well as the onset of antiferromagnetic fluctuations[39]. The presence of these phenomena in the $LaFeAsO_{1-x}F_x$ phase diagram (Fig. 3.1c) and their apparent competition with the superconducting phase further underscore the complex physics of the near E_F properties of these materials[40,42,43].

There were numerous prior angle integrated and angle resolved photoemission results that had appeared in the literature in the initial months after these 1111 materials made their appearance[44,45,46,47,48,49] as well as the first of the ARPES work on the Barium based 122 compounds[50,51]. Yet at the time, basic knowledge of the electronic structure of these materials, the importance of correlation effects, and how the spin physics modulates the near E_F states was still not fully understood (and those questions still remain significant). There was limited data on the orbital nature of the valence band spectra and no measurements of the proposed strong p-d hybridization in the literature. Additionally, significant, there was no understanding of the effect of the magnetic structural distortion[40,41] on the near E_F states. These concerns, along with the controversy over the role of spin fluctuations[40,42,43,30,52,53,54,55,56,57,58] in the explanation of the low energy features of the near E_F density of states, are fundamental issues. Addressing them would be of significant importance before one could come to a complete understanding of the physics of these materials.

So we focused our attention on the optimally doped, polycrystalline $LaFeAsO_{0.9}F_{0.1}$ (T_c=25K), being central to the debate. Because the aforementioned issues are intimately related to electronic states and the near E_F electronic density of states, we naturally used photoemission spectroscopy. In Chapter 2, our primary focus was on the angle resolved photoemission technique. Strictly speaking, Angle Integrated Photoemission Spectroscopy (AIPES) is a simplification of these ideas and of the photocurrent described in Eq. 2.42. The 2D spectra that are most common in ARPES are, within the data analysis, compacted down to a 1D spectral of photocurrent intensity vs. energy. But this, strictly speaking is not AIPES. If the sample is relatively single crystalline, then the 2D image being compacted still corresponds to a specific cut in momentum space, and thus probes the spectral function (and matrix element effects) for momentum values in that particular region. To truly integrate out all the angle (momentum) dependence, one must use a highly polycrystalline sample. In doing so, one can be assured of getting information on the spectral function from throughout momentum space due to the random orientation of the fine grain crystals. (The condition on photon energy and the ability to access electronic states throughout the momentum space described in Section 2.2 still remains, so sufficiently high photon energy remains important.) Thus, given a fine grained, polycrystalline sample with a sufficiently uncontaminated surface, one can take AIPES data. The effective integration over the momentum space, removes the k-dependence to the spectral function as well as the ARPES matrix element (as well as the polarization dependence). However, it does not remove the incident photon energy dependence of the photocurrent, a fact of vital importance to our analysis.

Our samples of polycrystalline $LaFeAsO_{0.9}F_{0.1}$ were synthesized by solid state reactions. La and As metals were mixed and reacted in an evacuated sealed quartz ampoule at 500C for 12 hours, followed by a reaction at 850C for 2 hours. The formation of LaAs was confirmed

by X-ray diffraction techniques. Fe_2O_3, Fe and LaF_3 were then mixed with LaAs and loaded into a tantalum tube. The amount of LaF_3 was calculated to provide 10 percent F. The tube was crimped and sealed in an evacuated quartz ampoule. The reaction was carried out at 1150C for 50 hours. The final product: LaAsFeOF was once again confirmed by X-ray diffraction. We determined the sample to have a critical temperature of 25K as determined by the diamagnetic transition in our zero field magnetization measurements (Meissner effect), shown in the inset of Fig. 3.2[59].

For these experiments, we used synchrotron based photoemission spectroscopy and the data were taken at Beamline 12.0.1 at the Advanced Light Source of the Lawrence Berkeley National Laboratory using a Scienta SES100 hemispherical analyzer and also at Beamline 5.4 at the Stanford Synchrotron Radiation Laboratory, using a Scienta R4000 analyzer. For our experiments, it was important to explore a range of electronic energy states. We can divide our study into core level electronic states (binding energy >20eV), valence band electronic states (binding energy <20eV), and finally the near E_F electronic states (binding energy <0.2eV). The energy resolution was 0.1eV for both the core level and valence band data. A resolution of 25meV was used for the near E_F data presented in in Fig. 3.4, while 5meV resolution was achieved for the data presented in Figs. 3.5 and 3.6. Having a surface devoid of absorbed molecules is critical to our data. Thus, sample surfaces were prepared both by cleaving the grown polycrystalline rod *in situ*, and both by cleaving immediately followed by a gentle scraping *in situ* of the exposed surface using a diamond file. Both were done at a temperature less than 25K and a base pressure better than 5×10^{-11} Torr. From our experiments and the data presented, we found no quantitative differences between these two methods.

3.3 Core level Photoemission

Fig. 3.2 shows core level spectra taken on the sample within in the superconducting phase. Panel a includes our determination of the atomic orbitals associated with these peaks. Within the energy window of Fig. 3.2, we identify the expected La core levels: La 5s at 35.0eV, La $5p_{1/2}$ at 19.0eV and La $5p_{3/2}$ at 17.5eV. Similarly, the only expected oxygen core level in this energy window is the O 2s peak, which is generally expected near 20eV in other oxides[60]. Thus, we identify it with the shoulder to the left of the aforementioned La 5p orbitals. We encounter a greater difficulty when we try to resolve the fluorine core level peaks. We expect that the F 2p binding energy should be only a few eV larger than the O 2p orbital[60]. Theory suggests and we will further argue in Section 3.4 that the spectral weight between 5 and 10 eV is dominated by the O 2p orbital, putting the likely weaker F 2p orbital contribution underneath this spectra. Nevertheless, we interpret the weak, broad feature at 27eV as the F 2s orbital expected at a roughly 20eV higher binding energy than F 2p.

Turning our attention to the orbitals associated with the critical FeAs plane, we can

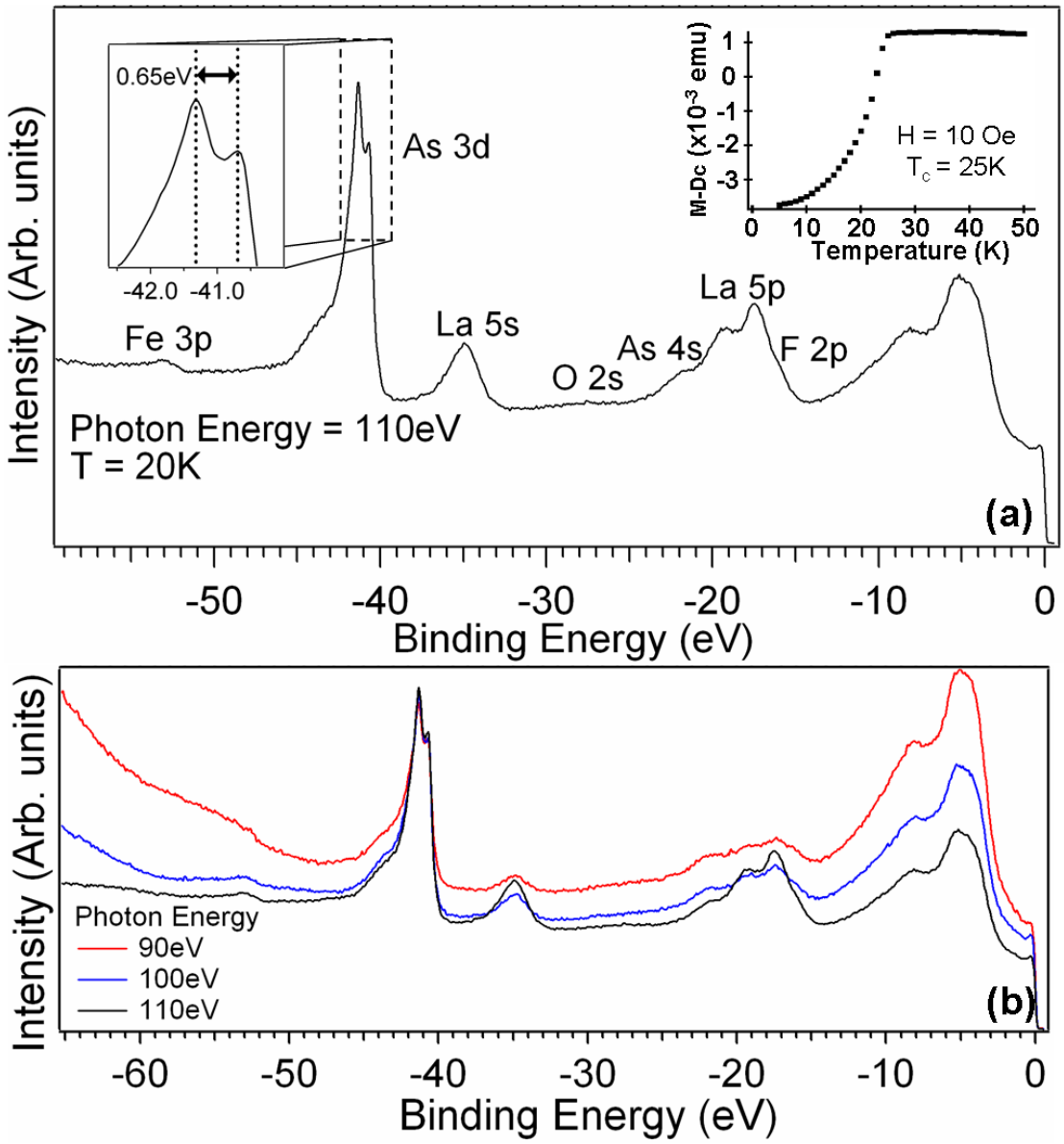

Figure 3.2. (a) Core level spectroscopy of $LaFeAsO_{0.9}F_{0.1}$ taken in the superconducting phase using 110eV photon energy. The upper right inset shows the measured T_c of our sample. (b) Core level spectrum from (a) taken at three different photon energies. The spectra are normalized to photon flux and show differing trends in intensity based on orbital character.

successfully resolve the Fe 3p orbital, although we are unable to resolve any potential splitting between the $3p_{1/2}$ and $3p_{3/2}$, most likely due to the weak intensity. But, to our initial surprise, when we look at the As 3d core level, we observe a splitting between the $3d_{3/2}$ (40.7eV) and $3d_{5/2}$ (41.3eV) peaks of ∼0.65eV. This is significant because it is a much larger splitting than what is observed for As in its natural form[61], and it is ∼.05eV[62] larger than what is observed in the undoped parent compound, LaFeAsO. Within our previously mentioned resolution, we find that the magnitude of this splitting is temperature independent, above and below T_c.

This large splitting suggests that we are in a regime where the hybridization between the Fe 3d and the As 4p orbitals is actually quite strong, as previously proposed by theoretical work[39,63]. We can model this splitting as due to hybridization between Fe $3p_{3/2}$ and the As $3d_{3/2}$ orbitals by using a basic quantum mechanical two level model[64]. Doing so, we can actually put experimental constraints on the magnitude of the Fe/As hybridization energy. The result of this analysis bounds the energy to be between 1.1 and 1.4eV. These values are significant because this range is consistent with the values that were required to explain the anomalously small Fe magnetic moment reported for these materials[39].

Our core level study did resolve two additional features which do not directly correspond to any known orbital core level: 1) a subtle shoulder at ∼16eV near the La 5p peaks and 2) a well-defined shoulder at ∼44eV, to the left of the As 3d peak. One possibility is that these correspond to multi-transition phenomena like an Auger transition. However, these transitions result in spectral peaks at fixed kinetic energies over a range of photon energies leading to binding energies which are photon energy dependent. (This is unlike actual core level peaks or band structure which is fixed in binding energy.) Thus, because their binding energies are photon energy independent, neither of these features can be associated with an Auger peak or any other related fixed kinetic energy phenomena.

When we reflect on this former feature, two possibilities come to mind. The first possibility is to associate it with the currently unresolved As 4s peak, although shifted by ∼4eV from its expected value. The second possibility is to consider it a satellite feature associated with the La 5p orbitals. By employing photon energy dependent studies, as we will explain later on, we are lead to the first conclusion, associating the feature with the weaker As 4s state. Yet, the reason for the apparent energy shift in this peak continues to be unclear.

Turning our attention to the latter feature (the ∼44eV shoulder to the left of the As 3d peak), the absence of any expected additional peak within the energy range leads us to suspect it to be a satellite feature of the As 3d peaks related to the critically important FeAs layer. In particular, it may be related to the Fe 3p-As 3d strong hybridization previously proposed to explain the observed As 3d splitting. This feature appears to be unchanged above and below T_c. Modeling the spectra near the As 3d peaks by fitting with multiple Lorentzian peaks, we estimate the peak in this satellite feature to be around ∼43eV, a separation of more than 1.5eV from the As $3d_{3/2}$ peak. The presence of satellite structures are important in the study of photoemission, providing information about the local environment of the element associated with the core level. The reason is that these satellites arise is from coulombic attraction between a core hole (localized on the elemental site) created by photoemission

and the more complicated valence band states near E_F. This work has been instrumental in the study of other materials of importance to correlated electronic systems: the Cu 2p orbital in high T_c cuprates[65] and the Ru 3d orbital in the ruthenates[66]. One possiblity that has occured is that the considerable As 4p character that theory expects around 1.5eV above E_F[30,63,67,37] could cause a satellite peak to form around 2-3 eV from the As 3d peaks as the As 3d core electrons are being photoemitted, potentially explaining the observed shoulder. But a solid explanation still remains unclear.

As has been alluded to earlier, we have performed a detailed photon energy dependent study of the entire core level region to further confirm our analysis. We discussed in the preceding section that though we are integrating over momentum space (a fact that is irrelevant for core levels which are dispersionless), the photon energy dependence of the photocurrent remains important. In the case of the core levels, photon energy dependent photoemission takes advantage of the fact that the photoemission cross section changes uniquely for different elements at different energies. This is also related to resonances associated with core levels enhancing photocurrent, as described in Section 2.2. Core level spectra at a few characteristic photon energies are shown in panel b of Fig.3.2. We have normalized the data to total photon flux and we can see a clear enhancement of the peaks near 35, 19, and 18 eV. Now, we have already identified these peaks with the La 5s and the 5p orbitals and this is supported as the enhancement occurs when our energy approaches the La 4d core level resonance (at $\sim$105eV). Not only does this support the La nature of these peaks, it gives weight to the prior hypothesis that the additional energy shoulder near 16eV, which is not similarly enhanced (appearing relatively stronger in the 90eV curve), is indeed unrelated to La and is likely of As 4s origin.

3.4 Valence Band Photoemission

With our analysis of the core level peaks taken care of, we can begin to move towards E_F and explore the electronic structure of the valence band states. In particular, we can begin the valuable step of identifying orbital character of the valence band region below 20 eV. Although much theoretical work has proposed that this region is mostly dominated by oxygen and iron contributions[30,67,37,63], there had not been a complete experimental characterization of this region for comparison with theory. As with our core level study, photon energy dependent photoemission can provide direct information on the electronic density of states since, as mentioned, the photoemission cross section changes uniquely for different elements.

In order to better discern the relative oxygen and iron concentrations expected by theory, panel a of Fig. 3.3 focuses on the valence band region between E_F and 25eV in binding energy. For this analysis, the spectra are renormalized to the peak near 5eV as opposed to total photon flux as in Fig 3.2. Doing this allows us to distinguish the 3-15eV valence band region from the sharp feature seen near-E_F at $\sim$0.3eV. We know independently that the photoemission cross-section decreases faster for oxygen than iron over this photon energy

range[68]. Thus, seeing the increase in the 0.3eV feature relative to the remaining valence band region helps confirm its orbital character as iron and, specifically, the Fe 3d orbital. This leaves the remaining valence band to have a majority O 2p character, which is also hinted at by prior density of states calculations[67,37,30]. It is also worth noting that although we clearly observe this Fe 3d peak at nearly 0.3eV when using higher photon energies (50-110eV), the peak does appear to be shifted closer to 0.2eV when we employ a lower photon energy (23eV) as will be evidenced in data presented in Section 3.5. But this is certainly not surprising since the peak we are seeing is quite likely composed of multiple bands which each may be relatively enhanced with different photon energies due to the photoemission matrix element.

Further exploring the orbital character within the valence band, panel b of Fig. 3.3 provides spectra taken with both 100eV and 50eV light. Although the proposed La 5p and Fe 3d peaks only change in relative peak intensity, it is quickly apparent that the remaining valence band is greatly affected, particularly when we focus near 10eV, where new peak features are enhanced. The proximity of the 50eV data to the expected Fe 3p resonance at 53eV (the core level observed in Fig. 3.2) leads us to focus on two points: First, the sudden appearance of a feature near 13eV in the 50eV data suggests that there is iron orbital character within this region of the valence band. When we examine this energy region (10 - 14eV) more closely within panel a, one finds that the spectral intensity actually does increase in a similar way to the increase we see in the 0.3eV feature. We've already attributed this feature to Fe 3d, and so one can speculate that this higher binding energy region of the valence band has a larger Fe 3d contribution to its electronic density of states than the remaining density of states at slightly lower binding energy (4-10eV). At the same time, this would explain the origin of the additional peak structure at $\sim$10eV appearing in the 50eV data when compared to the higher photon energy data.

Secondly, we can also attempt to make sense of the strong $\sim$5eV feature in the density of states. A close examination of the spectra in panel b and of this feature at higher photon energy strongly suggests that at least two peaks are likely responsible for the slightly asymmetric lineshape. The evolution in lineshape between the 100eV and 50eV spectra leads us to suspect that an additional, non-oxygen orbital may be contributing to the overall observed spectral weight. From our analysis of the spectra in Fig. 3.2b, lanthanum seems unlikely given its strong enhancement near 110eV. Furthermore, the bandwidth change between 100eV and 50eV of this feature appears to become narrower, suggesting that the additional spectral weight is weakened (or certainly not enhanced) at 50eV, making a significant Fe 3d contribution (unlike the 10-14eV range from before) unlikely. In light of these observations, we are inclined to propose that although the primary character of this peak certainly appears to be O 2p, this additional spectral weight at lower binding energy must be related to arsenic, and most likely, it is the reviously unaccounted for As 4p orbital whose hybridization with Fe 3d was so significant in our earlier discussion in Sections 3.2 and 3.3. And thus, before we transition to focusing solely on the near-E_F Fe 3d states, panel c of Fig. 3.3 provides a cartoon to qualitatively summarize all of our observations and conclusions from our photon energy studies regarding the orbital character of the valence band density of states.

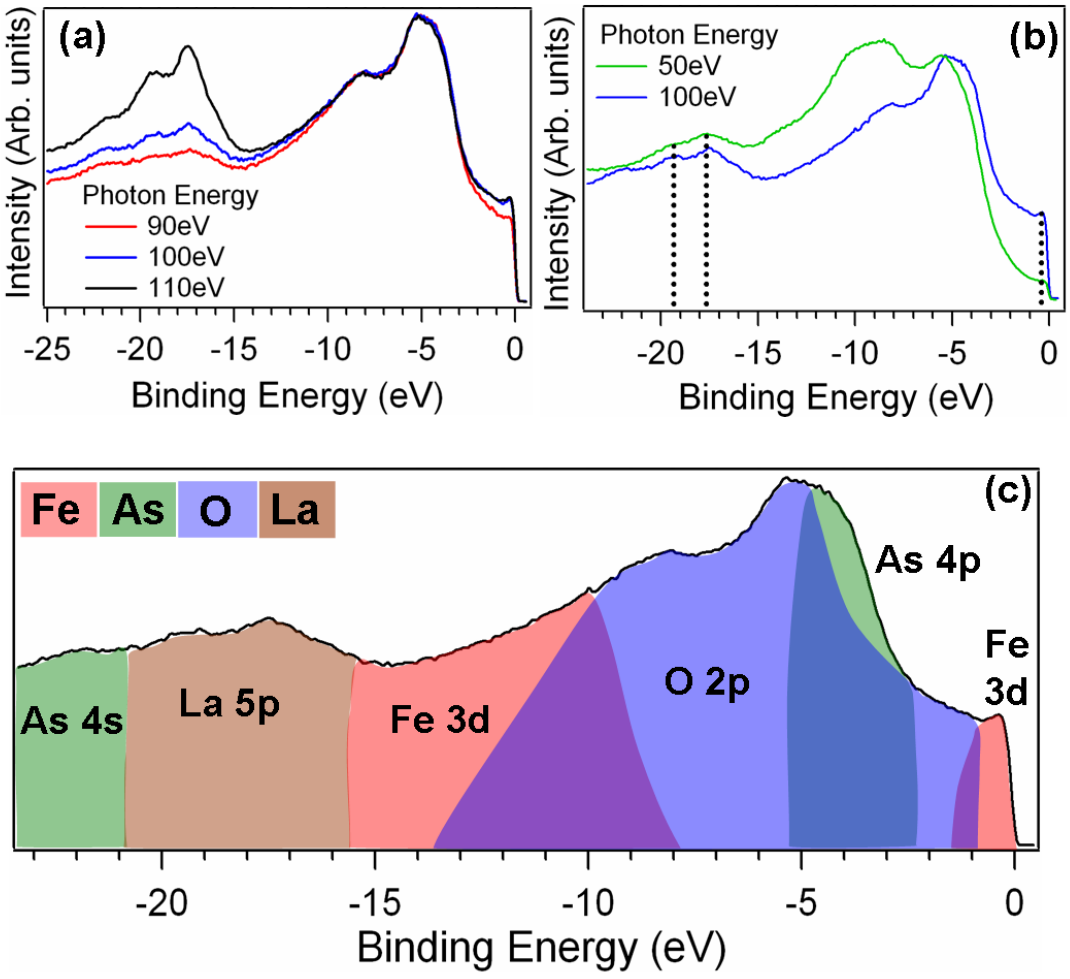

Figure 3.3. (a) The valence band region from Fig. 1b now normalized to the peak near 5eV binding energy. This helps distinguish Fe from O orbitals in the valence band. (b) VB spectra taken with 50eV and 100eV photon energy. The dashed lines mark the locations of the La 5p and Fe 3d peaks. (c) A cartoon summarizing our proposed assignments of orbital character to different regions of the VB DOS based on the data from Fig. 3.2 and 3.3a-b.

3.5 Angle Integrated Photoemission Near E_F

Despite the value of our work in the preceding sections, our greatest interest for these materials is to study the electronic states nearest E_F. It is here that high resolution AIPES may be able to observe unique and subtle effects in the electronic density of states related to the completing orders within the phase diagram. Some AIPES measurements have already been carried out in these materials[44,45,46,48], and by the time of our work, the first ARPES studies focusing on the near E_F region of the related 122 systems (and the sole 1111 work) were becoming available[49,50,51]. But those studies lack a detailed temperature dependence analysis which lead to a controversy on the origins of the different energy scales identified in these systems[45,46,47,48]. So with high resolution AIPES being able to directly measure the density of states, we can focus on the near E_F states to discern gap energy scales and perhaps even "pseudogap" features within the spectra[69].

Fig. 3.4 begins this exploration by showing us the photon energy dependence of the near E_F spectra within the superconducting phase. As was previously reported[45,46], the spectra show a sharp discontinuity near the Fermi level which we find is, in fact, robust over a wide range of photon energies. The challenge of resolving this feature clearly in the photocurrent in spite of the Fermi function, forces us to consider other EDC analysis techniques as described at the end of Section 2.4. Given the lower temperatures of many of our spectra as well as a general ambiguity over the appropriate width, Fermi function division was not a practical technique. Eventually, we decided to use an E_F symmetrization technique in an effort to better visualize the discontinuity and remove the contribution from the Fermi function (Fig. 3.4 inset). Looking at these spectra, it's worth noting that the symmetrization technique could lead one to think there is zero spectral intensity at E_F. But, we know this is not the case since the main Fig. 3.4 clearly shows otherwise. With the symmetrized data, the discontinuity manifests itself as a plateau region, where we estimate the width to be 30meV (as indicated by the blue dotted lines in the inset.) We believe this feature likely represents the previously reported 15meV gap seen by other groups[46,48]. From our photon energy dependent study, we find that this feature is enhanced when 50eV photons are used in our experiments. Of course, this is consistent with the Fe 3d nature of the near E_F bands since, as previously discussed, one expects a resonance at those energies due to the Fe 3p core level at 53eV. Since we are looking at energy gaps, it is also important to note that given the energy resolution of these data described in Section 3.2, we do not expect to cleanly resolve the small superconducting gap ($\Delta \sim$ 4meV at 5K[46]) in our data.

Understanding this 15meV gap and the nearby density of states is certainly crucial to understanding any potential competing orders acting within the system at this doping. And so to provide further light for the debate on the origin of this feature[45,46,47,48], Fig. 3.5 shows the temperature dependence by performing a high resolution study on the near E_F spectra. The critical 15meV feature is indicated by the dotted blue arrow in panel a. Even from this figure, one can see some indications of a gradual temperature dependence in the raw data. We can attempt to enhance this feature by taking the first derivative of the spectra which we plot in panel b. The challenge with taking the first derivative is that data needs

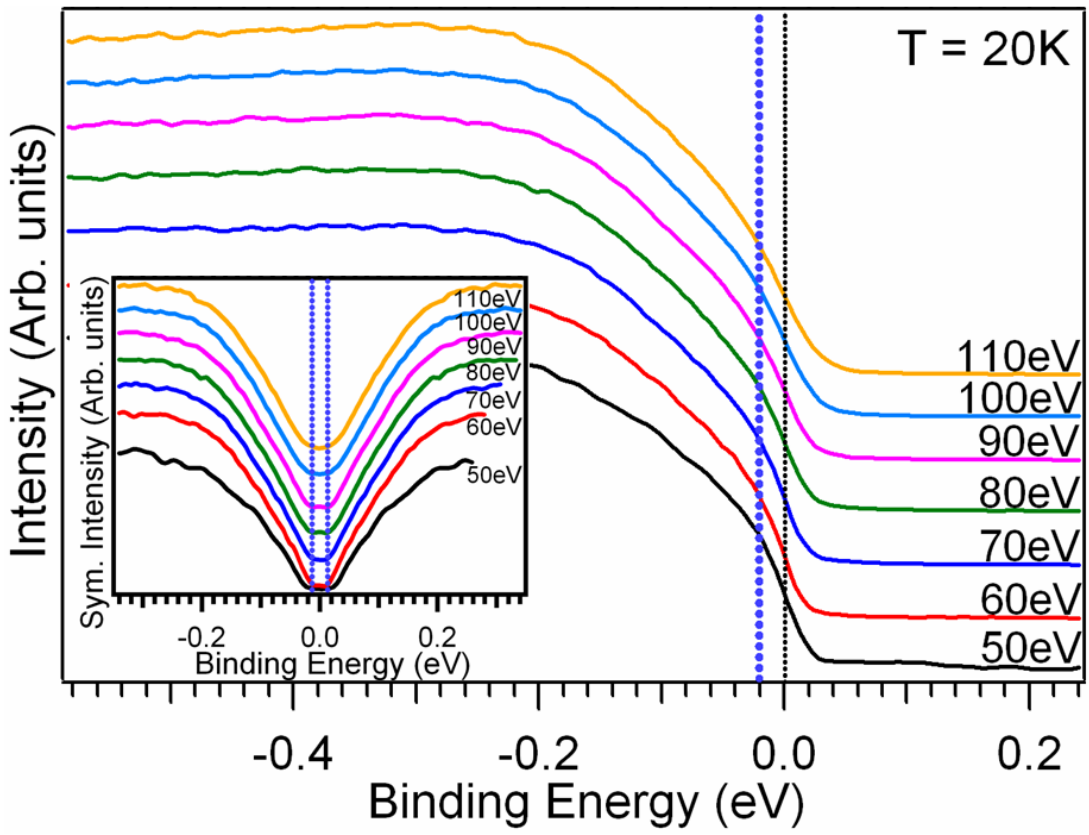

Figure 3.4. Near E_F data taken over a range of photon energies from 50 - 110eV at T=20K. The blue dotted line indicates the energy scale of the spectral feature 15meV below E_F. The inset symmetrizes the data to remove contributions from the Fermi function. The blue dotted lines indicate the 2Δ ~30meV gap feature which we see at all energies.

to be sufficiently smooth otherwise the noise will completely dominate the spectra. Even still, within the first derivative data we can observe a dip in the spectra localized near the blue dashed line at 15meV. Following that dip from bottom to top, we see its disappearance with temperature. But, it is apparent that this is not a preferred method of analysis since the broadening of the Fermi function may be damaging our spectra. At 100K, the width of the Fermi function would be just over 30meV. So to gain more detailed information on the temperature evolution, we symmetrized spectra from Fig. 3.5a to once again remove the thermal broadening contribution arising from the Fermi function. The results of this are seen in panels a and b of Fig. 3.6. We divide the temperature data into the two panels to illustrate that we are led to identify two characteristics temperatures: 1) T$\sim$90K Looking at Fig. 3.6a, the spectra and particularly the gap-like feature in the density of states seems to "close up" as a function of temperature. This is consistent with the evolution in the line shape suggested by the first derivative data (Fig. 3.5b). Upon reaching T=90K this evolution abruptly stops and the density of states becomes temperature independent as seen in the symmetrized data of panel a. 2) T$\sim$120K Between 110 and 135K, there is another abrupt change in the shape of the density of states (shown in Fig. 3.6b). The difference is that there is no gradual evolution leading up to this. Rather, it is simply abrupt and remains unchanged for all increasing temperatures, up to at least 180K.

These results are initially mysterious, but one can make progress in their origin if we examine the known phase diagram for the $LaFeAsO_{1-x}F_x$ system from Fig. 3.1. Fig. 3.6c includes data from this phase diagram[38]. As discussed in Section 3.2, the undoped parent compound contains both a magnetic ordering and a structural transition above 100K. The key question is whether such ordering is entirely suppressed by the Fluorine doping. Numerous experimental results on these compounds make this still a controversial question, suggesting the persistence of magnetic phenomena all the way to x=0.1 doping[53,54,55,56,57,58]. If we compare the extrapolated temperatures for both the structural (T_{STR} related to the T_S - gold dots) and SDW transitions (T_{SDW} related to the T_N or Neel temperature - blue dots), there is a good agreement between these two temperatures and the two temperatures identified in our data where the density of states undergoes changes. This has lead us to speculate that even though the electron doping of the parent compound clearly competes with the magnetic ordering and structural transition, there still exists some level of coexistence between these phases at higher doping, even where superconductivity exists. This would explain the observed features in our density of states and lead us to interpret the 15meV feature as related to the SDW magnetic ordering, which closes around T_{SDW}=90K. Similarly, we interpret the subtler effect in the density of states around T_{STR}=120K as the structural transition seen in the parent compound.

The obvious question that remains is how is this happening within the crystal? Competition between magnetic and superconducting phases is expected, although materials like the heavy fermion metals (e.g. UBe_{13}, UGe_2) have unconventional superconductivity in close proximity to magnetic phenomena. Even still, T_c for these materials is significantly lower (<1K) compared to what has been observed in these 1111 compounds. For our part, explanations revolve around two primary options. First, what we and others are seeing is

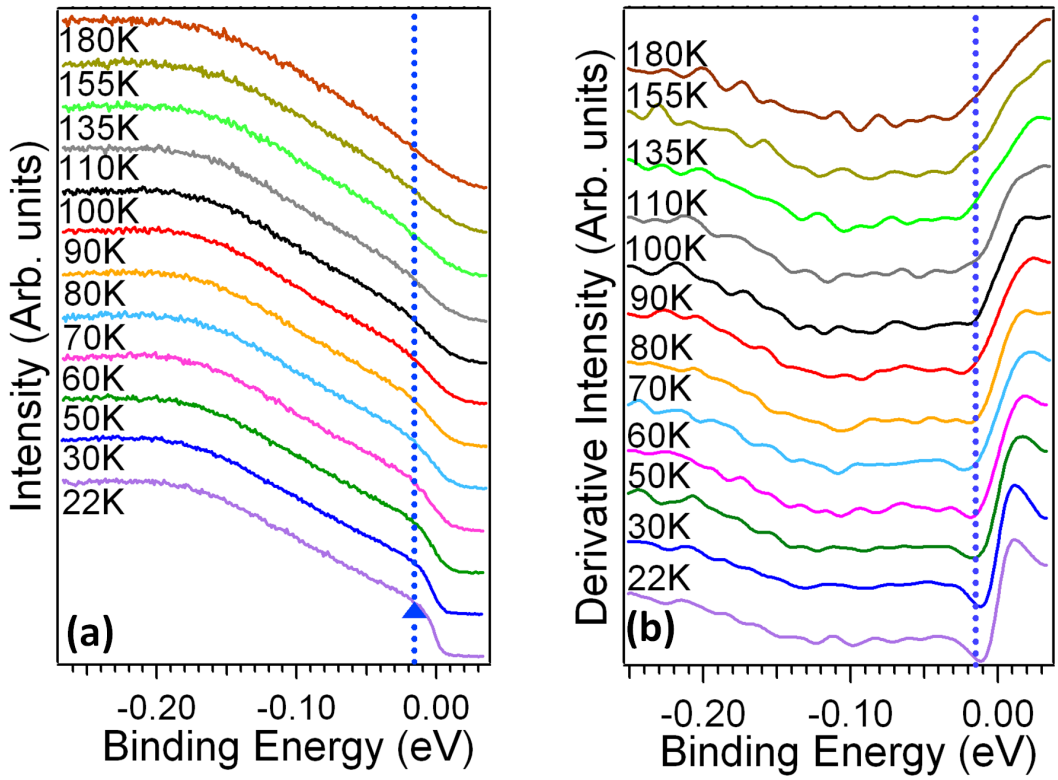

Figure 3.5. (a) Higher resolution temperature dependent data taken with 23eV photon energy. The blue dotted line with arrow indicates the near E_F features noted in Fig. 3.5 at 15meV. (b) First derivative taken of the data from (a). The temperature dependent dip near E_F corresponds to the 15meV feature and this energy scale is marked by the blue dotted line.

mesoscopic phase separation. There exist regions where magnetic order continues to exist as domanins or islands in a superconducting sea. Increased doping raises the sea level as it were and these islands begin to disappear as superconductivity becomes the dominant order in the system. Thus, AIPES sees both the predominant superconducting electronic state (or normal state above T_c) but also gets photocurrent from the magnetically ordered islands which is observed as a gap-like phenomena. Second, and perhaps more theoretically sophisticated, is the existence of dynamic magnetic domains as proposed initially by Mazin and Johannes[70]. In this model, the magnetic fluctuations from the parent compound's SDW continue but as a large moment, dynamic SDW, which could explain the presence of the "pseudogap" (so as not to correspond it with the cuprates) seen by experiments like ours.

3.6 Final Issues

Before concluding with our brief exploration of the pnictides, there are some final issues that deserve mentioning. First, if we see evidence of this at x=0.1 doping, what about at other dopings? Could one see a trend in the associated T_{STR} and T_{SDW}? How would it merge with other data in the phase diagram? This calls for a doping dependent study, particularly at lower dopings, to look for these temperature dependent changes in the near E_F density of states. This remains an interesting experiment to do but challenges have come up. First, there is the sensitivity of these samples to moisture in the air. Many of our samples became useless, and their cleaves produced grayish colors. Should anyone undertake this work, samples need to be well stored and/or used quickly. The second challenge has been the dominance of the 122 compounds among photoemission groups. As interesting as our results have been, ARPES is the technique everyone wants data from and as such the community has almost entirely neglected the 1111 compounds since.

Indeed, over the course of our study into the magnetic physics of the pnictides, we focused some attention on the hole doped (Ba,K)Fe_2As_2 system though our work is merely consistent with what has been found in the literature, finding basically isotropic gapping of 7±2meV for hole bands near the Γ point which disappear in the non-superconducting parent compound. This is consistent with earlier work[71] where two different gaps are found (α band of ∼12meV and a β band of ∼6meV) and our work was simply unable to find the larger gapped band. The larger community seems to be coming to the position that these materials have an isotropic gap magnitude, though the phase appears to change leading to a so-called s_{+-}-wave gap.

Still, the role of magnetism remains unclear and potentially different pnictide families may have more diversity on this point than expected. ARPES work has suggested that magnetic fluctuations are important to the emergence of superconductivity, in particular the manner in which electronic states near-E_F can be connected by a wavevector associated with the magnetic ordering[71]. Electronic states near the Brillouin zone center can be overlapped with states near the zone edge. As doping changes, this overlap is damaged and the resulting

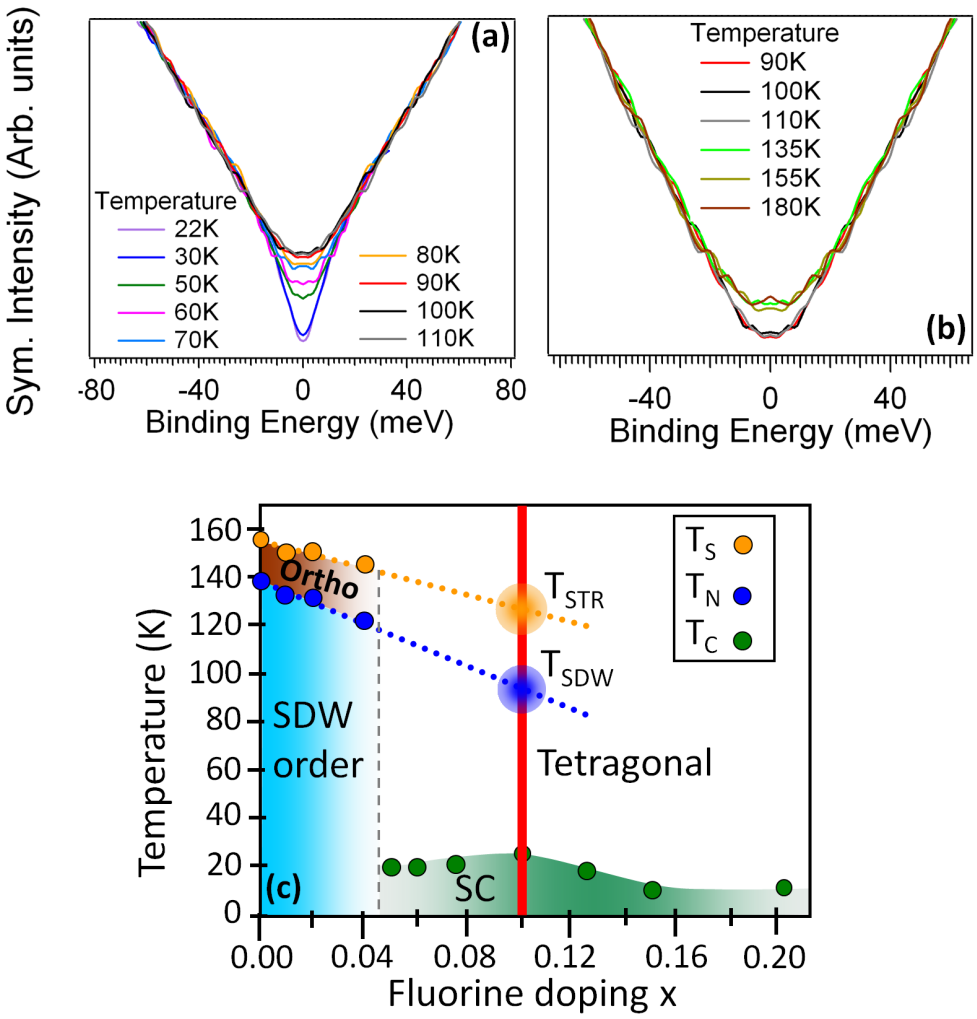

Figure 3.6. (a-b) Symmetrized data from Fig. 3.5(a) near E_F. In (a), we see the gradual temperature evolution of the 15meV pseudogap feature until the evolution stops around 90K. In (b), the temperature increase continues with a second, abrupt change in the near E_F DOS lineshape between 110 and 135K. (c) Using phase diagram data from[38], we take the T_N temperatures (blue dots) which define the SDW phase and extrapolate them (blue line) to determine the potential transition temperature for the SDW phase at doping x=0.1 (red line), finding a T_{SDW} ~90K, associating this with (a). This is similarly done for the orthorhombic-tetragonal structure transition temperatures, T_S (yellow dots), to find the potential transition temperature at x=0.1, T_{STR} ~120K, associating this with (b).

magnetic ordering is diminished[72]. However, there is additional work suggesting that this nesting is less relevant to the emergence of superconductivity[36 73], or that the relationship is more complicated[74]. Still, band structure measurements indicate that there is at least significant reconstruction of bands across the T_{SDW} transition[75]. This coupled with the surprisingly low magnetic moment in many of these compounds[39] means that though enormous progress has been made in less than 3 years, there still are issues to be resolved.

Chapter 4

Charge Density Wave Physics in $LaTe_2$

4.1 Introduction

As introduced in Section 1.4, a charge density wave (CDW) transition relates to the balance between electronic energy and lattice structural stability and has been the subject of research for over half a century. Below a critical temperature, the system finds it energetically favorable to introduce a new periodic ordering, allowing the Fermi surface to be gapped, and lowering the overall electronic energy. Because this ordering is mediated by strong electron-phonon interactions, CDW systems can provide excellent opportunities for theoretical investigation of how strongly-correlated electron-phonon systems behave and the effects on band structure. Furthermore, when one relates CDW and other charge ordering physics to systems exhibiting superconductivity, the interest becomes more pressing and exciting such as its competition of even coexistence with superconductivity[76,77,78,79,80,81], and its potential role in the superconducting cuprate phase diagram[82,83].

Recently the rare earth di- and tritelluride systems have attracted great interest due to their low dimensionality and the recent discovery of a pressure-induced superconducting state competing with a CDW phase and with antiferromagnetic order[81]. This interplay makes the tellurides the ideal system to investigate the consequences that the competition between charge density wave, antiferromagnetism and superconductivity has on fermionic excitations at the Fermi energy, E_F and to provide a deeper understanding of how superconductivity can emerge from such interplay, an issue of great interest in the solid state community. Additionally, the rare-earth tellurides appear to be "high temperature" CDW materials,

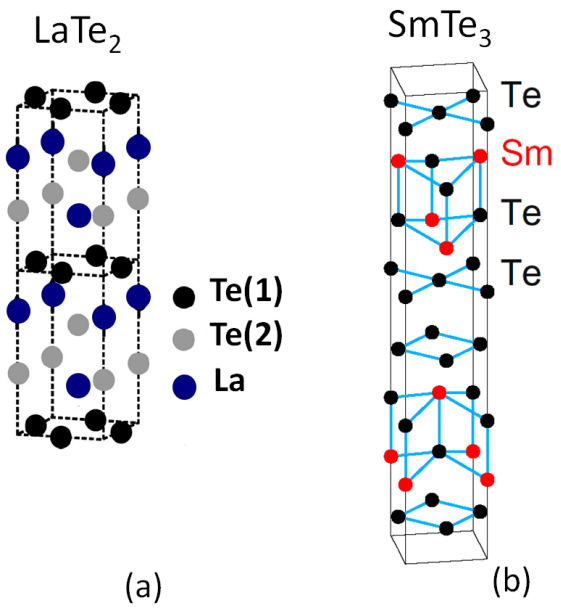

Figure 4.1. Crystal structures of (a) $LaTe_2$ and (b) $SmTe_3$. Panel b taken from Ref.[8]

with transition temperature potentially as high as the crystal melting temperature given the gap measurements[8,84,85]. Fig. 4.1 provides us with crystal structures for both di- and tritelluride compounds. Of importance is the quasi-2D nature of the crystal, made up of RTe slabs (R = rare earth) separated by single tellurium planes in the case of the ditelluride (panel a) and double planes in the case of the tritelluride (panel b). It is these square tiled tellurium planes which are critical to CDW formation since we will find that they dominate the near E_F band structure.

Traditional scattering techniques can reveal the structural modulations due to CDW phenomena, but in order to have a complete insight into the CDW phase and its formation, we require a direct probe of the electronic structure. This is an investigation that ARPES is well suited to do, in particular given its quasi-2D structure. As a result, the literature has many examples of ARPES work done on telluride systems prior to ours such as in the study of $SmTe_3$[8] and $CeTe_3$[84]. Yet, it was only recently that ARPES been used to study rare earth ditellurides such as $LaTe_2$[85].

The existence of a CDW phase in the ditellurides was first established by transmission electron microscopy (TEM)[86,85] and single crystal X-ray diffraction[87] experiments. TEM measurements had reported a long range distortion $\mathbf{q} = .5\mathbf{a}^*$[86] similar to the diselenides[88], while single crystal X-ray diffraction expanded on this suggesting a larger $2 \times 2 \times 1$ superstructure[87]. (Note: $\mathbf{a}^* = 2\pi/a$ where a is the lattice constant) Most recently, the TEM work of Shin et al. demonstrated a four-fold symmetric superstructure with a modified $\mathbf{q}$=.484$\mathbf{a}^*$ and proposed an additional CDW wave vector $\mathbf{q}$=.6$\mathbf{a}^*$+.2$\mathbf{b}^*$[85].

Recapping the CDW physics described in Section 1.4, we expect the CDW's effect on

the electronic structure to manifest itself through ARPES data in at least three ways: 1) Observing large regions of Fermi surface band structure which can be connected or "nested" by a single $\mathbf{q}_{CDW}$ 2) Gapping of near E_F band structure, which represents the energy gained by the instability 3) The appearance of "shadow bands" where the action of the CDW creates new states by shifting (or, more appropriately, scattering) the main band structure by $\mathbf{q}_{CDW}$. Thus, in this chapter we will do the following: We will first provide a large scale exploration of the $LeTe_2$ electronic structure near E_F. From this work we hope to provide insights into the successes and weaknesses of past theoretical studies as well as helping to clear up prior ambiguities by providing a firm experimental basis for future work in the tellurides. We will then focus on the near-E_F states and the three CDW characteristics we have described. The result of this study will be an interesting observation about the CDW physics in these materials compared to other materials in the literature of the time. We find that $LaTe_2$ is the first 2D CDW material (albeit probably not the only one) which displays all the qualities of their 1D cousins, namely a metal-insulator transition tied to a Fermi surface nesting instability driving the CDW formation.

For the work we are presenting, ARPES and Low Energy Electron Diffraction (LEED) data were taken on single crystals of $LaTe_2$ using beam lines 7.0.1 and 10.0.1 at the Advanced Light Source of the Lawrence Berkeley National Laboratory. These beam lines were equipped with Scienta SES100 and R4000 electron analyzers respectively. A total energy resolution of 40 meV or better was used, and the total angular resolution was set to 0.35 degrees. Our samples were cleaved *in situ* with a base pressure better than 7×10^{-11} Torr at low temperatures. As with all the studies in this thesis, the chemical potential, μ, is determined from gold foil in contact with the sample, which gave us an uncertainty of ± 0.5meV in μ. Samples for these studies have been prepared in a few ways and the question has arisen about whether these differences in sample preparation may be responsible for differences observed in the superstructure by XRD and TEM[85]. The samples we used for our study were grown using two different techniques: 1) Mineralization of a stoichiometric binary mixture of elements[89] and 2) A high-temperature Bridgeman method explained by Kwon et al.[90]. Over the course of our ARPES work, we were unable to discern any difference originating from the two preparations.

4.2 Electronic Band Structure Seen by ARPES

To begin our study, Fig. 4.2 shows the unsymmetrized Fermi surface maps of $LaTe_2$ for two different polarization vectors and photon energies, in order to vary the ARPES matrix element in the photocurrent (Eq. 2.42) and better explore the band structure. In panel a, we show data taken at 55eV using a polarization vector along the Γ-X direction (see inset). The map was collected beyond the first Brillouin zone (also valuable for matrix element reasons) and is integrated from E_F to 80meV in binding energy. The non-CDW LDA (Section 1.2) band structure calculation[91] (white dashed line) is overplotted on the same figure for comparison and shows an overall good agreement with the experimental data

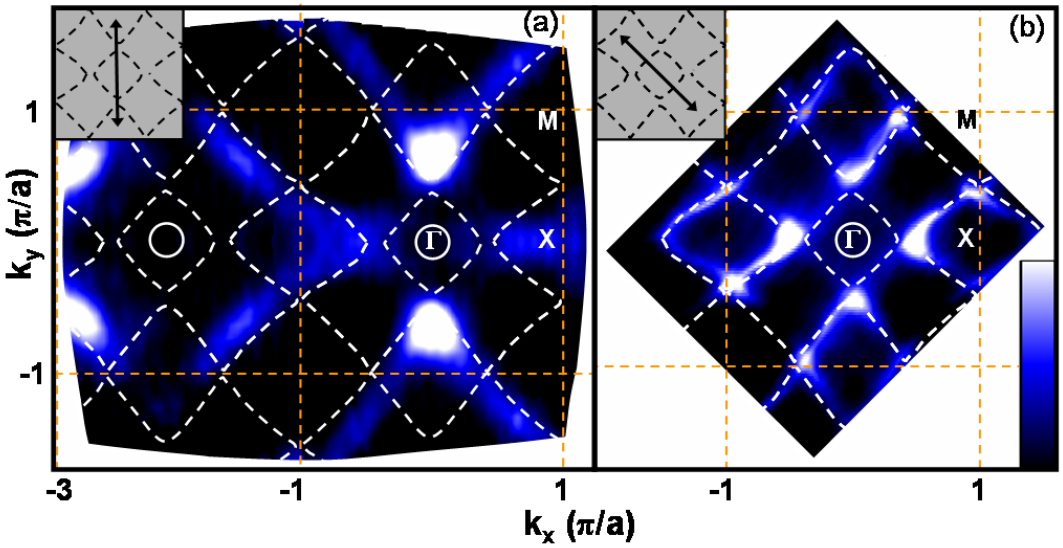

Figure 4.2. (a) ARPES constant energy intensity map averaged in energy from E_F to 80meV binding energy and symmetrized over ΓX. Beam energy was 55eV with a polarization reflected in the inset. Orange dashed lines indicate the Brillouin zone boundaries. Comparison with the non-CDW LDA FS calculation[91], indicated as white dashed lines, shows moderate agreement. However, as we approach a photon energy of 110eV, more features are revealed. (b) ARPES constant energy map, unsymmetrized, averaged from E_F to 100meV binding energy using 110eV photons.

both in the first and higher Brillouin zones. This supports the prediction that the near E_F band structure can be thought of 1D bands arising from the Te $5p_x$ and $5p_y$ orbitals in the Te square planes, as well as confirming the tetragonal picture expected for $LaTe_2$. However, a closer analysis does reveal deviations. In particular, we see the absence of the two features centered around the Γ point, a small electron pocket (solid white line) and an "inner diamond" band.

Compare these results to panel b, where data was taken with a different polarization vector, along the Γ-M direction (see inset), at 110eV photon energy. We find that when the photon energy is tuned close to the La and Te adsorption edges (La $4d_{3/2}$ ≈105eV, Te $4p_{3/2}$ ≈103.3eV) we can resolve, although still weak, the inner diamond at the Γ point, predicted by LDA but not observed before[85] within this energy range. We note, however, that despite our extensive search over a wide range of photon energies (between 80 and 200eV) and different polarization conditions, we were unable to resolve the electron pocket centered at the Γ point, suggesting that it was not merely that we were probing the wrong k_z value. In addition, we note that while the bands of panel b show a better overall agreement to theory, we suspect that the slight shift in band position between panels a and b is probably due to differences in the sample surface stoichiometry over time. This is related to the predictions of Luttinger's theorem, indicating that sample doping is reflected in the Fermi surface volume (see Section 2.4).

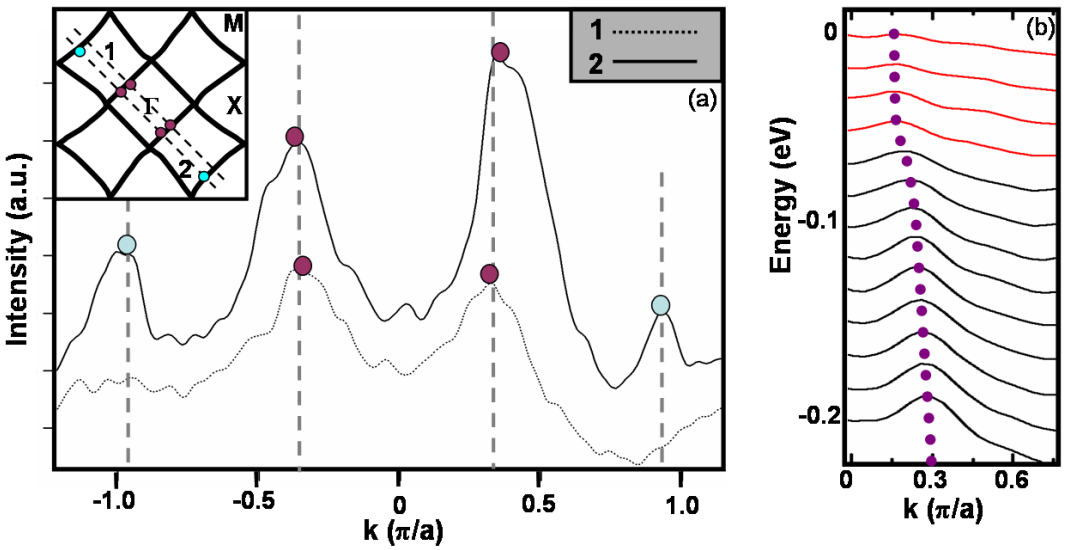

Figure 4.3. (a) Momentum distribution curves (MDCs) taken (1) along the M-Γ-M direction and (2) parallel to M-Γ-M but slightly shifted. From these we can discern the twin peaks of the inner diamond while the spectral of the bands near the M point is strangely suppressed but only along the high symmetry direction. (b) MDCs along Γ-M at increasing binding energies showing the dispersion of the inner diamond band up into the energy range of Fig. 4.2. Red MDCs indicate where the curve becomes dispersionless

We can further confirm the existence of this inner diamond band structure through using momentum distribution curves (MDCs). This is provided in Fig. 4.3 for cuts both along the M-Γ-M direction and slightly shifted off this high symmetry direction, cuts 1 and 2 respectively. In these cuts, we can clearly resolve the two peaks of the inner diamond band (marked by violet circles). For cut 2, we can resolve two additional peaks near π/a in momentum space, corresponding to the bands near the M point (marked by light blue circles). These additional bands are not resolved in cut 1 probably due to a matrix element effect. In panel b, we show the MDCs curves for a cut along the Γ-M direction at increasing binding energy. The peak in the MDCs spectra, corresponding to the inner diamond band and still marked by violet dots, can be clearly distinguished in the entire energy range, from E_F all the way to 200 meV binding energy. Significant for CDW physics, this peak disperses from 200 meV up to 50 meV where it suddenly stops (see peak position in the red curves). This suggests that the inner diamond is gapped by 50 meV due to the CDW formation. This is contrary to prior published work, taken at photon energy far from the resonance energy, where it had been suggested that the inner diamond band is gapped by as much as 600meV in binding energy[85]. By taking advantage of photon energies near the absorption edge (core level peaks), we were able to tease out this otherwise weak band structure. The consequences of this band structure and gap will be made more apparent in Section 4.3, and we will revisit it there.

Further complexities seem to appear as we increase the binding energy. Fig. 4.4a presents a constant energy plot of the electronic bands around 130meV in binding energy (as opposed to at E_F in Fig. 4.2). A closer examination of the four X points of the Brillioun zone reveals the onset of unpredicted features, indicated by the orange arrows. Particularly fascinating about these features is that they appear to break the mirror symmetry of the system (a symmetry we expect from the crystal structure - Fig. 4.1) and are completely unexpected from band structure calculation. These features appear to be more pronounced at lower temperatures, and they are dispersive, splitting as the binding energy increases (panel b). To shed more light on the possible origin of these bands, we have performed low energy electron diffraction (LEED) measurements on the sample surface, the results of which are shown in Fig. 4.4c. LEED is a natural partner for ARPES because, like ARPES, it is primarily a surface sensitive probe given the short mean free path of low energy electrons. The main Bragg spots we see are due to the orthorhombic unit cell and are indicated by arrows and Miller indices, as well as obeying an h + k = even condition[86,85]. But in addition to these main peaks, one can measure satellite peaks that appear to form a second superstructure which breaks mirror symmetry. This is indicated by the slightly rotated orange square relative to the main peaks which indicate the crystal's orientation. This allows us to at least confirm the sample surface does, in fact, break mirror symmetry. As we will see in Section 4.3, this order does not appear to correspond to a CDW phenomenon. Thus, a possible explanation for this superstructure comes from comparison with the structurally similar $LaSe_2$. When the material is slightly off in stoichiometry, the system is known to exhibit an ordered-defect superstructure which breaks mirror symmetry in the crystal's square chalcogenide planes[92,93]. It is possible that the stoichiometry of our samples also is

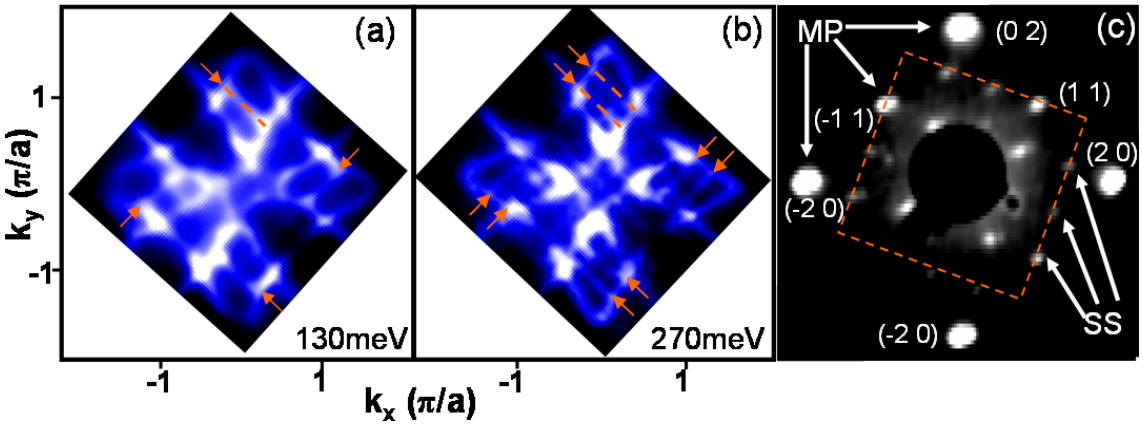

Figure 4.4. (a) ARPES constant energy image plot centered at 130meV and integrated over 60meV. Orange arrows indicate bands near the X points which break mirror symmetry. (b) A similar plot centered at 270meV and integrated over 80meV showing how the non-mirror symmetric bands disperse by splitting in two. (c) LEED done on $LaTe_2$ indicating both main peaks (MP) but also a superstructure (SS) which breaks mirror symmetry.

slightly less than perfect, either from synthesis or through change over time, and the observed band structure is due to a surface state forming on a non-mirror symmetric $LaTe_2$ surface.

Continuing to move away from E_F, Fig. 4.5 shows the evolution of the band structure as the binding energy is increased up to approximately 1eV. We found that subtle patterns appeared in the near Γ point (zone center) band structure, but observing them in a traditional ARPES intensity map was challenging. To address this, we show the first derivative of the ARPES constant energy maps, where the derivative was taken in the y-axis direction. For determining quantitative results, this is a challenging method to interpret. But for observing otherwise weak band structure, it can be very useful. As the binding energy increases, we can clearly distinguish the onset of complex patterns centered at the Γ point, which evolve into a checkerboard-like structure in momentum space as the binding energy increases toward 700meV (panel c). These structures continue to maintain the four-fold symmetry seen near E_F. To explain whether the onset of this complex structure is simply due to band structure or reflects some hidden order such as a CDW order, it is important to carefully examine the band structure along high symmetry directions and compare it with known LDA calculation[91]. We note that these complex patterns seem to be strongly sensitive to photon energy, as was the case for the inner diamond in Fig. 4.2b. In particular they can be enhanced for photon energies close to the La $4d_{3/2}$ adsorption edge ($\approx$105.3eV), suggesting that they are related to the LaTe layers.

In order to better investigate the origin of these complex patterns in the momentum space, we need to change our ARPES view. Instead of sitting at a fixed binding energy and looking at the band structure crossing this plane, we will take slices along high symmetry direction, and look at the electronic dispersions as a function of energy. This is particularly useful since it is for these high symmetry cuts that band structure is calculated by LDA.

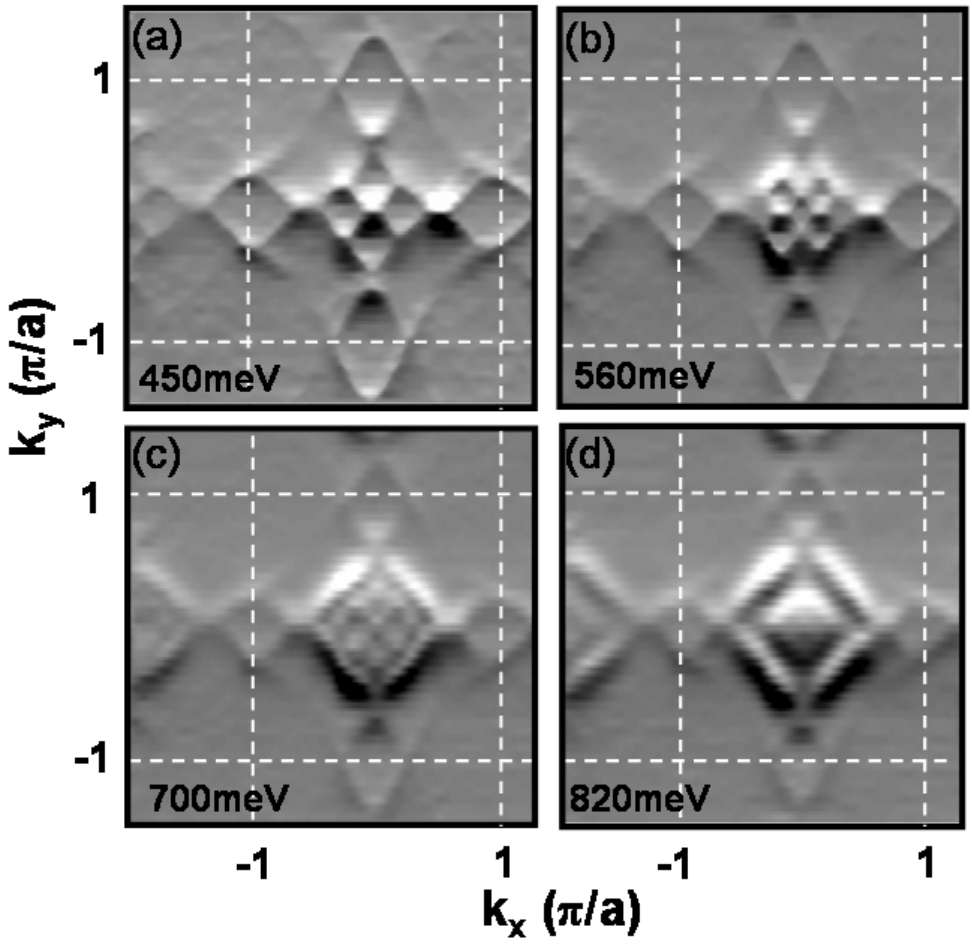

Figure 4.5. (a)-(d) Constant energy cuts integrated over 60meV, with first derivative used to enhance band edges, centered at binding energies 450, 560, 700, and 820meV respectively.

So Figs. 4.6-4.8 show a detailed analysis of the experimentally measured band structure along the high symmetry directions. In panels 4.6a-b, we present the raw ARPES image plots along the X-Γ-X direction, with the associated energy distribution curves (EDCs) shown in panel d. The direct comparison with the LDA calculation (panel c) show that far more bands are observed experimentally than the one predicted by the non-renormalized LDA within the 400-850meV energy range. However, bands arising from the square Te planes (β_1, β_2, and δ) are, for the most part, well modeled by the theory and require no renormalization. However, bands arising from the interlayer LaTe blocks (all other bands in the figure) require renormalization. This is summarized in Fig. 4.6c which illustrates our hypothesized renormalizations of the LDA band structure.

For the following reasons, we propose that the LaTe bands are being compressed into a smaller energy range, with at least three bands peaking at Γ between 0.5 and 1 eV in binding energy. First, α_1 was expected to rise to lower binding energy and nearly touch the circular electron pocket of earlier discussion. However, since this pocket cannot be resolved and we see no spectral weight at the Γ point until nearly 400meV, we infer that the hybridization between the two bands was simply underestimated by theory. A greater energy gap between the bands both forces the electron pocket above E_F (where ARPES cannot observe it) and pushes the α_1 band to higher binding energies, around 500meV. Secondly, it is important to be able to identify the γ_0 band in our data because it is the highest binding energy band of the LaTe block in our energy window of interest. We find a band in the data with the appropriate curvature but it has been renormalized to a far smaller binding energy as indicated in panel c. We take this as suggesting that the other LaTe block bands above it may require a similar renormalization pushing them all to lower binding energies and compressing them closer the energy range between 0.5 and 1.0eV. Thus, α_1 and γ_0 provide the 'bookends' which define the new, tighter energy range which the LaTe block bands exist in.

With these things in mind, we can examine the other high symmetry directions, M-Γ-M in Fig. 4.7, and M-X-M in Fig. 4.8, and we obtain a similar picture. The M-Γ-M band structure does reasonably well at explaining the β_3 and β_4 bands, responsible for the inner diamond and near M point band structure respectively. However, we can again identify the α_1 and γ_0 bands which suggest the aforementioned LaTe block band renormalization. It is also worth observing the strong increase in the spectral weight of the β_3 band (possibly due to the presence of α_1) at around 500meV as partly responsible for the large gap associated with this inner diamond band[85]. Also, we suspect the ζ band may also require a renormalization to help explain the data particularly near the M point in Fig. 4.7. However, we do not feel that our data provide enough insight to intelligently propose one, and thus we leave the band unchanged in Fig. 4.7. The M-X-M experimental band structure also demonstrates a reasonable level of agreement with theory in the case of the Te plane bands but renormalization is needed for the LaTe block bands. However, theory calculated for this symmetry direction appears far more discordant with actual experimental results than other symmetry directions. Whether the absence of bands is due to matrix elements or a particularly non-trivial renormalization, is unclear and requires more theoretical insight. It

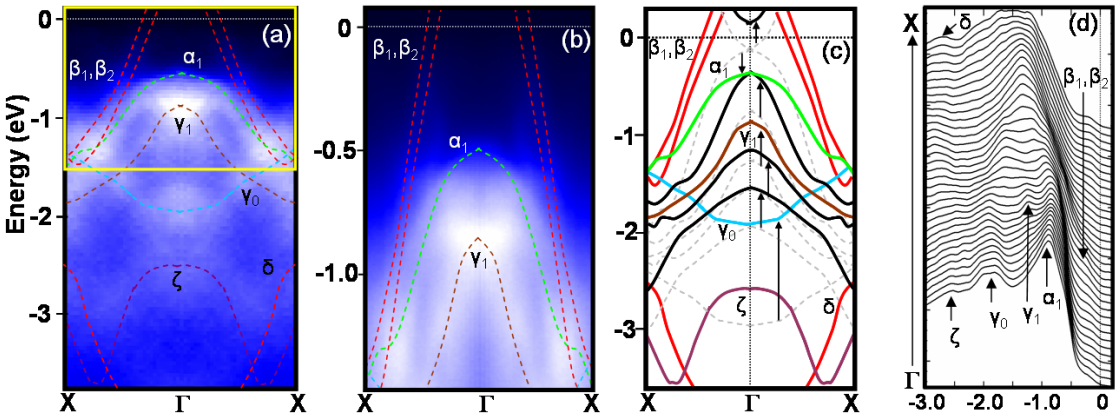

Figure 4.6. (a) ARPES image plot showing dispersions along X-Γ-X down to nearly 4eV in binding energy. (b) ARPES image plot showing dispersions along X-Γ-X down to nearly 1.5eV in binding energy. Overlaid on both plots is the predicted LDA band structure which, in some cases, is renormalized based on the data. (c) LDA band structure calculation along X-Γ-X. Bands that have been renormalized are indicated by arrows showing the proposed shift in energy from their original locations (gray dashed lines). (d) Energy distribution curves (EDC's) down to 3eV in binding energy taken along Γ-X direction.

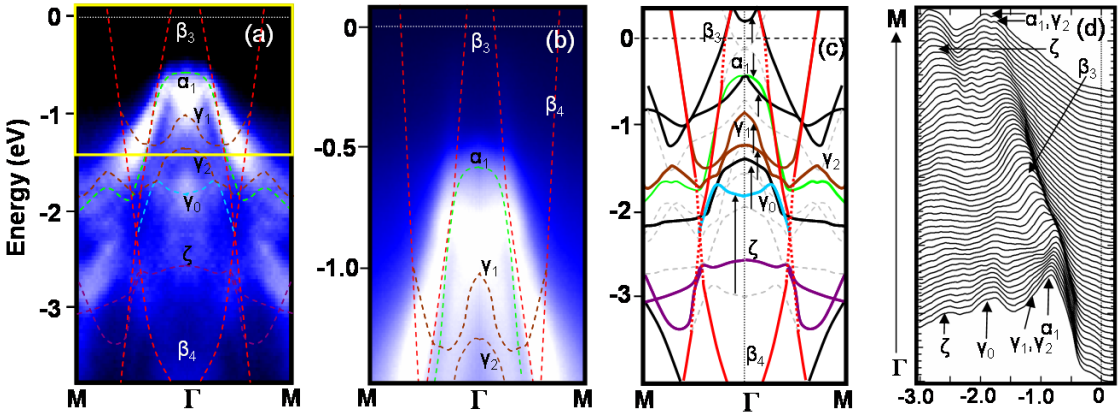

Figure 4.7. (a) ARPES image plot showing dispersions along M-Γ-M down to nearly 4eV in binding energy. (b) ARPES image plot showing dispersions along M-Γ-M down to nearly 1.5eV in binding energy. Overlaid on both plots is the predicted LDA band structure which, in some cases, is renormalized based on the data. (c) LDA band structure calculation along M-Γ-M. Bands that have been renormalized are indicated by arrows showing their proposed shift in energy from their original locations (gray dashed lines). (d) Energy distribution curves (EDC's) down to 3eV in binding energy taken along Γ-M direction.

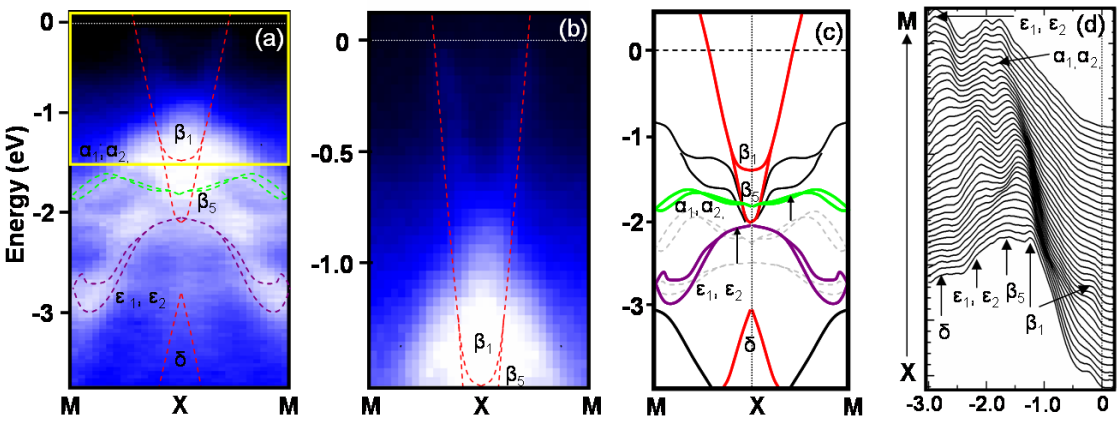

Figure 4.8. (a) ARPES image plot showing dispersions along M-X-M down to nearly 4eV in binding energy. (b) ARPES image plot showing dispersions along M-X-M down to nearly 1.5eV in binding energy. Overlaid on both plots is the predicted LDA band structure which, in some cases, is renormalized based on the data. (c) LDA band structure calculation along M-X-M. Bands that have been renormalized are indicated by arrows showing their proposed shift in energy from their original locations (gray dashed lines). (d) Energy distribution curves (EDC's) down to 3eV in binding energy taken along X-M direction.

is our opinion that this renormalization is responsible and can provide an explanation for the complex checkerboard-like structure observed in the first derivative constant energy maps discussed in Fig. 4.5.

So we have attempted to present a clear and comprehensive picture of the experimental band structure for $LaTe_2$ using the ARPES technique. Already by this point, we have seen evidence of CDW physics such as in panel b of Fig. 4.3. But of additional importance is that the band structure near E_F can be well modeled by non-CDW LDA band structure calculations and is dominated by contributions from the Te(1) layers. Other bands, particularly those associated with the LaTe block bands, require more energy renormalization. The inner diamond band structure with its smaller gap will be critical to the work to follow. Also, we have observed and attempted to explain the broken mirror symmetry seen in the band structure. This too turns out to be critically related to the debate over CDW physics in this material.

4.3 The Effect of CDW Physics on Near E_F states

Given our comprehensive study of the band structure, we begin to ask some more probing questions about CDW physics in this material. As mentioned, the origin of a CDW is most commonly traced to a Fermi surface nesting instability, i.e. the matching of sections of the Fermi surface to others by a single wave vector, $\mathbf{q}_N$. (Note: $\mathbf{q}_N = \mathbf{q}_{CDW}$ if the nesting

actually leads to a CDW.) But unlike the ideal 1D metal studied by Peierls, the Fermi surfaces in higher dimensional materials tend to remain metallic in the CDW phase, either due to imperfect nesting which leaves regions of the Fermi surface ungapped[8,94], or due to residual electron pockets formed by the CDW formation[84,95]. This is in contrast to the quasi-1D CDW systems, where a perfect nesting can be realized and the Fermi surface is fully gapped, which explains why all known quasi-1D CDW materials are semiconductors in the CDW phase[96,97,77]. While we can find a few examples of non-metallic 2D CDW systems, the origin of the CDW phase is not due to true Fermi surface nesting but rather due to Mott physics[98,99] or other non-nesting phenomena[100].

Therefore, a natural question is whether there exists any proven instance of a 2D CDW system where the CDW phase is driven by Fermi surface nesting, yet non-metallic. $LaTe_2$ is ideal to address this question, having been previously shown to be non-metallic[85,101] and supporting a CDW as has been established by TEM and x-ray diffraction. Yet, these results, presented in Section 4.1, demonstrated some ambiguity about the nature of this CDW, in particular its wavevector. In addition, there is some ambiguity about the size of the gap, particularly for bands near the Γ point. We have already begun to address this in the preceding section with the discovery of the inner diamond and its gap around 50meV (Fig. 4.6b).

Our intention is to demonstrate that $LaTe_2$ is indeed a CDW material where the nesting wavevector does correspond to the new periodicity of the lattice and that this nesting does indeed open up a non-zero gap throughout the band structure at E_F. This would be novel since it would represent the first 2D CDW system to actually behave like the ideal 1D system. Through this, we could also shed light on the ambiguity over the CDW wavevector seen by other probes, in particular the identity of the two orders observed by TEM: $\mathbf{q}=.5\mathbf{a}^*$ which we will refer to as $\mathbf{q_1}$ and $\mathbf{q}=.6\mathbf{a}^*+.2\mathbf{b}^*$ which we will refer to as $\mathbf{q_2}$.

Fig. 4.9a is a re-presentation of the data from Fig. 4.2b, showing the constant binding energy band structure of $LaTe_2$ near μ. As indicated before, there is particular interest in the small inner diamond square contour centered around the Γ point. Panel b is data similar to that shown in Fig. 4.3a except, as is crucial for our arguments about nesting, the MDC peaks are taken along both M-Γ-M directions to fully establish the inner diamond. The importance of both the inner diamond and the stronger outer contour (the yellow dashed line in this figure) lies in the essential role they play in determining the CDW formation. The reason for this is that the Fermi surface in panel a (as well as in Fig. 4.2) can be approximately represented by two perpendicular pairs of nearly 1D bands parallel to the Γ-M direction (see inset of Fig. 4.9c). This gives rise to an almost perfectly nested Fermi surface, favoring a CDW with nesting vector parallel to the Γ-X direction (red arrows in Fig. 4.9c inset). We can determine this nesting vector as $\mathbf{q}_N=.53\mathbf{a}^*$ which is determined from the separation between the MDCs peaks shown in Fig. 4.9c (yellow circles), taken for different cuts (1 to 9) along the Γ-X direction. This is consistent with prior scattering work regarding $\mathbf{q}_1$. This nesting is nearly perfect, with a variation in the peak to peak distance of ≈2% as compared to ≈20% in the imperfectly nested tritelluride compounds[8]. Finally, since the Fermi surface

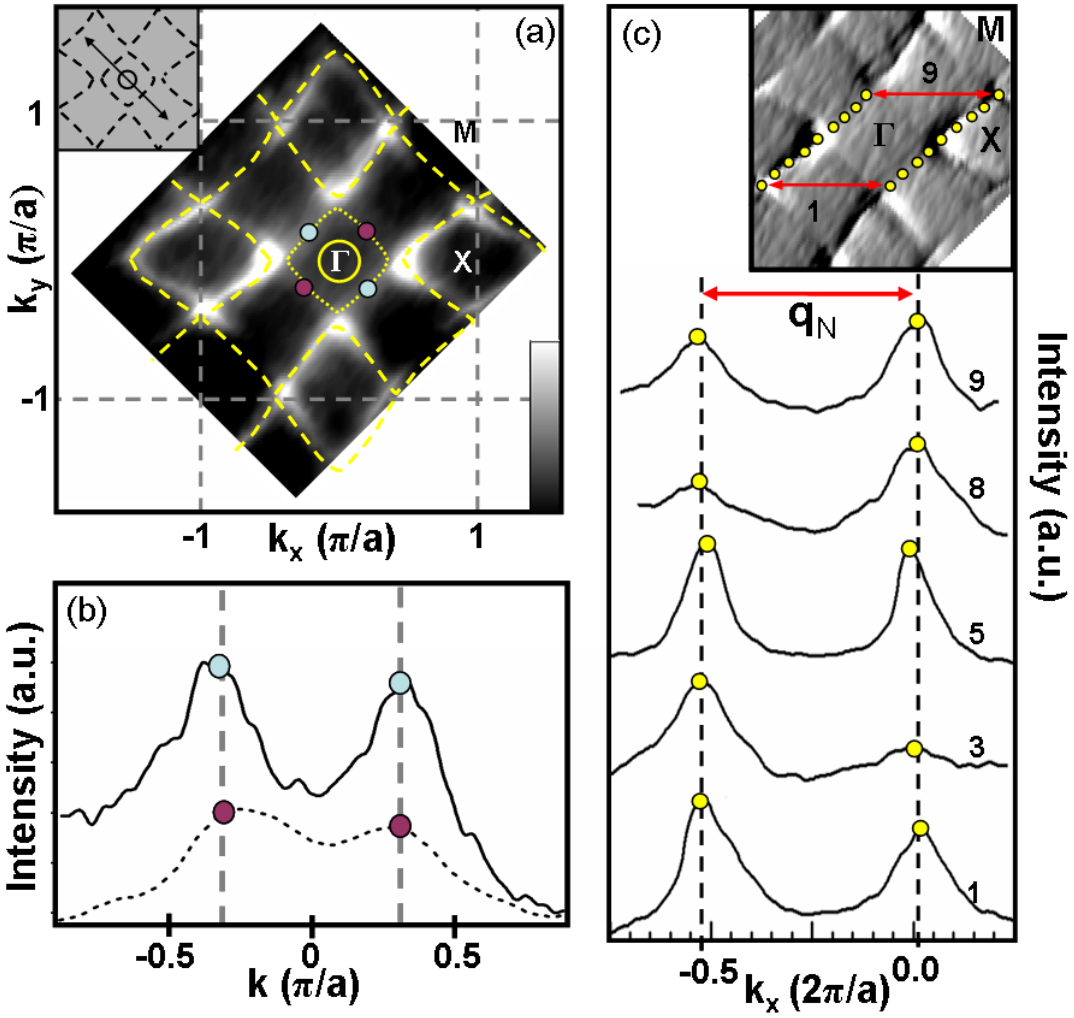

Figure 4.9. (a) Unsymmetrized FS map (integrated between +50 meV above to -100meV below the chemical potential, μ) at T=180K as seen in Fig. 4.2. White represents maximum intensity and black zero intensity with beam polarization displayed in the inset. The non-CDW LDA band structure at E_F[91] is shown as yellow lines. (b) MDCs through the inner diamond, along M-Γ-M directions. (c) Raw MDCs spectra near μ for cuts parallel to the Γ-X direction (1 - 9) as shown in the inset of the same figure, where the first derivative of the Fermi surface is shown. Each curve is shifted in k-space by a constant.

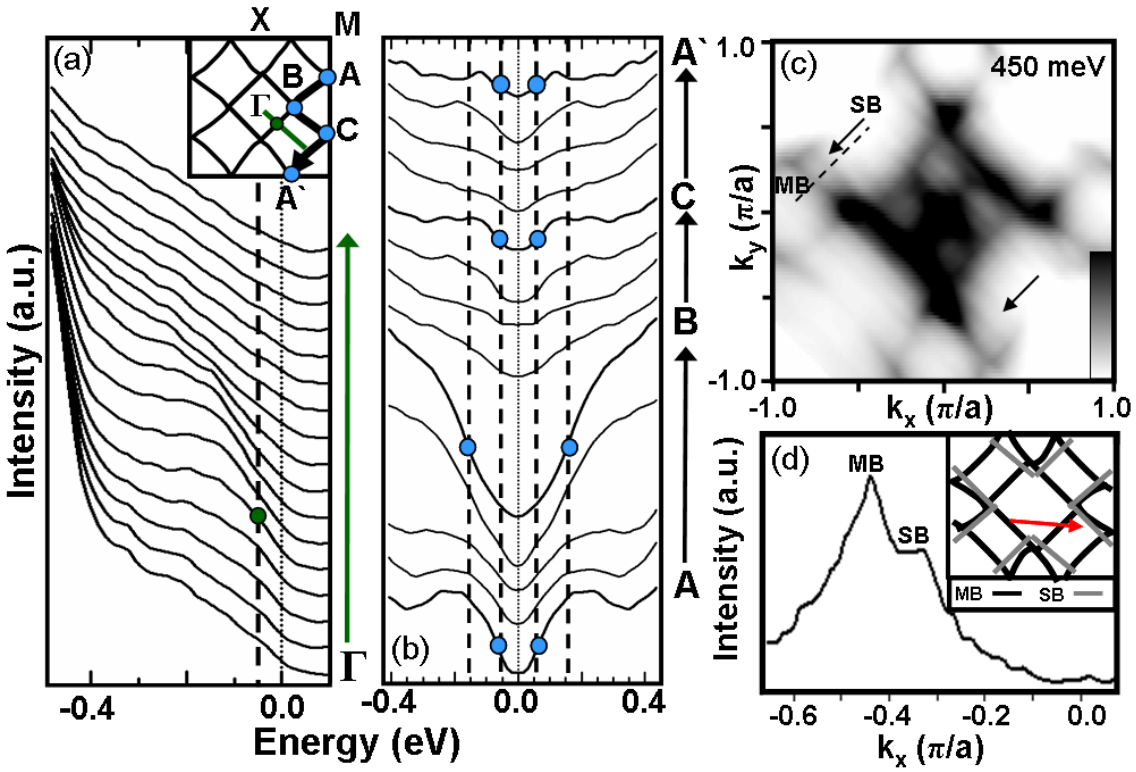

Figure 4.10. (a) EDCs stack taken along the green line (Γ-M) in the inset. (b) Symmetrized EDC stack at k_F along one quarter of the outer band contour as indicated in the inset of 2a, with T=50K. (c) Unsymmetrized constant energy cut at 450meV showing evidence of shadow bands indicated by black arrows, where black represents maximum intensity and white zero intensity. (d) MDC cut taken along the dashed line in panel c showing two peaks associated with the main band (MB) and the shadow band (SB). The inset illustrates how the shadow bands (gray line) arise by shifting the inner diamond by the nesting vector $\mathbf{q}_N$ (red arrow).

pattern is four-fold symmetric, the MDCs shown suggest that $\mathbf{q}_N$ also nests the entire Fermi surface, again explaining the $\mathbf{q}_1$ observed by TEM.

This is critical but still only half of the argument. We have shown that the entire Fermi surface can be nested by $\mathbf{q}_1$. But does it open up a gap everywhere it nests as expected in a 1D CDW system? The momentum dependent energy gap can be measured from the leading edge position of the energy distribution curves (EDC's) along k_F, as described in Section 2.4. Looking to panel a of Fig. 4.10 shows a series of EDCs for a cut parallel to the Γ-M direction (green line in the inset) over the inner diamond contour. This data is a subset of the data presented in Fig. 4.7d, but here we zoom in close to E_F to resolve subtle features in the β_3 band. This more careful EDC analysis resolved the small peak in the EDC, which disperses toward μ, yet never crosses it, and eventually recedes to higher binding energy. This allows us to estimate a leading edge midpoint gap of 50 ± 10meV (green circle), suggesting $\Delta \approx 100$ meV. This is consistent with the gap determined by the discontinuity in the band dispersion

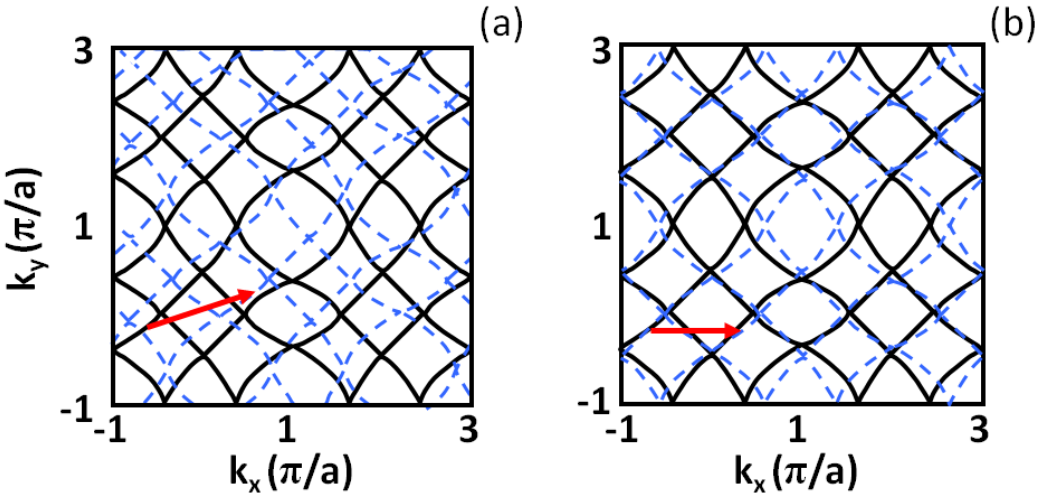

Figure 4.11. (a) Cartoon illustrating the experimental Fermi surface structure of Fig. 4.9 (black curves) shifted by $\mathbf{q}_2$ (red arrow and blue dashed lines) indicating a lack of any significant overlap by this wavevector for the data. (b) Here, the band structure is shifted by $\mathbf{q}_1$ and illustrates the nestable (closer overlap) regions examined in Fig. 4.9c

seen in the MDCs of Fig. 4.3b. Thus, is the first good characterization of the inner diamond gap since, as mentioned in the previous section, prior studies had not resolved this diamond and assigned $\Delta \approx 600$ meV[85].

With the inner diamond gap quantified and finite, we can turn our attention to the outer Fermi surface. In order to do this, Fig. 4.10b shows a stack of EDC spectra at k_F along the outer contour, from A to A' (inset of panel a). As is often the case, being able to determine the gap without the complexity of the Fermi function would help our analysis of the Fermi surface gapping. As described in Section 2.4, we will symmetrize these k_F EDCs to remove contributions by the Fermi function. As with the inner diamond, the midpoint of the leading edge show that the majority of the spectra are also gapped by $\approx 50 \pm 14$meV (blue circles at high symmetry points), although deviations from this are observed. This gap behavior is four-fold symmetric throughout the entire Brillouin zone. Surprisingly, the gap seems to anomalously increase near the B points, closest to Γ point, along the contour. Although a more complicated CDW origin for this anomalous gapping is possible, we propose a simpler explanation. Two bands are predicted to exist near the B point, one due to the inner diamond and other from the outer Fermi surface. The anomalous increase of the gap can then be explained as a shift of the relative spectral weight between these two bands. Admittedly, this still remains a mysterious aspect of the gap to us. But the larger message remains clear: the Fermi surface nested by our $\mathbf{q}_N$ is indeed gapped.

The observation of shadow bands corresponding to our $\mathbf{q}_N$ further supports it as the CDW vector of the system. Returning to the data from Fig. 4.5a taken at a constant 450meV

binding energy, we present it again in Fig. 4.10c but without taking the first derivative and instead oversaturating the image. A careful examination reveals unexplained band structure indicated by the black arrows. We can quantify this by taking an MDC along the dashed line and we find two peaks associated with the main and shadow bands in the MDC spectra (panel d). The inset illustrates how these twin peaks are produced by shifting the inner diamond main band by the $\mathbf{q}_N$ of Fig. 4.9c. It is somewhat surprising that these shadow bands only seems to appear around 450meV and are hard to resolve elsewhere. One possibility is that this region in binding energy is near a van Hove singularity and is causing an overall increase in the electronic density of states, the result of which makes the otherwise difficult to observe shadow band structure visible. But the larger conclusion is still confirmed: CDW formation via $\mathbf{q}_1$ is induced by a Fermi surface nesting instability, which leads to the opening of a CDW gap along the k_F where the majority of the contour is gapped on the order of 50meV measured from the leading edge. The fact that this gap persists over the entire Fermi surface is consistent with bulk measurements suggesting its semiconducting properties[101,85]. Additionally, the strong increase in band intensity we see near the Γ point for this constant energy cut (Fig. 4.10c) and even more so in the Γ-M and Γ-X slices of Figs. 4.6 and 4.7 overpowers the weaker low energy bands which the CDW actually gaps. This might be responsible for the fact that earlier tunneling reports of a much a much larger CDW gap (e.g. $\Delta = 0.45$eV[102]).

In contrast, it is hard to find any strong ARPES signature of the second CDW order $\mathbf{q_2}$[85]. Specifically, we could not identify any Fermi surface band structure which could be nested by this wavevector. A basic model is provided by Fig. 4.11 showing the relative ability of the FS to be nested by $\mathbf{q}_1$ but not $\mathbf{q}_2$. Also, the complex band structure of Fig. 4.5 doesn't appear to be explained by $\mathbf{q}_2$ creating an ordered state of some kind either. In fact, throughout our analysis, no wavevector could explain these patterns. Thus, as proposed in Section 4.2, this $\mathbf{q}_2$ likely corresponds to a ordered-defect in the crystal's square chalcogenide planes related to imperfect stoichiometry. The superposition of mirror symmetric superstructure domains explains the symmetry of TEM results. Yet at the surface, only the superstructure of a single Te plane is observed which breaks mirror symmetry, dominates the LEED pattern, and causes surface states reflecting this broken symmetry as seen in our ARPES data. We also speculate that defects mainly affect high energy states by trapping charges, and not the states near μ. One might ask in the LEED image of Fig. 4.4, why we see no evidence of a $2\times2\times1$ superstructure which would be consistent with our $\mathbf{q}_{CDW}$. The comparative weakness of the shadow bands in Fig. 4.10c-d suggests that the modulation in electron density is very small and would explain its absence in our LEED which only discerns total electron density.

4.4 Discussion

With these results in hand, we can ask the question, what could this work tell us about CDW phenomena in the tellurides. Our attention initially turns to the idea of layer dependence which plays an important role in the high temperature superconducting cuprates.

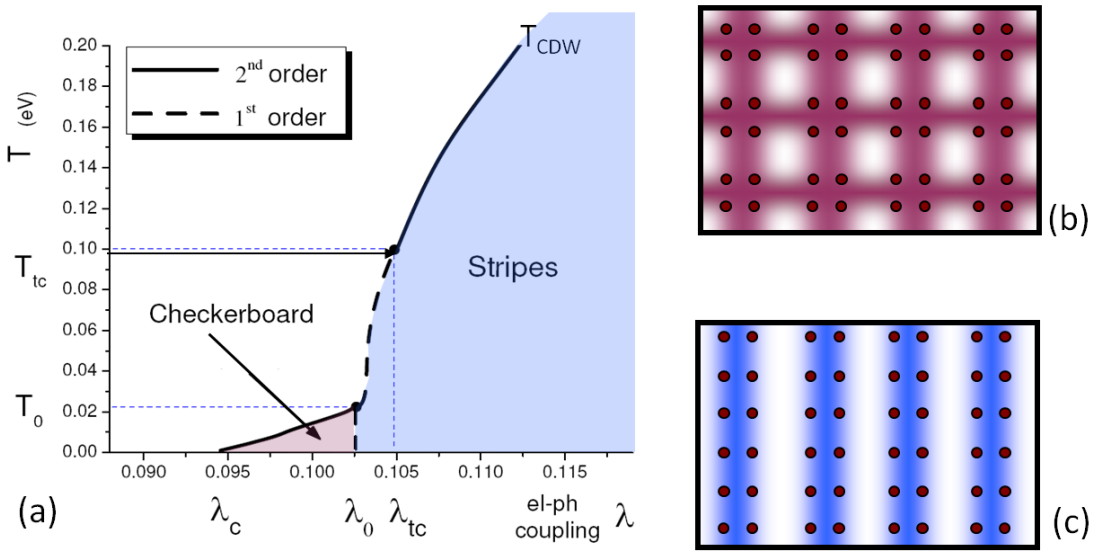

Figure 4.12. (a) Phase diagram of the tellurides from Ref.[103] showing the potential density wave phases which could occur with respect to temperature and coupling: (b) Checkerboard phase and (c) Stripe phase.

Comparing between the CDW phase observed in single layer $LaTe_2$ and double layer RTe_3, we come to a few important observations: First, this study suggests that the Fermi surface driven nature of the $\mathbf{q}_{CDW}$ does not change between double and single layer compounds, although the Fermi surface nesting in $LaTe_2$ appears more perfect than in tritellurides[8,84]. Second, the CDW gap is several times smaller that of tritellurides[8,84]. Finally, recent theory on the rare earth tellurides suggests two possible ordered phases: a stripe phase and a checkerboard phase[103] as illustrated in Fig. 4.12. Here we see that as electron-phonon coupling, λ, decreases, one could enter into a regime where basically 1D stripes associated with the CDW physics could give way into a 2D coexistence of CDW orders forming the checkerboard pattern. Comparing this with our experimental findings, the single layered compounds might fall closer to the CDW checkerboard phase than RTe_3 systems. It also seems possible that if CDW interaction is reduced, e.g. by applying pressure[77], the checkerboard pattern may emerge. Now, ARPES would be unable to distinguish between these two phases given the reality of crystalline domains which, considering the ARPES spot size, would always appear to have ordering in both orthogonal directions. Still, with the advent of nano-ARPES, perhaps this hurdle could be overcome and significantly small beam spots could reveal CDW physics (e.g. shadow bands) which are only two-fold and not four-fold symmetric.

As we conclude our work on the tellurides, our study of the CDW ordering should remain in our minds as we transition into the high temperature superconducting cuprates. Our study of the tellurides has pointed out the importance of layer dependence on the physics of this

density wave. With the existence of the well known bosonic kink[104] in cuprates which many associate with electron-lattice interaction, the physics of CDW ordering remains on the minds of those trying to understand the cuprate phase diagram, particularly the pseudopgap phase at low doping. It is well known that the number of layers plays a crucial, yet unexplained, role in determining T_c[105] and potentially a role in the pseudogap formation temperature based on similaries between samples of similar layer number[106]. Could such a density wave ordering be at work in these systems? Could nesting of the cuprate Fermi surface be important to these materials? Could this relate to the lower T_c and T^* of single layered cuprates? (e.g. LSCO, Bi2201) Or perhaps, we have this reversed since stripe physics is known to exist in single layer compounds like LSCO at 1/8 hole doping while double layer compounds like Bi2212 are believed to have checkerboard patterns from STM studies[83]. So, with the knowledge of CDW ordering as well as background in the novel magnetic orderings we have found in the iron arsenides of Chapter 3, our attention turns to the big game in condensed matter physics, the superconducting cuprates.

Chapter 5

Band Structure of Lanthanide Substituted Bi2201

5.1 Introduction

As described in Section 1.6, the high temperature superconducting cuprates represent a significant challenge for theory and remain, arguably, the most active single area of condensed matter research over the last two decades. Part of the challenge is explaining the cuprate phase diagram as seen in Fig. 1.3 and reproduced in Fig.5.1. Of particular interest is the mysterious pseudogap phase seen at low hole dopings. Although there are numerous superconducting cuprate systems that are the subject of active study by techniques such as ARPES and each has its unique quirks (e.g. stripe formation killing superconductivity in LSCO at 1/8 doping), essentially they are all sandwiches made up of Cu-O octahedral forming square planes (bread) separated by different kinds of meat. The number of Cu-O planes is curiously related to T_c with a monotonic increase with layer number[105], though peaking with the trilayer compounds (i.e. $Bi_2Sr_2Ca_2Cu_3O_{10+\delta}$ - Bi2223) and then consistently decreasing for materials with further increasing layer number. This curious parameter formed part of the motivation for our work on the rare earth tellurides in Chapter 4. But the primary motivation for our work in this chapter comes from two sources: Understanding the nature of the pseudogap phase in the midst of the current debates about its connection to superconductivity (see Section 1.6), and the potential role the lattice plays in the origin of self-energy contributions to the low energy electronic structure. In order to understand the work done both here and in Chapter 6, we need to use what we have already begun

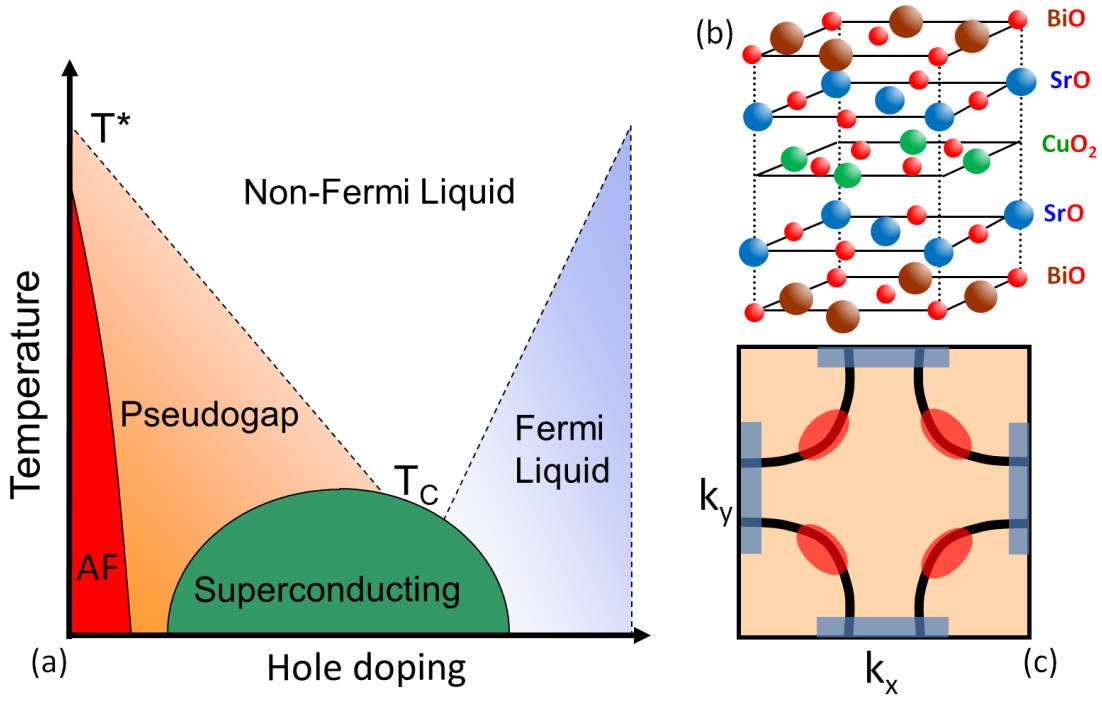

Figure 5.1. (a) The hole doped cuprate phase diagram illustrating the critical T^* and T_c of the pseudogap and superconducting phases, respectively. (b) General cuprate structure of the single layered Bi2201 cuprate. (c) The Fermi surface we will be exploring. Ovals indicate the "nodal" regions while the rectangles indicate the antinodal regions near the Brillouin zone edge.

explaining in Sections 2.3 and 2.4, and look at the specific case of the cuprates and bosonic phenomena as contributions to the self-energy, Σ, seen by ARPES.

We have already introduced the idea of how the electronic states can be coupled to by bosonic phenomena (as opposed to simply electron-electron interactions) in Section 1.4. Of particular interest in the study of superconductors, if only for historical reasons, is the role of electron-phonon coupling and whether it is significant since, as explained in Section 1.5, it plays such a critical role in conventional BCS superconductivity. However, the BCS model seems insufficient for the superconducting cuprates as well as the superconducting iron pnictides. Still, with our attention now turned to the cuprates, we will explore the question of electron-phonon (or electron-lattice) coupling once again. In doing so, we will discover that, although mysterious, the lattice continues to matter in these novel materials.

Stepping back for a moment, one can see the use of ARPES to study electron-phonon coupling as the union of two different approaches within the study of phonons. First, and the most direct, is the mapping of phonon dispersions using inelastic scattering techniques such as inelastic neutron and X-ray scattering (INS and IXS). Understanding phonons with a momentum space perspective is, as explored in Chapter 1, the most intuitive manner for

understanding phonon modes within a lattice. But, if we are seeking information about how electronic states interact with phonons, then the approach is, at best, an indirect technique. Historically important to the confirmation of the BCS theory, tunneling measurements done on conventional superconductors (e.g. Pb[107]) have provided insight into how electron-phonon coupling directly affects electronic states near the Fermi energy E_F. Besides the confirmation of an isotropic gap, there were unexpected features observed in the spectra which were later explained within a strong coupling form of the broader Migdal-Eliashberg theory[108]. As important as these tunneling measurements are, to be able to have both direct information of how phonon modes affect electronic states yet to also see this from within a momentum space perspective (tunneling is fundamentally a real-space spectroscopy), requires a different approach, an approach that ARPES is well-suited to offer.

Thus, remembering back to our discussion of self-energy analysis in Section 2.4, we can focus directly on the physics which results in the ARPES kink in the cuprates. Turning back to Eqs. 2.56 and 2.60, we can see they demonstrate that a sudden increase in the real part of $\Sigma(\mathbf{k},\omega)$ at a particular energy, ω, would lead to a deviation of the measured peak from the single electron bare band structure, $\epsilon(\mathbf{k})$, at that energy scale. The result is seen in Fig. 5.2 which shows superconducting phase data taken on the well-studied cuprate Bi2212 at its optimal doping (T_c=92K). The two ARPES cuts are taken for states both at (panels a-c) and off (panels d-f) the nodal ($\Delta = 0$) point. The different visualization methods that are used for each cut are designed to bring out some key characteristics of the ARPES kink phenomenon would be followed by a more detailed, quantitative approach involving curve fittings. As labeled in the figure caption, the "MDC map" allows us to track the MDC dispersion and width. This is similarly true for EDCs in the "EDC map." The color scaling is chosen to give the peak maximum and half maximum distinct colors, red and blue respectively.

From these maps, one can observe the following features: 1) The anisotropic d-wave nature of the superconducting gap is immediately apparent in the MDC "backbending" observed in panel (e) near E_F within the gap energy scale. This effect is related to the near vertical band structure we observed within the CDW gap (Fig. 4.3b), where the absence of a band is replaced with a waterfall of remaining spectral weight within the gap. This is confirmed when we find that evidence of this gap and the associated backbending disappears for the nodal cut (panels a-c). 2) An abrupt deviation in the electron dispersion can be seen around 70meV below E_F (large black arrow) for both nodal and off-nodal cuts. In both cases, this corresponds to slower electron dispersion (larger quasiparticle effective mass, m*) at lower energy while there is faster dispersion (smaller quasiparticle effective mass) at higher energies above the 70meV energy scale. 3) If we focus particularly on the off-nodal cut, we can see evidence, even in the raw map, of an intensity decrease forming a local minimum at the 70meV energy scale. This unusual lineshape, further enhanced by the EDC map (panel f), is known as a *peak-dip-hump*. This lineshape could be associated with the presence of self-energy effects due to the coupling of electrons with a bosonic mode leading to a redistribution of the spectral weight in the EDC spectra. (See the end of Section 2.3 and the start of Section 2.4 for details about how self-energy is connected to the presence of

a coherent and incoherent peak.) 4) From our understanding of Fermi liquid theory, both Eq. 1.10 and similarly (written as self-energy) Eq. 2.50 lead us to expect quasiparticles within this paradigm to become sharper (i.e. longer living) as one approaches E_F. Therefore, it is significant that the kink energy scale also defines a sudden change in the sharpness of the peaks. From the panels and, in particular, the EDC maps, we can see abrupt changes in the linewidths as one approaches states above and below the kink energy scale. So, to bring everything together, we can think about the ARPES kink as indicating an energy crossover which separates sharp, slowly dispersing, coherent states near E_F from broader, quickly dispersing incoherent states at higher energy.

Within our ARPES analysis, we will divide our work between states near the $\Delta = 0$ nodal region of the cuprate electronic structure and those far from it. This is more than just an organizational convenience as outside work suggests a significant difference between states near the node and those at the antinode at the Brillouin zone edge[110,111,112,113,114,115]. From an ARPES point of view, the essential foundation for discussions regarding the self-energy of the nodal quasiparticle states is the kink, already obvious in the spectra of Fig. 5.2 and initially discovered the double layered cuprate Bi2212[116]. On the heels of this discovery and the resulting debate, a systematic study regarding the origin of this kink discovered the feature's remarkable ubiquity at the nodal point at essentially the same energy, ~ 70 meV[104]. From this work, one finds evidence for a trend between doping and the strength (coupling constant, λ) of the mode with an enhancement of $\Sigma(\mathbf{k}, \omega)$ as one tends towards underdoping. Given the complex pseudogap physics in the underdoped region of the phase diagram, this may have particular significance.

Additionally important is the continued existence of this kink below *and* above the superconducting T_c (panel d-e), which already casts some doubt on scenarios which associate this effect with the superconducting gap opening and particularly scenarios involving magnetic modes[117,118,119,120,121]. Of course, if this bosonic coupling is related to phonons, understanding the identity of the phonon mode is key. When photoemission data is compared with the phonon energy at $q = (\pi, 0)$ (thick red arrow in panel a) and its dispersion (shaded area) as determined by inelastic neutron scattering[122] it was proposed[104] that the nodal kink results from coupling between quasiparticles and the zone boundary in-plane oxygen-stretching longitudinal optical (LO) phonon. It's been noted, however, that although this is the highest phonon mode contributing to the kink, quasiparticles are also coupled to other low energy phonon modes[123]. Furthermore, one finds a drop in the quasiparticle width (Fig. 5.3b-c) below the kink energy and the existence of a well-defined peak-dip-hump in the EDCs as mentioned in the discussion of Fig. 5.2. This latter phenomenon persists up to temperatures much higher than T_c[124]. All of this provides support that, at least for these nodal states, the lattice and phonon interactions are indeed important to the physics of the cuprates.

In light of this, it is natural to ask about states beyond the nodal point, such as those near the antinodal point (Cu-O bond direction). Here, many-body effects had been suspected for some time from earlier ARPES studies of the cuprates where evidence of the peak-dip-hump lineshape was reported[126,127]. Controversy has existed though because of the role of bilayer band splitting may have on the observed spectra in the double layered Bi2212

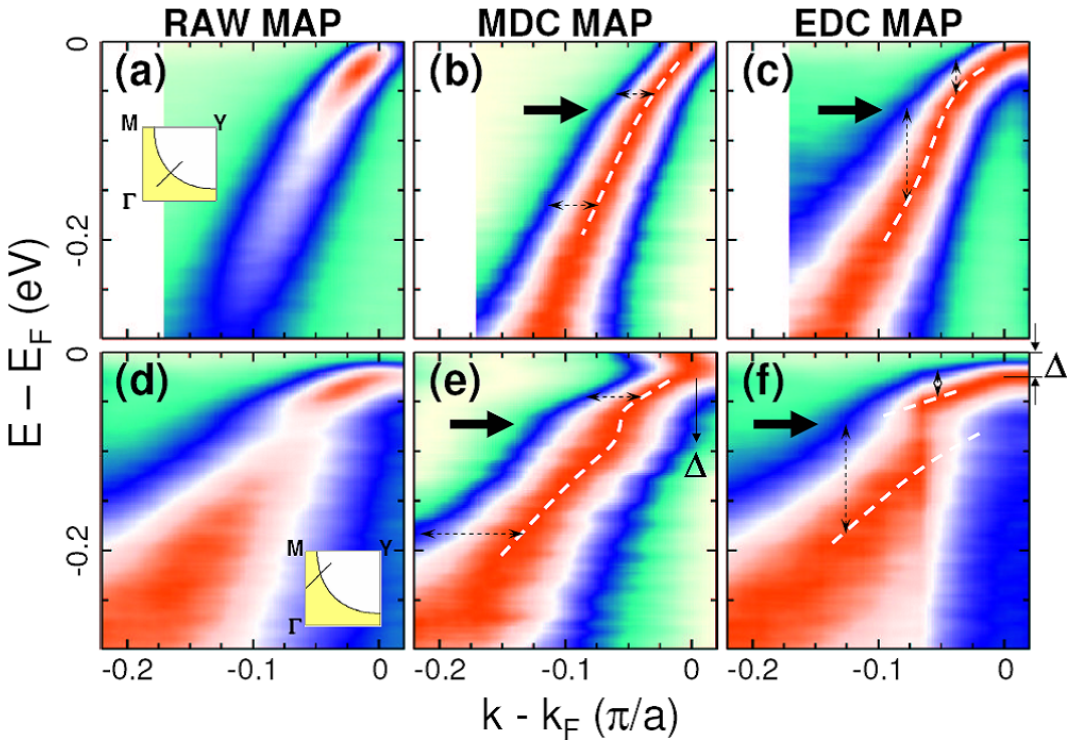

Figure 5.2. (a-c) ARPES data taken at 25 K on optimally doped Bi2212 superconductor (T_c = 92K), for a cut along the ΓY direction through the nodal point in momentum space (indicated in panel a inset). (d-f) The same sample and orientation, but taken nearer the Brillouin zone (BZ) edge (or antinodal point) in momentum space (indicated in panel d inset). (a,d) Raw ARPES data taken with a color scale where intensity increases from pale yellow to green to blue to white to red. Here, blue (white) corresponds to 1/2 (3/4) of the maximum intensity. (b,e) Same data but as an "MDC map," where each MDC has been normalized so that its maximum and minimum intensities are 1 and 0, respectively. (c,f) Same data but now each EDC has been appropriately normalized to create an "EDC map." Thick black arrows indicate the energy of the bosonic mode while the Δ is the superconducting gap. Energy resolution used here is ∼ 15 meV. Figure from Ref.[109]

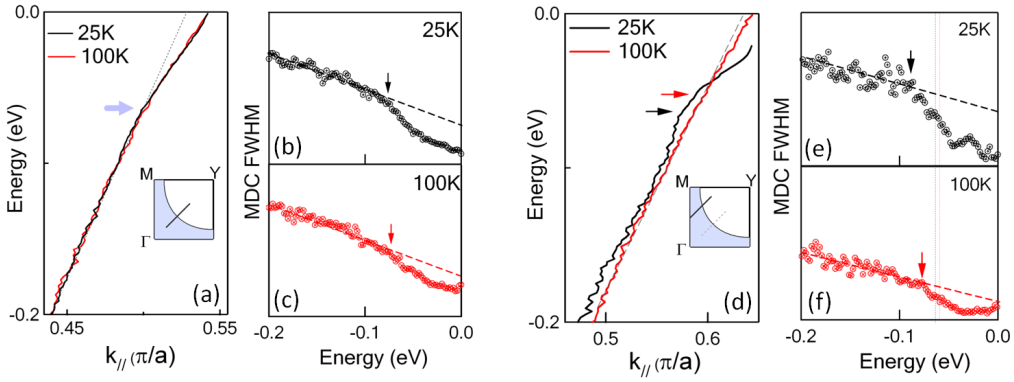

Figure 5.3. ARPES MDC dispersion data taken optimally doped $Bi_2Sr_2CaCu_2O_{8+\delta}$ (T_c = 92 K) as discussed in Ref.[125]. Nodal point data (see inset) comparing (a) dispersion and (b-c) MDC full width half max showing little change in the energy of the ARPES kink with T_c. As discussed in Section 2.4The MDC FWHM is related to the $\mathrm{Im}\Sigma(\mathbf{k},\omega)$. (d-f) Same analysis for band structure closer to the antinodal point.

compounds. This splitting of the band is due to interactions between the different Cu-O layers in the multi-layer compounds and is particularly pronounced as one moves towards the antinodal point in the Brillouin zone. In fact, this is one reason for our focus on the single layered compounds within this thesis which lack this. Still, this peak-dip-hump lineshape, indicative of a bosonic mode, was initially interpreted in terms of a magnetic phenomenon which had been observed in YBCO and Bi2212 by inelastic neutron scattering[128,129,130]. As the community got a better handle on the bilayer splitting[131,132,133], a low energy kink of approximately 40meV near the antinodal region was reported for Bi2212[134,135,136].

Yet here the controversy continues to fester. Some have argued that this kink disappears above T_c and, along with the decrease of its strength as one moves along k_F away from the antinodal region, the interpretation has been that of coupling to collective magnetic excitations[134,136,135]. However other more recent work[137,125] has reported that the near antinode kink does indeed persists above T_c, as seen in panels d-f of Fig. 5.3, but with a shift towards higher energy, from 40meV to 70meV, upon going below T_c. This shift could simply be caused by the opening of the superconducting gap (∼30meV at the antinodal point.) This has led people to wonder if the antinodal kink is also better understood in terms of electron-phonon coupling (e.g. the B_{1g} phonon mode[137] which has the right energy and momentum.) The Marginal Fermi Liquid theory alluded to in our discussion of self-energy (Eq. 2.51) gives a partial solution, invoking spin fluctuations in the normal phase and is consistent with the measured dispersions. But it doesn't currently explain any of the drops in the MDC linewidths.

A final significant way in which one can see that the lattice must play an important role in the cuprates is the via the isotope effect. Previously, this physical observation around 1950 was significant in how it focused attention towards phonons in conventional BCS su-

perconductors. ARPES has been used to probe the isotope effect in other samples such as the surface state on tungsten induced by H chemisorption[138]. This work was consistent with the predictions of the strong coupling form of the aforementioned Migdal-Eliashberg theory. But the isotope effect seen in the double layered cuprate Bi2212 (using ^{16}O and ^{18}O) presents more complexities. Figures 5.4 and 5.5 summarize the critical results of this work.

First, one notices the effect isotope substitution has on the bosonic kink binding energy. Panels a-b are MDC maps, normalized in a manner like those in Fig. 5.2. They represent data taken at the nodal point in the Γ-Y direction. Doing an MDC fitting analysis, panel c shows the electronic dispersion for both isotopes plus a re-exchanged sample, $^{16}O_{Re-exch}$ (a studied ^{18}O sample with ^{16}O re-exchanged back into the lattice.) There is a subtle shift in the kink energy of approximately 5meV. One can additionally quantify the kink by estimating the bare single electron dispersion (using a linear approximation) as described in Section 2.4 and extracting the real part of the electron self-energy, $\mathrm{Re}\Sigma(\mathbf{k},\omega)$, (see Eq. 2.56.) The location of the peak in the $\mathrm{Re}\Sigma(\mathbf{k},\omega)$ corresponds to the kink energy, and there is similarly a shift in this peak with isotope change.

Just as before, we have started with the nodal point but what about moving beyond towards the antinodal point? This is illustrated in Fig. 5.5 which provides the same type of MDC dispersions for slices aligned parallel to Γ-Y moving outward from the nodal point towards the antinode, both above and below T_c. Just as in Fig. 5.4, the kink energy shows a subtle shift of approximately 5meV for all momentum cuts. But from comparing panel a with b, it appears that the magnitude of the isotope effect may be, for all curves, diminished above T_c. Additionally, the intensity of the effect remains relatively weak near the node while comparatively more pronounced near the antinode. Plotting this isotope effect shift with respect to the isotope averaged superconducting gap, results in a linear relationship plotted in the inset of panel a. Finally, there appears to be a sign change between the two dispersions as we transition from the node towards the antinode, which also appears both above and below T_c. Although all of these effects underscore the larger ways in which electron-phonon physics must be important to the cuprates, this final point is additionally significant and we will return to it later since this sign change will motivate particular aspects of our research.

There is one other area of ARPES research that argues for the importance of electron-lattice interactions which we will mention since it plays an important role in the data presented particularly in Chapter 6. Already motivated by evidence of significant electron-phonon coupling in the cuprates, a natural direction to explore would be to more carefully map the phonon dispersion in addition to the electronic dispersion. This can reveal interesting physics such as when a phonon wavevector matches $2k_F$, where k_F is the Fermi momentum, leading to the well-known Kohn anomaly discussed in Section 1.4. Also, nesting of the Fermi surface in systems with particularly strong electron-lattice coupling can drive the formation of charge density waves as we have observed in the tellurides (Chapter 4). Thus, comparing data that directly probes the phonon mode dispersions within the Cu-O plane with the observations of the ARPES kink would potentially be significant.

The result of this work is discussed in better detail by J. Graf et al.[140] and we will only briefly illustrate some the significant points. IXS work was done on the single lay-

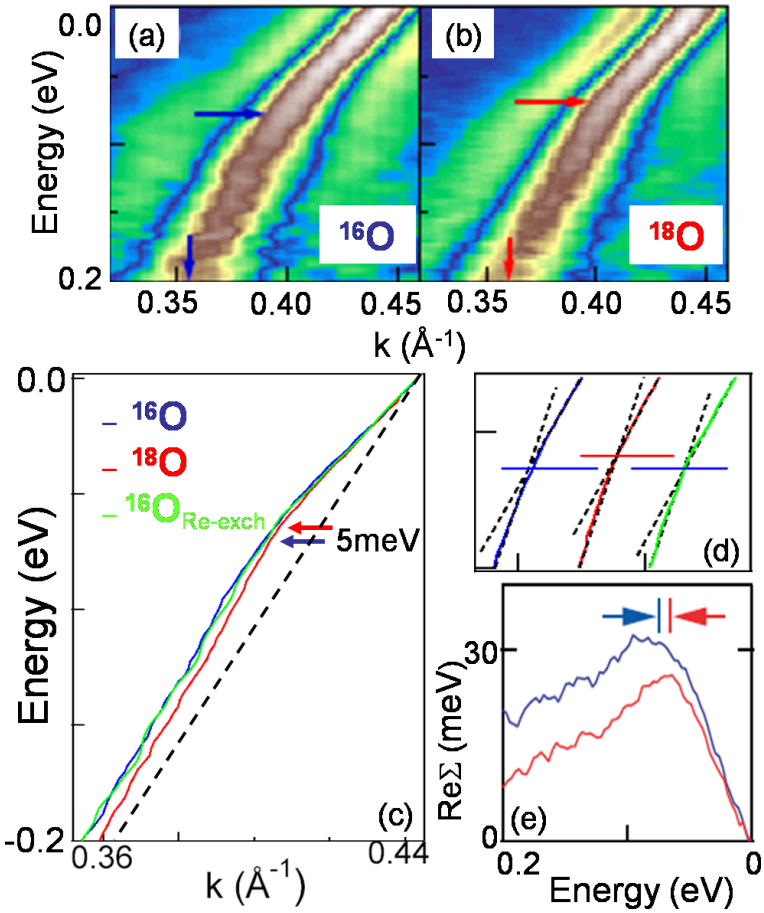

Figure 5.4. (a-b) MDC maps of the nodal point electronic states for cuts along the Γ-Y direction. (a) The ^{16}O sample and (b) the ^{18}O substituted sample with the horizontal arrows indicating the shift in ARPES kink energy with oxygen isotope. (c) The MDC dispersions determined from the ^{16}O, ^{18}O as well as a re-substituted ^{16}O samples for the cuts in (a-b). (d) Cartoon illustration of the kink shift in (c). (e) Real part of the electron self-energy, $\mathrm{Re}\Sigma(\mathbf{k},\omega)$, determined from the MDC dispersion using a linear approximation for the single electron bare band. As before, the ARPES kink position, defined by the peak in $\mathrm{Re}\Sigma(\mathbf{k},\omega)$, is shifted to higher energy as indicated by the arrows. Figure from Ref.[109]

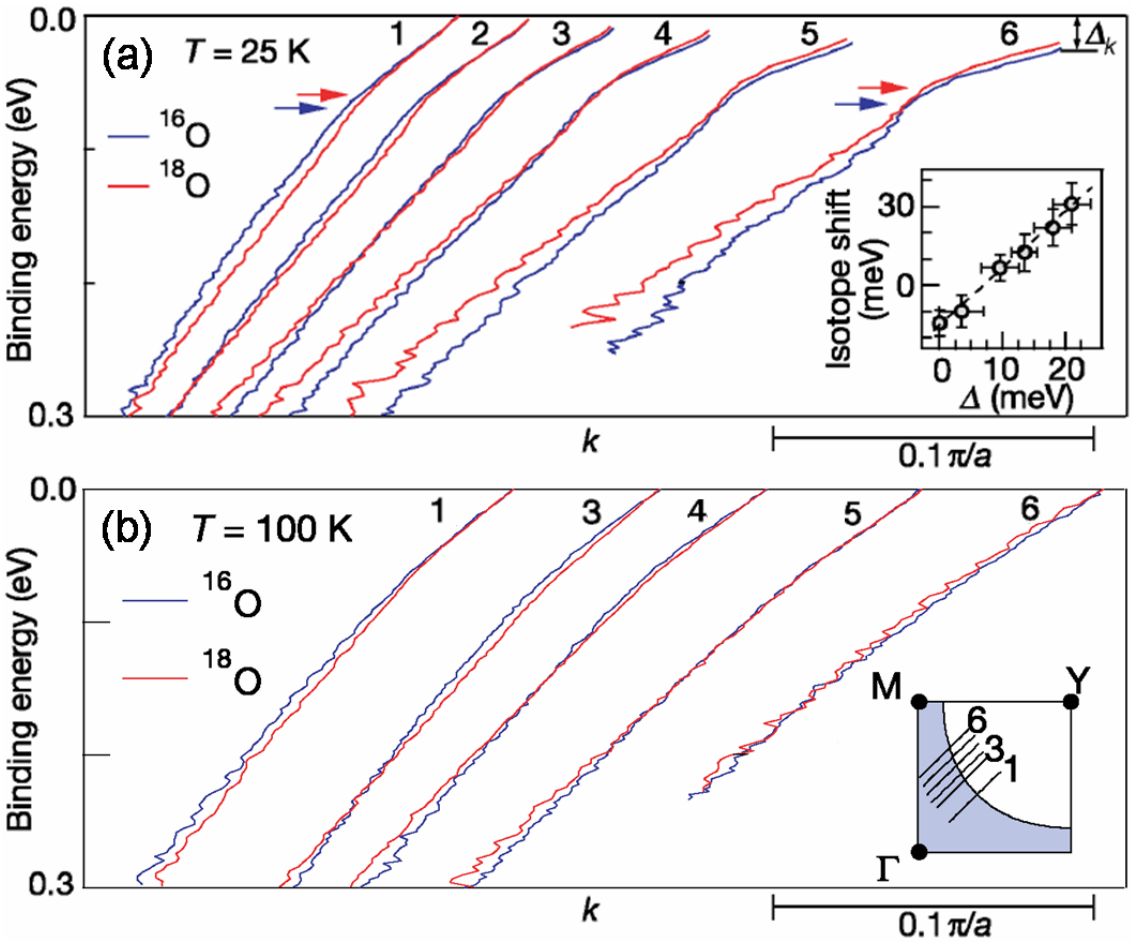

Figure 5.5. MDC dispersions from cuts parallel to Γ-Y taken off node towards the antinodal point. (a) Data taken in the superconducting phase (T = 25K). The inset shows the isotope energy shift vs the isotope-averaged superconducting gap, Δ. The isotope shift is measured at the momentum value where the isotope-averaged binding energy is 220 meV. The apparent linear correlation indicated by the dashed line is independent of the binding energy used. (b) MDC dispersions from the same cuts measured above T_c (T = 100 K). The inset illustrates the location of the cuts. Figures from Ref.[139].

ered $Bi_2Sr_{1.6}La0.4Cu_2O_{6+\delta}$ (La-Bi2201) which has never shown any evidence of magnetic resonance modes. This simplifies the comparison between ARPES kink and scattering by removing another potentially additional bosonic mode. The focus was on resolving the dispersion of Cu-O bond stretching (BS) mode. Focusing on these higher energy longitudinal optical modes (as described in Section 1.4), one can map out their dispersion across the Brillouin zone from the center towards the zone face.

When you compare these results with ARPES studies focusing on the kink in La-Bi2201, there is a suggestive correlation as Fig. 5.6 attempts to display. Panel a shows MDC analysis of the electronic dispersions taken at the nodal point (curve 1) and away from the node (curves 2 and 3) as indicated by the slices along the Fermi surface in panel b. We see the well established higher energy kink appearing here at 63±5meV for the nodal cut. As one moves away from the node, this kink abruptly disappears between curves 2 and 3, replaced with only a lower energy kink of 35meV. As we will explore in more depth in Chapter 6, we believe it is significant that this shift occurs near the tips of the "Fermi Arc," region of the Fermi surface (see Section 1.6) where the electronic structure becomes partially ungapped at temperatures above the superconducting T_c but below the pseudogap temperature, T^* [26]. It is this transition point in momentum space between the arc and where the gap opens that curves 2 and 3 straddle. However, it is worth noting that the data was taken in the superconducting phase, so this is a more subtle point.

Comparing this with the IXS data as seen in the inset of panel b, one finds that the 63meV kink has an energy that corresponds well to the energy associated with the softened BS mode. Even more interesting, as the grey shaded region in panel b illustrates, the region where the 63meV kink is observed corresponds to a section of the Fermi surface nestable by wavevectors within the softened part of the phonon mode dispersion from IXS. Related to this, the sudden disappearance of this kink between curves 2 and 3 corresponds to the stiffening (higher energy) of the BS mode as seen in the inset when $\xi < 0.22$. Just like in the case of CDW physics, this ability to nest the Fermi surface topology with a phonon mode, once again underscores the importance of electron-phonon interactions to the physics of the superconducting cuprates.

From this survey, we hope to have both demonstrated that there is good reason to believe electron-lattice interactions play a significant, though unclear, role in the cuprates, as well as plant some seeds for work we will now present. Indeed, further analysis on the isotope effect alone suggests that not only is electron-phonon physics important, the prevailing models which could incorporate it (Migdal-Eliashberg theory) are insufficient, needing to incorporate electron-phonon coupling with a strength beyond the traditional paradigm of the theory [142]. But how do we marry this idea to our quest for a better understanding of the cuprate phase diagram? To accomplish this, we should look to an additional trend in the field of superconducting cuprates.

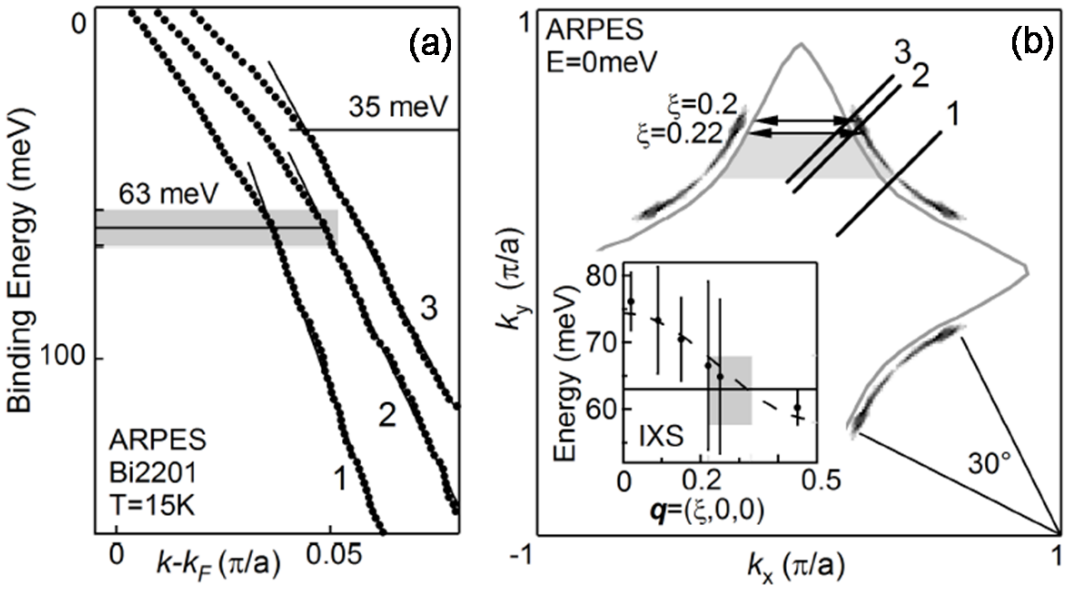

Figure 5.6. (a) MDC dispersions measured for three different momentum cuts along the Γ-Y orientation with cut 1 at the nodal point while cuts 2 and 3 are further toward the Brillouin zone boundary, near to the edge of the pseudogap phase Fermi arcs[141]. (b) Experimentally determined Fermi surface with the cuts from (a) indicated. The solid line indicates a constant energy contour at the kink energy, 63meV, while the shadow area indicates the region where the nodal kink appears bounded by the indicated nesting wavevectors. The inset shows the IXS dispersion and peak FWHM (seen as error bars) of the BS mode. Note: The apparent Fermi arcs seen are due to the experimental resolution. Figures can be found in Ref.[140].

5.2 Lanthanide Substituted Bi2201

It is well known that the application of external pressure can affect the superconducting T_c, sometimes in unexpected ways[143]. There has been growing independent work from a variety of experimental probes[144,145,146] arguing that the role of the lattice is not simply a source of self-energy effects on the near-E_F low energy electronic states but potentially an additional axis within the hole-doped phase diagram. In particular, it is the effect of lattice strain, both external and internal (via chemical pressure - e.g. Ref.[147]), which offers us access to this new axis of the cuprate phase diagram and seeing its effect on the superconducting dome. Work using external pressure has indicated critical pressures where the T_c appears to saturate for a range of cuprate hole dopings[144] as well as being coupled to other physical quantities suggesting a significant new critical point along this axis[145]. Very recent work on the trilayer cuprate Bi2223 has even suggested multiple peaks in the T_c vs pressure diagram, arguing that pressure may reveal a crossover from a competing order to superconductivity in the CuO_2 planes[143]. This result is additionally significant in light of the still mysterious nature of the pseudogap phase. Using chemical pressure, work has suggested that combining doping with strain on the Cu-O layer also reveals that the true quantum critical point is, indeed, shifted along the strain axis[146]. Furthermore, effects related to lattice disorder, particularly in the Sr-O blocks nearest the Cu-O planes, may also have a dramatic effect on the formation of the superconducting phase within the cuprates[148]. So, this represents the marriage we are looking for, to both explore the effect of electron-lattice physics as well as the physics of the larger cuprate phase diagram. But to complete the courtship, we need the right system to study.

When we consider the experimental considerations involved in an ARPES study, the best method for introducing strain into the lattice is via chemical pressure. Additionally, when we look in the literature, there is an ideal candidate. Lanthanide substituted single-layered $Bi_2Sr_{1.6}Ln_{0.4}CuO_6$ (Ln = substituted lanthanide) has been synthesized for a variety of different lanthanides with differing atomic radii and allow us to access the strain axis of the cuprate phase diagram in a tunable way[106]. First, the use of single-layered cuprates has many advantages for an ARPES study: 1) Like other bismuth superconducting cuprates, the sample surfaces are known to be of good quality for use in ARPES experiments (unlike more challenging single layered cuprates like LSCO or LBCO.) 2) As pointed out previously, these samples have shown no evidence of magnetic resonance modes. This will hopefully simplify our analysis so we can focus our attention on the electron-phonon aspect of the physics affected by strain and not other bosonic modes (i.e. magnons.) 3) Also as mentioned in the context of the antinodal peak-dip-hump, the single layer cuprates lack bilayer splitting of their bands, which has presented challenges to the analysis of other cuprates (e.g. Bi2212). 4) Since our interest is in part driven by the pseudogap phase, the phase diagram of the single-layered cuprates differs from their double-layered brethren when it comes to this. Given an optimally doped sample, the pseudogap temperature, T^* is basically the same as T_c in the double-layered Bi2212. But in the single-layered compound, T^* is still significantly above T_c. This allows one to, in principle, access all three regions (superconducting, pseudogap, and 'normal phase') with an optimally doped Bi2201 sample. Additionally, there is already

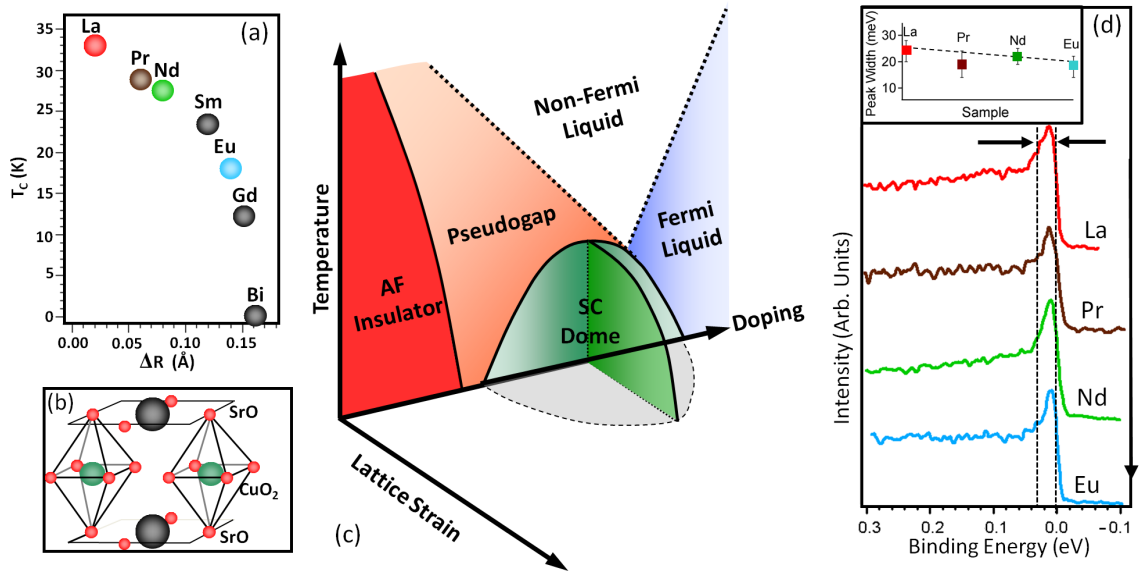

Figure 5.7. (a) Superconducting T_c for optimally doped $Bi_2Sr_{1.6}Ln0.4Cu_2O_6$ for a series of substituted Lanthanides (Ln) with increasing atomic radius mismatch, $\Delta R = |R_{Sr} - R_{Ln}|$. See Ref.[106]. (b) Cartoon illustrating the location of the substituted Lanthanide right above the Cu-O plane. (c) Proposed strain phase diagrams d) Nodal point EDCs illustrating the quasiparticle peak for samples with increasing strain, colored in (a), from La to Eu. Inset quantifies the half-width half-max of the peaks for these samples.

reason to believe that the strain could be leading to stronger pseudogap phases in these materials[149 150].

All the of these single crystal samples were grown using the traveling solvent floating-zone technique which is described in more detail by Eisaki et al.[106]. The results are optimal doping samples, which simplify the analysis by making the focus solely on the tuning parameter of strain. As Fig. 5.7 illustrates, as we substitute the lanthanide elements for the strontium in the site just above the critical Cu-O plane (panel b), there is a monotonic decrease in the measured T_c of the samples (panel a). The critical variable to quantify this T_c-competing strain is the atomic radius mismatch, ΔR, as seen on the abscissa of panel a. This value is determined by the difference between the strontium and the substituted lanthanide atomic radii, $|R_{Sr} - R_{Ln}|$. It will be this value which we associate with "strain" within the lattice in a quantitative way.

Our synchrotron ARPES data were taken at Beamline 10.0.1 at the Advanced Light Source of the Lawrence Berkeley National Laboratory as well as Beamline 5.4 at the Stanford Synchrotron Radiation Laboratory, using a Scienta R4000 analyzer. We found that Beamline 5.4 did produce consistently better ARPES results and nearly all the data presented in this chapter came from this beamline. Reasons for this could be higher energy resolution, matrix elements due to the polarization of the light, or the beamline's optimization at lower photon

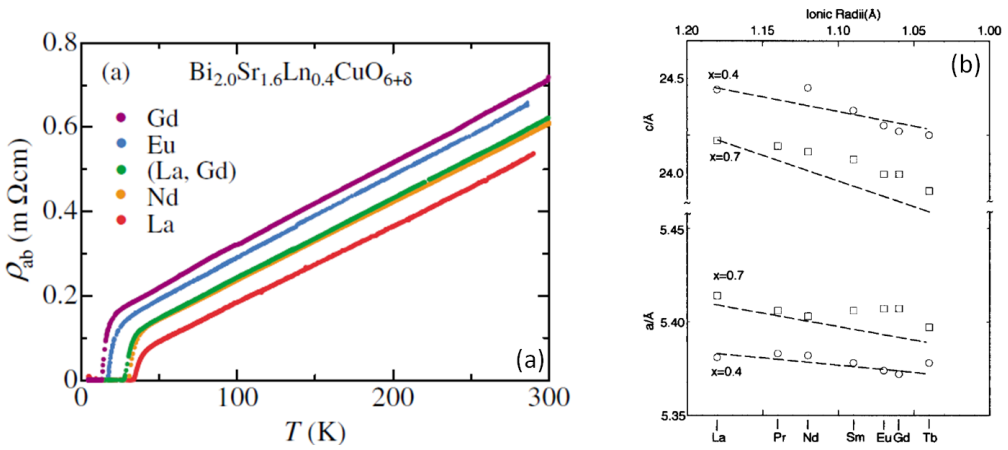

Figure 5.8. (a) Transport measurements by Ref.[151] on the Ln-Bi2201 systems. (b) X-ray diffraction measurements of the lattice constants of these systems. Figure from Ref.[152]

energies. A total energy resolution of <15meV was achieved for data taken on the strained samples, with an angular resolution better than 0.35° and fresh sample surfaces were prepared by cleaving the sample *in situ* at a base pressure $<5x10^{-11}$ Torr at low temperatures.

With the remarkably high quality of ARPES data that one can get from the double-layered Bi2212 compound, in many respects, the single layered compound has received comparatively less attention. Combined with the relatively recent appearance of the lanthanide substituted version of these compounds, there is limited work, particularly in the ARPES field, on these strained compounds. Thermodynamic and structural work has been done including transport[151] (Fig. 5.8a), thermopower[150], and lattice constants[152] (see Fig. 5.8b). Initial ARPES work has been done on some compounds by a few groups[153 150 149]. These results have generally suggested a decoupling of the superconducting T_c and the antinodal gap and have been interpreted as consistent with the "two gap" models described in Section 1.6. They find evidence of an increased antinodal gap and a depressed superconducting gap near the nodal point. This is also supported by scanning tunneling microscopy (STM)[154] on these samples. Addionally, estimates have been made of the T^* for a few compounds[150] leading to the previously suggested correlation.

Throughout our work, we have been able to take ARPES data throughout the Brillouin zone on samples across the spectrum strain. This is briefly displayed in Fig. 5.9 where near E_F images are provided for samples we have studied. This raw data leads to some immediate questions that we can begin to address right away. First, when one looks at the samples synthesized in Fig. 5.7a, there are samples missing from our spread in Fig. 5.9. For many reasons, some which remain confusing, certain samples presented significant challenges, in particular, Ln = Pr, Sm, and Gd. For Pr, we were eventually successful though the relative quality of its spectra is poorer than other compounds. The spectra we were able to take on Sm were simply too noisy to allow for any trustworthy ARPES analysis to be undertaken

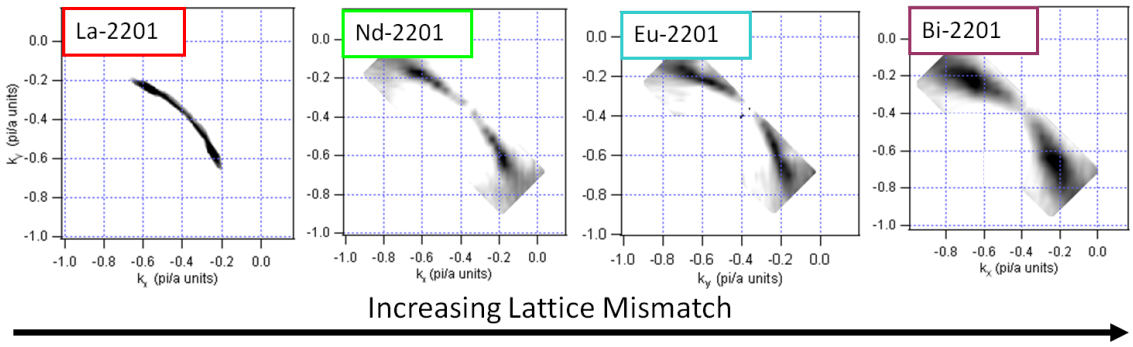

Figure 5.9. Near E_F band structure showing the ARPES Fermi surface for La, Nd, Eu, and Bi substituted Bi2201. Images have been taken with the analyzer slit in the MY geometry and symmetrized about ΓY.

(as well as being complicated by very small crystals.) Our work on Gd was also particularly frustrating given work done by other ARPES groups[149]. Despite these interesting results on that highly strained sample, we never achieved any ARPES spectra despite numerous efforts and cleaves. The reasons could range from a poor batch of samples to bad luck with ARPES worthy sample surfaces.

Nevertheless, with the samples we have been able to achieve satisfactory ARPES results on, the spectrum of radius mismatch has been covered. Although these samples do provide us with a lattice-based, tunable parameter which competes with superconductivity, one can, and should, pose the question if what we are seeing should be thought of within a lattice strain or lattice disorder paradigm. Indeed, it is quite obvious from the panels of Fig. 5.9 that the introduction of strain certainly affects the quality of the ARPES. This could be due to more irregular surfaces in samples with larger ΔR. Could disorder be widening the quasiparticle peaks as the mean free path (lifetime) of these states becomes shorter? The aforementioned work from STM suggests broadening of the coherent quasiparticle peaks with lattice mismatch. However, this represents more of an integration over the momentum space and as such, one finds general agreement between this and the data presented in Fig. 5.9.

Panel d of Fig. 5.7 provides evidence that, at least for the nodal states, the strain paradigm appears to remain valid. With increasing lattice mismatch, the width of the quasiparticle peak does not increase but, on close examination, may even be decreasing with increased strain. As an aside, this decrease in the width should be taken with a grain of salt as illustrated by the cartoon in Fig. 5.10. All other things being equal, if the result of the strain is to change the v_F, then it is possible that our EDC analysis might result in a slightly sharper peak due to resolution effects. Still, one can forgo complicated explanations and settle on the fact that within our error bars, the peakwidth remains unchanged. At this point, we should acknowledge the absence of the highly strained, non-superconducting Bi-Bi2201 (Ln=Bi so the formula would be $Bi_{2.4}Sr_{1.6}CuO_6$). It will be a reoccurring hypothesis of ours that this compound represents something fundamentally different. Despite the relatively

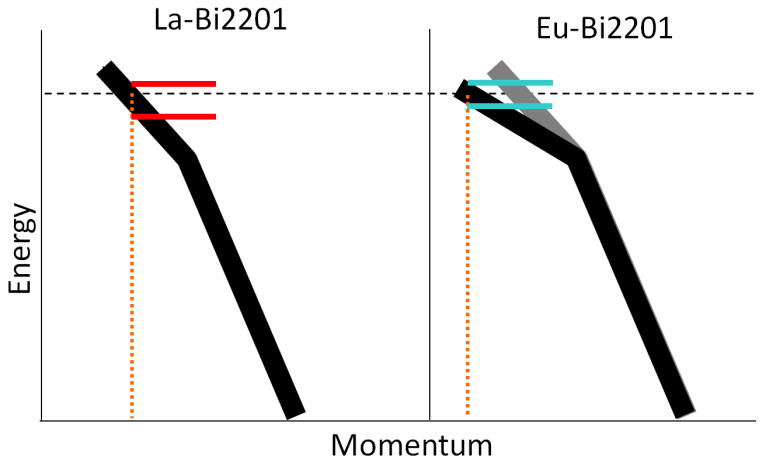

Figure 5.10. Cartoon illustrating the potential origin of the decrease in EDC width as related to a v_F change.

small difference in strain between Eu-Bi2201 and Bi-Bi2201, we have never been able to resolve a quasiparicle peak in the latter compound. So, this argument for a strain paradigm certainly fails for the Bi-Bi2201 compound from our experimental perspective. Nevertheless, for the remaining compounds, this result is significant since it has been broadly suggested within the ARPES cuprate community that observing a sharp quasiparticle peak at the nodal point is necessary for confirming that the cleaved surface can provide trustworthy ARPES results. Still, this adds reason for the division in our data between nodal states and those beyond this point. It is possible that scattering may have a greater effect on certain electron momentum states than others (i.e. nodal states). Furthermore, we will continue to return to the hypothesis that it is disorder, and not strain, that represents the primary effect that lattice mismatch has on the physics of these materials. Indeed, efforts to decouple these two effects have been undertaken in other cuprates for some time[155], and even work on these materials have led some to propose a disorder paradigm[151]. Still, bolstered by our observation at the nodal point, we will continue in our analysis focusing initially on these nodal states.

5.3 Analysis of Near Nodal States

In our introduction, the kink near the node illustrated the importance of electron-phonon coupling in the physics of the cuprate. So, we will focus again on the MDC analysis of these electronic states, but this time with tuning parameter of lanthanide substitution on the lattice. Fig. 5.11 presents our findings for substituted Ln=La, Pr, Nd, Eu. The nodal point band structure from Ln=Bi was significantly weaker (no quasiparticle peak was ever

observed) and didn't follow any obvious trend as compared to the other strained compounds. This could be a sign that Bi-Bi2201 is a fundamentally different system or that the quality of the data damages the analysis too much.

Looking at the data presented, there are two aspects of these dispersions we wish to focus on that may be significant. First, we see agreement with the earlier work on the La-Bi2201 system probed via the IXS-ARPES work discussed in Section 5.1. We can observe a kink around 55-60meV and it appears, to remain at that energy, for the most part, throughout the strain spectrum. This would suggest that the origin of this bosonic mode is generally unaffected by the substituted lanthanide. For instance, it is not greatly softened or stiffened, which would result in a shift in its binding energy. Of course, given the very real error bars associated with quantifying the binding energy of the kink given ARPES data of this quality, there is still room for a shift ($\sim \pm$10meV potentially). However, what does appears to change with strain is the electron-coupling constant, λ which is associated with the renormalization of these states. In the same manner as was done for the cuprate systems described in Section 1.4, we can estimate λ for this mode, which is plotted in panel b. We find the strength of this mode appears enhanced by the increasing strain of the lattice mismatch with a generally linear behavior. Equivalently, one can plot λ as a function of sample T_c (panel b inset) and, as one would expect, there is a negative, linear relationship between the superconducting T_c and strength of this phonon mode. A natural conclusion one may draw is that this mode is somehow connected to a phenomenon which competes with the formation of the superfluid. This is consistent with the observation that the nodal kink is unaffected by the superconducting transition.

The second thing that we observe is perhaps more peculiar and potentially revealing of the nature of the lanthanide substitution's effect on the Bi2201 compound. Although the dispersion appears linear for the La-Bi2201 at energies less than the 60meV kink all the way to E_F, the more strained compounds appear to have an additional rounding of the band structure closer to E_F, the most obvious being in the highly strained Eu-Bi2201. Initially, this just made our analysis more complicated until we decided to discriminate between the change in slope at different binding energies. This potentially strain-emergent mode appears to be around 25-30meV which could be important since this is closer to the mode energy observed near the antinodal point (as discussed in Section 5.1) from the peak-dip-hump EDC lineshape. It is also worth noting that we have observed this kink in the MDC analysis in a region of the Fermi surface that is beyond the nestable region of the IXS softened phonon mode illustrated in Fig. 5.6. This could mean that the mode seen closer to the antinodal point actually does exist near nodal point, but is significantly weaker without the effect of strain.

Naturally, to aid our analysis, we can attempt to extract the λ from this more elusive mode in a manner independent of the 60meV kink, the result of which is seen in panel c. Unlike the higher energy mode which is apparent in all strain, this lower energy feature appears to "turn on" at the node only as strain is introduced, leading to a broadly linear relationship similar to the higher energy mode. Having observed this effect, we obviously wish to identify its origin. However, it remains as mysterious as the antinodal point kink.

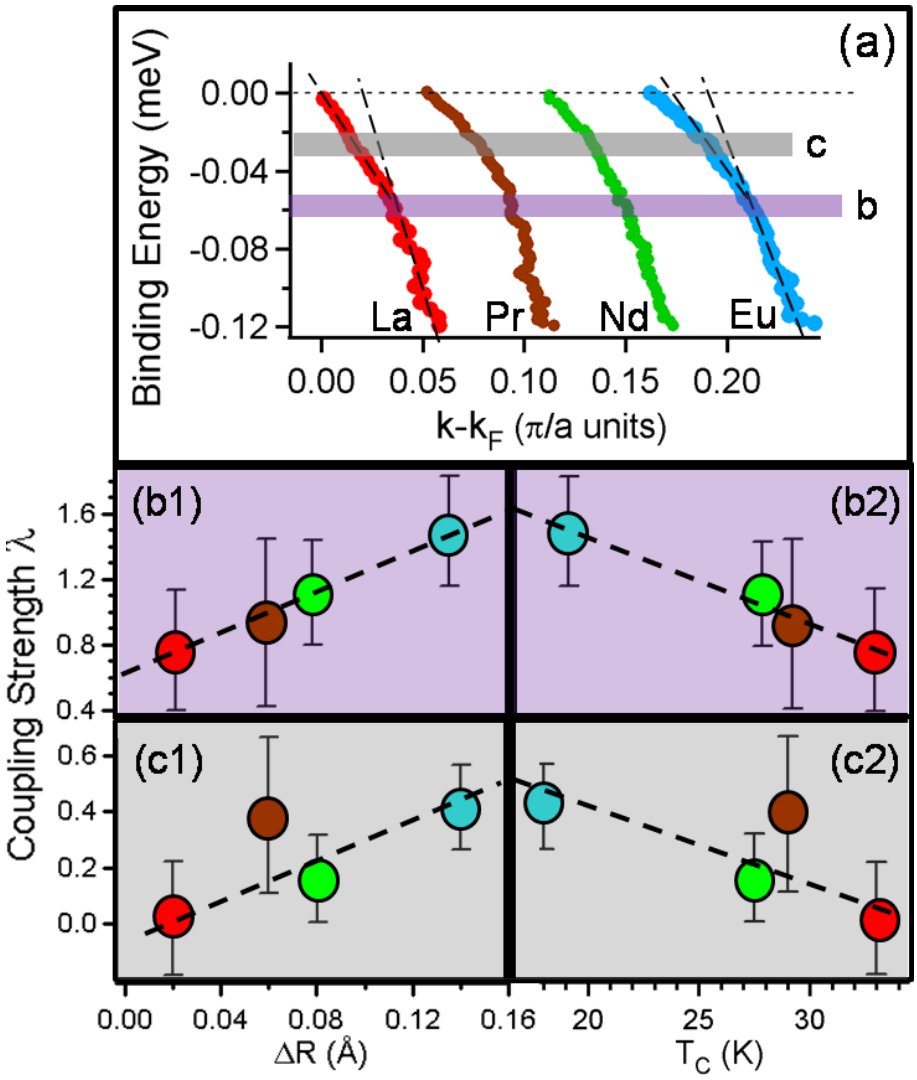

Figure 5.11. (a) Nodal point MDC dispersions taken from Γ-Y cuts on four different samples of increasing strain (La, Pr, Nd, and Eu). Lines serve as guides to determine deviation from the expected dispersion. Horizontal shaded regions correspond to the two potential ARPES kink energy scales. (b-c) Estimating the electron coupling λ on the electronic states from each of the two regions indicated in (a). (b1-2) Higher energy kink λ for each strain as a function of (1) Lattice mismatch Δ and (2) T_c. (c1-2) Lower energy kink λ analyzed like (b).

The introduction of lanthanides does introduce new magnetic moments into the lattice. But the general linear behavior makes this somewhat difficult to understand. Despite the absence of a magnetic moment in La^{3+}, the remaining lanthanides have basically the same μ_{eff} of 3.3 - 3.6μ_B due to the occupied f-orbitals[156], generally inconsistent with the monotonic behavior. The other option we have explored for this kink is that it is related to an apical oxygen mode, or a mode associated with the oxygen above the Cu-O plane within the octahedra seen in the general structure illustrated by Fig. 5.7b. When we think about the way in which the substituted lanthanides sit in the crystal, as seen in that panel, this possibility carries more weight. But this remains challenging to understand particularly in light of the inconsistencies we still see in the data. This is due to later work at different photon energies on highly strained Eu-Bi2201 that was unable to reveal this effect, and indicated that the dispersion was basically linear for energies below 60meV all the way to E_F (like La-Bi2201.) Could the effect be photon energy dependent? This would be strange as the nodal kink, in general, is so ubiquitous. Could our initial work be flawed? This remains a possibility where the appearance of a "lower energy mode" is just a broadened kink perhaps due to sample surface quality (though poorer sample surface quality should not enhance a kink.) Also, since the newer data was taken at lower photon energies, perhaps what was previously seen was more surface sensitive. But there really is no reason for this to enhance the kink either. Could our samples be changing with time? It is possible given the elapsed time of our work that the effect has become less pronounced but this makes further efforts to explore these issues problematic without more samples. The final possibility is that a misalignment of the a-b plane in the azimuthal direction is causing the observed affects. Thus, the cut is not strictly along the Γ-Y direction and perhaps introducing some curvature. Modeling the effect of azimuthal misalignment so far doesn't seem consistent with this. And so, in spite of the ambiguity, we will continue to propose this effect is real, though we have not felt the confidence to publish the work given these unresolved issues.

Assuming these results are trustworthy, we can see their significance for at least three reasons. First, the prevailing thought within the field has been that the electronic states at the nodal point are uniquely unaware of the entry into the superconducting phase. With the d-wave symmetry of the gap function, the nodal point states are certainly the only electronic states that have no gap opening despite crossing through T_c. Additionally, one could argue that the continued appearance of a sharp quasiparticle at the node is merely because these states are protected from the superconducting physics. However, one sees the affect of lattice strain on these states and this same strain is related to the weakening of the superconducting state, thus linking the superconducting phenomena to the electronic dispersion of the nodal quasiparticles. Secondly, as somewhat addressed, these results add additional evidence that the ∼60meV kink has its origin in the physics of the lattice. The appearance and potential enhancement of the lower energy kink with lattice strain would tentatively suggest its origin is also somehow connected to the lattice (such as the aforementioned apical oxygen mode) and not merely a magnetic mode at the nodal point. However, even in our best data, we were unable to resolve a convincing peak-dip-hump seen in the double layered Bi2212 compounds. Still this is not entirely surprising as outside ARPES work has already suggested that this feature is stronger with increased layer number[157]. Finally, at least for the 60meV mode,

one finds evidence that this phonon mode is somehow connected to the formation of the superconducting phase. From its behavior, it appears to be related to a competing order, associated with the lattice, which may be affecting the formation of the superfluid. This makes understanding the nature of this lattice excitation all the more important particularly if it is related to the pseudogap phase.

Before we conclude on these nodal states, one might be asking whether anything can be gleaned about the effective mass and transport measurement. From the trends described in Fig. 5.11, we can use ideas such as Eq. 1.5 and Fermi Liquid theory to determine m* and estimate the conductivity in a basic Drude model, $\rho = m*/ne^2\tau = \hbar k_F \Delta k/ne^2$ for the single hole band which crosses E_F[23]. This estimate assumes, obviously erroneously, that v_F is the same all along this hole band manifold (or that Δk is the same for the entire manifold at E_F.) Also, because it is the hole band that is contributing to the transport, k_F is determined from the Brillouin zone edge, or the (π,π) point. Although this curve is not strictly circular, we will assume it is with a radius of k_F for the nodal point. With these assumptions, we can determine these Drude model values from the ARPES data taken on La-Bi2201, Nd-Bi2201, and Eu-Bi2201 and compare them to the resistivity data presented in Fig. 5.8a. Unsurprisingly, we find evidence that m* increases with lanthanide strain, corresponding to a larger ρ which we see in the resistivity data at a fixed temperature for those lanthanides. Determining a trend in the resistivity data is a little problematic because if we use Δk as suggested by the second equation, other effects (e.g. surface quality) can interfere with our measure of Δk for the MDC at E_F. Nevertheless, we can determine a numeric value (using a carrier concentration of n=1-x) of $\sim 2 \times 10^{-6} \Omega$ m. This is consistent with the transport measurements in Fig. 5.8 for $\sim$ 50K (between 1.0 - 1.5$\times 10^{-6} \Omega$ m). This gives us some confidence that what we are observing is bulk and provides a consistency check with the trends we see in our v_F measurements. One could argue that the introduction of lanthanide strain is causing the samples to become polaronic (strong phonon interactions) but without the corresponding weakening of the quasiparticle peak, but this position needs more investigation. Indeed, our efforts to measure the quasiparticle weight, z_A, via total area under the peak or other metrics were generally inconclusive since there appeared to be too much variation from the cleaves to establish a proper trend. This issue of inconsistent sample surfaces leading to doubts about lineshape related quantities was a re-occurring issue throughout our data analysis.

5.4 Analysis Beyond Nodal States

As we move beyond the nodal point, additional topics of interest emerge as well as additional challenges. First, we have the Fermi arc phenomenon and our attempts understand if the strain axis we are accessing has an effect on these features. It is known that these Fermi arc increase with increasing doping[114,115], though this seems more a consequence of the T/T* Fermi arc scaling relation combined with the decrease of T* with increased doping. Prior work has suggested that T* does increase with lanthanide strain but our efforts to

determine the effect on Fermi arc have been challenged by the relatively small gaps observed in these systems. Our initial work has suggested an increase in the Fermi arc length with strain, but later analysis cast doubt on it, instead arguing that the Fermi arc length doesn't show significant dependence with strain. Chapter 6 will revisit this in the case of Nd-Bi2201, but we find that within our error, the Fermi arc stretches from the node to ∼15 - 17° off the node for these optimally doped samples (where a fully closed gap would be a Fermi arc of 45°.) These measurements were generally taken near 35K, but the temperature seemed to have little effect. An exception was Bi-Bi2201 whose Fermi arc appeared to be very large in some measurements, but one could wonder if it would even support a Fermi arc at all since it never shows superconductivity.

This work with Fermi arcs underscores some of the difficulties we've encountered getting consistent gap measurements. Given the quality of the data off the nodal point, determining the gap by the leading edge is our only way. Our attention naturally turns to the gap near the antinodal point (M point), but though the single layered compounds lack bilayer splitting, the existence of superstructure bands frustrates analysis. Believed to be related to oxygen ordering in the BiO layers[158], the superstructure bands are effectively similar to the shadow bands discussed in the context of CDW physics in Section 4.3. The ordering results in scattering the electronic states along a wavevector oriented in the Γ-Y direction, $\sim (0.2, 0.2)\pi/a$. This breaks the four-fold symmetry, making analysis of only two of the four nodal point in the first Brillouin zone possible (although Pb doping can diminish this effect). But near the antinodal point, the superstructure bands re-cross the main band structure, potentially obscuring our gap measurements. This is particularly the case for Nd-Bi2201 where the superstructure is quite strong. In fact, in some cases the higher order superstructure (multiples of the ordering wavevector) can lead to crossing of the main band structure that, if too quickly analyzed, can make the main band structure look like hole pockets straddling the Γ-Y line. Given the interest in finding evidence of a nodal pocket for consistency with quantum oscillation measurements, the presence of this superstructure needs to be carefully dealt with. For all our samples, however, this superstructure presented particular analysis difficulties for the antinodal point. Some of these challenges were addressed by using lower photon energies which, due to the ARPES matrix elements, weaken the spectral weight of the superstructure bands. Despite these problems as well as the findings by other work[149], Fig. 5.12b plots our final findings of the gap at the antinodal point. Because of the challenges associated with the superstructure, we do not show the Nd-Bi2201 data which anomalously has a M point gap at apparently less than half the value of these points. From the leading edge gap we find dramatically little change in the gap with a slight overall increase with lanthanide substitution. Additionally, the magnitude of the gap we find is larger than expected for these systems, possibly due to the Δk integration window or perhaps other issues. Still, the trend we see is small but positive, with the Δ_{LE} increasing by around 3-4meV. We can look at data taken at different temperatures as in panel c, but the only trend one could deduce is in the La-Bi2201. If we linearly extrapolate the data, it would suggest the M point closes around 130K, providing an estimate of T* that is slightly larger than other work[159].

The final area of study for our data was the band structure topology itself. This relates to

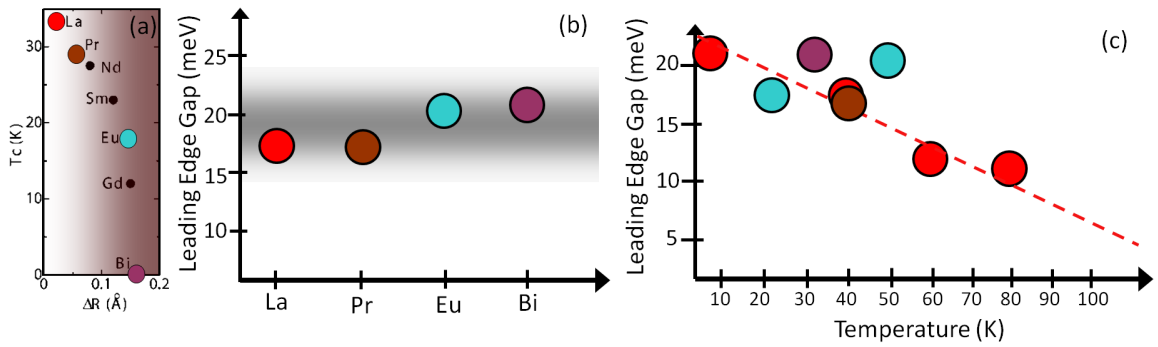

Figure 5.12. Plot of our work attempting to quantify the band gap at the antinodal point (the M point of the Brillouin zone) (a) Strain location of samples studied. (b) Leading edge gap determined for the strain samples identified in (a) with error bar comparable to the circle size. (c) Plot of the antinodal gap for numerous experiments on the samples from (a) at different temperatures. Red dashed line indicates the trend associated with La-Bi2201. T* estimated from its crossing is ∼130K.

the idea explored in Section 5.1 regarding the isotope effect, in particular the sign change seen in Fig. 5.5. This sign change is significant since one can identify its location in momentum space. When we plot the crossover points for the dispersions, we find that they fall along a line defined in momentum space as $\mathbf{q_{CO}} = 0.21\ \pi/a$, where a is the lattice constant of the CuO_2 plane. This line is illustrated in Fig. 5.13. Now, this particular wavevector (panel a) is important since it is in excellent agreement with the charge ordering wavevector seen in the far underdoped Bi2212 cuprate at low temperatures when explored by STM[83] (panel b). This implies that the high energy part of the electronic structure is strongly coupled to the order parameter, and this, in turn, is strongly coupled to the lattice.

If we try to understand why it is that at the $\mathbf{q_{CO}}$ line the isotope effect changes sign, we can use a simple charge density wave formation model to show how an ordering mechanism can affect the quasiparticle dispersion at all energies. In panels c-d, we present the opening of a gap in the dispersion at the $\mathbf{q_{CO}}$ vector, due to a charge density wave formation, just as we explored in Chapter 4. Based on evidence that the T* is strongly isotope dependent and increases for the ^{18}O sample[160,161,162], we assume that the magnitude of the gap is different between the two isotope samples, (e.g. larger for the ^{18}O sample - panel d). This would automatically lead to the appearance of the sign change at $\mathbf{q_{CO}}$ that migrates to lower energy as we move away from the node, just like seen in the data. Thus, the question is naturally asked, could the pseudogap opening be, in fact, due to an ordering phenomena that has never been observed in any ARPES experiment so far, perhaps due to the short range nature of such ordering[163,164]. As one approaches the states nearer to the antinodal point, one could potentially see evidence of a crossover into this ordering.

Although we will be exploring the idea of an actual crossover point along k_F in more detail in Chapter 6, one naturally wonders, given the near-E_F electronic structure seen in Fig. 5.9, if the introduction of strain might be able to enhance or otherwise affect some potential

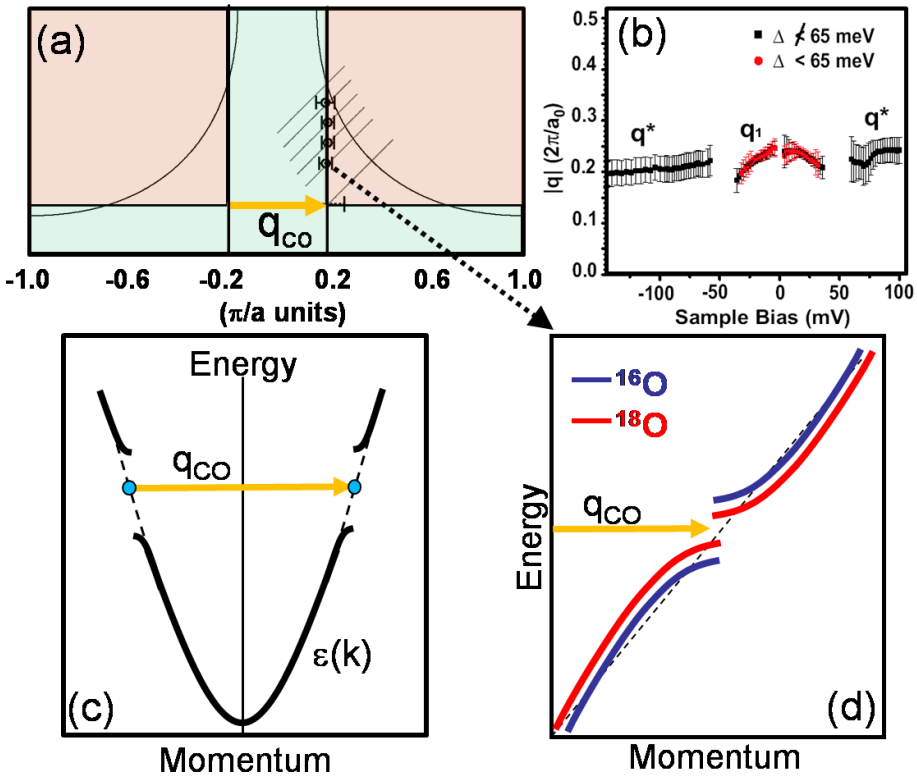

Figure 5.13. (a) Fermi surface of the upper half of the first Brillouin zone. Diagonal lines indicate cuts used in Fig. 5.5 while circles indicate the location in momentum space of the sign change crossover point for each of those cuts. These lie on a line indicated by the wavevector, $\mathbf{q_{CO}}$ and illustrated by the colored regions. (b) STM data independently determining this wavevector taken from Ref.[83]. (c) Cartoon illustrating how the charge ordering wavevector, $\mathbf{q_{CO}}$, can open a gap at a binding energy where the electronic states are nestable. (d) Additional cartoon illustrating how the splitting, if slightly different in magnitude between the isotopes, can explain the observed sign change in the bands and its evolution as the dispersions intersect with $\mathbf{q_{CO}}$.

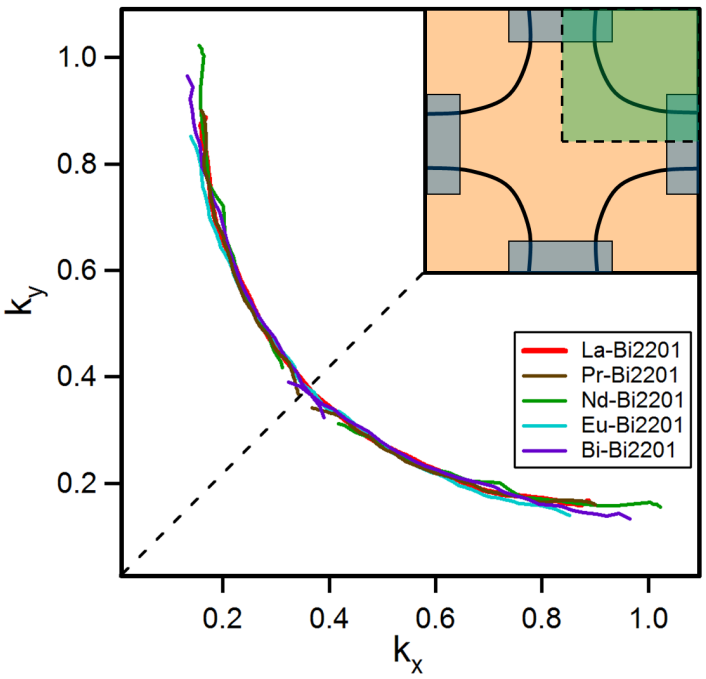

Figure 5.14. Near-E_F hole band structure fit with lorenzians for the indicated lanthanide substituted Bi2201 compounds. Inset shows the hole pocket Fermi surface with the antinodal regions again indicated with rectangles and the quadrant our associated with our data in the shaded square. We reflected our data over the ΓY axis indicated by the dashed line.

ordering near the Brillouin zone edge. Perhaps, as the cartoon proposes in Fig. 5.13a, the band structure could even be better nested near the antinodal point as we move along this strain axis, leading to distortion in the Fermi surface. We can better quantify this by integrating a narrow energy window near E_F to get a band structure without worrying about the gap. Then, we fit the Fermi surface with Lorentzians as far as we can before the overlapping superstructure or lack of spectral weight makes fitting impossible. Unfortunately, our analysis as seen in Fig. 5.14 suggests that for as far as we can fit our Fermi surfaces from the nodal to the antinodal point, the overlap is very good. This shows us that if there is distortion in the band structure near the antinodal point, it is beyond the region we can accurately fit and explore.

This is additionally confirmed by our attempts to fit the band structure manifold to a tight binding model like that described in Section 1.2. Of interest would be to see if the introduction of the lanthanide (either in a strain or disorder paradigm) could affect the different hopping parameters. Thus, instead of using a model with only one hopping parameter, t, as described by Eq. 1.8, we will include a second nearest neighbor parameter, t', for our model of the Cu-O square plane. This is illustrated in the inset of Fig. 5.15 for the CuO_2 structure responsible for the hole band observed at E_F. We fit our data from E_F down to higher binding energies ($\sim$150meV) following the band manifold for numerous samples we studied in both the superconducting and pseudogap phases. There was no consistent difference in the parameters between the two phases, which fits with our expectations based on our earlier work. The results of these fits are shown in panel b which plots the valuable t'/t ratio compared to other work on superconducting cuprates[165]. There are two things worth noting about these results. First, as indicated by the bunching of the points which straddle $t'/t \sim 0.42$, the introduction of strain appears to have little effect on the observed and fitable Fermi surface topology. This is consistent with the previous work shown in Fig. 5.14 at E_F where little variation in topology was seen. Here, however, the statement is stronger since we are including far more data and fits at multiple binding energies. The second curious observation is that our work though generally consistent with the prior Bi2201 data point, appear the buck the trend of lower T_c corresponding to lower t'/t ratio. Rather, it suggests that this ratio generally falls in a well defined region between $\sim$0.36-0.46 for nearly all the cuprates except for the single layered LSCO, which now appears to be anomalous. It lends credence to the position that it is not the hopping parameters that hold the key to the increased superconducting T_c

5.5 Discussion

By this point, one could say that we have more questions than answers when it comes to these lanthanide substituted single-layered cuprates. Superstructure and inconsistent sample surfaces, particularly at higher strain, have made the kind of confident analysis we seek regarding the gap, quasiparticle shape, and near antinodal band structure challenging. Additionally, one could argue that the features we are looking for within the dispersion are

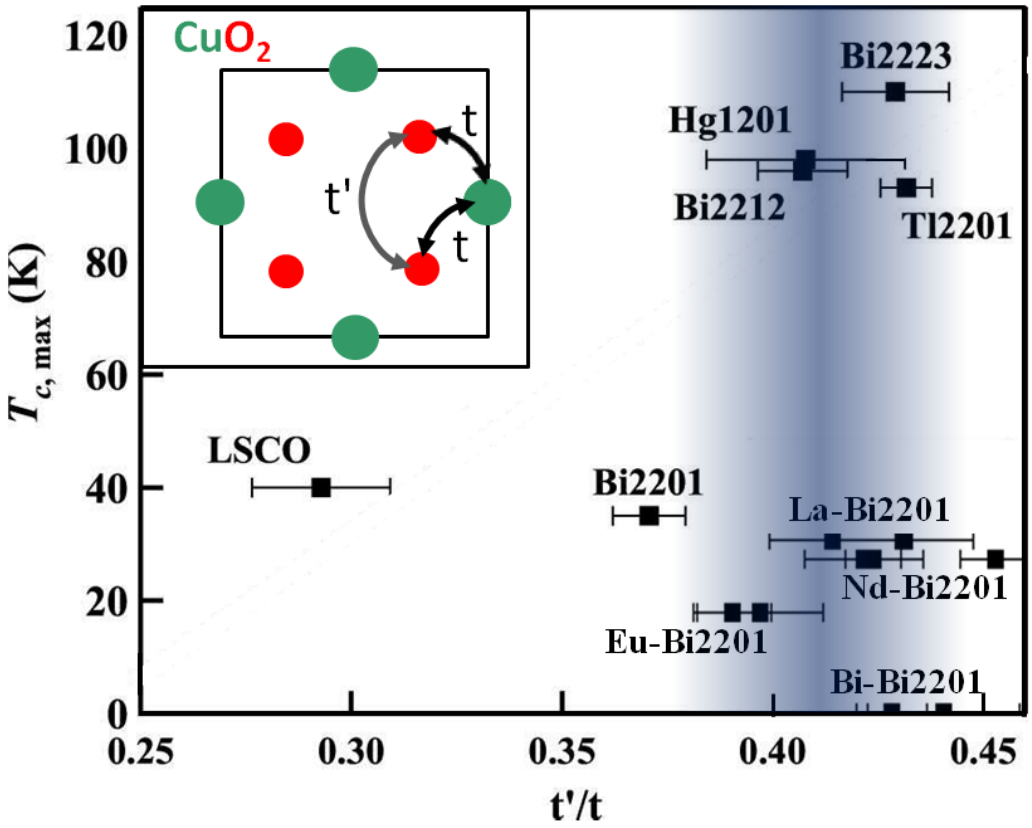

Figure 5.15. Plot of T_c vs. t'/t tight binding parameters ratio for numerous cuprate samples. Shaded region indicating the general range of the T_c vs. t'/t ratio for the vast majority of the samples. Inset shows the hopping parameters as defined in the CuO_2 plane. Non strain data taken from Ref.[165].

simply too subtle to be observed within our experimental setup given both sample quality as well as experimental issues (e.g. non-linear pixel/angle calibration issues). But there are a few things we feel some confidence in. First, whatever the effect the substitution has on the lattice, the nodal point states appear to be less effected when it comes to the coherence of the states. The general affect of the lattice mismatch, for the majority of the Fermi surface, is less coherence, and broader peaks. The second issue is that, for the most part, the effect of the substitution has very little effect on many of the features of the band structure such as the Fermi surface topology, dispersions, the kink energies, Fermi arc, and even the antinodal gap. Curiously, with the exception of the gap measurements, this is generally consistent with the only other major ARPES work on the strained Bi2201 compounds[149]. It also found very little of any effect of lanthanide substitution on either Fermi surface shape or band structure save the effect on gap. Even a close examination of their data regarding the gap suggests an increase of only about 6meV in the M point gap from La-Bi2201 to Gd-Bi2201. This is a little larger than we observe, though not much. Furthermore, the depression in the nodal point states they observe is very subtle and arguably within their stated error bars. Still, this proposed contradiction regarding the gap leads us to speculate if sample degradation or other processes could be to blame for the lack of variation among the samples. This makes the idea of comparing the strain axis to the doping axis (e.g. equating greater lattice mismatch with underdoping) inappropriate as none of the trends seem to coincide. Rather, one could argue that this work is consistent with a model that increased disorder is the primary consequence of the lanthanide substitution and it affects the coherence of states along the Cu-O bond direction.

Throughout this work, we were often surprised by the quality of data we were able to get from the strained Nd-Bi2201 sample, in spite of the challenges with the superstructure. We initially observed very unusual gap values and were able to observe a coherent peak quite far towards the antinodal point. Why this strained compound provided such good data remains mysterious but we discovered that if we turned our focus from a strain dependent comparison, which was yielding very little, and focused on only on this Nd-Bi2201 compound as well as a slightly overdoped version of the compound, our analysis could reveal some significant results about the states near E_F. It is this work that we will now turn our attention towards.

Chapter 6

Band Structure Crossover Point in Nd-Bi2201

6.1 Introduction

In our work on the strained $Bi_2Sr_2CuO_{6+\delta}$ (Bi2201) compounds as described in Chapter 5, we were continually surprised by the uniqueness of the Neodymium substituted compound, Nd-Bi2201. As previously mentioned, this compound gave surprisingly good ARPES data but was somewhat challenging to study otherwise. The presence of strong superstructure bands makes quantification of the near antinodal gap problematic, appearing smaller than it should be. But it was quickly apparent that if we focused our attention on this compound alone, we might be able to address certain issues related to the nature of the Fermi surface in these single layered cuprates.

Consistent with our motivation for much of the strain work, our understanding of the near-E_F electronic band structure is truly essential to our ability to make sense of the superconducting cuprate phase diagram. Currently there have been an increasing number of studies which are suggesting that the Fermi surface may be better thought of as being divided into regions along k_F [166,167,168]. We have already discussed some examples of this. The partial gapping of the Fermi surface in the pseudogap phase leading to the aforementioned Fermi arcs (see Section 1.6) is an obvious example. Although the Fermi arcs appear to scale with T^* [26] and so their tips may represent a fluid boundary, the initial region in which they form near the nodal point when one moves just above T_c remains mysterious and may be significant. In addition to this, there is the work relating to the controversy over the "one-gap" vs. "two gap" pictures of cuprate superconductivity as also described

in Section 1.6. As alluded to in that section, there have been recent experiments which have indicated that the superconducting gap departs from a simple d-wave form. Furthermore, there appear to be opposing gap trends within different areas of the Fermi surface. All of this would point to the existence of an additional energy scale within the superconducting gap function[169 170 171 110 149 141]. Yet, this is certainly a very contentious issue and remains the subject of debate[28 172 173]. Still, if it were true, the consequence could like be a division of the Fermi surface where electronic states near the node are uniquely related to superconductivity while the antinode would be associated with an additional, potentially competing, phenomenon corresponding to the pseudogap phase[110 111 112 113 114 115]. This is certainly what was motivating our work examining the Fermi surface and the potential for charge ordering near the antinode as suggested by the isotope effect (Section 5.4).

There are additional boundaries for the band structure along E_F observed by probes like STM. Here, work has suggested a potential crossover region on the Fermi surface associated with the antiferromagnetic zone boundary, characterized by the disappearance of the coherent quasiparticle peak[174]. This antiferromagnetic zone boundary comes from the ordering of spins in the Cu-O plane that is most obvious in the undoped antiferromagnetic Mott insulating phase. Thus, the new Brillouin zone defined by this cell is smaller and rotated by 90 degrees. The interaction between the electronic band structure and this new Brillouin zone is a critical question for ARPES.

We have also seen evidence of a potential crossover in the combined IXS and ARPES work described in Section 5.1 where the bosonic mode responsible for the band structure kink in the near-E_F band structure suddenly shifts in energy. This shift may also define a key region of the Fermi surface which may be related with the softening of the Cu-O bond stretching phonon[140].

As a final point, there has been recent quantum oscillation data[175 176] which has suggested quite a different picture of the Fermi surface than the one generally seen by ARPES. Work on materials like YBCO has suggested that the Fermi surface is indeed separated into hole and electron pockets and that they may be oriented at the nodal and antinodal points, providing another crossover region for the low energy quasiparticle states. This presents some issues though since ARPES on the materials studied by quantum oscillation is very difficult in practice, and materials that produce excellent ARPES (the bismuth based cuprates) are far to disordered to do quantum oscillation measurements on. In spite of this challenge and controversy, evidence for a hole pocket on the Fermi surface has been recently provided by photoemission experiments[177]. Even though its true nature remains obscure, it and all of these examples underscore the importance of exploring the physics of these different regions. Particularly in the case of discerning between a single or dual energy scale to the superconducting phase, relying on d-wave gap measurements alone cannot entirely avail us given the strong disagreement between different experimental groups and the potential to explain deviations via arguments based on higher harmonics[178 179].

So, like other groups, if there is really evidence of more complicated physics in the superconducting phase, we need to start looking for how different electronic states are affected in the Brillouin zone. And if such regions exist, the boundary between them may be the best

place to explore. With the attention given to the nodal and antinodal states, focusing on the middle region can help us complete the picture. The single layered Nd-Bi2201 turns out to provide us with an excellent opportunity. Additionally, though these samples were grown as described in Section 5.2, we determined (initially from the Luttinger area of the hole bands then by magnetometry) that at least some of our sample was overdoped. From the diamagnetic transition, seen in Fig. 6.1a, we can see that though the T_c has shifted from its expected value of T_c=27.5K, we clearly see evidence of a discontinuity in the magnetization at this temperature. This leads us to believe that this sample started off as optimally doped but became more hole doped (oxygen doped) with time, possibly due to excessive heating in the ARPES sample preparation process. We also found distortion in the band structure leading to increased Fermi surface area consistent with overdoping as illustrated in Fig. 6.1b. From this, we are inclined to accept that we are seeing electronic structure from a predominantly overdoped sample whose T_c we will estimate around 10K. Additionally important for our data is the work referenced earlier that places the pseudogap transition temperature T^* well above the peak T_c for the optimally doped sample[180] and suggests the pseudogap phase is stronger in Nd-Bi2201 than nonstrained Bi2201 systems[149]. Being able to put an estimate on the T^* will be important later when we address the issue of Fermi arcs because of the potential scaling relation.

Consistent with the strain samples in Chapter 5, this synchrotron ARPES data were taken solely at Beamline 5.4 at the Stanford Synchrotron Radiation Laboratory, using a Scienta R4000 analyzer. As mentioned previously, Beamline 5.4 produced consistently better ARPES results and the Nd-Bi2201 data were a significant example of this. A total energy resolution of <13meV was achieved for data taken on the optimally doped sample while a resolution of <8meV was achieved for data taken on the overdoped sample of Nd-Bi2201. In both cases, the angular resolution was better than 0.35° and fresh sample surfaces were prepared by cleaving the sample *in situ* at a base pressure $<5\text{x}10^{-11}$ Torr at low temperatures. An additional reason for the higher energy resolution is the use of lower photon energies ($h\nu$ =8eV) for the data taken on this overdoped sample whereas we were only able to take data at larger photon energies ($h\nu$ >21eV) for the optimally doped sample. Finally, the data we will focus on here were taken with the analyzer slits oriented in the MY geometry (45 degrees rotated from the ΓY geometry.) This geometry has advantages to studying the gap particularly as we approach the antinodal region, but the cuprate matrix element kills off spectral weight on one side of the ΓY line. The result is a much weaker spectral weight at the nodal point than would otherwise be expected. For this reason, the relative spectral weight was not considered a trustworthy measurement to make much of in our analysis.

6.2 EDC Analysis

We'll start with analysis related to the EDCs determined along k_F in the first Brillouin zone. A stack of these EDCs are provided in Fig. 6.2a for the optimally doped sample. We determined the k_F value by using MDC analysis, fitting the individual MY slices to

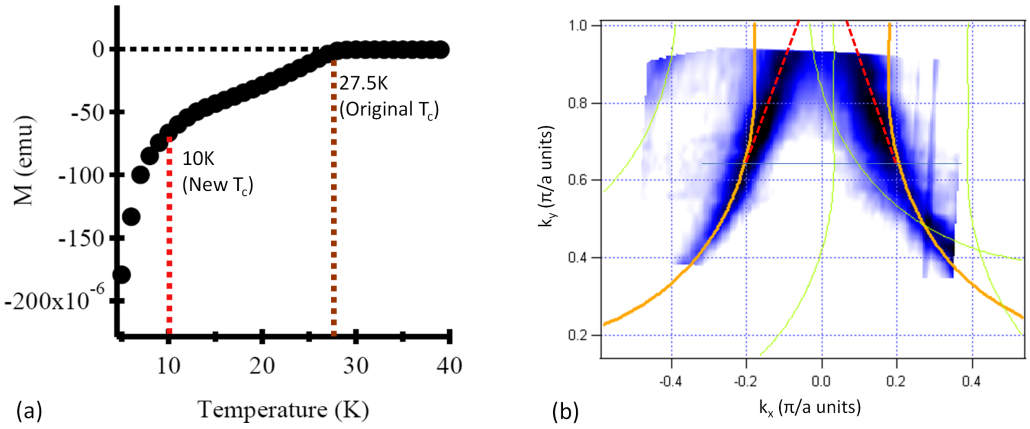

Figure 6.1. (a) Magnetization vs. temperature for the overdoped sample indicating the new lower $T_c \sim 10$K. (b) Near-E_F band structure illustrating the deviation of the band structure (red dashed line) from the expected curvature (orange curve) consistent with overdoping.

lorentzians. Then, we linearly fit the data from 10 to 30meV and extrapolate where it intersects E_F to determine k_F from this. We choose the energy range so as to avoid any potential lower energy kink but not include the effect of the opening of the gap at E_F. Though the peaks are scaled to peak height, one can actually see in the bottom curves (at the node) a weaker peak due to the matrix element described at the end of the preceding section.

Because of the sharp peak features, we will use the binding energies of the quasiparticle peak to quantify the gap function as long as the peak can be clearly observed over the rising background at higher binding energy. To plot the peak gap, we will take advantage of the expected functional form of a $d_{x^2-y^2}$ wave gap $\Delta_k = \Delta(cos(k_x a) - cos(k_y a))/2$. (Aside: Often people use $\Delta_\theta = \Delta\cos(2\theta)$ to quantify the d-wave gap where theta is angle with respect to the Brillouin zone edge. This is an approximate based on a perfectly circular hole band which is not quite the case in the cuprates. Because of this, we use the more general equation, Δ_k, though the difference is very small.) Using this functional form, we can plot the peak gaps we extract with respect to this function on the abscissa axis as commonly done [171 149 115]. The result will reveal potential deviations from a single d-wave gap, which should appear as a straight line in this scaling. This is displayed in panel b where a clear deviation from a pure d-wave is observed. This is certainly similar to other cuprate studies [169 171 110 149 141 115] although, as previously mentioned, it is still controversial. I've highlighted this proposed location for the crossover in violet since it will be a reoccurring theme.

With this gap feature in hand, we could explore issues related to the Fermi arc and its formation. As discussed earlier, even though the Fermi arc is believed to scale with T/T^*, the initial Fermi arc length may indicate a significant point in the Brillouin zone. In order to explore the connection between this crossover and Fermi arc formation, Fig. 6.3a shows the gap along k_F above T_c as determined from the leading edge. Panel b provides a cartoon to

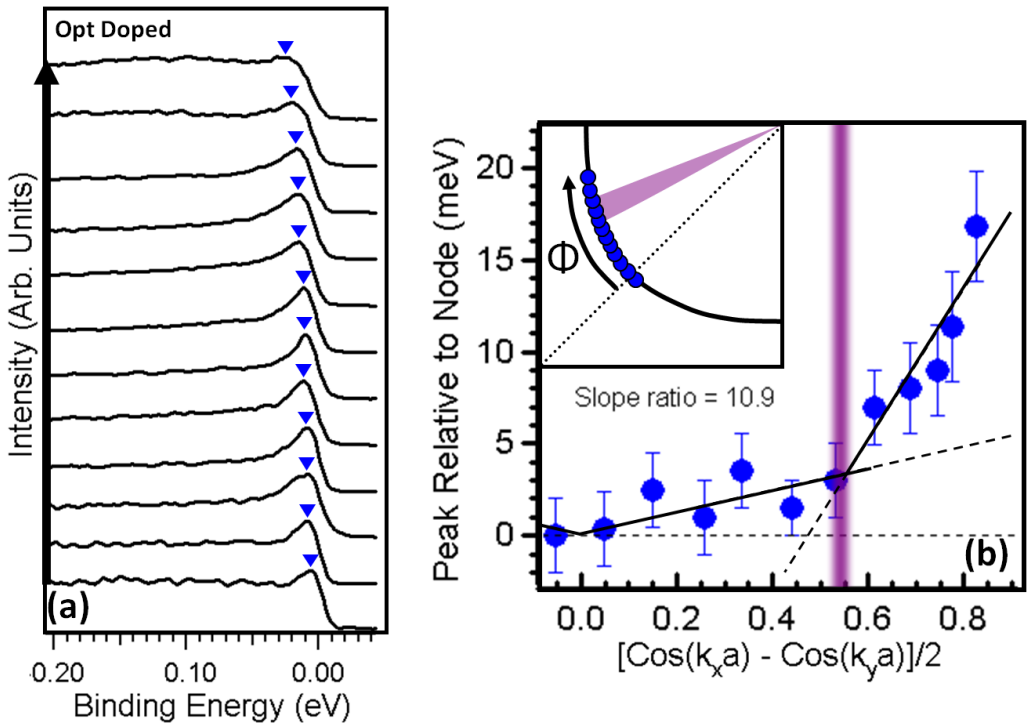

Figure 6.2. (a) EDC spectra taken at T=8K on the optimally doped Nd-Bi2201 at k_F along the band structure. (b) The quasiparticle peak binding energy positions indicated by the blue triangles in (a) and shifted relative to the nodal point peak. Inset shows locations of these EDC spectra at E_F. The lines are guides to the eye, indicating a deviation from a pure d-wave gap function when plotted on this abscissa. The violet shaded area in all these panels indicates a point 18°±1° away from the nodal point.

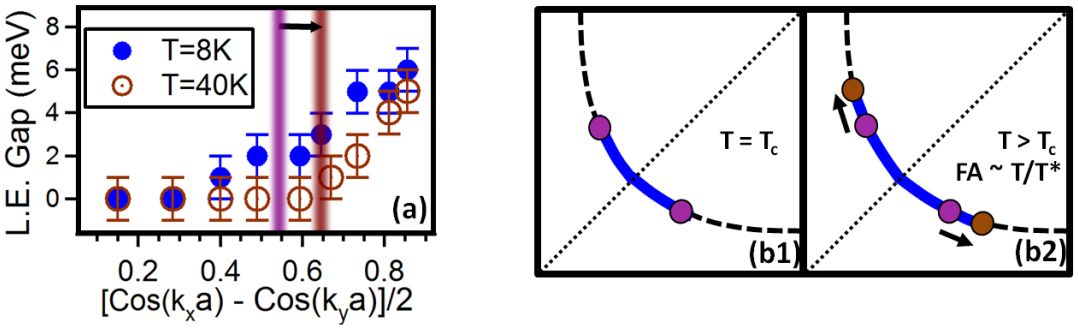

Figure 6.3. (a) Leading edge gap data for both SC and PG phases. Here the violet region is shifted to include the expected FA scaling for T=40K (indicated by the brown line).(b) Cartoon explaining it all.

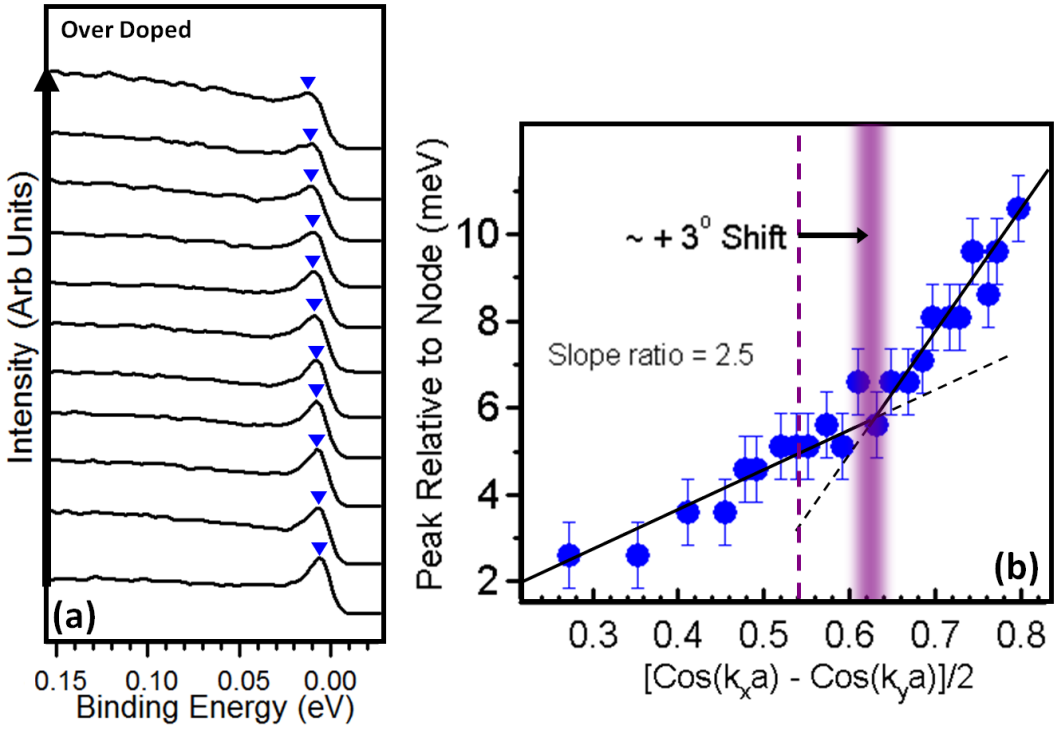

Figure 6.4. (a) Sampling of EDC spectra taken at T=8K on the overdoped Nd-Bi2201 along k_F. (b) Quasiparticle peak binding energy positions indicated by the blue triangles in (a), shifted relative to the nodal point peak, for all EDCs measured along E_F. The lines are guides to the eye indicating a deviation from a pure d-wave gap function. The violet shaded area in these panels indicates a point shifted by ∼3° from Fig. 6.2 (dashed line).

illustrate the nature of the expected T/T^* temperature dependence[26] and our compensation for it (violet to brown line in the figure). To do this, we are using T^*=140K[149 180], and thus we can compare the location of the crossover identified in Fig. 6.2 to the size of the Fermi arc when it first forms above T_c. After doing this correction, we find that the location of the crossover lies approximately where this initially formed Fermi arc terminates (the gap finally opens). If we look in the literature, this correlation seems consistent with other published Bi2212 ARPES studies[115] although it isn't clearly pointed out. This suggests a potential connection between Fermi arc formation in the psuedogap phase and the separation we are seeing as the two d-wave gaps in the superconducting phase.

Our attention now turns to the overdoped Nd-Bi2201 sample as displayed in Fig. 6.4 Just as before, panel a shows the evolution of the quasiparticle peak at k_F for a sampling of EDCs along the hole band. And, once again, we can plot the peak binding energies for all EDCs in the manner of Fig. 6.2. Because of the lower photon energy and a desire to better quantify the crossover, there are significantly more data points, corresponding to a greater number

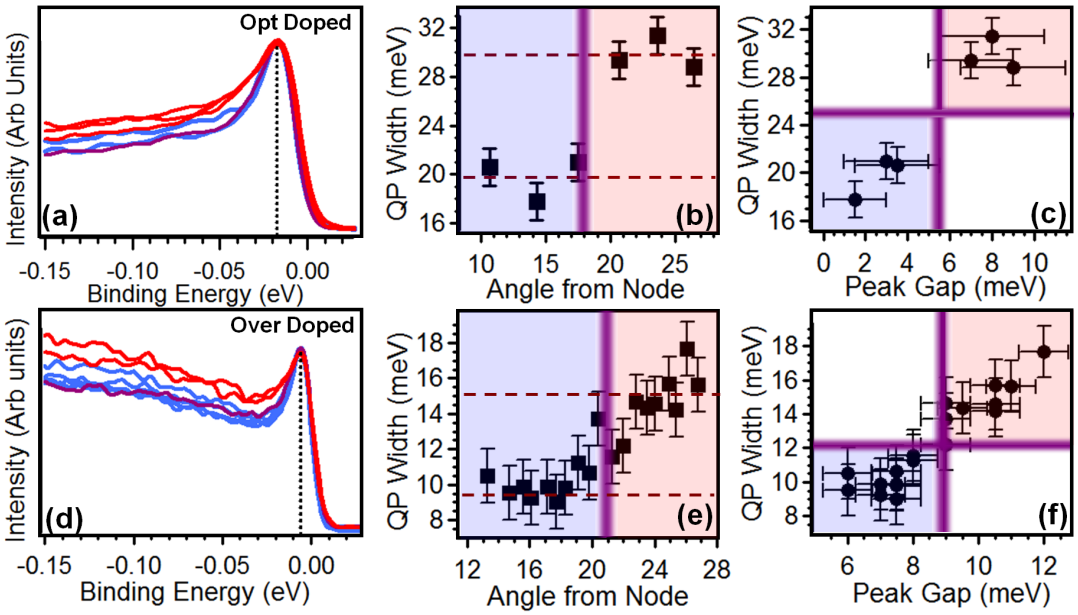

Figure 6.5. Quasiparticle peak width data taken in the superconducting phase for (a)-(c) Optimally doped and (d-f) overdoped samples. (a,d) Selected EDCs from Fig. 1a and 2a, respectively, with their peaks aligned, normalized to quasiparticle peak height, taken on both sides of the crossover region. Blue (red) curves indicate the nodal (antinodal) side of the crossover. The violet curve sits right on the crossover region. (b,e) Fitted quasiparticle widths quantifying the energy broadening through the crossover region with error determined from fit. (c,f) Quasiparticle widths plotted versus their associated peak gap from Figures 6.2 and 6.4.

of slices to move through the consequently larger Brillouin zone. Curiously, there remains some evidence of a deviation from a pure d-wave gap function when we plot it. However, clearly this deviation is less pronounced that the optimally doped sample with the ratio of the two slopes being ∼3 for the overdoped. This is compared to ∼11 for the optimally doped sample. This is not surprising though since it has been suggested that deviations from a pure d-wave gap do tend to disappear with overdoping in the cuprates and consistent with the suspicion that they are due to the physics of the pseudogap phase (which also dies away at higher dopings.) In that respect, its continued presence in our data may be a bit surprising and could be related to the increased strain within the lattice caused by the substituted Neodymium. Secondly, as illustrated in panel b, there might be evidence of a shift in this region at this new doping. We estimated the shift to be about 3 degrees more from the nodal point towards the antinodal point. Still, this must be taken with a grain of salt given uncertainties in sample alignment as well as the resolution of the experiment. All of this is generally consistent with our data above T_c, where we were unable to find clear evidence of Fermi arcs. This is further confirmation that our data is predominantly representative of an overdoped region of the phase diagram, where T^* becomes closer to T_c or below it.

We can go further with this, turning our attention from the gap to the quasiparticle peaks themselves. As we've discussed in the context of Fermi Liquid theory and the self-energy described in Section 2.3, the lineshape of the EDC provides us with critical information about (among other things) the lifetime of the quasiparticle states. So, we naturally look for further signatures of the crossover in the lineshape. Extracting this information is very challenging since the lineshape is affected by so many contributions. But let's start simple and return to the individual EDCs in the region near the purple crossover point. We find evidence of sudden changes in the quasiparticle lifetime (associated with the peak width) occurring near the crossover region. This is in comparison to the gradual increase in lifetime previously observed in the normal phase between the nodal and antinodal points[181]. This is summarized in Fig. 6.5 for both dopings. In panel a, peak-aligned EDCs from near the crossover region of the optimally doped sample (Fig. 6.2a) are stacked and shaded as blue and red curves. This corresponds to the angular region they are in with blue = nodal and red = beyond nodal. The violet curve is associated with a data point effectively at the crossover point identified previously. This suggests that the electronic states closer to the node (blue) are suddenly altered upon passing through the violet crossover region towards antinodal states (red) along the near E_F band structure.

Certainly, one concern that can arise would be discerning between a widening peak and simply a weakening peak over the background (which we believe to be predominantly inelastic scattering.) First, even if this were the case, the sudden drop in quasiparticle spectral weight could then be interpreted as the indicator of passing through the crossover region, still affirming the crossover's effect on the spectral lineshape. There is no known reason why this would be associated with a matrix element effect either. Secondly, we can better quantify this change by extracting the quasiparticle lifetime-related energy width, Γ, through fitting the spectra. In order to accomplish this, we use a resolution broadened spectral function incorporating a well-known self-energy model for the cuprates[24] $\Sigma(k_F, \omega) = -i\Gamma + \Delta^2/\omega$ within the Green's function. Using the associated spectral function, $A(\mathbf{k}, \omega)$, we modify it with the expected Fermi function, and place it on top of a variable inelastic background. This background is modeled simply as a much broader Fermi function whose edge (inflection point) sits near the binding energy of peak. This fitting was attempted on other samples but the results were often erratic and inconclusive. The quality of the data we find for the Nd-Bi2201 however allows us to make some intelligent progress with this analysis and the results are displayed in panel b. Again, we see the change in quasiparticle width occurring near the violet crossover region, identified in Fig. 6.2b, for the optimally doped sample.

Similarly, we can examine this effect in our overdoped samples In panel d, the we present the EDCs from Fig. 6.4b. One can initially see that the peak width appears sharper, a feature once again consistent with increased doping in the bismuth cuprates[169 182]. And once again, we can make out a change in the spectra associated with passing through the violet crossover EDC into the red EDCs. It is worth noting, that the violet region chosen is specifically the one from Fig. 6.4, which incorporates the 3 degree shift previously mentioned. The fact this appears more appropriate is still consistent with the idea that a general misalignment could still be responsible for this difference. As before, we can use the previously described fitting

techniques to better explore the quasiparticle lifetime. However, this was more challenging given the strong rise in the inelastic background as one goes further from E_F. The consequence is simply that the energy window of the EDC we could fit became smaller, and consequently closer to the peak and E_F. All of this is plotted in panel e with the violet crossover region flanked by the blue and red nodal and beyond nodal regions. Despite the fitting challenges, this finer survey of Γ again suggests that the quasiparticle width begins to rise as we pass through the crossover, although it is certainly more gradual than we observed in the case of optimal doping. We also include panels c and f to examine and consequently underscore the relation between the gap and this peak width. Here we plot the gap data from Figs. 6.2b and 6.4b versus the quasiparticle width data to underscore the correlation between the identified blue and red regions. The decrease in the lifetime of the quasiparticle electronic states as they approach the antinodal point seems to be in agreement with studies in the literature that suggest, as we've discussed previously, that the gap near the antinodal point is actually due to some competing phase[111,112,113,110,114,115]. A strong example of this is how both the location of our crossover region for the optimally doped sample, as well as even the potential trend with doping, corresponds well with the maximum in the coherent peak weight, W_{CP}, seen by Kondo et al. on the unstrained Bi2201[110], where a competitive relationship between the superconducting and pseudogap phases is suggested.

Before continuing to our MDC analysis, we should take stock of where we are as summarized by the cartoon in Fig. 6.6. The states near the node (indicated in blue) are separated by a crossover region (violet circles) from states closer to the antinodal point (indicated in red.) As mentioned, our data suggests this crossover region might be shifting away from the nodal point with overdoping. We can estimate the crossover location at 18°±1° from the nodal point or near ($\pm\pi/4.3a_0$, $\pm\pi/1.6a_0$) ± 5% in momentum space for the optimally doped sample. For the overdoped compound, the crossover seems to occur at 21°±1° or near ($\pm\pi/5a_0$, $\pm\pi/1.6a_0$) ± 5%, shifted (∼3°) away from the node. Still, at this point, two issues must be clarified to avoid the risk of confusion. First, it is not at all clear from the data (nor from the remaining analysis to come) that this crossover necessarily represents a finite region of states along k_F that are separate from the nodal and antinodal states. The resolution of the ARPES experiment is consistent with both a finite, but small (∼5 degree), crossover region along k_F as well as something even sharper. Second, although the cartoon includes all the states beyond the violet crossover as red, strictly speaking this is not correct since we are unable to fully explore all of the states nearest the antinodal point, for the reasons explored in Section 5.4. This means there could conceivably be an additional crossover which happens much nearer to the antinodal point. In that case, this red region may in fact be an actual larger finite middle region and not extend all the way to the Brillouin zone edge[168].

6.3 MDC Analysis

Now we will turn our attention to the MDC analysis of the data. In a sense, we have already taken advantage of this analysis when we determined the k_F for the EDCs using the

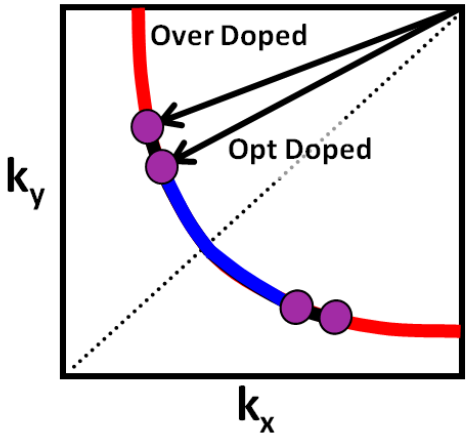

Figure 6.6. Cartoon illustrating the regions (blue and red) identified in Figures 1 and 2 and small shift in location of the crossover (violet circles) between the dopings.

Lorentzian fits to our MDC data. But, as discussed in the context of the strain comparison data, the near E_F slope can be used to determine things like v_F and, correspondingly, m*. We summarize our findings for the overdoped sample in Fig. 6.7, superimposing the crossover region we have already been establishing from our EDC analysis. Comparing v_F to the location of the crossover point is suggestive but presents some challenges. We see that the experimentally determined v_F does appear to vary in the region of the crossover point between the values indicated by the dotted lines, but the correspondence is not as good. We present only data from the overdoped samples because the sampling is sufficiently high to potentially reveal a change in what is a very noisy plot. It does suggest that effective mass increases upon passing through the crossover point. Still, this data is challenged by two issues. First, determining v_F requires determining the slope of the band structure dispersion very well. The challenge is the very real pixel to angle inhomogeneity in our 2D images. This means that as the band structure simply moves across the screen, the measured slope will change slightly. To combat this, we took the same cut of the band structure in momentum space but shifted so it appears at different places on the screen. From determining the variation in the slope, we can provide a linear correction. This has already been incorporated into the data seen in Fig. 6.7 but the correction likely still not perfect. The second issues is the effect of the opening of the gap which, despite our choice of fitting window, may still affect our data and could inadvertently result in a correlation with the crossover point. In fact, the choice of fitting window does, as expected, have a somewhat unsettling effect on the v_F so that, although the trend we see is generally replicated, it is not as robust as desired.

If the Fermi velocity analysis may be problematic, then we should turn our attention to the higher binding energy dispersion instead. Specifically, we could consider how the bosonic renormalizations (kink) may be affected along k_F. As described in Section 5.1 and 6.1, the potential for a shift in the kink is particularly significant because it may be connected to the softening of a particular phonon mode with a characteristic wavevector like that seen by

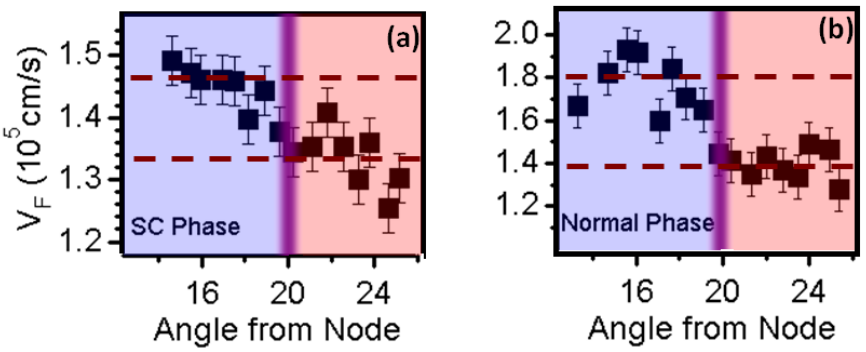

Figure 6.7. Fermi velocities for the band structure as a function of angle from the nodal point for the finely sampled overdoped sample. Both the data in the (a) superconducting and (b) normal phase shows some decrease in the neighborhood of the crossover (violet line) corresponding to an increase in the effective mass.

IXS in La-Bi2201[140]. As described in the preceding chapter, the general shifting of the kink energy from the node to the antinodal point has long been observed in the double layered bismuth cuprates[137 134 183]. In Fig. 6.8a, we show the peak position from lorentzian fits of the MDCs from our optimally doped data, again taken from slices in the MY direction. We can see a continuity with the prior work on La-Bi2201, finding evidence of a shift in the kink as indicated by the blue and red shaded regions, although the energy of both modes is slightly less then observed in that prior work. Based on prior work, we associate the blue higher energy kink with a similar feature that seen throughout the cuprates[104]. This shift is generally consistent with the location where we expect the IXS wavevector from La-Bi2201 to nest the Fermi surface of the optimally doped Nd-Bi2201. Additionally important is comparing the location of the kink shift to the crossover region. Here we find that the transition between the kink energies occurs roughly between 14° and 18° off the nodal point, close enough to the crossover region to suggest a connection given the sampling and k-space uncertainties.

Of course we can turn to the overdoped samples as in panel b where we show the peak from the fitted dispersions. When we examine these curves, we find the same shift in the bosonic kink between the two energy scales. Its location, curiously, appears to be roughly between 18° and 20° off the nodal point, which again places it close to the crossover as it is observed in the overdoped sample, keeping the consistency of the $\sim 3°$ shift. One issue that does arise, however, is that nesting the Fermi surface of this overdoped compound with the IXS wavevector from the optimally doped La-Bi2201 work does not correspond well to the location of this shift. But this is not surprising and with no sufficient quality IXS data on any overdoped Bi2201 nor the strained Nd-Bi2201, there is no reason to suppose the associated wavevector of the phonon softening would remain the same magnitude in this system. What matters is simply the observation that this crossover point also affects the bosonic kink, which, given its probable phonon origin, once again brings the lattice into the forefront in trying to understand these regions of the Fermi surface.

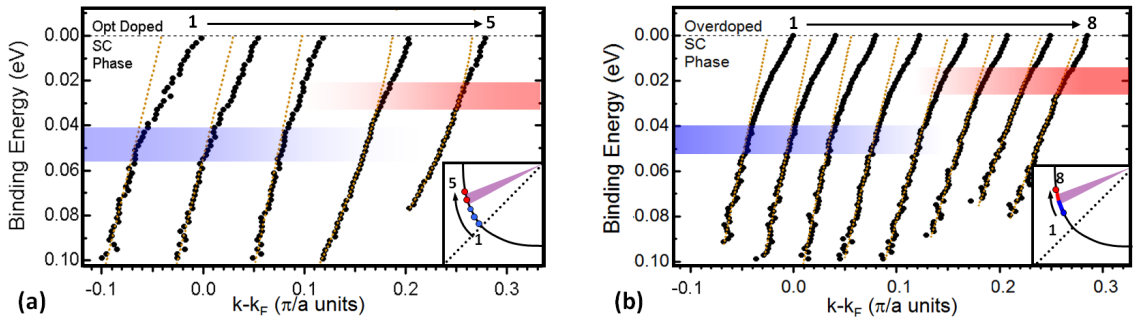

Figure 6.8. (a-b) Fitted band dispersions near E_F, horizontally shifted, from ARPES data on (a) OP and (b) OD samples in the SC phase. Data is taken near the crossover region, indicated in the respective insets, with dashed lines as guides to the eye, and high and low energy kinks indicated by blue and red, respectively.

6.4 Discussion

With these observations, it's worth spending some time to consider their potential significance. Some of this is summarized in Fig. 6.9 which provides a cartoon meant to bring together the several threads associated with this crossover region and its potential origin. The first and most important aspect of this crossover region (again indicated in violet) is that all of the effects discussed are sufficiently far from the antiferromagnetic zone boundary (dashed line) to preclude it as an explanation for what we observe. The role of this zone boundary may indeed be significant, perhaps providing another bookend to the effect that we are observing. The general proximity of the bosonic shift to the crossover region still seems to suggest a connection between the crossover and the softened Cu-O bond stretching phonon (region shaded gray). As mentioned, the associated softening wavevector, $\mathbf{q_{BS}}$, could connect the Fermi surface near the location of our crossover region.

But this points to a larger theme when we look at the literature on single layered compounds. For instance, one finds that this region also falls close to other Bi2201 work on Fermi arc formation using ARPES to determine the initial length[159]. Additionally, we have the aforementioned evolution in coherent peak spectral weight in the single layered bismuth compound, where the critical point of this spectral weight along k_F falls close to our region[110], and the doping trend is consistent. For their work, they associated this critical point with a crossover between nodal and antinodal states with anticorrelated behaviors. The most recent work on the La-Bi2201 compound by J. Meng et al.[177] is also strangely significant here as well. As particularly illustrated in Fig. 6.9, their ARPES work finds evidence of what appears to be a hole band pocket, symmetric over the ΓY line, which appears to reconnect with the main band structure in the k-space vicinity of our crossover point[177]. It is worth noting that this is observed in the underdoped compound, while being difficult to observe at optimal doping. Still, it is possible we are still seeing some effect related to this band crossing in our optimally doped data. The separation of the cuprate Fermi surface into hole and electron pockets has been strongly proposed by quantum oscillation[175,176]. Still,

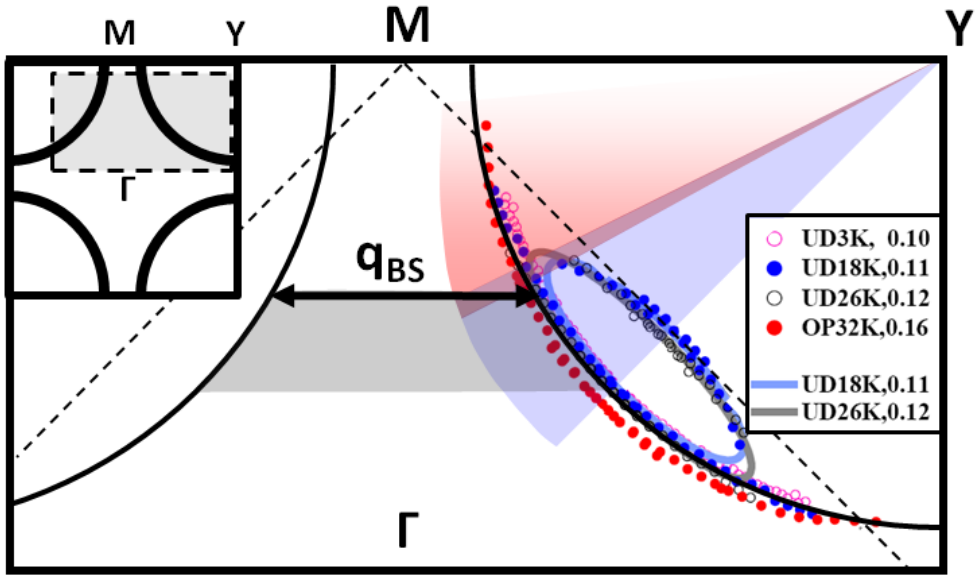

Figure 6.9. (a) Fermi surface cartoon summarizing the different issues associated with the crossover region. Colored angular regions correspond to the optimally doped sample's division of the Fermi surface. Grayed area corresponding to the region of the softened Cu-O BS phonon mode from Ref.[140]. Circular data points come from Ref.[177] indicating the Fermi surface pocket in La-Bi2201.

the correlation between the ARPES work and the pockets observed by quantum oscillation remains controversial.

Certainly, further work should be done on other strain compounds to look for evidence of this crossover. One might be tempted to look for trends in the bond stretching phonon for the different Bi2201 compounds like Nd-Bi2201. But this could be practically challenging since precisely identifying the softening of the wavevector may be difficult given how small a change could result in a substantial shift in the nesting location. However on the ARPES end, the challenge has been getting data of consistently significant quality beyond the nodal point in these compounds to allow for a convincing analysis. Indeed, the sharpness of the Nd-Bi2201 data is surprising given that the quasiparticle peak can be followed well beyond the antiferromagentic zone boundary. However, despite the disappearance of the quasiparticle peak coherence seen in STM for states beyond this zone boundary, this persistence in the peak we observe in ARPES is not necessarily surprising[184]. Although the angular range which one could observe the quasiparticle peak does shrink with increased strain (potentially a sign of increased disorder which scatters states near the zone edge and then states closer and closer to the nodal point) the Nd-Bi2201, however was a dramatic exception to this trend. This would lead one to wonder if there really is something special about the Nd-Bi2201 or if one should be able to get similarly good data on the other strain compounds as well. Finally, looking for evidence of these crossover effects in the double layered Bi2212 compounds is certainly important. From our study of the literature, one might be led to believe that this effect, whatever its origin, is more pronounced in the single layered compounds. Certainly single layered compounds host some interesting phenomena like stripe phenomena in 1/8 doped LSCO. It is possible that the low dimensionality of these systems allows for certain competing orders to be more pronounced and, thus, evidence of the crossover is more dramatic. But, it remains a subject in need of further study.

Chapter 7

Summary

Throughout this thesis, we have examined a variety of materials with different competing orders which affect the electronic band structure near E_F. By using Angle Resolved Photoemission Spectroscopy, we have the ability to directly see how those orders and effects modify these states giving us insight into the fundamental physics that is hosted by those systems. Our journey has taken us from evidence of magnetic orderings, to charge density wave orderings, to lattice strain/disorder effects, culminating in the specific case of Nd-Bi2201 where evidence of additional order beyond superconductivity could be responsible for the crossover between the nodal states and those further from the nodal point.

On the subject of magnetic ordering, we have used angle-integrated photoemission spectroscopy to explore core level peaks, the valence band density of states, and near E_F features in polycrystalline $LaFeAsO_{0.9}F_{0.1}$. Among our study of the core level peaks and features, we have found an anomalously large splitting of the As 3d peak and have explained it as a consequence of the anomalously low Fe magnetic moment. More significantly, we have identified two characteristic temperatures: 90K where a gap-like feature closes up and 120K where a more sudden change in the density of states occurs. Considering the antiferromagnetic ordering of the parent compound, we associate these with the spin density wave magnetic ordering and structural transition temperatures, respectively, which are seen at low doping. This result suggests that the electron doped superconducting phase does not entirely suppress the magnetic phenomena in the FeAs plane as recent theory has suggested[70]. This leads one naturally to wonder about magnetic phenomena in other materials like the superconducting cuprates.

When we switched gears and explored charge density wave phenomena in $LaTe_2$, we once again underscore the power of the ARPES technique in the study of these materials. Beyond the band structure comparisons, we have presented evidence that charge density wave formation in the single layer $LaTe_2$ system is a Fermi surface driven phenomena characterized by a CDW gap which opens over the entire Fermi surface despite its 2D nature. These results

establish $LaTe_2$ as the first proven instance of a quasi-2D CDW material whose CDW phase is both driven by Fermi surface nesting and semiconducting. The significant changes that we find associated with the number of Te layers as they reduce from two (in RTe_3) to one (in RTe_2) are intriguing: a large decrease of CDW gap size, and a large increase of gap isotropy besides the emergence of superconductivity ($CeTe_{1.82}$[81]). Understanding these changes may shed light on other correlated electron problems such as high temperature superconductivity, where the number of layers is already known to play a crucial role in determining the pseudogap formation temperature.

The controlled substitution of the single layered Bi2201 compounds with a spectrum of lanthanides has presented us with many exciting prospects but still nagging questions. Our work has shown that, regardless of the nature its effect on the lattice (strain or disorder inducing), the substituted lanthanides do not significantly affect the lifetime of electronic states along the ΓY direction while probably affecting those along the Cu-O bond direction significantly. We have shown evidence that although the lifetime is generally unaffected, the nodal states provide evidence of an additional bosonic kink which appears at lower binding energy than the well known $\sim$ 70meV kink. The proximity of the energy of this kink to that seen closer to the antinodal point (or which appears beyond the crossover in the Nd-Bi2201) may suggest a connection. This is particularly true if it is related to coupling to an additional mode such as the apical oxygen mode, which may be increasing the effective mass of the quasiparticles. For the most part, further study is needed to better understand the effect of the lanthanide substitution on the cuprates, whether it indeed couples to potentially competing orders that affect the antinodal states. Our current hypothesis is that it basically increasing disorder in the systems which affects antinodal states more. However, the sharpness of the quasiparticle along k_F for the strained Nd-Bi2201 as well as other unusual results, still casts doubt on this idea.

Still, bringing all these issues together, Nd-Bi2201 does present us with some remarkable conclusions which add weight to the importance of additional orderings (whether charge ordering, magnetic, or other lattice phenomena) to our understanding of these single layered cuprates. By studying both the optimally and overdoped regions of the phase diagram, we have found evidence of a narrow crossover region associated with: 1) A transition between two d-wave like gaps with different energy scales, 2) The initial formation of the Fermi arc in the pseudogap phase as seen in our optimally doped data, 3) An anomalous increase in the quasiparticle lifetime, and 4) The shift in the binding energy of the kink in the near E_F band structure. Although more work is needed to unravel the nature of this crossover considering its appearance in other single layered cuprate work, the transition between these two kink energy scales suggests a potential connection between the softening Cu-O bond stretching mode and the crossover.

With the growing power of time resolved and pump-probe ARPES experiments, the future study of many of these issues remains bright. Further study on the pnictides using laser based systems is greatly improved by the significant amount of important band structure near the Γ point. We have only begun to explore how strain may be affecting the nodal quasiparticle peak in pump-probe experiments. The interpretation of the data remains

challenging but the observation of effects such as the recovery of quasiparticle spectral weight and potential variation with strain is a curious result. Additionally, studying the effect of pump probe techniques on charge density wave materials may be crucial to understanding how states affected by this order behave differently in such experiments than states affected by superconductivity. This knowledge could be crucial when pump-probe measurements begin accessing the antinodal states, resulting in either provocative similaries, or clarifying differences between the antinodal gap and charge ordering phenomena. In any event, from our initial quantum mechanical explanation of band structure, to these profound intricacies of collective orderings, we hope that one can see how the field of correlated electronic physics, as studied by probes like ARPES, offers much for the student interested in the profound puzzles of nature.

Bibliography

1. Ashcroft, N. W. & Mermin, N. D. *Solid State Physics* (Saunders College Publishing, Fort Worth, 1976).

2. Valla, T. *et al.* Evidence for Quantum Critical Behavior in the Optimally Doped Cuprate Bi2Sr2CaCu2O8+. *Science* **285**, 2110–2113 (1999). URL `http://www.sciencemag.org/cgi/content/abstract/285/5436/2110`.

3. Peierls, R. Zur Theorie der elektrischen und thermischen Leitfahigkeit von Metallen. *Annals of Physics (Leipzig)* **4**, 121 (1930).

4. Peierls, R. E. *Quantum Theory of Solids* (Oxford: Clarendon Press, 1955).

5. Peierls, R. E. *More Surprises in Theoretical Physics* (Princeton University Press, Princeton, 1991).

6. Coleman, L. B., Cohen, M. J., Sandman, D. J., Yamagishi, F. G., Garito, A. F. & Heeger, A. J. Superconducting fluctuations and the peierls instability in an organic solid. *Solid State Communications* **12**, 1125–1132 (1973). URL `http://www.sciencedirect.com/science/article/B6TVW-46X9H57-9W/2/f602965642cc2abb5f370d024e40ff6f`.

7. Boswell, F. & Bennett, J. (eds.). *Advances in the Crystallographic and Microstructural Analysis of Charge Density Wave Modulated Crystals,* (Kluwer Academic Publishers, London, 1999).

8. Gweon, G.-H. *et al.* Direct Observation of Complete Fermi Surface, Imperfect Nesting, and Gap Anisotropy in the High-Temperature Incommensurate Charge-Density-Wave Compound $SmTe_3$. *Physical Review Letters* **81**, 886– (1998). URL `http://link.aps.org/doi/10.1103/PhysRevLett.81.886`.

9. A. M. Gabovich, A. I. Voitenko, J. F. A. & Ausloos, M. Charge- and Spin-Density-Wave Superconductors. *Superconding Science and Technology* **14**, R1–27 (2001).

10. Overhauser, A. W. Giant Spin Density Waves. *Phys. Rev. Lett.* **4**, 462– (1960). URL `http://link.aps.org/doi/10.1103/PhysRevLett.4.462`.

11. Rice, T. Band-Structure Effects in Itinerant Antiferromagnetism. *Physical Review B* **2**, 36193630 (1970).

12. Varma, C. M., Littlewood, P. B., Schmitt-Rink, S., Abrahams, E. & Ruckenstein, A. E. Phenomenology of the normal state of Cu-O high-temperature superconductors. *Phys. Rev. Lett.* **63**, 1996– (1989). URL http://link.aps.org/doi/10.1103/PhysRevLett.63.1996.

13. Xu, Z., Ong, N., Wang, Y., Kakeshita, T. & Uchida, S. Vortex-Like Excitations and the Onset of Superconducting Phase Fluctuation in Underdoped $La_{2-x}Sr_xCuO_4$. *Nature* **406**, 486–488 (2000).

14. Yuan, H. Q., Singleton, J., Balakirev, F. F., Baily, S. A., Chen, G. F., Luo, J. L. & Wang, N. L. Nearly isotropic superconductivity in (Ba,K)Fe2As2. *Nature* **457**, 565–568 (2009). URL http://dx.doi.org/10.1038/nature07676.

15. Traum, M. M., Smith, N. V. & Di Salvo, F. J. Angular Dependence of Photoemission and Atomic Orbitals in the Layer Compound 1 T-TaSe $_2$. *Phys. Rev. Lett.* **32**, 1241– (1974). URL http://link.aps.org/doi/10.1103/PhysRevLett.32.1241.

16. Rowe, J. E., Traum, M. M. & Smith, N. V. Measurement of the Angle of Dangling-Bond Photoemission from Cleaved Silicon. *Phys. Rev. Lett.* **33**, 1333– (1974). URL http://link.aps.org/doi/10.1103/PhysRevLett.33.1333.

17. Shen, Z.-X. *et al.* Anomalously large gap anisotropy in the a-b plane of Bi $_2$Sr $_2$CaCu $_2$O $_{8+\delta}$. *Phys. Rev. Lett.* **70**, 1553– (1993). URL http://link.aps.org/doi/10.1103/PhysRevLett.70.1553.

18. Koralek, J. D. *et al.* Laser Based Angle-Resolved Photoemission, the Sudden Approximation, and Quasiparticle-Like Spectral Peaks in $Bi_2Sr_2CaCu_2O_{8+\delta}$. *Phys. Rev. Lett.* **96**, 017005– (2006). URL http://link.aps.org/doi/10.1103/PhysRevLett.96.017005.

19. Hüfner, S. *Photoelectron Spectroscopy* (Springer, Berlin, 1995).

20. Seah, M. P. & Dench, W. A. Quantitative electron spectroscopy of surfaces: A standard data base for electron inelastic mean free paths in solids. *Surf. Interface Anal.* **1**, 2–11 (1979). URL http://dx.doi.org/10.1002/sia.740010103.

21. Sakurai, J. *Modern Quantum Mechanics Revised Edition* (Addison-Wesley, Reading, Massachusetts, 1994).

22. Randeria, M. *et al.* Momentum Distribution Sum Rule for Angle-Resolved Photoemission. *Phys. Rev. Lett.* **74**, 4951– (1995). URL http://link.aps.org/doi/10.1103/PhysRevLett.74.4951.

23. Yoshida, T. *et al.* Thermodynamic and transport properties of underdoped cuprates from ARPES data. *Physica B: Condensed Matter* **351**, 250–255 (2004). URL http://www.sciencedirect.com/science/article/B6TVH-4CYGWT3-3/2/463664f1f992589482e2a355e974d894.

24. Norman, M. R., Randeria, M., Ding, H. & Campuzano, J. C. Phenomenology of the low-energy spectral function in high-T $_c$ superconductors. *Phys. Rev. B* **57**, R11093– (1998). URL http://link.aps.org/doi/10.1103/PhysRevB.57.R11093.

25. Valla, T., Fedorov, A. V., Lee, J., Davis, J. C. & Gu, G. D. The Ground State of the Pseudogap in Cuprate Superconductors. *Science* **314**, 1914–1916 (2006). URL http://www.sciencemag.org/cgi/content/abstract/314/5807/1914.

26. Kanigel, A. *et al.* Evolution of the pseudogap from Fermi arcs to the nodal liquid. *Nat Phys* **2**, 447–451 (2006). URL http://dx.doi.org/10.1038/nphys334.

27. Rameau, J., Yang, H.-B. & Johnson, P. Application of the Lucy-Richardson deconvolution procedure to high resolution photoemission spectra. *Journal of Electron Spectroscopy and Related Phenomena* **181**, 35–43 (2010). URL http://www.sciencedirect.com/science/article/B6TGC-507BHKF-2/2/fd797942d3a09108c6c4f87d1feb56cd.

28. Yang, H.-B., Rameau, J. D., Johnson, P. D., Valla, T., Tsvelik, A. & Gu, G. D. Emergence of preformed Cooper pairs from the doped Mott insulating state in Bi2Sr2CaCu2O8+d. *Nature* **456**, 77–80 (2008). URL http://dx.doi.org/10.1038/nature07400.

29. Kamihara, Y., Watanabe, T., Hirano, M. & Hosono, H. Iron-Based Layered Superconductor La[O1-xFx]FeAs (x = 0.05-0.12) with Tc = 26 K. *Journal of the American Chemical Society* **130**, 3296–3297 (2008). URL http://dx.doi.org/10.1021/ja800073m.

30. Ma, F. & Lu, Z.-Y. Iron-based layered compound LaFeAsO is an antiferromagnetic semimetal. *Phys. Rev. B* **78**, 033111– (2008). URL http://link.aps.org/doi/10.1103/PhysRevB.78.033111.

31. Ren, Z.-A. *et al.* Superconductivity at 55 K in Iron-Based F-Doped Layered Quaternary Compound Sm[O1-xFx] FeAs. *Chinese Physics Letters* **25**, 2215 (2008).

32. Ren, Z.-A. *et al.* Superconductivity in the iron-based F-doped layered quaternary compound Nd[$O_{1-x}F_x$]FeAs. *Europhysical Letters* **82**, 57002 (2008).

33. Yang, J. *et al.* Superconductivity at 53.5 K in $GdFeAsO_{1-\delta}$. *Superconductor Science and Technology* **21**, 082001 (2008).

34. Ren, Z. A. *et al.* Superconductivity at 52 K in iron based F doped layered quaternary compound Pr[$O_{1-x}F_x$]FeAs. *Materials Research Innovations* **12**, 105–106 (2008).

35. Rotter, M., Tegel, M. & Johrendt, D. Superconductivity at 38 K in the Iron Arsenide ($Ba_{1-x}K_x$)Fe_2As_2. *Phys. Rev. Lett.* **101**, 107006– (2008). URL http://link.aps.org/doi/10.1103/PhysRevLett.101.107006.

36. Borisenko, S. V. *et al.* Superconductivity without Nesting in LiFeAs. *Phys. Rev. Lett.* **105**, 067002– (2010). URL http://link.aps.org/doi/10.1103/PhysRevLett.105.067002.

37. Singh, D. J. & Du, M.-H. Density Functional Study of LaFeAsO $_{1-x}$F $_x$: A Low Carrier Density Superconductor Near Itinerant Magnetism. *Phys. Rev. Lett.* **100**, 237003– (2008). URL http://link.aps.org/doi/10.1103/PhysRevLett.100.237003.

38. Luetkens, H. *et al.* The electronic phase diagram of the LaO1-xFxFeAs superconductor. *Nat Mater* **8**, 305–309 (2009). URL http://dx.doi.org/10.1038/nmat2397.

39. Wu, J., Phillips, P. & Castro Neto, A. H. Theory of the Magnetic Moment in Iron Pnictides. *Phys. Rev. Lett.* **101**, 126401– (2008). URL http://link.aps.org/doi/10.1103/PhysRevLett.101.126401.

40. de la Cruz, C. *et al.* Magnetic order close to superconductivity in the iron-based layered $LaO_{1-x}F_xFeAs$ systems. *Nature* **453**, 899–902 (2008). URL http://dx.doi.org/10.1038/nature07057.

41. Klauss, H.-H. *et al.* Commensurate Spin Density Wave in LaFeAsO: A Local Probe Study. *Phys. Rev. Lett.* **101**, 077005– (2008). URL http://link.aps.org/doi/10.1103/PhysRevLett.101.077005.

42. Dong, J. *et al.* Competing orders and spin-density-wave instability in La(O1-xFx)FeAs. *Europhysics Letters* **83**, 27006 (2008).

43. Kitao, S. *et al.* Spin Ordering in LaFeAsO and Its Suppression in Superconductor $LaFeAsO_{0.89}F_{0.11}$ Probed by Mossbauer Spectroscopy. *J. Phys. Soc. Jpn.* **77**, 103706– (2008).

44. Ou, H. W.and Zhao, J. F. *et al.* Angle Integrated Photoemission Study of SmO0.85F0.15FeAs. *Chinese Physics Letters* **25**, 2225 (2008).

45. Ishida, Y. *et al.* Temperature-dependent pseudogap in the oxypnictides LaFeAsO $_{1-x}$F $_x$ and LaFePO $_{1-x}$F $_x$ seen via angle-integrated photoemission. *Phys. Rev. B* **79**, 060503– (2009). URL http://link.aps.org/doi/10.1103/PhysRevB.79.060503.

46. Sato, T. *et al.* Superconducting Gap and Pseudogap in Iron-Based Layered Superconductor $La(O_{1-x}F_x)FeAs$. *J. Phys. Soc. Jpn.* **77**, 063708– (2008).

47. Liu, H. *et al.* Pseudogap and Superconducting Gap in Sm FeAs(O1-xFx) Superconductor from Photoemission Spectroscopy. *Chinese Physics Letters* **25**, 3761 (2008).

48. Jia, X. *et al.* Common Features in Electronic Structure of the Oxypnictide Superconductors from Photoemission Spectroscopy. *Chinese Physics Letters* **25**, 3765 (2008).

49. Liu, C. *et al.* Fermi surface and strong coupling superconductivity in single crystal $NdFeAsO_{1-x}F_x$. *arXiv:cond-mat/0806. 2147* (2008).

50. Liu, C. *et al.* K-Doping Dependence of the Fermi Surface of the Iron-Arsenic Ba $_{1-x}$K$_x$Fe$_2$As $_2$ Superconductor Using Angle-Resolved Photoemission Spectroscopy. *Phys. Rev. Lett.* **101**, 177005– (2008). URL `http://link.aps.org/doi/10.1103/PhysRevLett.101.177005`.

51. Zhao, L. *et al.* Multiple Nodeless Superconducting Gaps in (Ba0.6K0.4)Fe2As2 Superconductor from Angle-Resolved Photoemission Spectroscopy. *Chinese Physics Letters* **25**, 4402–4405 (2008).

52. Mazin, I. I., Singh, D. J., Johannes, M. D. & Du, M. H. Unconventional Superconductivity with a Sign Reversal in the Order Parameter of LaFeAsO $_{1-x}$F $_x$. *Phys. Rev. Lett.* **101**, 057003– (2008). URL `http://link.aps.org/doi/10.1103/PhysRevLett.101.057003`.

53. Nowik, I., Felner, I., Awana, V. P. S., Vajpayee, A. & Kishana, H. 57Fe Mossbauer spectroscopy and magnetic measurement studies of oxygen deficient LaFeAsO. *Journal of Physics: Condensed Matter* **20**, 292201 (2008).

54. Felner, I., Nowik, I., Tsindlekht, M. I., Ren, Z.-A., Shen, X.-L., Che, G.-C. & Zhao, Z.-X. Magnetic measurements and 57Fe Mossbauer spectroscopy in oxygen deficient SmFeAsO0.85. *arXiv:0805.2794v2* (2008).

55. Ahilan, K. *et al.* ^{19}F NMR investigation of the iron pnictide superconductor LaFeAsO $_{0.89}$F $_{0.11}$. *Phys. Rev. B* **78**, 100501– (2008). URL `http://link.aps.org/doi/10.1103/PhysRevB.78.100501`.

56. Zhu, Z. W. *et al.* Nernst effect of a new iron-based superconductor LaO1-xFxFeAs. *New Journal Physics* **10**, 063021 (2008).

57. Gonnelli, R. S., Daghero, D., Tortello, M., Ummarino, G. A., Stepanov, V. A., Kim, J. S. & Kremer, R. K. Coexistence of two order parameters and a pseudogaplike feature in the iron-based superconductor LaFeAsO $_{1-x}$F $_x$. *Phys. Rev. B* **79**, 184526– (2009). URL `http://link.aps.org/doi/10.1103/PhysRevB.79.184526`.

58. Drew, A. J. *et al.* Coexistence of static magnetism and superconductivity in SmFeAsO$_{1-x}$F$_x$ as revealed by muon spin rotation. *Nat Mater* **8**, 310–314 (2009). URL `http://dx.doi.org/10.1038/nmat2396`.

59. In spite of these mentioned post-synthesis analyses, it should be noted that the final Flourine concentration was not additionally verified by any chemical analysis of the final product. (2008).

60. Sawatzky, G. Private Communication (2008).

61. Cardona, M. & Ley, L. (eds.). *Photoemission in Solids I: General Principles* (Springer-Verlag, Berlin, 1978).

62. Koitzsch, A. *et al.* Valence-band and core-level photoemission spectroscopy of LaFeAsO $_{1-x}$F $_{x}$. *Phys. Rev. B* **78**, 180506– (2008). URL http://link.aps.org/doi/10.1103/PhysRevB.78.180506.

63. Cao, C., Hirschfeld, P. J. & Cheng, H.-P. Proximity of antiferromagnetism and superconductivity in LaFeAsO $_{1-x}$F $_{x}$: Effective Hamiltonian from ab initio studies. *Phys. Rev. B* **77**, 220506– (2008). URL http://link.aps.org/doi/10.1103/PhysRevB.77.220506.

64. Phillips, P. (2008). Private Communication.

65. Shen, Z.-x. *et al.* Anderson Hamiltonian description of the experimental electronic structure and magnetic interactions of copper oxide superconductors. *Phys. Rev. B* **36**, 8414– (1987). URL http://link.aps.org/doi/10.1103/PhysRevB.36.8414.

66. Kim, H.-D., Noh, H.-J., Kim, K. H. & Oh, S.-J. Core-Level X-Ray Photoemission Satellites in Ruthenates: A New Mechanism Revealing The Mott Transition. *Phys. Rev. Lett.* **93**, 126404– (2004). URL http://link.aps.org/doi/10.1103/PhysRevLett.93.126404.

67. Haule, K., Shim, J. H. & Kotliar, G. Correlated Electronic Structure of LaO $_{1-x}$F $_{x}$FeAs. *Phys. Rev. Lett.* **100**, 226402– (2008). URL http://link.aps.org/doi/10.1103/PhysRevLett.100.226402.

68. Yeh, J.-J. & Lindau, I. Atomic Subshell Photoionization Cross Sections and Asymmetry Parameters: 1<Z<103,. *At. Data Nucl. Data Tables* **32**, 1 (1985).

69. Hashimoto, M. *et al.* Distinct doping dependences of the pseudogap and superconducting gap of La $_{2-x}$Sr $_{x}$CuO $_{4}$ cuprate superconductors. *Phys. Rev. B* **75**, 140503– (2007). URL http://link.aps.org/doi/10.1103/PhysRevB.75.140503.

70. Mazin, I. I. & Johannes, M. D. A key role for unusual spin dynamics in ferropnictides. *Nat Phys* **5**, 141–145 (2009). URL http://dx.doi.org/10.1038/nphys1160.

71. Ding, H. *et al.* Observation of Fermi-surface dependent nodeless superconducting gaps in $Ba_{0.6}K_{0.4}Fe_2As_2$. *Europhysics Letters* **83**, 47001 (2008).

72. Sato, T. *et al.* Band Structure and Fermi Surface of an Extremely Overdoped Iron-Based Superconductor KFe_2As_2. *Phys. Rev. Lett.* **103**, 047002– (2009). URL http://link.aps.org/doi/10.1103/PhysRevLett.103.047002.

73. Chen, F. *et al.* Electronic structure of $Fe_{1.04}Te_{0.66}Se_{0.34}$. *Phys. Rev. B* **81**, 014526– (2010). URL http://link.aps.org/doi/10.1103/PhysRevB.81.014526.

74. Xia, Y. *et al.* Fermi Surface Topology and Low-Lying Quasiparticle Dynamics of Parent Fe_{1+x}Te/Se Superconductor. *Phys. Rev. Lett.* **103**, 037002– (2009). URL http://link.aps.org/doi/10.1103/PhysRevLett.103.037002.

75. Yi, M. *et al.* Unconventional electronic reconstruction in undoped (Ba,Sr)Fe_2As_2 across the spin density wave transition. *Phys. Rev. B* **80**, 174510– (2009). URL http://link.aps.org/doi/10.1103/PhysRevB.80.174510.

76. Morris, R. C. Connection between Charge-Density Waves and Superconductivity in NbSe $_2$. *Phys. Rev. Lett.* **34**, 1164– (1975). URL http://link.aps.org/doi/10.1103/PhysRevLett.34.1164.

77. Nunez-Regueiro, M., Mignot, J.-M., Jaime, M., Castello, D. & Monceau, P. Superconductivity under pressure in linear chalcogenides. *Synthetic Metals* **56**, 2653–2659 (1993). URL http://www.sciencedirect.com/science/article/B6TY7-48CX1GY-MX/2/fbd8ea98be8b1401f433a9f7c1201710.

78. Singh, Y., Nirmala, R., Ramakrishnan, S. & Malik, S. K. Competition between superconductivity and charge-density-wave ordering in the Lu $_5$Ir $_4$(Si $_{1-x}$Ge $_x$) $_{10}$ alloy system. *Phys. Rev. B* **72**, 045106– (2005). URL http://link.aps.org/doi/10.1103/PhysRevB.72.045106.

79. Fang, L. *et al.* Fabrication and superconductivity of Na $_x$TaS $_2$ crystals. *Phys. Rev. B* **72**, 014534– (2005). URL http://link.aps.org/doi/10.1103/PhysRevB.72.014534.

80. Morosan, E. *et al.* Superconductivity in CuxTiSe2. *Nat Phys* **2**, 544–550 (2006). URL http://dx.doi.org/10.1038/nphys360.

81. Jung, M. H. *et al.* Superconductivity in magnetically ordered CeTe $_{1.82}$. *Phys. Rev. B* **67**, 212504– (2003). URL http://link.aps.org/doi/10.1103/PhysRevB.67.212504.

82. Li, J.-X., Wu, C.-Q. & Lee, D.-H. Checkerboard charge density wave and pseudogap of high- T $_c$ cuprate. *Phys. Rev. B* **74**, 184515– (2006). URL http://link.aps.org/doi/10.1103/PhysRevB.74.184515.

83. McElroy, K. *et al.* Coincidence of Checkerboard Charge Order and Antinodal State Decoherence in Strongly Underdoped Superconducting Bi $_2$Sr $_2$CaCu $_2$O $_{8+\delta}$. *Phys. Rev. Lett.* **94**, 197005– (2005). URL http://link.aps.org/doi/10.1103/PhysRevLett.94.197005.

84. Brouet, V. *et al.* Fermi Surface Reconstruction in the CDW State of CeTe $_3$ Observed by Photoemission. *Phys. Rev. Lett.* **93**, 126405– (2004). URL http://link.aps.org/doi/10.1103/PhysRevLett.93.126405.

85. Shin, K. Y., Brouet, V., Ru, N., Shen, Z. X. & Fisher, I. R. Electronic structure and charge-density wave formation in LaTe $_{1.95}$ and CeTe $_{2.00}$. *Phys. Rev. B* **72**, 085132– (2005). URL http://link.aps.org/doi/10.1103/PhysRevB.72.085132.

86. DiMasi, E., Foran, B., Aronson, M. C. & Lee, S. Stability of charge-density waves under continuous variation of band filling in LaTe $_{2-x}$Sb $_x$. *Phys. Rev. B* **54**, 13587– (1996). URL http://link.aps.org/doi/10.1103/PhysRevB.54.13587.

87. Stowe, K. Crystal Structure and Electronic Band Structure of LaTe2. *Journal of Solid State Chemistry* **149**, 155 (2000).

88. Marcon, J. P. & Pascard, R. *Comptes Rendus Academy Science Paris* **266**, 270 (1968).

89. Jung, M.-H. *et al.* Anisotropic Transport and Magnetic Properties and. *J. Phys. Soc. Jpn.* **69**, 937– (2000).

90. Kwon, Y. S. & Min, B. H. Anisotropic transport properties in RTe2 (R: La, Ce, Pr, Sm and Gd). *Physica B: Condensed Matter* **281-282**, 120–121 (2000). URL http://www.sciencedirect.com/science/article/B6TVH-400WKV6-1R/2/f9058e404ab0f9cf084ff89d96324b4e.

91. Shim, J. H., Kang, J.-S. & Min, B. I. Electronic Structures of RTe_2 (R=La,Ce): A Clue to the Pressure-Induced Superconductivity in $CeTe_{1.82}$. *Phys. Rev. Lett.* **93**, 156406– (2004). URL http://link.aps.org/doi/10.1103/PhysRevLett.93.156406.

92. Grupe, M. & Urland, W. Darstellung und Kristallstruktur von LaSe1,9. *Journal of the Less Common Metals* **170**, 271–275 (1991). URL http://www.sciencedirect.com/science/article/B759D-48GNKK1-244/2/6c54afe67d52ba63fe2ab82b8ea847e1.

93. Lee, S. & Foran, B. Rationalization and prediction of rare earth selenide superstructures. *Journal of the American Chemical Society* **116**, 154–161 (1994). URL http://dx.doi.org/10.1021/ja00080a018.

94. Gweon, G. H. *et al.* Direct Fermi-surface image of hidden nesting for $NaMo_6O_{17}$ and KMo_6O_{17}. *Physical Review B* **55**, R13353– (1997). URL http://link.aps.org/doi/10.1103/PhysRevB.55.R13353.

95. Yokoya, T., Kiss, T., Chainani, A., Shin, S., Nohara, M. & Takagi, H. Fermi Surface Sheet-Dependent Superconductivity in 2H-NbSe2. *Science* **294**, 2518–2520 (2001). URL http://www.sciencemag.org/cgi/content/abstract/294/5551/2518.

96. Grüner, G. *Density Waves in Solids* (Addison-Wesley, Reading, Massachusetts, 1994).

97. Gweon, G.-H. *et al.* Fermi surfaces and single-particle spectral functions of low-dimensional inorganic non-cuprate compounds: the molybdenum bronzes. *Journal of Physics: Condensed Matter* **8**, 9923 (1996).

98. Colonna, S., Ronci, F., Cricenti, A., Perfetti, L., Berger, H. & Grioni, M. Mott Phase at the Surface of 1T-$TaSe_2$ Observed by Scanning Tunneling Microscopy. *Phys. Rev. Lett.* **94**, 036405– (2005). URL http://link.aps.org/doi/10.1103/PhysRevLett.94.036405.

99. Kim, J.-J., Yamaguchi, W., Hasegawa, T. & Kitazawa, K. Observation of Mott Localization Gap Using Low Temperature Scanning Tunneling Spectroscopy in Commensurate 1T-$TaSa_2$. *Phys. Rev. Lett.* **73**, 2103– (1994). URL http://link.aps.org/doi/10.1103/PhysRevLett.73.2103.

100. Kidd, T. E., Miller, T., Chou, M. Y. & Chiang, T.-C. Electron-Hole Coupling and the Charge Density Wave Transition in TiSe $_2$. *Phys. Rev. Lett.* **88**, 226402– (2002). URL http://link.aps.org/doi/10.1103/PhysRevLett.88.226402.

101. Kwon, Y. S. & Min, B. H. Anisotropic transport properties in RTe2 (R: La, Ce, Pr, Sm and Gd). *Physica B* **281-282**, 120–121 (2000).

102. Jung, M. H., Ekino, T., Kwon, Y. S. & Takabatake, T. Tunneling spectroscopy of RTe $_2$ (R=La, Ce) and possible coexistence between charge-density waves and magnetic order. *Phys. Rev. B* **63**, 035101– (2000). URL http://link.aps.org/doi/10.1103/PhysRevB.63.035101.

103. Yao, H., Robertson, J. A., Kim, E.-A. & Kivelson, S. A. Theory of stripes in quasi-two-dimensional rare-earth tellurides. *Phys. Rev. B* **74**, 245126– (2006). URL http://link.aps.org/doi/10.1103/PhysRevB.74.245126.

104. Lanzara, A. *et al.* Evidence for ubiquitous strong electron-phonon coupling in high-temperature superconductors. *Nature* **412**, 510–514 (2001). URL http://dx.doi.org/10.1038/35087518.

105. Chakravarty, S., Kee, H.-Y. & Volker, K. An explanation for a universality of transition temperatures in families of copper oxide superconductors. *Nature* **428**, 53–55 (2004). URL http://dx.doi.org/10.1038/nature02348.

106. Eisaki, H. *et al.* Effect of chemical inhomogeneity in bismuth-based copper oxide superconductors. *Phys. Rev. B* **69**, 064512– (2004). URL http://link.aps.org/doi/10.1103/PhysRevB.69.064512.

107. Rowell, J. M., Anderson, P. W. & Thomas, D. E. Image of the Phonon Spectrum in the Tunneling Characteristic Between Superconductors. *Phys. Rev. Lett.* **10**, 334– (1963). URL http://link.aps.org/doi/10.1103/PhysRevLett.10.334.

108. Schrieffer, J. R., Scalapino, D. J. & Wilkins, J. W. Effective Tunneling Density of States in Superconductors. *Phys. Rev. Lett.* **10**, 336– (1963). URL http://link.aps.org/doi/10.1103/PhysRevLett.10.336.

109. Garcia, D. & Lanzara, A. Through a Lattice Darkly Shedding Light on the Electron-Phonon Coupling in the High Tc Cuprates. *Advances in Condensed Matter Physics - Phonons and Electron Correlations in High-Temperature and Other Novel Superconductors (HTS)* **2010**, Article ID 807412 (2010).

110. Kondo, T., Khasanov, R., Takeuchi, T., Schmalian, J. & Kaminski, A. Competition between the pseudogap and superconductivity in the high-Tc copper oxides. *Nature* **457**, 296–300 (2009). URL http://dx.doi.org/10.1038/nature07644.

111. Emery, V. & Kivelson, S. Frustrated electronic phase separation and high-temperature superconductors. *Physica C: Superconductivity* **209**, 597–621 (1993).

URL http://www.sciencedirect.com/science/article/B6TVJ-46JH1GP-P3/2/230ec511b0a037f647c4cafe7b18cdac.

112. Castellani, C., Di Castro, C. & Grilli, M. Singular Quasiparticle Scattering in the Proximity of Charge Instabilities. *Phys. Rev. Lett.* **75**, 4650– (1995). URL http://link.aps.org/doi/10.1103/PhysRevLett.75.4650.

113. Saini, N. L. *et al.* Topology of the Pseudogap and Shadow Bands in $Bi_2Sr_2CaCu_2O_{8+\delta}$ at Optimum Doping. *Phys. Rev. Lett.* **79**, 3467– (1997). URL http://link.aps.org/doi/10.1103/PhysRevLett.79.3467.

114. Tanaka, K. *et al.* Distinct Fermi-Momentum-Dependent Energy Gaps in Deeply Underdoped Bi2212. *Science* **314**, 1910–1913 (2006). URL http://www.sciencemag.org/cgi/content/abstract/314/5807/1910.

115. Lee, W. S. *et al.* Abrupt onset of a second energy gap at the superconducting transition of underdoped Bi2212. *Nature* **450**, 81–84 (2007). URL http://dx.doi.org/10.1038/nature06219.

116. Bogdanov, P. V. *et al.* Evidence for an Energy Scale for Quasiparticle Dispersion in $Bi_2Sr_2CaCu_2O_8$. *Phys. Rev. Lett.* **85**, 2581– (2000). URL http://link.aps.org/doi/10.1103/PhysRevLett.85.2581.

117. Rossat-Mignod, J. & et al. *Physica (Amsterdam)* **59**, 235C (1994).

118. Fong, H. F., Keimer, B., Milius, D. L. & Aksay, I. A. Superconductivity-Induced Anomalies in the Spin Excitation Spectra of Underdoped $YBa_2Cu_3O_{6+x}$. *Phys. Rev. Lett.* **78**, 713– (1997). URL http://link.aps.org/doi/10.1103/PhysRevLett.78.713.

119. Arai, M. *et al.* Incommensurate Spin Dynamics of Underdoped Superconductor $YBa_2Cu_3O_{6.7}$. *Phys. Rev. Lett.* **83**, 608– (1999). URL http://link.aps.org/doi/10.1103/PhysRevLett.83.608.

120. Dai, P., Mook, H. A., Hayden, S. M., Aeppli, G., Perring, T. G., Hunt, R. D. & Dogan, F. The Magnetic Excitation Spectrum and Thermodynamics of High-Tc Superconductors. *Science* **284**, 1344–1347 (1999). URL http://www.sciencemag.org/cgi/content/abstract/284/5418/1344.

121. Dai, P., Yethiraj, M., Mook, H. A., Lindemer, T. B. & Dogbrevean, F. Magnetic Dynamics in Underdoped $YBa_2Cu_3O_{7-x}$: Direct Observation of a Superconducting Gap. *Phys. Rev. Lett.* **77**, 5425– (1996). URL http://link.aps.org/doi/10.1103/PhysRevLett.77.5425.

122. McQueeney, R. J., Petrov, Y., Egami, T., Yethiraj, M., Shirane, G. & Endoh, Y. Anomalous Dispersion of LO Phonons in $La_{1.85}Sr_{0.15}CuO_4$ at Low Temperatures. *Phys. Rev. Lett.* **82**, 628– (1999). URL http://link.aps.org/doi/10.1103/PhysRevLett.82.628.

123. et al., X. J. Z. *"Treatise of High Temperature Superconductivity", Handbook of High-Temperature Superconductivity: Theory and Experiment* (Springer, 2007).

124. Lanzara, A. *et al.* Normal state spectral lineshapes of nodal quasiparticles in single layer Bi2201 superconductor. *Journal of Physics and Chemistry of Solids* **67**, 239–243 (2006). URL http://www.sciencedirect.com/science/article/B6TXR-4HM87GN-1/2/f12649afff898a3bcb1e605a766538e7.

125. Gweon, G. H., Zhou, S. Y. & Lanzara, A. Strong influence of phonons on the electron dynamics of Bi2Sr2CaCu2O8+[delta]. *Journal of Physics and Chemistry of Solids* **65**, 1397–1401 (2004). URL http://www.sciencedirect.com/science/article/B6TXR-4BWMNJ5-1/2/d6da4b495d466190826c14fbaf16a59d.

126. Dessau, D. S. *et al.* Anomalous spectral weight transfer at the superconducting transition of $Bi_2Sr_2CaCu_2O_{8+\delta}$. *Phys. Rev. Lett.* **66**, 2160– (1991). URL http://link.aps.org/doi/10.1103/PhysRevLett.66.2160.

127. Hwu, Y. *et al.* Electronic spectrum of the high-temperature superconducting state. *Phys. Rev. Lett.* **67**, 2573– (1991). URL http://link.aps.org/doi/10.1103/PhysRevLett.67.2573.

128. Rossat-Mignod, J. *et al.* Neutron scattering study of the YBa2Cu3O6+x system. *Physica C: Superconductivity* **185-189**, 86–92 (1991). URL http://www.sciencedirect.com/science/article/B6TVJ-46WX8TF-V/2/badbbe6369fa5949b748c06a3b85c286.

129. Mook, H. A., Yethiraj, M., Aeppli, G., Mason, T. E. & Armstrong, T. Polarized neutron determination of the magnetic excitations in YBa $_2$Cu $_3$O $_7$. *Phys. Rev. Lett.* **70**, 3490– (1993). URL http://link.aps.org/doi/10.1103/PhysRevLett.70.3490.

130. Fong, H. F. *et al.* Neutron scattering from magnetic excitations in Bi2Sr2CaCu2O8+[delta]. *Nature* **398**, 588–591 (1999). URL http://dx.doi.org/10.1038/19255.

131. Feng, D. L. *et al.* Bilayer Splitting in the Electronic Structure of Heavily Overdoped Bi $_2$Sr $_2$CaCu $_2$O $_{8+delta}$. *Phys. Rev. Lett.* **86**, 5550– (2001). URL http://link.aps.org/doi/10.1103/PhysRevLett.86.5550.

132. Chuang, Y.-D. *et al.* Doubling of the Bands in Overdoped Bi $_2$Sr $_2$CaCu $_2$O $_{8+delta}$: Evidence for c-Axis Bilayer Coupling. *Phys. Rev. Lett.* **87**, 117002– (2001). URL http://link.aps.org/doi/10.1103/PhysRevLett.87.117002.

133. Bogdanov, P. V. *et al.* Photoemission study of Pb doped Bi $_2$Sr $_2$CaCu $_2$O $_8$: A Fermi surface picture. *Phys. Rev. B* **64**, 180505– (2001). URL http://link.aps.org/doi/10.1103/PhysRevB.64.180505.

134. Gromko, A. D. *et al.* Mass-renormalized electronic excitations at (pi ,0) in the superconducting state of Bi $_2$Sr $_2$CaCu $_2$O $_{8+delta}$. *Phys. Rev. B* **68**, 174520– (2003). URL http://link.aps.org/doi/10.1103/PhysRevB.68.174520.

135. Kaminski, A. *et al.* Renormalization of Spectral Line Shape and Dispersion below T_c in $Bi_2Sr_2CaCu_2O_{8+\delta}$. *Phys. Rev. Lett.* **86**, 1070– (2001). URL http://link.aps.org/doi/10.1103/PhysRevLett.86.1070.

136. Kim, T. K., Kordyuk, A. A., Borisenko, S. V., Koitzsch, A., Knupfer, M., Berger, H. & Fink, J. Doping Dependence of the Mass Enhancement in (Pb,Bi) $_2$Sr $_2$CaCu $_2$O $_8$ at the Antinodal Point in the Superconducting and Normal States. *Phys. Rev. Lett.* **91**, 167002– (2003). URL http://link.aps.org/doi/10.1103/PhysRevLett.91.167002.

137. Cuk, T. *et al.* Coupling of the B $_{1g}$ Phonon to the Antinodal Electronic States of Bi $_2$Sr $_2$Ca $_{0.92}$Y $_{0.08}$Cu $_2$O $_{8+delta}$. *Phys. Rev. Lett.* **93**, 117003– (2004). URL http://link.aps.org/doi/10.1103/PhysRevLett.93.117003.

138. Rotenberg, E., Schaefer, J. & Kevan, S. D. Coupling Between Adsorbate Vibrations and an Electronic Surface State. *Phys. Rev. Lett.* **84**, 2925– (2000). URL http://link.aps.org/doi/10.1103/PhysRevLett.84.2925.

139. Gweon, G.-H., Sasagawa, T., Zhou, S., Graf, J., Takagi, H., Lee, D.-H. & Lanzara, A. An unusual isotope effect in a high-transition-temperature superconductor. *Nature* **430**, 187–190 (2004). URL http://dx.doi.org/10.1038/nature02731.

140. Graf, J. *et al.* Bond Stretching Phonon Softening and Kinks in the Angle-Resolved Photoemission Spectra of Optimally Doped Bi $_2$Sr $_{1.6}$La $_{0.4}$Cu $_2$O $_{6+\delta}$ Superconductors. *Phys. Rev. Lett.* **100**, 227002– (2008). URL http://link.aps.org/doi/10.1103/PhysRevLett.100.227002.

141. Kondo, T., Takeuchi, T., Kaminski, A., Tsuda, S. & Shin, S. Evidence for Two Energy Scales in the Superconducting State of Optimally Doped (Bi,Pb) $_2$(Sr,La) $_2$CuO $_{6+\delta}$. *Phys. Rev. Lett.* **98**, 267004– (2007). URL http://link.aps.org/doi/10.1103/PhysRevLett.98.267004.

142. Gweon, G.-H., Zhou, S. Y., Watson, M. C., Sasagawa, T., Takagi, H. & Lanzara, A. Strong and Complex Electron-Lattice Correlation in Optimally Doped Bi $_2$Sr $_2$CaCu $_2$O $_{8+delta}$. *Phys. Rev. Lett.* **97**, 227001– (2006). URL http://link.aps.org/doi/10.1103/PhysRevLett.97.227001.

143. Chen, X.-J., Struzhkin, V. V., Yu, Y., Goncharov, A. F., Lin, C.-T., Mao, H.-k. & Hemley, R. J. Enhancement of superconductivity by pressure-driven competition in electronic order. *Nature* **466**, 950–953 (2010). URL http://dx.doi.org/10.1038/nature09293.

144. Chen, X.-J., Struzhkin, V. V., Hemley, R. J., Mao, H.-k. & Kendziora, C. High-pressure phase diagram of Bi $_2$Sr $_2$CaCu $_2$O $_{8+delta}$ single crystals. *Phys. Rev. B* **70**, 214502– (2004). URL http://link.aps.org/doi/10.1103/PhysRevB.70.214502.

145. Cuk, T. *et al.* Uncovering a Pressure-Tuned Electronic Transition in Bi $_{1.98}$Sr $_{2.06}$Y $_{0.68}$Cu $_2$O $_{8+\delta}$ using Raman Scattering and X-Ray Diffraction. *Phys. Rev. Lett.*

100, 217003– (2008). URL http://link.aps.org/doi/10.1103/PhysRevLett.100.217003.

146. Bianconi, A., Agrestini, S., Bianconi, G., Di Castro, D. & Saini, N. A quantum phase transition driven by the electron lattice interaction gives high TC superconductivity. *Journal of Alloys and Compounds* **317-318**, 537–541 (2001). URL http://www.sciencedirect.com/science/article/B6TWY-42SH1F1-5K/2/d2e4c001b1f9a6d6b48066d57e47bb60.

147. Sanna, S., Agrestini, S., Zheng, K., De Renzi, R. & Saini, N. L. Experimental evidence of chemical-pressurecontrolled superconductivity in cuprates. *Europhysics Letters* **86**, 67007 (2009).

148. Hobou, H., Ishida, S., Fujita, K., Ishikado, M., Kojima, K. M., Eisaki, H. & Uchida, S. Enhancement of the superconducting critical temperature in Bi $_2$Sr $_2$CaCu $_2$O $_{8+\delta}$ by controlling disorder outside CuO $_2$ planes. *Phys. Rev. B* **79**, 064507– (2009). URL http://link.aps.org/doi/10.1103/PhysRevB.79.064507.

149. Hashimoto, M. *et al.* Effects of out-of-plane disorder on the nodal quasiparticle and superconducting gap in single-layer Bi $_2$Sr $_{1.6}$L $_{0.4}$CuO $_{6+\delta}$ (L=La,Nd,Gd). *Phys. Rev. B* **79**, 144517– (2009). URL http://link.aps.org/doi/10.1103/PhysRevB.79.144517.

150. Okada, Y., Takeuchi, T., Baba, T., Shin, S. & Ikuta, H. Origin of the Anomalously Strong Influence of Out-of-Plane Disorder on High-Tc Superconductivity. *Journal of the Physical Society of Japan* **77**, 074714 (2008).

151. Fujita, K., Noda, T., Kojima, K. M., Eisaki, H. & Uchida, S. Effect of Disorder Outside the CuO2 Planes on Tc of Copper Oxide Superconductors. *Physical Review Letters* **95**, 097006 (2005).

152. Nameki, H., Kikuchi, M. & Syono, Y. Effects of lanthanoid substitution on superconductivity and modulated structure of Bi2Sr2CuOy. *Physica C: Superconductivity* **234**, 255–262 (1994). URL http://www.sciencedirect.com/science/article/B6TVJ-46SNMRS-1D/2/584028ede8d42029e5076fae0a642dfc.

153. Okada, Y. *et al.* Momentum dependence of the energy gap in the superconducting state of optimally doped Bi2(Sr,R)2CuOy (R=La and Eu). *Journal of Physics: Conference Series* **150**, 052197 (2009).

154. Sugimoto, A. *et al.* Enhancement of electronic inhomogeneities due to out-of-plane disorder in Bi2Sr2CuO6+d superconductors observed by scanning tunneling spectroscopy. *Phys. Rev. B* **74**, 094503 (2006).

155. Attfield, J. P., Kharlanov, A. L. & McAllister, J. A. Cation effects in doped La2CuO4 superconductors. *Nature* **394** (1998).

156. Carlin, R. L. *Magnetochemistry* (1986).

157. Sato, T., Matsui, H., Nishina, S., Takahashi, T., Fujii, T., Watanabe, T. & Matsuda, A. Low Energy Excitation and Scaling in Bi $_2$Sr $_2$Ca $_{n-1}$Cu $_n$O $_{2n+4}$: Angle-Resolved Photoemission Spectroscopy. *Phys. Rev. Lett.* **89**, 067005– (2002). URL `http://link.aps.org/doi/10.1103/PhysRevLett.89.067005`.

158. Koitzsch, A. *et al.* Origin of the shadow Fermi surface in Bi -based cuprates. *Phys. Rev. B* **69**, 220505– (2004). URL `http://link.aps.org/doi/10.1103/PhysRevB.69.220505`.

159. Nakayama, K. *et al.* Evolution of a Pairing-Induced Pseudogap from the Superconducting Gap of $(Bi,Pb)_2Sr_2CuO_6$. *Phys. Rev. Lett.* **102**, 227006– (2009). URL `http://link.aps.org/doi/10.1103/PhysRevLett.102.227006`.

160. Andergassen, S., Caprara, S., Di Castro, C. & Grilli, M. Anomalous Isotopic Effect Near the Charge-Ordering Quantum Criticality. *Phys. Rev. Lett.* **87**, 056401– (2001). URL `http://link.aps.org/doi/10.1103/PhysRevLett.87.056401`.

161. Lanzara, A. ., Zhao, G.-M., Saini, N. L., Bianconi, A., Conder, K., Keller, H. & Mller, K. A. Oxygen-isotope shift of the charge-stripe ordering temperature in La2-xSrxCuO4 from x-ray absorption spectroscopy. *Journal of Physics: Condensed Matter* **11**, L541 (1999).

162. Rubio Temprano, D., Mesot, J., Janssen, S., Conder, K., Furrer, A., Mutka, H. & Müller, K. A. Large Isotope Effect on the Pseudogap in the High-Temperature Superconductor HoBa $_2$Cu $_4$O $_8$. *Phys. Rev. Lett.* **84**, 1990– (2000). URL `http://link.aps.org/doi/10.1103/PhysRevLett.84.1990`.

163. Bianconi, A. *et al.* Determination of the Local Lattice Distortions in the CuO $_2$ Plane of La $_{1.85}$Sr $_{0.15}$CuO $_4$. *Phys. Rev. Lett.* **76**, 3412– (1996). URL `http://link.aps.org/doi/10.1103/PhysRevLett.76.3412`.

164. Seibold, G. & Grilli, M. Influence of incommensurate dynamic charge-density-wave scattering on the photoemission line shape of superconducting high-T $_c$ cuprates. *Phys. Rev. B* **63**, 224505– (2001). URL `http://link.aps.org/doi/10.1103/PhysRevB.63.224505`.

165. Lee, W. *et al.* Study of $HgBa_2CuO_{4+\delta}$ by Angle-Resolved Photoemission Spectroscopy. *arXiv:cond-mat/0606347v1* (2006).

166. Norman, M. R. Chasing Arcs in Cuprate Superconductors. *Science* **325**, 1080–1081 (2009). URL `http://www.sciencemag.org`.

167. Perali, A., Castellani, C., Di Castro, C., Grilli, M., Piegari, E. & Varlamov, A. A. Two-gap model for underdoped cuprate superconductors. *Phys. Rev. B* **62**, R9295– (2000). URL `http://link.aps.org/doi/10.1103/PhysRevB.62.R9295`.

168. Bianconi, A. *et al.* Stripe structure in the CuO $_2$ plane of perovskite superconductors. *Phys. Rev. B* **54**, 12018– (1996). URL http://link.aps.org/doi/10.1103/PhysRevB.54.12018.

169. Harris, J. M. *et al.* Measurement of an Anisotropic Energy Gap in Single Plane Bi $_2$Sr $_{2-x}$La $_x$CuO $_{6+\delta}$. *Phys. Rev. Lett.* **79**, 143– (1997). URL http://link.aps.org/doi/10.1103/PhysRevLett.79.143.

170. Deutscher, G. Coherence and single-particle excitations in the high-temperature superconductors. *Nature* **397**, 410–412 (1999). URL http://dx.doi.org/10.1038/17075.

171. He, R.-H. *et al.* Energy gaps in the failed high-Tc superconductor La1.875Ba0.125CuO4. *Nat Phys* **5**, 119–123 (2009). URL http://dx.doi.org/10.1038/nphys1159.

172. Kanigel, A., Chatterjee, U., Randeria, M., Norman, M. R., Koren, G., Kadowaki, K. & Campuzano, J. C. Evidence for Pairing above the Transition Temperature of Cuprate Superconductors from the Electronic Dispersion in the Pseudogap Phase. *Phys. Rev. Lett.* **101**, 137002– (2008). URL http://link.aps.org/doi/10.1103/PhysRevLett.101.137002.

173. Meng, J. *et al.* Monotonic d -wave superconducting gap of the optimally doped $Bi_2Sr_{1.6}La_{0.4}CuO_6$ superconductor by laser-based angle-resolved photoemission spectroscopy. *Phys. Rev. B* **79**, 024514– (2009). URL http://link.aps.org/doi/10.1103/PhysRevB.79.024514.

174. Kohsaka, Y. *et al.* How Cooper pairs vanish approaching the Mott insulator in Bi2Sr2CaCu2O8+[d]. *Nature* **454**, 1072–1078 (2008). URL http://dx.doi.org/10.1038/nature07243.

175. Doiron-Leyraud, N. *et al.* Quantum oscillations and the Fermi surface in an underdoped high-Tc superconductor. *Nature* **447**, 565–568 (2007). URL http://dx.doi.org/10.1038/nature05872.

176. Sebastian, S. E. *et al.* A multi-component Fermi surface in the vortex state of an underdoped high-Tc superconductor. *Nature* **454**, 200–203 (2008). URL http://dx.doi.org/10.1038/nature07095.

177. Meng, J. *et al.* Coexistence of Fermi arcs and Fermi pockets in a high-Tc copper oxide superconductor. *Nature* **462**, 335–338 (2009). URL http://dx.doi.org/10.1038/nature08521.

178. Borisenko, S. V. *et al.* Superconducting gap in the presence of bilayer splitting in underdoped $(Pb,Bi)_2Sr_2CaCu_2O_{8+\delta}$. *Phys. Rev. B* **66**, 140509– (2002). URL http://link.aps.org/doi/10.1103/PhysRevB.66.140509.

179. Mesot, J. *et al.* Superconducting Gap Anisotropy and Quasiparticle Interactions: A Doping Dependent Photoemission Study. *Phys. Rev. Lett.* **83**, 840– (1999). URL http://link.aps.org/doi/10.1103/PhysRevLett.83.840.

180. Lavrov, A. N., Ando, Y. & Ono, S. Two mechanisms of pseudogap formation in Bi-2201: Evidence from the c-axis magnetoresistance. *Europhysical Letters* **57**, 267 (2002).

181. Kaminski, A. *et al.* Momentum anisotropy of the scattering rate in cuprate superconductors. *Phys. Rev. B* **71**, 014517– (2005). URL `http://link.aps.org/doi/10.1103/PhysRevB.71.014517`.

182. Yoshida, T. *et al.* Electronlike Fermi surface and remnant (pi ,0) feature in overdoped La $_{1.78}$Sr $_{0.22}$CuO $_{4}$. *Phys. Rev. B* **63**, 220501– (2001). URL `http://link.aps.org/doi/10.1103/PhysRevB.63.220501`.

183. Terashima, K., Matsui, H., Sato, T., Takahashi, T., Kofu, M. & Hirota, K. Anomalous Momentum Dependence of the Superconducting Coherence Peak and Its Relation to the Pseudogap of La $_{1.85}$Sr $_{0.15}$CuO $_{4}$. *Phys. Rev. Lett.* **99**, 017003– (2007). URL `http://link.aps.org/doi/10.1103/PhysRevLett.99.017003`.

184. Lee, D.-H. Private Communication (2008).